UC Santa Barbara
UC Santa Barbara Electronic Theses and Dissertations

Title
Searching for higgsinos with the CMS experiment

Permalink
https://escholarship.org/uc/item/56d5x8sr

Author
Oshiro, Michael

Publication Date
2023

Peer reviewed|Thesis/dissertation

eScholarship.org Powered by the California Digital Library
University of California

University of California
Santa Barbara

Searching for higgsinos with the CMS experiment

A dissertation submitted in partial satisfaction
of the requirements for the degree

Doctor of Philosophy
in
Physics

by

Michael C. Oshiro

Committee in charge:

Professor Jeffrey Richman, Chair
Professor David Stuart
Professor Nathaniel Craig

June 2023

The Dissertation of Michael C. Oshiro is approved.

Professor David Stuart

Professor Nathaniel Craig

Professor Jeffrey Richman, Committee Chair

May 2023

Searching for higgsinos with the CMS experiment

Copyright © 2023

by

Michael C. Oshiro

Acknowledgements

As with all scientific pursuits, the work in this thesis was only possible because of the giants on whose shoulders I have stood. Starting with the more scientific meaning of the phrase, I have been extremely fortunate, not just to have the privilege of working on the CMS experiment at the LHC, but also to have been guided by an amazing team of mentors. In addition to my advisor Jeffrey Richman, professors Claudio Campagnari, David Stuart, Nathaniel Craig, Keith Ulmer, Bill Ford, and Anders Ryd have all been amazing teachers without whom the work in this thesis would not be. Thanks is also due to my undergraduate mentors Simone Pagan Griso and Laura Jeanty for being my first teachers of high energy physics. I would also be remiss not to attribute much of my learning to postdocs Hualin Mei, whose work on ODMB software and firmware was of great assistance; Ana Ovcharova, who helped me get off to a great start in the Richman group; and Jaebak Kim, whose mentorship contributed to essentially every section of this thesis. I will forever miss the pre-pandemic lunches with Ana, Jaebak, and Alex. My graduate student mentors include Sicheng Wang, Emily Fair, and Alex Dorsett. In particular, Alex provided me with more mentorship than anyone else, and his work on his own thesis contributed greatly to the quality of this one. Thanks is also due to Anders Barzdukas, who has been a wonderful collaborator; I couldn't think of anyone better to take the role of senior graduate student in the Richman group. I look forward to continuing to work with Jeff, Anders Barzdukas, Jaebak, Anders Ryd, and the rest of the Cornell group.

Less obvious but no less important are the giants who provided friendship and emotional support. The virtual companionship of my highschool friends Samir Quadri, Kaudry King, and Troy Reed as well as college friend Amit Akula greatly helped get me through the strange years that were the COVID-19 pandemic. Also indispensable was the companionship of my friends in graduate school including the trailer and board game crews, Alex Dorsett, and Anders Barzdukas, the latter two of whom have been wonderful post-pandemic lunch partners. I would also not be here without the support of my family. I must thank my mother, who drove all the way to Santa Barbara to look after me when I had pneumonia; my father, whose regular warning texts and emails demonstrate his commitment to my safety in his own way; and my brother, who has been a wonderful conversation partner.

Last but not least, I must acknowledge my biggest supporter, my partner Priyam Das. I know it is hard to judge the effects of emotional support, but believe me when I write that I absolutely would not have succeeded if I did not have your support the whole way. Thank you for commiserating with me as a fellow graduate student. Thank you for humoring my moves to distant and remote locations like Santa Barbara, Geneva, and Ithaca. Thank you for all your companionship. I am so happy I have been able to spend these years with you, and I look forward to many more.

Curriculum Vitæ

Michael C. Oshiro

Education

2023	Ph.D. in Physics (Expected), University of California, Santa Barbara.
2021	M.A. in Physics, University of California, Santa Barbara.
2018	B.A. in Physics and Mathematics, University of California, Berkeley.

Papers

- CMS Collaboration, *Search for higgsinos decaying to two Higgs bosons and missing transverse momentum in proton-proton collisions at* $\sqrt{s} = 13$ TeV *JHEP* **05** (2022) 014 [arXiv:2201.04206]

- CMS Collaboration, *Combined search for electroweak production of winos, binos, higgsinos, and sleptons in proton-proton collisions at* $\sqrt{s} = 13$ TeV CMS Physics Analysis Summary (2023) [CDS]

Public Talks

- "Search for New Physics in Channels with Two Higgs Bosons Decaying to b Quarks and Missing Transverse Momentum in Proton-Proton Collisions at 13 TeV". APS April Meeting, April 17-20, 2021.

Abstract

Searching for higgsinos with the CMS experiment

by

Michael C. Oshiro

Natural supersymmetry is one well-motivated theory that could explain the apparent fine-tuning of the Higgs potential in the standard model. Natural supersymmetry predicts the existence of higgsinos, fermionic partners of Higgs bosons, with mass not far from the electroweak scale. Such higgsinos should be producible with the CERN LHC. This thesis presents a search for higgsinos with 137 fb^{-1} of proton-proton collision data collected by the CMS experiment in final states with two Higgs bosons, each decaying via the process $\text{H} \to \text{b}\overline{\text{b}}$, and large missing transverse momentum. This search is sensitive to the case the higgsinos are considerably heavier than the lightest supersymmetric particle. The observed event yields are consistent with standard model predictions, and the results are interpreted in simplified models to exclude electroweak production of nearly degenerate higgsinos with mass between 175 and 1025 GeV and production of higgsino in gluino decays with gluino mass up to 2330 GeV at the 95% confidence level. The analysis is also combined with other searches for electroweak supersymmetric particles to produce limits on more general models with higgsinos.

Contents

Introduction

One of the important goals of physics is to understand the fundamental laws of nature. Historically, physicists have worked toward this goal by constructing theories whose predictions are verified by experimental measurements. Today, the best theory of this type is called the standard model (SM), augmented with gravity in the framework of effective field theory (EFT). This theory makes predictions consistent with an extremely large number of experimental results. However, the SM is known to only be an approximation, and there exist experimental measurements and theoretical mysteries that point to new laws of physics, which will be generically referred to as physics beyond the standard model (BSM). For example, astronomical measurements suggest that in order to explain the large scale structure of the universe, there must exist an unknown type of matter called "dark matter" comprising about 85% of the total matter in the universe. This observation cannot be explained with just the SM.

Particle colliders are powerful experimental tools that can be used to produce heavy unstable particles and study the laws of physics. The Large Hadron Collider (LHC) at the European Laboratory for Particle Physics (CERN) is currently the world's highest-

energy particle collider. At the LHC, there are two general purpose experiments, ATLAS and CMS. In 2012, the ATLAS and CMS collaborations announced the discovery of a new particle [1,2], which is now known to be consistent with the Higgs boson of the SM. In the SM, the Higgs boson is an excitation of a scalar field, the Higgs field. Such a scalar field is unique in that it can have a potential energy for which the vacuum expectation value (VEV) is nonzero. The Higgs field VEV of the SM is responsible for breaking the gauge symmetries of the electroweak interactions and for generating the masses of the fundamental particles. However, the form of the Higgs potential in the SM is extremely sensitive to the high-energy parameters of the theory. So far, LHC experiments have not observed any new particles or deviations from SM predictions. The discovery of a single scalar boson and nothing else is somewhat surprising, as the SM Higgs potential requires considerable fine-tuning of model parameters in the absence of new laws of physics at a similar energy scale. This possible fine-tuning is called the "hierarchy problem."

Supersymmetry (SUSY) is a hypothetical symmetry that pairs particles from two classes, fermions and bosons. Theories of SUSY predict that there exist hereto undiscovered supersymmetric partners for each of the known particles as well as additional Higgs bosons and their supersymmetric partners. There are several reasons why theories of SUSY are particularly interesting. One reason is that SUSY can modify the gauge couplings of the SM in a way that causes them to unify at a high energy scale as required by some grand unified theories. Another reason is that the lightest supersymmetric particle (LSP) can be a good dark matter candidate. SUSY can also alleviate the extreme

sensitivity of the Higgs potential to high-energy parameters and thus solve the hierarchy problem. Theories of SUSY that succesfully remove most of this sensitivity are referred to as "natural supersymmetry."

In natural SUSY, the supersymmetric partners that must be relatively light include the higgsinos, the top squarks, a bottom squark, and the gluinos; these are the respective supersymmetric partners of the Higgs bosons, the top quark, the bottom quark, and the gluons. LHC experiments are the most sensitive to squark and gluino production since these particles interact through the strong interaction. So far, no evidence for squarks or gluinos has been observed. This puts stringent bounds on the masses of squarks and gluinos. Although experimental sensitivity to higgsinos is lower, the higgsinos are typically required to be quite light in natural SUSY and are thus an interesting search target in scenarios where the squarks and gluinos are too heavy to be observed by LHC experiments. Comprehensively searching for higgsinos requires one to consider many different possible experimental signatures of higgsinos that depend heavily on the particular model of SUSY. The main topic of this thesis is a search that is sensitive in the case the higgsinos are much heavier than the LSP. Specifically, this search targets models where a pair of neutral higgsinos each decay into a Higgs boson and an LSP, and the Higgs bosons each decay into a bottom quark-antiquark pair. Each bottom quark or antiquark generates a collomated spray of hadrons called a jet, and the undetected LSPs generate an imbalance in transverse momentum. Dedicated algorithms are used to identify jets generated by bottom quarks or antiquarks as "b jets." This search is called the HH(4b)+$p_{\mathrm{T}}^{\mathrm{miss}}$ analysis

and is described in Ref. [3]. However, considerable more detail and background is given in this thesis. The HH(4b)+$p_{\mathrm{T}}^{\mathrm{miss}}$ search is also combined with several other searches for electroweak supersymmetric partners in Ref. [4]. This thesis also covers the combined results and interpretations in models of higgsino production.

Chapter 1 begins by reviewing the framework of quantum field theory (QFT) and effective field theory. In these theories, particles are interpreted as excitations in quantum fields, and the probability for physical processes such as particle scattering or decay can be calculated using correlation functions of quantum fields. Two concrete examples of quantum field theories, the SM and minimal supersymmetric standard model (MSSM), are described. Some of the problems with the SM are reviewed, and SUSY is highlighted as a possible solution to the hierarchy problem. The second half of the chapter discusses the ways in which particles are detected in experiments and how the detected particles can be combined into "physics objects" that are in rough correspondance with fundamental particles. The most important physics objects in the HH(4b)+$p_{\mathrm{T}}^{\mathrm{miss}}$ analysis include the b jets that are used as a proxy for bottom quarks and the missing transverse momentum $p_{\mathrm{T}}^{\mathrm{miss}}$ that is used as a proxy for the undetected LSPs.

Chapter 2 describes the experimental setup used in the analysis. Proton-proton collisions are provided by the LHC, and the particles produced in the collisions are then detected by the Compact Muon Solenoid (CMS) experiment. A brief overview of the LHC as well as a more thorough review of the CMS experiment are provided. The CMS detector includes an inner tracker that can reconstruct the trajectories of

charged particles, calorimeter systems that measure the energy of incident particles, a superconducting magnet, and a muon system that provides additional measurements of muon trajectories. Some of the ongoing upgrades of the CMS experiment are mentioned, and the current status of the optical data acquisition motherboard 7/5 (ODMB7/5) upgrade is highlighted. The chapter concludes with a description of the reconstruction algorithms used to reconstruct physics objects from the data recorded by CMS.

Chapter 3 describes the signal models, the selections on physics objects, the method used to reconstruct the Higgs candidates, and the real and simulated data sets used in this analysis. The HH(4b)+$p_{\mathrm{T}}^{\mathrm{miss}}$ analysis targets models with direct production of higgsino pairs in proton-proton collisions as well as models where the higgsinos are produced in the decay of gluinos. The physics objects used in the analysis include electrons, muons, photons, isolated tracks, jets, and missing transverse momentum. In particular, Higgs boson candidates are reconstructed from pairs of b jets or from fat "double-b jets" formed by a collomated bottom quark-antiquark pair. The real and simulated data sets are listed, and various filters and corrections used to address problems in the detector and simulation process are described.

Chapter 4 presents the analysis strategy. The analysis procedure depends on whether the two Higgs boson candidates are reconstructed as two resolved b jet pairs (the resolved topology) or as two double-b jets (the boosted topology), though the two procedures are largely analogous. A loose "baseline selection" is used to select events with pairs of Higgs boson candidates and large missing transverse momentum as expected of higgsino

production, then events are split into various categories to enhance sensitivity to certain SUSY scenarios. Even in the absence of higgsino production, some SM background events are expected to enter the various analysis categories. The presence of higgsinos would manifest as a significant excess of events over the background-only prediction. For each analysis category, events may fall into a signal region, which requires a certain number of b-tagged or double-b-tagged jets and Higgs boson candidates with mass near the nominal Higgs boson mass, or outside of the signal regions. The minimal correlation between the Higgs boson candidates' masses and the number of b- or double-b-tagged jets in background events is used to estimate the number of events in each signal region from the events falling outside of the signal regions. The uncertainty on the predicted background yields as well as the signal yields is evaluated. Finally, the full statistical model used to measure or constrain the presence of supersymmetric particles is described.

Chapter 5 reports the results of the HH(4b)+$p_{\mathrm{T}}^{\mathrm{miss}}$ search. The measured number of events and background prediction in each signal region is reported. The results are then interpreted in simplified models of supersymmetry, and large regions of the considered parameter space are found to be excluded at the 95% confidence level. The second part of the chapter covers the combination of electroweak SUSY analyses described in Ref. [4]. The models of higgsino production considered by the combination are reviewed, a brief overview of the other analyses used in the combination is given, and the interpretations of the combined results for the higgsinos models are presented. Again, large regions of the considered parameter space are found to be excluded at the 95% confidence level.

In the absence of any strong evidence for SUSY, it is worth also considering other solutions to the hierarchy problem. BSM theories that seek to alleviate the sensitivity of the Higgs potential to high-energy parameters often substantially affect the couplings of the SM Higgs boson. Measurements of processes involving the Higgs boson thus provide an indirect method of probing such theories. Chapter 6 begins by describing some of the ongoing work on a search for the rare decay of the Higgs boson to a Z boson and a photon. Work on the trigger strategy used to save data and the categorization scheme is described. Finally, a summary of the thesis is provided along with an outlook on supersymmetry and the hierarchy problem.

Chapter 1

Background

The standard model is a type of theory called a quantum field theory (QFT). The first section of this chapter provides some background on concepts in QFT. It explains how particles can be interpreted as excitations in quantum fields, and how probabilities for particles interacting in different ways can be calculated using correlation functions involving quantum fields. It then goes into some subtleties of such calculations, including the fact that parameters in QFT are effectively scale-dependent and that there are problems with the naive formalism that arise with massless particles. Gauge interactions are introduced and used to explain the electroweak and strong interactions of the SM. Immediate extensions of the SM to include gravity and neutrino masses using the formalism of effective field theory are also noted. Then, problems of the SM are described and one potential solution to some of these problems, supersymmetry, is outlined.

The second half of the chapter then provides some detail on how theories such as the SM are tested at collider experiments. After a brief description of quantities used in experimental measurements, the ways in which particles interact with macroscopic matter

and can thus be detected are described. The correspondence between detected particles and fundamental particles at collider experiments is then explained, and a description of common processes seen in proton-proton collisions is given. Finally, the section concludes by noting how experiment and theory can be more directly compared using simulation.

1.1 Theoretical background

1.1.1 Particles and quantum field theory

In particle physics experiments, one measures the probabilities for particles to interact and behave in different ways. The state of a single particle is given by specifying its energy, its momentum, and its intrinsic angular momentum, or spin. A theory of particle physics should provide the probability (density) $P(ab \to ABC...)$ for starting with some particle(s) a, b in a given initial state and ending with some particles A, B, C, etc., in a given final state. Note that processes with two initial particles ($ab \to ABC...$) are called scattering, while processes with a single initial particle ($a \to ABC...$) are called decays. Currently, the best tested theories of physics fall into a class of theories called quantum field theories. The eponymous quantum fields are a class of entities that are defined throughout spacetime. Fields typically possess a lowest energy state called the ground state or vacuum, as well as higher energy excited states. The key idea is that the excitations in quantum fields can be identified as particles. An in-depth motivation and development of QFT can be found in Ref. [5] and Ref. [6]. The development of QFT in

this and the following sections is based primarily on Ref. [5].

There are many reasons why QFT makes an appealing framework for particle physics. Since all particles of the same type are excitations in the same field, it is clear why they should all have identical properties. Furthermore, QFT is inherently a multiparticle theory and supports creation and annihilation of particles. Some types of fields support two types of excitations with opposite quantum numbers, which are identified as antiparticles. This thesis will not distinguish between particles and antiparticles unless explicitly stated. Thus a "muon" should be taken to mean a muon or an antimuon and an "electron" to mean an electron or an antielectron, which is also called a positron.

Another benefit is compatibility with special relativity. The universe possesses a four-dimensional spacetime with a Lorentzian geometry. In particular, any fundamental theory of physics must treat space and time in a symmetric fashion since the division into space and time is frame-dependent. The conversion rate between space and time is the constant c, which is about 3×10^8 m/s. This is also the maximum speed at which information can propagate without violating causality by propagating backward in time. For particle physics processes, this thesis uses a system of natural units in which $c = 1$ and thus will not be explicitly written. QFT naturally treats spacetime in a unified fashion and also naturally avoids causality-violating information transfer faster than c.

QFT is also a quantum theory, which has several implications. Quantum mechanical theories provide complex probability amplitudes $\mathcal{A}$ whose magnitude squared is the probability (density) for going from a given initial state to a given final state. In particle

physics, these amplitudes between free particle states are also referred to as (S-)matrix elements. This document will use the terms amplitude and matrix element interchangeably. This amplitude involves the sum of all possible intermediate processes that begin with the given initial state and end with the given final state. Quantum mechanics also imposes canonical commutation or anticommutation relations that relate coordinates to their conjugate momenta. Most notably, this imposes a inverse relationship between spacetime scales and energy-momentum scales. For this reason, "long distance" and "low energy" will be used interchangeably as will "short distance" and "high energy". The constant $\hbar$, which is about 6.6×10^{-16} eV $\cdot$ s, sets the conversion between time and energy scales. Like c, for particle physics processes, this thesis will use natural units in which $\hbar = 1$. The (anti)commutation relations also determine whether the excitations in a field fall into a class of particles called bosons (commutation relations) or fermions (anticommutation relations). In natural units, bosons have an integer spin while fermions have half-odd-integer spin. Multiple bosons can occupy the same quantum state while fermions cannot.

1.1.2 The Lorentz group

As far as current measurements can determine, the laws of physics are independent of location in spacetime, spatial orientation, and velocity [7]. In the language of Lie groups, the laws of physics are said to be invariant under the (proper orthochronous) Poincaré group. Invariance under boosts and rotations, the (proper orthochronous)

Lorentz group, imposes particularly interesting constraints on possible mathematical descriptions of physics. This section reviews some of the implications of these constraints.

Mathematically, a field is a function associating a value to each point in spacetime that is self-consistent with respect to Lorentz transformations. In the language of Lie groups, the possible mathematical values are said to transform in a particular representation of the Lorentz group. The representations of the Lorentz group can be indexed by a pair of positive integers. The SM features scalars $((1,1))$, left-handed spinors $((2,1))$, right-handed spinors $((1,2))$, and vectors $((2,2))$. The explicit forms of transformations for these representations can be found in Ref. [5].

A classical scalar quantity consists of a single real or complex number. In quantum mechanics, each real number is replaced by a Hermitian operator, which can be concretely represented as a Hermitian matrix. Classical and quantum scalars are invariant under the proper orthochronous Lorentz transformations. The excitations in scalar fields correspond to spin 0 bosons.

Vectors are four-component objects consisting of four classical numbers or operators. The components of a Lorentz vector A are denoted as A^μ where μ is an index that can take on a value from 0 to 3. For example, the components of a spacetime position x^μ are, in order, the time coordinate and the x, y, and z spatial coordinates. The metric tensor for flat spacetime, $g_{\mu\nu}$, can be used to combine two vectors so that the quantity

$$g_{\mu\nu}A^\mu B^\nu = A_\rho B^\rho \tag{1.1}$$

is a scalar. This equation employs the summation convention whereby any repeated index (in this case μ, ν, and ρ) is summed over. It also uses the convention by which A_μ denotes $g_{\mu\nu}A^\nu$. Given a vector A^μ, the scalar quantity $A_\mu A^\mu$ is called the invariant magnitude of A. Note that this document will use the mostly minus convention for the Lorentzian metric tensor. The four-gradient

$$\partial = \left(\frac{\partial}{\partial t}, \frac{\partial}{\partial x}, \frac{\partial}{\partial y}, \frac{\partial}{\partial z}\right) \tag{1.2}$$

can also be naturally contracted with a vector $\partial_\mu A^\mu$ to yield a scalar. The excitations in vector fields correspond to spin 1 bosons.

The left- and right-handed (Weyl) spinors of interest are two component objects where each component is a classical Grassmann number or a quantum mechanical operator. Right-handed spinors can always be written as the Hermitian conjugate (denoted by †) of a left-handed spinor. A left-handed spinor is denoted as ψ_a where a is an index running from 1 to 2, and similarly, a right-handed spinor is denoted as $\psi^\dagger_{\dot{a}}$. With the invariant symbol $\epsilon^{ab} = \epsilon^{\dot{a}\dot{b}}$, two left-handed spinors, ψ and χ, or two right-handed spinors, $\psi^\dagger$ and $\chi^\dagger$, can be combined into a scalar as follows:

$$\begin{aligned} \psi\chi &= \epsilon^{ab}\psi_b\chi_a \\ \psi^\dagger\chi^\dagger &= \epsilon^{\dot{a}\dot{b}}\psi^\dagger_{\dot{a}}\chi^\dagger_{\dot{b}}. \end{aligned} \tag{1.3}$$

As shown above, these products will be simply denoted as $\psi\chi$ or $\psi^\dagger\chi^\dagger$, omitting the

sum, indices, and ϵ symbol. With the invariant symbol $\bar{\sigma}^{\mu\dot{a}b}$, a left-handed spinor and a right-handed spinor can be combined into a vector with the equation

$$\psi^\dagger \bar{\sigma}^\mu \chi = \psi^\dagger_{\dot{a}} \bar{\sigma}^{\mu\dot{a}b} \chi_b. \tag{1.4}$$

The excitations in a spinor field are spin 1/2 fermions. Four-component Majorana and Dirac spinors are also commonly encountered. A Majorana spinor is constructed from a lef-handed spinor and its right-handed complex conjugate $(\psi, \psi^\dagger)$ while a Dirac spinor is constructed from a left-handed spinor and a separate right-handed spinor $(\psi, \chi^\dagger)$. Two Dirac/Majorana spinors (arranged as a column) can be combined into a vector using the symbol

$$\gamma^\mu = \begin{pmatrix} 0 & \epsilon_{ac}\epsilon_{\dot{b}\dot{c}}\bar{\sigma}^{\mu\dot{c}c} \\ \bar{\sigma}^{\mu\dot{a}b} & 0 \end{pmatrix}. \tag{1.5}$$

The full Lorentz group also includes two discrete transformations, a reversal of all the spatial axes called parity, $\mathcal{P}$, and time reversal, $\mathcal{T}$. These need not be symmetries of a general theory. Pseudoscalar fields are similar to scalar fields with the difference that they reverse sign under $\mathcal{P}$. Similarly, pseudovectors have an extra sign reversal of all components under $\mathcal{P}$. The charge conjugation operator $\mathcal{C}$ is a transformation not included in the Lorentz group. $\mathcal{C}$ switches particles and antiparticles. The laws of physics need not be invariant under $\mathcal{C}$, $\mathcal{P}$, or $\mathcal{T}$. However, for the fields considered here, invariance under proper orthochronous Lorentz transformations together with a condition on weak

local commutativity at Jost points [8] imply that the laws of physics are invariant under the combination $\mathcal{CPT}$ [9–11].

1.1.3 Calculations in quantum field theory

A quantum field is a function that associates a quantity such as an operator, a spinor of operators, or a vector of operators to each point in spacetime. This section will outline how calculations with quantum fields can be used to derive sums of terms represented by Feynman diagrams that approximate the probability amplitudes for processes measured in particle physics experiments. For simplicity, the examples in this section will use scalar fields, though the procedure is analogous for fields of higher spin.

The Klein-Gordon equation, the equation of motion for a free scalar field, is given by

$$(\partial^2 + m^2)\phi(x) = 0. \tag{1.6}$$

A free field is a field for which the equation of motion has no nonlinear terms. Any nonlinear terms in an equation of motion are called interaction terms and the numerical coefficients of such terms are called coupling constants.

Notably, ϕ and its conjugate momentum $\Pi = \dot{\phi}$ are required to satsify the canonical commutation relations

$$\begin{aligned} [\phi(\vec{x}, t), \phi(\vec{x}', t)] = [\Pi(\vec{x}, t), \Pi(\vec{x}', t)] = 0, \\ [\phi(\vec{x}, t), \Pi(\vec{x}', t)] = i\delta^3(\vec{x} - \vec{x}'). \end{aligned} \tag{1.7}$$

The general solution to the Klein-Gordon equation is given by

$$\phi(x) = \int \frac{d^3p}{(2\pi)^3 2E(\vec{p})} \left(a(\vec{p}) e^{-i(E(\vec{p})t - \vec{p}\cdot\vec{x})} + a^\dagger(\vec{p}) e^{i(E(\vec{p})t - \vec{p}\cdot\vec{x})} \right), \tag{1.8}$$

where $E(\vec{p}) = |\vec{p}|^2 + m^2$ and the coefficients a and $a^\dagger$ are defined to extract a factor of $1/(2E(\vec{p}))$ in order to make the integration measure Lorentz invariant. The canonical commutation relations of ϕ and Π also impose commutation relations on a and $a^\dagger$.

The states of this theory can all be expressed as some collection of creation operators $a^\dagger(\vec{p}_i)$ acting on the vacuum state $|0\rangle$. Moreover, the state $a^\dagger(\vec{p}_i)|0\rangle$ is an energy-momentum eigenstate with momentum $\vec{p}$ and an energy $E(\vec{p})$. Thus, $|0\rangle$ is interpreted as the state with no particles and each creation operator as creating a particle of definite four-momentum. The probability amplitude for scattering two ϕ particles starting with momenta $\vec{p}_1$, $\vec{p}_2$ and ending with momenta $\vec{p}_3$, $\vec{p}_4$ is

$$\begin{aligned} \langle f|i\rangle =& \langle 0|a(\vec{p}_3)a(\vec{p}_4)a^\dagger(\vec{p}_1)a^\dagger(\vec{p}_2)|0\rangle \\ =& \int d^3x_1 d^3x_2 d^3x_3 d^3x_4 \langle 0|(e^{-ip_3^\mu x_{3\mu}} \overleftrightarrow{\partial} \phi(x_3))(e^{-ip_4^\mu x_{4\mu}} \overleftrightarrow{\partial} \phi(x_4)) \\ & (e^{ip_1^\mu x_{1\mu}} \overleftrightarrow{\partial} \phi(x_1))(e^{ip_2^\mu x_{2\mu}} \overleftrightarrow{\partial} \phi(x_2))|0\rangle, \end{aligned} \tag{1.9}$$

where in the second line, the a and $a^\dagger$ are re-expressed in terms of ϕ using the shorthand $f \overleftrightarrow{\partial}_\mu g = f(\partial_\mu g) - (\partial_\mu f)g$ and the four-vector $p_n^\mu = (E(\vec{p}_n), \vec{p}_n)$. In the noninteracting case, this amplitude is trivial, being precisely 1 when p_1 and p_2 match p_3 and p_4 and zero otherwise.

In an interacting theory, the Lehmann-Symanzik-Zimmermann (LSZ) reduction formula

$$\begin{aligned}\langle f|i\rangle = \int \prod_j \left(\frac{-i(p_j^2 - m^2)}{\sqrt{Z_{\text{wf}}}}\right) d^4x_j e^{-i(x_j \cdot p_j)} \\ \prod_{j'} \left(\frac{-i(p_{j'}^2 - m^2)}{\sqrt{Z_{\text{wf}}}}\right) d^4x_{j'} e^{i(x_{j'} \cdot p_{j'})} \\ \langle 0|T\{\phi_1(x_1)...\phi_{1'}(x_{1'})...\}|0\rangle\end{aligned} \tag{1.10}$$

provides an analogous equation that can be used to calculate probability amplitudes [12]. An n-point correlation function is an expression of the form $\langle 0|T\{\phi_1(x_1)...\phi_n(x_n)\}|0\rangle$ where T is the time ordering symbol, meaning that the enclosed fields should be ordered so the largest x_i^0 is on the left and the smallest x_i^0 on the right. After performing a four-dimensional Fourier transform on each spacetime coordinate, the n-point correlation function has a pole near where the invariant magnitude of each p_i is $p_i^\mu p_{i\mu} = m^2$. This is referred to as the on-shell condition. The LSZ reduction formula shows that when the Fourier-transformed n-point correlation function is evaluated near these poles, it is proportional to the amplitude $\langle f|i\rangle$ with an overall normalization factor built from powers of one or more constants Z_{wf}. In the LSZ reduction formula, the particles $i = 1, 2, ...$ are the initial-state particles with associated fields ϕ_i and the particle $i' = 1', 2', ...$ are the final-state particles with associated fields $\phi_{i'}$. The formulas for spinor and vector fields are analogous but feature additional spinor or vector factors.

The functional or path-integral formulation of quantum mechanics can be used to

calculate n-point correlation functions and thus probability amplitudes. In this formulation, a probability amplitude is given by a functional integral over every classical path between some initial and final state

$$Z(J) = \int \mathcal{D}\phi e^{i\int d^4x\mathcal{L}+J(x)\phi(x)}, \tag{1.11}$$

where $J(x)$ is an arbitary function inserted for later convenience that can be taken to be 0. Each path contains a weighting factor $\exp(i\int d^4x\mathcal{L})$, where $\mathcal{L}$ is a scalar called the Lagrangian that describes the theory of interest. The functional formulation serves as an equivalent alternative to operator formulation. This functional integral describing the amplitude to stay in the ground state, denoted $Z(J=0)$, is called the path integral or the partition function.

The extra $J(x)\phi(x)$ term is used to compute time-ordered excitation values by taking the functional derivative with respect to J. After taking the derivatives, J can be taken to be 0, resulting in the following formula:

$$\langle 0|T\{\phi(x_1)...\phi(x_n)\}|0\rangle = \frac{1}{i}\frac{\delta}{\delta J(x_1)}...\frac{1}{i}\frac{\delta}{\delta J(x_n)}Z(J)|_{J=0}. \tag{1.12}$$

For most theories, the path integral cannot be evaluated exactly. Theories of noninteracting fields are an exception. Splitting the noninteracting Lagrangian $\mathcal{L}_0$ from the part containing interaction terms $\mathcal{L}_1$, the interaction terms can be expressed using functional

derivatives,

$$Z(J) \propto e^{i\int d^4x \Lambda_1\left(\frac{1}{i}\frac{\delta}{\delta J(x)}\right)} Z_0(J). \tag{1.13}$$

$Z(J)$ is typically approximated by performing a Taylor expansion around 0 in both the coupling and J. This works for theories in which the couplings are small; theories with large couplings require other approximation techniques. Taking the expansion for $Z(J)$, evaluating the functional derivatives of Equation 1.12, and plugging this back into the LSZ reduction formula results in an expression for probability amplitudes consisting of the sum of various combinatorial terms that can be pictorially organized using diagrams called Feynman diagrams. The Lagrangian of a theory determines the Feynman rules for constructing diagrams and numerically evaluating them.

The Feynman diagrams for a given n-point correlation function must have n external lines, each of which corresponds to a particular field. Each external line has one end free and the other end attached to a vertex; the possible vertices are determined by the terms of the Lagrangian. For example, if ψ, ϕ, and χ are scalar fields, a Lagrangian term proportional to $\psi\phi\chi$ will allow diagrams with a vertex at which a ψ line, a ϕ line, and a χ line to meet. Fields with distinct particles and antiparticles will have an inherent direction that also must match vertex rules. A diagram may have additional internal lines, which connect to a vertex at either end. A momentum and direction is then assigned to every line and conservation of momentum is applied at each vertex. Each such diagram corresponds to a numerical value that is the product of factors from the internal lines, external lines, and vertices, integrated over any internal momenta not

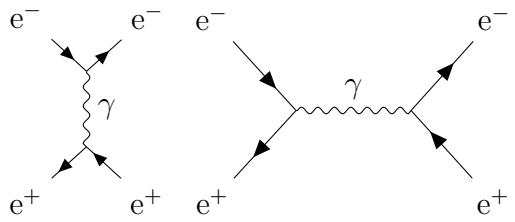

Figure 1.1: The two Feynman diagrams that contribute to $e^+e^- \to e^+e^-$ at LO. In this document, initial-state particles will be shown on the left and final-state particles on the right.

fixed by the external ones and conservation of momentum. The value of a correlation function is the sum over all connected Feynman diagrams with the appropriate external lines. Since each vertex introduces a factor of a coupling constant, which is assumed to be small, diagrams with smaller numbers of vertices are numerically larger and more important. The correlation function is typically approximated by terminating the series to a finite order of the coupling constant. The lowest order at which there are non-vanishing diagrams is called leading order (LO), followed by next-to-leading order (NLO), next-to-next-to-leading order (NNLO), and so forth.

To provide a concrete example, consider the process $e^+e^- \to e^+e^-$, electron-positron to electron-positron scattering in quantum electrodynamics. Electrons are spin-1/2 particles whose fields are denoted e with a coupling terms to the electromagnetic potential A that is proportional to $\bar{e}\gamma^\mu e A_\mu$. This means these vertices should have one incoming electron line, one outgoing electron line, and a photon line. There are thus two diagrams that contribute to the correlation function $\langle 0|T\{ee\bar{e}\bar{e}\}|0\rangle$ at LO, which are shown in Figure 1.1.

1.1.4 Effective field theory

The previous section discussed how S-matrix elements can be approximated by summing Feynman diagrams. The naive version of the outlined procedure can fail due to the fact that in parameters in QFT are effectively scale dependent and thus may not remain small enough for the perturbative approximation to work at all scales. The framework of effective field theory and the renormalization group provide a way to calculate how parameters change as a theory is coarse-grained. This can be used to perform calculations in a particular regime, even if the theory cannot be applied at all scales. It also has important implications for the behavior of a theory at different scales.

The Lagrangian for so-called $\lambda\phi^4$ theory is given by

$$\mathcal{L} = \frac{1}{2}\partial^\mu\phi\partial_\mu\phi - \frac{1}{2}\mu^2\phi^2 - \frac{1}{4!}\lambda\phi^4. \tag{1.14}$$

The Feynman rules for this Lagrangian allow four-point vertices which contribute a factor of $-i\lambda$, while lines of particle ϕ with four-momentum p contribute a factor of $\frac{i}{p^2-\mu^2+i\epsilon}$. The diagram shown in Figure 1.2 is encountered when calculating the S-matrix element for $\phi\phi \to \phi\phi$ at one-loop order. This diagram contributes a value of

$$\lambda^2 \int \frac{d^4p}{(2\pi)^4} \left(\frac{1}{p^2-\mu^2+i\epsilon}\right) \left(\frac{1}{(p-p_{\text{ext}})^2-\mu^2+i\epsilon}\right), \tag{1.15}$$

where p_{ext} is a constant based on the momenta of the external legs of the diagram in order to conserve momentum at both vertices. Noting that d^4p is equal to $d|p||p|^3$ times

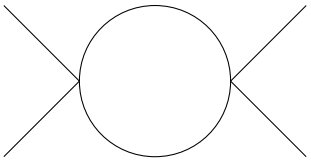

Figure 1.2: One Feynman diagram that contributes to the scattering amplitude for $\phi\phi \to \phi\phi$ at order λ^2. Directly applying the Feynman rules to this diagram gives a divergent integral.

an angular measure, this integral asymptotically behaves as

$$\int \frac{d|p|}{|p|} \sim \log(|p|), \tag{1.16}$$

which diverges as $|p|$ is integrated to ∞. In general, any diagram with an internal loop will feature an integral over four-momenta, and whether or not a given loop diverges depends on the factors of $|p|$ associated with the internal lines. The divergences caused by these small loops are called ultraviolet (UV) divergences.

The following discussion will follow the ideas summarized in Ref. [13] with the notation of Ref. [5]. Performing a change of variable from time t to $\tau = it$ yields the Wick-rotated partition function

$$Z(J) = \int \mathcal{D}\phi e^{-S_{\mathrm{E}} - \int d^4x J(x)\phi(x)}, \tag{1.17}$$

where S_{E} is the Euclidean action, which is the integral of the Euclidean Lagrangian $\mathcal{L}_{\mathrm{E}}$. Working with the Fourier transform of the field(s) $\phi(x)$, denoted $\tilde{\phi}(p)$, the functional integral over $\tilde{\phi}(p)$ can be split into two parts: an integral over $\tilde{\phi}$ with $|\vec{p}| < \Lambda$ and an

integral over $\tilde{\phi}$ with $|\vec{p}| > \Lambda$ for some cutoff Λ:

$$\begin{aligned} Z(J) &= \int \mathcal{D}\tilde{\phi}_{|p|<\Lambda} \left(\int \mathcal{D}\phi_{|\vec{p}|>\Lambda} e^{-S_{\mathrm{E}}} \right) e^{-\int d^4x J(x)\phi(x)} \\ &= \int \mathcal{D}\tilde{\phi}_{|p|<\Lambda} e^{-S_{\mathrm{eff}}} e^{-\int d^4x J(x)\phi(x)}, \end{aligned} \tag{1.18}$$

where the second line defines the Wilsonian effective action S_{eff}, which can be written as the integral of some effective Lagrangian density $\mathcal{L}_{\mathrm{eff}}$ that depends only on $\tilde{\phi}(p)$ with $|p| < \Lambda$. In the second line, the large $|p|$ (equivalently, short distance) degrees of freedom have been integrated out, leaving only the coarse-grained/low energy theory. The effective Lagrangian can be computed from the full one by integrating out all contributions from the large $|p|$ fields and thus will have different coupling coefficients or even additional terms that did not appear in the full Lagrangian.

For example, in the case of the $\lambda\phi^4$ Lagrangian introduced earlier, integrating out the $|p| > \Lambda$ fields causes the effective Lagrangian to have a new coefficient $\mu^2(\Lambda)$ for the ϕ^2 term. Up to order λ^2, the new coefficient contains contributions from the Feynman diagrams shown in Figure 1.3, the original μ^2 as well as a correction from integrating out the high $|p|$ fields. Following the Feynman rules for this theory, $\mu^2(\Lambda)$ is given by

$$\mu^2(\Lambda) = \mu^2 + \frac{1}{2}\lambda \int_{\Lambda}^{\infty} \frac{d^4p}{(2\pi)^4} \frac{1}{p^2 + \mu^2} + \text{higher order terms}, \tag{1.19}$$

From Equation 1.19, it is clear that a divergence arises from the high energy/short distance physics that was integrated out. In the high energy regime, perturbation theory

Figure 1.3: The two Feynman diagrams that contribute to the $\frac{1}{2}\mu^2(\Lambda)\phi^2$ in the effective Lagrangian up to order λ^2. The dashed lines indicate the large $|p|$ fields that are integrated out while the solid lines are the low $|p|$ that remain in the effective Lagrangian.

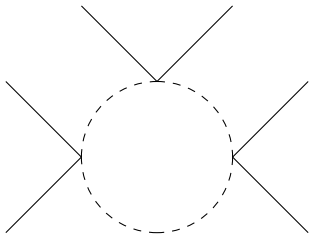

Figure 1.4: One Feynman diagram contributing to the coefficient of the ϕ^6 term in the effective Lagrangian. The dashed lines indicate the large $|p|$ fields that are integrated out while the solid lines are the low $|p|$ that remain in the effective Lagrangian.

may break down or the theory may become altogether unphysical. To avoid this, the high energy regime can be discarded altogether and the effective couplings at some cutoff scale Λ_0 can be taken as the fundamental starting point. The couplings at lower scales can be evaluated by integrating fields of intermediate momentum $\Lambda < |p| < \Lambda_0$. This approach is called effective field theory (EFT), and the running of effective couplings as the theory is coarse grained by integrating out high momentum scales is referred to as the renormalization group (RG) flow.

Returning to Equation 1.19, the EFT approach replaces μ with $\mu(\Lambda_0)$, λ with $\lambda(\Lambda_0)$, and ∞ with Λ_0, thus providing a finite integral. The same procedure can also be performed for λ as well as $c_{2n,i}$, the coefficient of the ϕ^{2n} term. Even if not present at the EFT starting point, such terms will arise due to diagrams such as the one shown in

Figure 1.4. Assuming $c_{2n,i}(\Lambda_0) = 0$, the effective values of μ^2, λ, and $c_{2n,1}$ at a scale Λ are calculated in Ref. [5] and given by:

$$\begin{aligned}
\mu^2(\Lambda) &= \mu^2(\Lambda_0) + \frac{1}{16\pi^2}\lambda(\Lambda_0)(\Lambda_0^2 - \Lambda^2) + \text{higher order terms} \\
\lambda(\Lambda) &= \lambda(\Lambda_0) - \frac{3}{2}\lambda^2(\Lambda_0)\log\frac{\Lambda_0}{\Lambda} + \text{higher order terms} \\
c_{2n,1}(\Lambda) &= -\frac{(-1)^n}{32\pi^2 2^n n(n-2)}\lambda^n(\Lambda_0)\left(\frac{1}{\Lambda^{2n-4}} - \frac{1}{\Lambda_0^{2n-4}}\right) + \text{higher order terms.}
\end{aligned} \tag{1.20}$$

These equations describe the running of the parameters $\mu^2(\Lambda)$, $\lambda(\Lambda)$, and $c_{2n,1}(\Lambda)$ under the RG flow. Note that the amplitudes in physical observables will in general have dependence on Λ both explicitly and implicitly through the couplings such as $\mu^2(\Lambda)$, $\lambda(\Lambda)$, and so forth. Since Λ is arbitrary, the dependence on Λ cancels exactly when all orders of perturbation theory are considered, but there may be some dependence when truncating to finite order. Since this dependence must be compensated for by higher orders in perturbation theory, varying the renormalization scale Λ is used to give an order-of-magnitude estimate for the uncertainty on a finite order truncation of the perturbative series.

Notably, the $c_{2n,1}$ terms feature the difference of inverse powers of Λ and Λ_0. In the limit $\Lambda \to 0$, the corrections to $c_{2n,1}$ are dominated by the low energy/long distance contributions and the short distance contributions including $c_{2n,1}(\Lambda_0)$ can be safely ignored. This is generally true of all coefficients with dimensions of energy to a negative power. For this reason, such terms are called irrelevant. Conversely, terms such as $\mu^2\phi^2$, whose coefficients have dimensions of energy to a positive power, are called relevant. Relevant

parameters have corrections dominated by high energy/short distance contributions and will be further discussed in Section 1.1.9. Finally, terms such as $\lambda\phi^4$, whose coefficients are dimensionless, are called marginal, and typically vary logarithmically with scale. The part of an EFT Lagrangian term multiplied by the coefficient is called an operator. Operators are classified by their dimensionality in units of powers of energy. They also inherit the descriptors of relevant, marginal, and irrelevant from their coefficients, which correspond to dimension less than four, four, and greater than four respectively.

In practice, different approaches to renormalization not discussed here, such as dimensional regularization, are more commonly used to perform calculations.

1.1.5 Infrared divergences and resummation

Another complication that can arise in the calculation of S-matrix elements is the failure of the LSZ reduction formula in theories with massless particles. The presence of massless particles causes divergences in both loop diagrams, as well as diagrams when one of the external legs is a massless particle, as shown in Figure 1.5. This class of divergences caused by massless particles is called infrered (IR) divergences. For diagrams with massless particles in the final state, the matrix element diverges in the limit that the particle energy E goes to 0, or in the limit that the angle θ between the massless particle and the particle that radiated it goes to 0. These types of divergences are called soft and collinear, respectively.

Infrared divergences can be tamed using the observation that production of an addi-

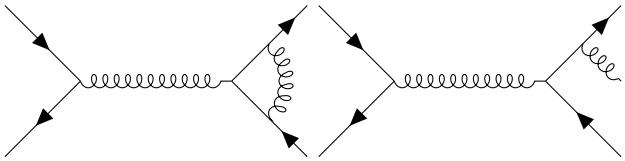

Figure 1.5: Examples of diagrams with gluons, represented by spiral lines, that include loop corrections (left) as well as final-state radiation of gluons (right). Because gluons are massless, both loop corrections involving gluons as well as initial-state and final-state radiation of gluons cause IR divergences.

tional massless particle in the very soft or collinear limit cannot be distinguished from the nonproduction of such a particle. Indeed, the original source of infrared divergences is the lack of an energy gap between the vacuum and 1 particle states for massless fields, which is assumed in the LSZ derivation. With an appropriate choice of infrared regularization and renormalization scheme, the divergences in loop and radiative diagrams can be made to cancel against each other to yield an overall finite matrix element. This cancellation is guaranteed by a general theorem of quantum field theory called the Kinoshita-Lee-Naumberg (KLN) theorem [14–16]. Organizing this cancellation of divergent pieces presents a numeric challenge that limits the precision of typical modern simulation of collider processes to NLO or NNLO. NLO calculations typically include diagrams with a loop, as well as those with one additional radiated particle, NNLO calculations typically contain diagrams with two loops, a single loop and one extra radiated particle, or two extra radiated particles, and so on for N^3LO.

Although the divergences can be cancelled between loop and radiative diagrams, finite terms of the form $\alpha^n \log^m(Q/\mu_F)$ remain, where α is a coupling constant, μ_F is the low-energy cutoff or "factorization" scale, and Q is some energy scale associated with the

process being studied. If Q is much larger than μ_F, these so-called large logs can ruin the perturbative expansion since, if higher order terms do not decrease quickly enough, truncating a series to finite order no longer provides a good approximation to the total sum. In fact, the same phenomenon occurs for UV divergences if the renormalization scale Λ is picked to be too different from the scale of the process considered.

The simplest approach for dealing with large logs is to set the factorization scale near the scale of the process being studied. Then at the matrix element level, only infrared safe observables, those that are unaffected by the emission of an additional soft or collinear particle, are well defined. For example, the amplitude for $\mathcal{A}(\mathrm{e^+e^-} \to \mathrm{e^+e^-})$ explicitly excluding any final state photons is not well defined at the matrix element level and must be extended to $\mathcal{A}(\mathrm{e^+e^-} \to \mathrm{e^+e^-}(+\text{soft/collinear photons}))$, which allows additional photons that are softer or more collinear than the factorization scale cutoff.

The physics below the factorization scale is commonly parametrized in a number of ways. For initial-state radiation, physics below the factorization scale is often absorbed into universal parton distribution functions (PDFs). This is possible due to a number of factorization theorems reviewed in Ref. [17] that intuitively stem from the fact that radiation from a given leg of a diagram is independent of the rest of the diagram. PDFs are functions of the form $f(x, Q^2)$ that originate in nonperturbative structure functions of composite particles, such as hadrons, and describe the density of fundamental particles or "partons" carrying a fraction x of the hadrons' momentum (at LO) when probed at a scale Q^2 [18]. Since scattering involving partons inside a hadron is effectively inco-

herent, the total cross section has the schematic form $\int dx f(x, Q^2)\sigma(x, Q^2)$ where σ is the cross section calculated at matrix-element level as a function of parton momentum fraction of x. The same parametrization can be used after radiative corrections are incorporated, which introduces Q^2 dependence into PDFs that is absent at leading order in the naive parton model. This dependence is called Bjorken scaling violation [19]. By using the recursive structure of radiative corrections, the Q^2 dependence of the PDFs can be calculated in perturbation theory with the Dokshitzer-Gribov-Lipatov-Altarelli-Parisi (DGLAP) equations [20–23] or their higher order analogs, which allow resummation of large logs. Thus, PDFs need only be derived from data at one scale Q^2, and can then be run to any scale needed. Once radiative corrections are included, effective PDFs can be defined for observing any parton inside any particle including those that are nominally fundamental since radiative branching can generate other particles.

A common analogous way to address final state radiation below the factorization scale is the usage of parton shower procedures, which are universal rules that produce probabilities for exclusive final states starting from a given parton at matrix-element level, effectively resumming large logs to leading order by using the recursive structure of final state radiation. Numerical methods using the parton shower procedure are briefly mentioned in Section 1.2.5. It should also be noted that there exist analytic methods to reorganize the perturbative expansion and resum the large logs such as those reviewed in Ref. [24] that do not resort to the factorization methods described here.

1.1.6 Symmetries and gauge theory

This section concerns symmetries, transformations that leave the laws of physics invariant, with a focus on a special class of gauge symmetries that specify interactions called gauge interactions.

In mathematical physics, Noether's theorem shows that there is a fundamental duality between symmetries and conservation laws [25]. In the context of classical field theory, if $\delta\phi_a$ are continuous transformations that leave the Lagrangian invariant up to a divergence $\partial_\mu K^\mu$, then there is a locally conserved current

$$j^\mu = \frac{\partial \mathcal{L}}{\partial(\partial_\mu \phi_a)} \delta\phi_a - K^\mu. \tag{1.21}$$

In a quantum theory, there exist symmetries that leave the Lagrangian invariant up to a divergence but change the path integral measure and thus fail to be symmetries of the full theory. These symmetries are said to be anomalous. For nonanomalous symmetries, the generalized Ward-Takahashi identity states that a current inside an expectation value is locally conserved, up to contact terms that appear when the spacetime argument of the current matches that of another field in the expectation value [26–28]. Similar considerations hold for discrete symmetries, which give rise to discrete multiplicatively conserved charges.

The Coleman-Mandula theorem [29] states that given a theory with well defined S-matrix elements that meet a few basic conditions, the symmetries of the theory locally

described by Lie algebras consist only of the direct product of the Poincaré group and any internal symmetry groups. The Poincaré group includes spacetime translations, spatial rotations, and boosts. The conserved charges associated with the Poincaré group include energy, spatial momentum, angular momentum, and center of momentum. Internal symmetry groups are transformations of the fields of the theory aside from spacetime transformations. Examples of global (non-spacetime-dependent) internal symmetries will be discussed in the next section.

One particular type of internal symmetries are gauge symmetries, whose transformations locally form a compact Lie group but are allowed to smoothly vary across spacetime. Invariance under gauge transformations necessitates the introduction of a gauge interaction [30,31]. The locally conserved quantity charge associated with the gauge symmetry is also the charge that determines field behavior with respect to the interaction. The gauge transformations themselves are in a certain sense unphysical as any choice of gauge will provide equally valid laws of physics.

In the case of an abelian U(1) gauge symmetry, each field is assigned a numerical charge describing its transformation. For nonabelian gauge symmetries, fields are grouped into multiplets that are each assigned a representation of the gauge group describing how they transform into each other. Gauge invariance then necessitates the introduction of a gauge field, a special type of vector field, which is included in the

Lagrangian by replacing spacetime derivatives ∂_μ with covariant derivatives D_μ such as

$$\begin{aligned} i\psi^\dagger\bar{\sigma}^\mu\partial_\mu\psi &\to i\psi^\dagger\bar{\sigma}^\mu D_\mu\psi \\ (\partial^\mu\phi)^\dagger(\partial_\mu\phi) &\to (D^\mu\phi)^\dagger(D_\mu\phi), \end{aligned} \tag{1.22}$$

where ψ and ϕ are spinor and scalar fields respectively. The covariant derivative D_μ is defined by

$$D_\mu = \partial_\mu - igT^a_{\text{rep}}A^a_\mu, \tag{1.23}$$

where g is the coupling for the gauge interaction, T^a_{rep} are the generator matrices in an appropriate representation for nonabelian gauge theories or the charge in the abelian case, and A^a_μ are the gauge fields. The gauge field itself is uncharged in the abelian case and is in the adjoint representation in the nonabelian case, meaning that the index a will match the generators of the adjoint representation. Also consistent with gauge symmetry are kinetic terms of the form $F^a_{\mu\nu}F^{a\mu\nu}$ where

$$F^a_{\mu\nu} = \partial_\mu A^a_\nu - \partial_\nu A^a_\mu + gf^{abc}A^a_\mu A^b_\nu \tag{1.24}$$

and f^{abc} are the structure coefficients of the Lie group. The gauge fields are not ordinary vector fields since they must satisfy an additional gauge symmetry condition. Excitations in gauge fields are thus forced to be massless and cannot be longitudinally polarized. The redundant degrees of freedom present in a normal vector field must be eliminated by working in a particular gauge or using nonphysical Faddeev-Popov ghost fields to cancel

the redundant degree of freedom [32].

For abelian gauge groups, the gauge coupling runs to smaller values as the renormalization group is run to low energies/long distances. For nonabelian gauge groups, the gauge coupling can increase or decrease at low energies depending on the exact gauge group and the effective number of interacting fields. If the interaction strength increases at low energies/long distances and decreases at high energies/short distances, the interaction is said to be asymptotically free.

Even if a theory possesses a symmetry at a fundamental level, it is possible for the symmetry to be hidden by spontaneous symmetry. The canonical case can be seen by considering a scalar field with a potential:

$$\mathcal{L} = (\partial^\mu \phi)^\dagger (\partial_\mu \phi) - \mu^2 \phi^\dagger \phi - \lambda (\phi^\dagger \phi)^2. \tag{1.25}$$

When $\mu^2 < 0$, ϕ acquires a non-zero vacuum expectation value (VEV) in the ground states, specifically $\langle \phi \rangle = \sqrt{-\mu^2/2\lambda} e^{i\theta}$ for any real θ. The Lagrangian is invariant under the transformation $\phi \to \phi e^{i\theta}$, but a particular ground state will be sent to a different ground state. In this case, it is said that the symmetry has been spontaneously broken. Continuous symmetries generically guarantee that the ground state will be degenerate and moreover that there are directions of flat potential along the degenerate ground states. This implies the existence of massless Nambu-Goldstone fields that correspond to the broken degrees of freedom of the original symmetries [33–35]. In the case a gauge symmetry is spontaneously broken, working in unitary gauge reveals that the goldstone

bosons disappear and are instead incorporated into the "would-be" gauge fields, giving them a mass and a longitudinal polarization. This process is called the Higgs mechanism and was discovered by several independent groups in 1964 [36–38], and later applied to electroweak physics [39, 40].

1.1.7 The standard model

This section describes the standard model of physics using the framework of QFT described in the previous sections.

The standard model can be completely specified by its field content and symmetries. The explicitly imposed symmetries of the SM are Poincaré symmetry and the SM gauge symmetries. The SM gauge group is $\mathrm{SU(3)_C} \times \mathrm{SU(2)_L} \times \mathrm{U(1)_Y}$ [39–44] where the C, L, and Y stand for color, left-handed isospin, and hypercharge. These are the names given to the properties transformed by the gauge transformations. Invariance under $\mathrm{SU(3)_C}$ specifies the strong interaction, also called quantum chromodynamics (QCD). Invariance under $\mathrm{SU(2)_L} \times \mathrm{U(1)_Y}$ specifies the electroweak interaction. The gauge fields for $\mathrm{SU(3)_C} \times \mathrm{SU(2)_L} \times \mathrm{U(1)_Y}$ are denoted G^a_μ, W^b_μ, and B_μ respectively and their field strength tensors are denoted $G^a_{\mu\nu}$, $W^b_{\mu\nu}$ and $B_{\mu\nu}$.

The SM features five sets of left-handed spinor field multiplets: Q, $\bar{u}$, $\bar{d}$, L, and $\bar{e}$. Each of these is a triplet of three "generations" that have identical representations with respect to the SM gauge interactions. Each generation consists of gauge multiplets described by the representations of each field given in Table 1.1. There is, additionally,

Table 1.1: Representations of spinor and scalar fields in the SM.

Field	$SU(3)_C$	$SU(2)_L$	$U(1)_Y$
Q	3	2	1/6
$\bar{u}$	$\bar{3}$	1	-2/3
$\bar{d}$	$\bar{3}$	1	1/3
L	1	2	-1/2
$\bar{e}$	1	1	1
ϕ	1	2	-1/2

one complex scalar field ϕ whose representations are also provided in Table 1.1. In particular, each generation of $\bar{u}$ and $\bar{d}$ consists of three different colors of fields, each generation of L consists of two different left-handed isospins of fields, each generation of $\bar{e}$ is a single field, and each generation of Q consists of six different fields of varying color and left-handed isospin. The field ϕ also consists of two complex fields with differing left-handed isospin.

The Lagrangian density for the standard model $\mathcal{L}_{SM}$ is then given by all nonconstant marginal and relevant terms that respect Lorentz symmetry and the SM gauge

symmetries. The standard model Lagrangian is thus

$$\begin{aligned}\mathcal{L}_{\mathrm{SM}} = &-\frac{1}{4}G^a_{\mu\nu}G^{a\mu\nu} - \frac{1}{4}W^a_{\mu\nu}W^{a\mu\nu} - \frac{1}{4}B_{\mu\nu}B^{\mu\nu} \\ &- \frac{g_s^2\theta}{64\pi^2}\epsilon^{\mu\nu\rho\sigma}G^a_{\mu\nu}G^a_{\rho\sigma} \\ &+ iL^\dagger\bar{\sigma}^\mu D_\mu L + i\bar{e}^\dagger\bar{\sigma}^\mu D_\mu\bar{e} \\ &+ iQ^\dagger\bar{\sigma}^\mu D_\mu Q + i\bar{u}^\dagger\bar{\sigma}^\mu D_\mu\bar{u} + i\bar{d}^\dagger\bar{\sigma}^\mu D_\mu\bar{d} \\ &- (LY_e\epsilon\phi\bar{e} + QY_d\epsilon\phi\bar{d} + QY_u\phi^\dagger\bar{u}) - \text{h.c.} \\ &+ (D^\mu\phi)^\dagger D_\mu\phi - \left(\mu^2\phi^\dagger\phi + \lambda(\phi^\dagger\phi)^2\right).\end{aligned} \tag{1.26}$$

In this equation, Y_u, Y_d, and Y_e are Yukawa coupling matrices that mix generational multiplets. The quantities μ^2, λ, g_s, g_1, and g_2 are coupling constants, the latter three of which are embedded in the definition of the covariant derivative. The fully antisymmetric tensor with four indices, $\epsilon^{\mu\nu\rho\sigma}$, appears in the so-called theta term involving the QCD gauge fields. The invariant symbol ϵ allows two $\mathrm{SU}(2)_\mathrm{L}$ multiplets in the (anti)fundamental representation to be combined into an $\mathrm{SU}(2)_\mathrm{L}$ invariant term. In principle, there also exists a term proportional to $\epsilon^{\mu\nu\rho\sigma}W^a_{\mu\nu}W^a_{\rho\sigma}$; however, this term can be canceled by an appropriate redefinition of the spinor fields and is thus omitted.

While potential terms for the SM spinors are irrelevant or forbidden by gauge symmetry, the scalar ϕ experiences a potential $V(\phi) = \mu^2\phi^\dagger\phi + \lambda(\phi^\dagger\phi)^2$. When μ^2 is negative, the configuration of minimum energy corresponds to ϕ taking on a nonzero vacuum expectation value, which, with an appropriate choice of global gauge transformation, can be expressed as $(v, 0)$ where $v = \sqrt{-\frac{\mu^2}{2\lambda}}$. The field ϕ thus spontaneously breaks the

$\mathrm{SU(2)_L} \times \mathrm{U(1)_Y}$ gauge symmetry down to a single $\mathrm{U(1)_{EM}}$ symmetry. Using a change of basis, W^1, W^2, W^3, and B can be reexpressed in terms of mass eigenstate fields W^+, W^-, Z, and A, the last of which is the massless field corresponding to the residual $\mathrm{U(1)_{EM}}$ symmetry. The massless A part of the electroweak interaction is called electromagnetism while the massive W/Z part is called the weak interaction. After three real degrees of freedom of ϕ are incorporated into the weak bosons, there remains a single real scalar field whose excitations are called Higgs bosons.

The Higgs VEV also affects the spinor fields Q, $\bar{u}$, $\bar{d}$, L, and $\bar{e}$. Let the left-handed isospin components of L and Q be called (ν, e) and (u, d) respectively. The mass eigenstate fields are most easily expressed in terms of the Dirac spinors $\mathcal{E} = (e, \bar{e}^\dagger)$, $\mathcal{D} = (d, \bar{d}^\dagger)$, $\mathcal{U} = (u, \bar{u}^\dagger)$, and the Majorana spinor $\mathcal{N} = (\nu, \nu^\dagger)$. The SM provides the freedom to work in a generation basis where Y_e, Y_u, and Y_d are diagonal and thus there exist three mass eigenstates each for $\mathcal{E}$, $\mathcal{D}$, $\mathcal{U}$, and $\mathcal{N}$ with the last of these consisting of three massless fields. This yields a total of 12 physical fermion mass eigenstates. In the case of $\mathcal{U}$ and $\mathcal{D}$, working in the mass eigenbasis introduces terms of the form $W^+_\mu \bar{\mathcal{U}} V \gamma^\mu \mathcal{D}$ that mix generations of $\mathcal{U}$ and $\mathcal{D}$. The matrix of constants V controlling these mixing terms is called the Cabibbo-Kobayashi-Masakawa (CKM) matrix [45, 46].

The SM mass eigenstates corresponding to the observed particles together with the names of the particles and experimentally measured values of selected properties are summarized in Table 1.2. Since the $\mathrm{SU(3)_C}$ gauge symmetry is not spontaneously broken, the different colors of quarks and gluons have identical mass and by convention are not

Table 1.2: Mass eigenstates of the SM. Note that the u, d, s, c, and b quark masses are quoted in the modified minimal subtraction renormalization scheme at a scale of 2 GeV (u, d, s) or the mass of the quark (c, b) while other masses given are the pole mass. While neutrino masses are exactly 0 in the SM, it is known that neutrinos have $O(0.01$ eV) scale masses from measurements of neutrino oscillation (see next section). Cosmological data bounds the sum of neutrino masses below about 0.15 eV [47]. Experimental values taken from Ref. [48].

Field	Particle Name	Symbol	$SU(3)_C$	$U(1)_{EM}$	Mass	Mean Lifetime [s]
Generation of $\mathcal{U}$	up quark	u	3	2/3	2.16 MeV	-
Generation of $\mathcal{U}$	charm quark	c	3	2/3	1.27 GeV	-
Generation of $\mathcal{U}$	top quark	t	3	2/3	172.7 GeV	4.64×10^{-25}
Generation of $\mathcal{D}$	down quark	d	3	-1/3	4.67 MeV	-
Generation of $\mathcal{D}$	strange quark	s	3	-1/3	93.4 MeV	-
Generation of $\mathcal{D}$	bottom quark	b	3	-1/3	4.18 GeV	-
Generation of $\mathcal{E}$	electron	e	1	-1	0.511 MeV	∞
Generation of $\mathcal{E}$	muon	μ	1	-1	105.7 MeV	2.20×10^{-6}
Generation of $\mathcal{E}$	tau	τ	1	-1	1.777 GeV	2.90×10^{-13}
Generation of $\mathcal{N}$	neutrino 1	ν_1	1	0	$<\sim 0.15$ eV	-
Generation of $\mathcal{N}$	neutrino 2	ν_2	1	0	$<\sim 0.15$ eV	-
Generation of $\mathcal{N}$	neutrino 3	ν_3	1	0	$<\sim 0.15$ eV	-
G	gluon	g	8	0	0	-
A	photon	γ	1	0	0	∞
$W^{\pm}$	W boson	W	1	1	80.38 GeV	3.16×10^{-25}
Z	Z boson	Z	1	0	91.19 GeV	2.64×10^{-25}
Component of ϕ	Higgs boson	H	1	0	125.2 GeV	2.1×10^{-22}

distinguished. The strong interaction is asymptotically free, which typically causes quarks and gluons to confine into composite particles called hadrons at low energies. The top quark is excepted as it decays before it can hadronize. Figure 1.6 shows the masses and lifetimes for the SM particles commonly observed in isolation as well as the masses and lifetimes for a selection of hadrons.

In addition to Lorentz and gauge symmetry, which are explicitly imposed, the SM Lagrangian features a number of additional accidental symmetries that simply arise because there exist no marginal or relevant terms consistent with the explicitly imposed

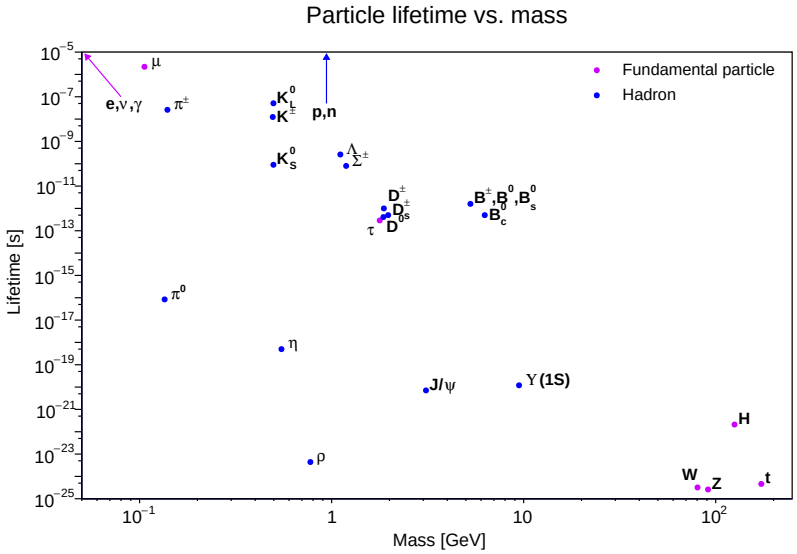

Figure 1.6: Particle lifetime vs. mass for fundamental particles observed in isolation (violet) as well as for a selection of hadrons (blue).

symmetries that would violate them. These are typically parametrized as baryon number, electron number, muon number, and tau number, and are provided for the SM particles in Table 1.3. Note that the latter three symmetries are generation specific. However, all four of these symmetries are anomalous and are thus violated by nonperturbative effects. The combination $B - L$ where B is baryon number and L is lepton number, the sum of electron, muon, and tau number, is nonanomalous, but the violation of each of the four accidental symmetries is highly suppressed and typically negligible regardless. Furthermore, the anomaly only violates B and L by multiples of 3, which is sufficient to ensure the stability of the proton, a hadron that is the lightest particle with nonzero baryon number in the standard model.

Table 1.3: Quantum numbers associated with accidental symmetries of the Standard model. Note that L is split into its generational components (ν_e, e), (ν_μ, μ), and (ν_τ, τ) while $\bar{e}$ is similarly split into its generational components, $\bar{e}$, $\bar{\mu}$, and $\bar{\tau}$. The conserved numbers of the symmetry groups $U(1)_B$, $U(1)_e$, $U(1)_\mu$, and $U(1)_\tau$ correspond to baryon number, electron number, muon number, and tau number respectively.

Field	$U(1)_B$	$U(1)_e$	$U(1)_\mu$	, $U(1)_\tau$
Q	1/3	0	0	0
$\bar{u}$	-1/3	0	0	0
$\bar{d}$	-1/3	0	0	0
e, ν_e	0	1	0	0
μ, ν_μ	0	0	1	0
τ, ν_τ	0	0	0	1
$\bar{e}$	0	-1	0	0
$\bar{\mu}$	0	0	-1	0
$\bar{\tau}$	0	0	0	-1
ϕ	0	0	0	0

1.1.8 Gravity, neutrino masses, and EFT

Gravity and neutrino masses are two well known phenomena that are not formally included in the original standard model. However, both can both be incorporated using effective field theory.

In the weak field limit, gravity is analogous to a gauge theory except that the group being gauged is not an internal symmetry group but rather the $\mathbb{R}^4$ symmetry group of spacetime translations [49]. This means that the metric $g_{\mu\nu}$ becomes a dynamical quantity. The conserved charges associated with spacetime translational symmetry, momentum and energy, thus serve as the charge for gravity. As with the SM gauge groups, this requires one to promote ∂_μ to a covariant derivative D_μ with a connection $\Gamma^\lambda_{\mu\nu}$ the classical details of which can be found in General Relativity textbooks such as Ref. [50].

The dynamics of gravity are most easily expressed in terms of the scalar curvature R, the Ricci curvature tensor $R_{\mu\nu}$, and the Riemann curvature tensor $R_{\mu\nu\rho\sigma}$, which are functions of the connection.

Gravity can be quantized with a similar procedure to that used for the SM gauge interactions. The reason why gravity is not included in the original SM is because it is nonrenormalizable. Nonrenormalizable does not mean that the running of couplings in the theory cannot be calculated but rather that the Lagrangian must include an infinite number of terms to do so. In the case of the standard model and gravity, there exist only finitely many marginal and relevant terms. This means that predictions can be made at low energies by approximating to a finite number of terms.

From the discovery of neutrino flavor oscillations [51–53], it is also known that neutrinos have mass, which is not the case in the original standard model. This means that, like the quark sector, the lepton sector has particles whose mass states are mixtures of different flavor states. It is not yet known how neutrino masses are generated, but one minimal extension of the SM that is consistent with neutrino masses is the Weinberg operator $(\phi^\dagger L)Y_\nu(\phi^\dagger L)/\Lambda_{\rm UV} + \text{h.c.}$ where Y_ν is a dimensionless coupling matrix and $\Lambda_{\rm UV}$ is the EFT cutoff scale. This operator can be generated by any UV theory that violates lepton number by 2 such as the seesaw mechanism [54–58]. This solution is quite natural as in the EFT framework, one includes all higher dimensional operators consistent with the symmetries of the theory, which includes the Weinberg operator. Furthermore, the smallness of the neutrino masses (~ 0.1 eV) is then explained by the irrelevance of the

Weinberg operator if the cutoff scale is around 10^{14} GeV. As in the quark sector, the neutrino mass eigenstates are not weak interaction eigenstates, with the relation between the two given by the PMNS matrix [59,60]. Typically, neutrinos are produced in a flavor eigenstate, which can then oscillate to other flavor eigenstates due to the flavor states not being mass eigenstates.

The Lagrangian

$$\begin{aligned}
\mathcal{L}_{\text{SM++}} =&\sqrt{-g}\Big\{ -\Lambda - \frac{2}{\kappa^2}R + c_1 R^2 + c_2 R_{\mu\nu}R^{\mu\nu} \\
&- \frac{1}{4}G^a_{\mu\nu}G^{a\mu\nu} - \frac{1}{4}W^a_{\mu\nu}W^{a\mu\nu} - \frac{1}{4}B_{\mu\nu}B^{\mu\nu} \\
&- \frac{g_s^2\theta}{64\pi^2}\epsilon^{\mu\nu\rho\sigma}G^a_{\mu\nu}G^a_{\rho\sigma} \\
&+ iL^\dagger\bar{\sigma}^\mu D_\mu L + i\bar{e}^\dagger\bar{\sigma}^\mu D_\mu \bar{e} \\
&+ iQ^\dagger\bar{\sigma}^\mu D_\mu Q + i\bar{u}^\dagger\bar{\sigma}^\mu D_\mu \bar{u} + i\bar{d}^\dagger\bar{\sigma}^\mu D_\mu \bar{d} \\
&- (LY_e\epsilon\phi\bar{e} + QY_d\epsilon\phi\bar{d} + QY_u\phi^\dagger\bar{u}) - \text{h.c.} \\
&+ (D^\mu\phi)^\dagger D_\mu\phi - \left(\mu^2\phi^\dagger\phi + \lambda(\phi^\dagger\phi)^2\right) \\
&+ \frac{1}{\Lambda_{\text{UV}}}(\phi^\dagger L)Y_\nu(\phi^\dagger L) + \text{h.c.} \\
&+ c_3 R\phi^\dagger\phi + \text{higher dimensional operators}\Big\}
\end{aligned} \tag{1.27}$$

describes an extended version of the SM with gravity and neutrino masses. This equation includes all terms of the Lagrangian up to dimension 5 as the Weinberg operator is the only dimension-five operator consistent with gauge and Lorentz symmetry. This Lagrangian is consistent with almost all known physics, though there still exist unexplained

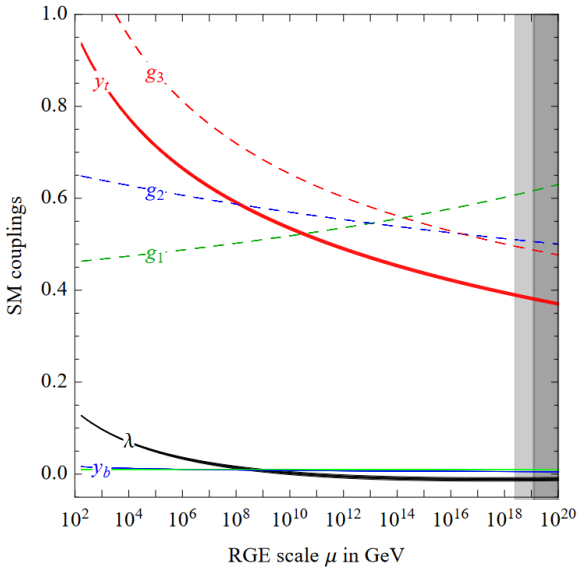

Figure 1.7: Running of dimensionless couplings in the renormalizable standard model in the $\overline{\text{MS}}$ scheme. Figure from Ref. [61].

mysteries that are detailed in the next section.

At very high energies/short distances, the effects of the infinite irrelevant operators associated with gravity will cease to be negligible and the effective field theory will break down. This is likely to occur near 10^{19} GeV, the Planck scale. Even without gravity, it is possible that the SM may need to be considered as an EFT with a cutoff. Figure 1.7 shows the running of the renormalizable SM couplings other than μ^2. Notably, the coupling g_1 continues to increase with energy and is expected to encounter a Landau pole at a scale near 10^{40} GeV. At this point, assuming the SM is still valid, nonperturbative effects become relevant and it becomes difficult to determine the behavior of the theory, but this may be a sign that the standard model should be replaced at or before this scale.

1.1.9 Beyond the standard model

The SM makes many precise predictions that have been measured to great accuracy, such as the proton-proton cross sections shown in Figure 1.16. The nonrenormalizability of gravity guarantees that the effective field theory must break down, but there are also various experimental observations and theoretical mysteries that point toward physics beyond the standard model. This section gives an overview of four major pieces of evidence for BSM physics: the arbitariness of the SM, naturalness, baryon asymmetry, and dark matter.

Arbitrariness

The standard model possesses a large number of seemingly arbitrary features and parameters, with 19 constants in its minimal incarnation given by Equation 1.26. In the gauge sector of the SM, arbitrary choices include the choice of the nonsimple gauge group $\mathrm{SU(3)_C}\times\mathrm{SU(2)_L}\times\mathrm{U(1)_Y}$, the choices of representations given in Table 1.1, the values of the interaction couplings at some reference scale, and the QCD θ coefficient at some reference scale. One striking feature is that there are exactly three copies of each fermion with the same quantum numbers, the three generations. The Higgs sectors also features a large number of arbitrary features in the form of the Higgs potential parameters and the Yukawa coupling matrices at some reference scale. These determine the masses of the known particles, which span almost 6 orders of magnitude, excluding neutrinos. They also determine the CKM and PMNS flavor mixing matrices. The CKM matrix is

curiously quite close to the identity.

The paradigm of grand unification generally seeks to reduce the number of arbitrary choices and parameters in the theory by combining particle multiplets into larger multiplets of some larger gauge group that is spontaneously broken down to the SM gauge group. The first example of a grand unified theory (GUT) was the Pati-Salam model [62], which features the gauge group $\mathrm{SU}(4)_\mathrm{C}\times\mathrm{SU}(2)_\mathrm{L}\times\mathrm{SU}(2)_\mathrm{R}$. The idea of the Pati-Salam model is to unify leptons and quarks by making lepton number the fourth "color" in the (anti)fundamental representation of SU(4). A single generation of SM fermions plus an extra singlet is contained two multiplets in the representations $(4,2,1)$ and $(\bar{4},1,2)$ respectively. The smallest simple group that can be broken to the standard model gauge groups is SU(5), which is the basis for the Georgi-Glashow model of grand unification [63]. A single generation of SM fermions is contained in two multiplets in the 10 and $\bar{5}$ representations. The smallest gauge group in which all SM fermions are contained in a single multiplet is SO(10), which contains all fermions plus an extra singlet in the 16 representation [64, 65]. Larger groups can also be considered such as in Ref. [66].

If the SM arises from a grand unified theory with a simple gauge group, then the gauge couplings should unify at some scale. As shown in Figure 1.7, the standard model couplings do approach each other near a scale of 10^{16} GeV, but they do not perfectly intersect. Indeed, in the absence of additional BSM physics, current data excludes unification to a high significance [67]. Grand unified theories with a simple gauge group thus predict undiscovered new physics, typically at relatively low energies, to ensure gauge

coupling unification.

Grand unified theories also generically predict baryon number violating processes that induce proton decay, which appear as effective dimension-six operators. Proton decay has not been observed, and current bounds on proton decay [68, 69] put an upper bound on the dimension six operator coefficients, which is now approaching a scale of 10^{16} GeV, the GUT scale indicated by gauge coupling unification.

Naturalness

Worse than simply being arbitrary, the SM features several parameters that may be fine tuned or unnatural. The first of these is the QCD θ parameter. The QCD θ parameter is one of two sources of CP violation in the strong interaction, the other being the up-type quark and down-type quark Yukawa couplings Y_u and Y_d. Experimental measurements of the neutron electric dipole moment put a strong upper bound on CP violation in the strong sector [70]. The CP violation from the Yukawa couplings is quite small and thus does not generate a large θ if $\theta(\Lambda_{\rm UV}) \approx 0$ at some relatively large cutoff scale $\Lambda_{\rm UV}$ [71], but the question still remains why θ should be so close to 0 at the cutoff scale when CP is not a general symmetry of the SM.

As demonstrated in Equation 1.20, the relevant coefficients in EFTs are generally driven towards $\Lambda_{\rm UV}^n$ with an appropriate power n by quantum corrections when running the theory to low energies/long distances. A value of coupling that strongly differs from the cutoff typically indicates large cancellations. The relevant operators in Equation 1.27

thus suggest EFT cutoffs in order to avoid such fine tuning. The Einstein gravitational constant κ^2, the cosmological constant Λ, and the μ^2 parameter in the Higgs potential imply cutoffs at 10^{19} GeV, 10^{-42} GeV, and 100 GeV, respectively. Of these, the cosmological constant is the most troubling as the implied cutoff scale to avoid fine tuning is 10^{-42} GeV, yet no signs of any mechanism for setting Λ to such a small value have been observed, despite measurements to much short distances/higher energies [72]. In contrast, μ^2 implies that a cutoff scale near 100 GeV is needed to avoid fine tuning [73–76]. This scale is precisely that being currently probed by contemporary experiments, and although no clear signs of BSM physics have been seen yet, there is still some hope for an $O(\text{ TeV})$ mechanism that sets the scale μ^2. See below in Sections 1.1.10 and 6.3.2.

Baryon asymmetry

In the SM, conservation of electric charge and conservation of baryon number (mod 3) lead to the absolute stability of isolated (anti)protons and (anti)electrons. (Anti)neutrons can also be approximately stabilized when bound together with protons into atomic nuclei. In the context of cosmology, the contents of the universe that move at nonrelativistic speeds are referred to as matter. Protons, neutrons, and electrons are specifically called baryonic matter.

It is not known why the matter in the universe consists primarily of baryonic matter rather than their antiparticles. For such an asymmetry to arise, both $\mathcal{C}$ and $\mathcal{CP}$ asymmetry, nonconservation of baryon and lepton numbers, and thermal nonequilibrium in the

early universe are required [77]. While the SM does contain sources of $\mathcal{CP}$ violation and baryon number violation, these sources are not nearly sufficient to produce the observed asymmetry between matter and antimatter. This suggests the existence of additional BSM mechanisms for generating baryon asymmetry.

Dark matter

Various astronomical measurements are not consistent with a universe described only by the standard model plus neutrino masses and EFT gravity. The simplest and most compelling explanation is that the majority of matter in the universe is not baryonic matter, but rather an unknown substance termed dark matter. Evidence for the existence of dark matter can be found in a large number of measurements including but not limited to Ref. [78–81]. The most precise measurement of the cosmic microwave background puts dark matter as constituting about 84% of the matter in the universe [82]. Dark matter models display excellent agreement with measurements of the large scale structure of the universe.

The paradigm of big bang nucleosynthesis provides an accurate prediction for the amount of baryonic matter in the universe and largely rules out nonluminescent baryonic matter as a dark matter candidate [83]. This leaves undiscovered BSM particles and primordial black holes created before big bang nucleosynthesis as the leading dark matter candidates. Although primordial black holes are predicted by regular SM cosmology, the abundance needed to constitute the observed dark matter density would likely require

BSM physics regardless [84].

One particularly simple class of dark model candidates are thermal relics, particles whose relic abundance is set by freeze out. In such models, particles of dark matter created in the early universe annihilate with other dark matter or even non-dark matter particles until the universe has expanded to the point that the annihilation rate drops below the Hubble rate and the density of particles is too low for significant annihilation to continue. To account for the observed dark matter density, such thermal relic dark matter would need to have a mass between about 1 keV and 10 PeV, depending on the annihilation mechanism [85]. The primary constraints on particle dark matter from astrophysical measurements are on its charge and decay rate since it cannot interact strongly with electromagnetism, nor can it decay much faster than cosmological time scales.

1.1.10 Supersymmetry

Supersymmetry is one popular class of BSM theories that relates fermionic and bosonic fields. Supersymmetry has the potential to explain the scale of the Higgs potential μ^2 parameter, gauge coupling unification, and the identity of dark matter. This section provides an overview of supersymmetry following Ref. [86] and Ref. [5]. The next section provides an overview of the simplest realistic models of supersymmetry.

Although the Coleman-Mandula theorem places strong constraints on the symmetries of a QFT locally described by a Lie algebra, spacetime and internal symmetries can

be related by considering Lie superalgebras with anti-commuting generators [87]. This section will consider $N = 1$ supersymmetry with a single copy of the supersymmetry generators since theories with additional generators do not support chiral fermions or parity violation.

Superspace is the extension of spacetime coordinates x^μ to superspace coordinates containing an extra anticommuting left-handed spinor coordinate θ_a and its conjugate $\theta^*_{\dot{a}}$. A scalar field in superspace, $\Phi(x, \theta, \theta^*)$, is called a superfield. A power series expansion of Φ in θ and θ^* is finite due to the anticommutativity of these coordinates. The series expansion of Φ shows that it can be parametrized by four complex scalar fields, a complex vector field, and four complex spinor fields. However, this most general Φ lives in a reducible representation of the supersymmetric algebra, and it is convenient to work instead with irreducible chiral and vector superfields.

A left-handed chiral superfield is a superfield Φ satisfying

$$\left(-\frac{\partial}{\partial\theta^{*\dot{a}}} + i\theta^c\sigma^\mu_{c\dot{a}}\partial_\mu\right)\Phi(x, \theta, \theta^*) = 0, \tag{1.28}$$

where the differential operator in parentheses is called a supercovariant derivative $\mathcal{D}^*_{\dot{a}}$. The Hermitian conjugate of a left-handed chiral superfield is a right-handed chiral superfield that satisfies an analogous equation with the supercovariant derivative $\mathcal{D}_a$. Using the substitution $y^\mu = x^\mu - i\theta^c\sigma^\mu_{c\dot{c}}\theta^{*\dot{c}}$, a general left-handed chiral superfield can be written

$$\Phi(x, \theta, \theta^*) = A(y) + \sqrt{2}\theta\psi(y) + \theta\theta F(y), \tag{1.29}$$

where there are only two complex scalar fields A and F and a single complex left-handed spinor field ψ. A vector chiral superfield is a hermitian superfield Φ.

The most general form of a vector superfield is

$$\begin{aligned}\Phi(x,\theta,\theta^*) =& C(x) + \theta\chi(x) + \theta^*\chi^\dagger(x) + \theta\theta M(x) + \theta^*\theta^* M^\dagger(x) + \theta\sigma^\mu\theta^* v_\mu(x) \\ &+ \theta\theta\theta^*\lambda^\dagger(x) + \theta^*\theta^*\theta\lambda(x) + \frac{1}{2}\theta\theta\theta^*\theta^* D(x),\end{aligned} \tag{1.30}$$

where there are two real scalar fields C and D, a complex scalar field M, two left-handed spinor fields χ and λ, and a real vector field v_μ. Gauge superfields can be constructed by introducing a vector superfield V^a in the adjoint representation of a gauge group. Given a left-handed chiral superfield Φ in a representation of the gauge group with generators or charge T^a, gauge symmetry will mean invariance under the following supergauge transformation.

$$\begin{aligned}\Phi &\to e^{-2ig\Xi^a T^a}\Phi \\ \Phi^\dagger &\to \Phi^\dagger e^{2ig(\Xi^a T^a)^\dagger} \\ e^{-2gV^a T^a} &\to e^{-2ig(\Xi^a T^a)^\dagger} e^{-2gV^a T^a} e^{2ig(\Xi^a T^a)},\end{aligned} \tag{1.31}$$

where Ξ^a is any multiplet of left-handed chiral superfields. By picking Ξ^a corresponding to the Wess-Zumino gauge, it is possible to eliminate C, χ, and M, reducing the vector superfield to

$$V = (\theta\sigma^\mu\theta^*)v_\mu + \theta\theta\theta^*\lambda^\dagger + \theta^*\theta^*\theta\lambda + \frac{1}{2}\theta\theta\theta^*\theta^* D \tag{1.32}$$

with only a real vector field v_μ, a complex left-handed spinor field λ, and a real scalar field D. Note that this choice of gauge leaves the residual non-super gauge freedom.

Superspace extends the generators of translations from the usual four-momentum P^μ to include an additional supercharge Q_a with its conjugate $Q^\dagger_{\dot{a}}$. For consistency of the supersymmetric algebra, the supercharges must generate the following transformations on a superfield Φ:

$$\begin{aligned}[\Phi, Q_a] &= -i\left(\frac{\partial}{\partial\theta^a} + i\sigma^\mu_{a\dot{c}}\theta^{*\dot{c}}\partial_\mu\right)\Phi \\ [\Phi, Q^\dagger_{\dot{a}}] &= -i\left(-\frac{\partial}{\partial\theta^{*\dot{a}}} - i\theta^c\sigma^\mu_{c\dot{a}}\partial_\mu\right)\Phi.\end{aligned} \tag{1.33}$$

Applying these relations to the forms for chiral and vector superfields derived earlier reveals that the F scalar of a chiral superfield and the D scalar of a vector superfield commute with Q_a and $Q^\dagger_{\dot{a}}$ up to an overall divergence and thus are invariant up to an overall divergence under supersymmetry transformations.

Supersymetrically-invariant Lagrangians can thus be built by using the F-terms of chiral superfields and the D-terms of vector superfields. For example, given a chiral superfield Φ and a gauge superfield V^a, $\Phi^\dagger e^{-2gV^aT_a}\Phi$ is a vector field and

$$\begin{aligned}\Phi^\dagger e^{-2gV^aT_a}\Phi\Big|_D =& (D^\mu A)^\dagger(D_\mu A) + i\psi^\dagger\bar{\sigma}^\mu D_\mu\psi + F^\dagger F \\ &+ \sqrt{2}g\psi^\dagger\lambda^\dagger A + \sqrt{2}gA^\dagger\lambda\psi - gA^\dagger DA \\ &+ \text{overall divergence},\end{aligned} \tag{1.34}$$

where D is the normal covariant derivative involving the gauge field v_μ. This can produce kinetic terms for chiral superfields. Notably, F has trivial equations of motion and thus is called an auxiliary field.

Defining the field strength superfield

$$\begin{aligned} W_a &= -\frac{1}{8g}\mathcal{D}^*_{\dot{a}}\mathcal{D}^{*\dot{a}}\mathcal{D}_a V \text{ (abelian case)} \\ W_a &= -\frac{1}{8g}\mathcal{D}^*_{\dot{a}}\mathcal{D}^{*\dot{a}} e^{2gV^{a'}T_{a'}}\mathcal{D}_a e^{-2gV^{a''}T_{a''}} \text{ (non-abelian case),} \end{aligned} \tag{1.35}$$

where T_a are the generators of the gauge transformation in the adjoint representation, kinetic terms for gauge superfields can be derived using the F term of WW and its complex conjugate. The relevant F-term is

$$\begin{aligned} \frac{1}{4}\left(WW + W^\dagger W^\dagger\right)\Big|_F &= i\lambda^{a\dagger}\bar{\sigma}^\mu\partial_\mu\lambda^a - \frac{1}{4}F^{\mu\nu}F_{\mu\nu} + \frac{1}{2}D^2 + \text{divergence} \\ &\text{(abelian case)} \\ \frac{1}{4T(R)}\text{Tr}\left(WW + W^\dagger W^\dagger\right)\Big|_F &= i\lambda^{a\dagger}\bar{\sigma}^\mu D_\mu\lambda^a - \frac{1}{4}F^{a\mu\nu}F^a_{\mu\nu} + \frac{1}{2}D^2 + \text{divergence} \\ &\text{(non-abelian case),} \end{aligned} \tag{1.36}$$

where $T(R)$ is the index of the adjoint representation and D_μ is the covariant derivative in the adjoint representation. Similarly to the F of chiral superfields, the D of vector superfields is simply an auxiliary field.

For abelian theories, one can also include the D-term of V itself in the Lagrangian, which is called the Fayet-Iliopoulos term. For nonabelian gauge superfields, the kinetic

term can be slightly amended to include the usual CP-violating θ-term. Neither of these will be described here.

Any polynomial of chiral superfields is itself a chiral superfield whose F term is supersymmetry invariant. A polynomial of chiral superfields and their complex conjugates that appears in the Lagrangian of a supersymmetric theory is called the superpotential. This allows for the construction of potential and Yukawa terms.

1.1.11 The minimal supersymmetric standard model

The MSSM Lagrangian

The simplest supersymmetric extension of the standard model is called the minimal supersymmetric standard model (MSSM). The supersymmetry-invariant MSSM Lagrangian is given by

$$\begin{aligned}\mathcal{L}_{\text{MSSM}} =& \frac{1}{12}\text{Tr}\left(GG + G^\dagger G^\dagger\right)\Big|_F + \frac{1}{8}\text{Tr}\left(WW + W^\dagger W^\dagger\right)\Big|_F + \frac{1}{4}\left(BB + B^\dagger B^\dagger\right)\Big|_F \\ &+ Q^\dagger e^{-2\sum_i g_i V_i^a T_{Ri}^a} Q\Big|_D + \bar{u}^\dagger e^{-2\sum_i g_i V_i^a T_{Ri}^a}\bar{u}\Big|_D + \bar{d}^\dagger e^{-2\sum_i g_i V_i^a T_{Ri}^a}\bar{d}\Big|_D \\ &+ L^\dagger e^{-2\sum_i g_i V_i^a T_{Ri}^a} L\Big|_D + \bar{e}^\dagger e^{-2\sum_i g_i V_i^a T_{Ri}^a}\bar{e}\Big|_D \\ &+ H_u^\dagger e^{-2\sum_i g_i V_i^a T_{Ri}^a} H_u\Big|_D + H_d^\dagger e^{-2\sum_i g_i V_i^a T_{Ri}^a} H_d\Big|_D \\ &+ \left(QY_u\epsilon H_u\bar{u} - QY_d\epsilon H_d\bar{d} - LY_e\epsilon H_d\bar{e} + \mu H_u\epsilon H_d\right)\Big|_F + \text{h.c.},\end{aligned} \tag{1.37}$$

Table 1.4: Representations of chiral superfields in the MSSM.

Field	$SU(3)_C$	$SU(2)_L$	$U(1)_Y$
Q	3	2	1/6
$\bar{u}$	$\bar{3}$	1	-2/3
$\bar{d}$	$\bar{3}$	1	1/3
L	1	2	-1/2
$\bar{e}$	1	1	1
H_u	1	2	1/2
H_d	1	2	-1/2

where Q, $\bar{u}$, $\bar{d}$, L, $\bar{e}$, H_u, and H_d are chiral superfields in representations of the SM gauge groups shown in Table 1.4, and the sum in the exponential runs includes the G, W, and B gauge superfields with their associated couplings and representations. Note that Q, $\bar{u}$, $\bar{d}$, L, and $\bar{e}$ each consist of 3 generations, as in the SM.

In the MSSM, each gauge field in the SM is extended to a gauge superfield containing a gauge field and a spinor; each spinor field in the SM is extended to a chiral superfield containing a spinor and a scalar; and the ϕ scalar of the standard model is extended to two chiral superfield multiplets, H_u and H_d, each containing spinors and scalar. Due to experimental constraints, it is known that H_d and L cannot be identified as the same chiral superfield, despite having identical representations with respect to the SM gauge groups. The MSSM thus predicts that each known gauge boson comes with a corresponding fermion called a gaugino and that each known fermion comes with an additional scalar boson for each chirality called a sfermion. It further predicts eight scalar Higgs bosons and four fermionic higgsinos from the H_u and H_d fields.

Even neglecting theta and Fayet-Iliopoulos terms, the Lagrangian in Equation 1.37

notably does not contain all marginal and relevant terms consistent with gauge and superspace symmetries. There exist additional superpotential terms, namely $L\epsilon L\bar{e}$, $L\epsilon Q\bar{d}$, $L\epsilon H_u$, and $\bar{u}\lambda\bar{d}\bar{d}$ where ϵ and λ are appropriate invariant symbols. These terms violate baryon and lepton number conservation, ruining the accidental perturbative symmetries that appear in the standard model and, assuming relatively small masses for supersymmetric partners, inducing processes such as proton decay in strong violation of experimental bounds.

Baryon and lepton number violating terms are typically disallowed by imposing a new discrete symmetry called R-parity or equivalently matter parity [88–91]. R-parity assigns a value of 1 to the quarks and leptons, the Higgs bosons, and the gauge bosons while assigning a value of -1 to the squarks and sleptons, the higgsinos, and the gauginos. Theories of supersymmetry in which R-parity is conserved are called R-parity conserving (RPC) supersymmetry, while those in which R-parity is not conserved are called R-parity violating (RPV). Theories with small or controlled R-parity violation can be phenomenologically acceptable under certain circumstances and are reviewed in Ref. [92], though they will not be considered in this thesis.

Supersymmetry breaking

The lack of discovery of supersymmetric partners thus far also implies that if supersymmetry exists, it must be spontaneously broken. The equation

$$\begin{aligned}\mathcal{L}_{\text{MSSM soft}} = &-\frac{1}{2}\left(M_3\tilde{g}\mathbb{I}\tilde{g} + M_2\tilde{W}\mathbb{I}\tilde{W} + M_1\tilde{B}\mathbb{I}\tilde{B} + \text{h.c.}\right) \\ &-\left(\tilde{Q}a_u\epsilon H_u\tilde{\bar{u}} - \tilde{Q}a_d\epsilon H_d\tilde{\bar{d}} - \tilde{L}a_e\epsilon H_d\bar{e}\right) \\ &-\tilde{Q}^\dagger m_Q^2\tilde{Q} - \tilde{\bar{u}}^\dagger m_u^2\tilde{\bar{u}} - \tilde{\bar{d}}^\dagger m_d^2\tilde{\bar{d}} - \tilde{L}^\dagger m_L^2\tilde{L} - \tilde{\bar{e}}^\dagger m_e^2\tilde{\bar{e}} \\ &-H_u^\dagger m_{Hu}^2 H_u - H_d^\dagger m_{Hd}^2 H_d - (bH_u\epsilon H_d + \text{h.c.})\end{aligned} \tag{1.38}$$

gives the effective RPC relevant supersymmetry-breaking terms that can be added to the Lagrangian in terms of individual gaugino, sfermion, and Higgs fields. The gaugino and sfermion fields are denoted as the superfield with a tilde, H_u and H_d specifically denote the Higgs scalars, and $\mathbb{I}$ represents the identity in the appropriate adjoint representation. The a's, m's, and b's are various Yukawa and mass matrices.

Including these soft supersymmetry-breaking terms brings the total number of physical parameters in the MSSM Lagrangian to 105, many of which cause violation of experimental measurements of processes such as K^0-$\overline{\mathrm{K}}^0$ oscillations or muon decay [93]. This observation suggests that the mechanism for supersymmetry breaking should have certain flavor and CP universal properties that constrain the large number of parameters in the softly broken MSSM.

The spontaneous breaking of supersymmetry gives rise to a massless goldstino fermion in analogy with Goldstone's theorem for ordinary symmetries. Gravity can be introduced

through the gauging of superspace transformations [94–98]. In such theories of supergravity, spontaneous breaking of supersymmetry does not yield goldstinos but rather contributes a mass and two additional polarization states to the gravitino as part of the super-Higgs mechanism [99].

It has been shown that one can construct models whose ground states or metastable states spontaneously break supersymmetry [88, 100–102], however there are no suitable fields in the MSSM that could be responsible for supersymmetry breaking. It is thus necessary to introduce a new supersymmetry-breaking sector. Furthermore, the new supersymmetry-breaking sector should have only weak or indirect couplings to the visible sector in order to comply with experimental bounds on superpartners. Two of the most well studied mechanisms for communicating supersymmetry breaking to the MSSM are gravity-mediated or Planck-scale-mediated supersymmetry breaking (PMSB) [103–109] and gauge-mediated supersymmetry breaking (GMSB) [110–115] in which a messenger particle from the SUSY breaking sector is charged under the MSSM gauge interactions.

In PMSB models, the couplings of the induced terms are of order $m_{\text{soft}} = \langle F \rangle / M_{\text{planck}}$ where $\langle F \rangle$ is the VEV in the supersymmetry-breaking sector, which implies a VEV near $\sqrt{\langle F \rangle} \approx 10^{11}$ GeV in order to generate an MSSM supersymmetry-breaking scale near 100 GeV. In general, gravity mediation does not guarantee any sort of flavor universality and can in general generate troublesome flavor and CP-violating effects. For this reason, a special scenario called minimal supergravity (MSUGRA) or the constrained minimal supersymmetric standard model (CMSSM) is often considered. In the CMSSM, the

gaugino masses are all identical, the squark and slepton mass matrices are a constant m_0 times the identity, the Higgs masses are m_0, and the a Yukawa couplings are proportional to the usual Y Yukawa couplings at the Planck scale. While there exist theories that give rise to CMSSM like conditions in certain limits [116], the main motivation for considering the CMSSM is experimental constraints.

In GMSB models, the induced couplings are of order $m_{\text{soft}} = (g/4\pi)^2\langle F\rangle/M_{\text{mess}}$ where g is an appropriate gauge coupling and M_{mess} is the scale of the messenger particles that communicate the supersymmetry breaking. This leaves a large range of allowed VEVs $\langle F\rangle$ that could yield a supersymmetry-breaking scale of 100 GeV in the MSSM. Notably, the mass of the gravitino in supergravity is $\langle F\rangle/M_{\text{planck}}$, which means that for messenger scales well below the Planck scale, the gravitino is the lightest R-parity odd particle. A particularly attractive feature of GMSB models is that the experimentally disfavored flavor nonuniversal and CP-violating are naturally absent.

Advantages of the MSSM

The first advantage of the MSSM over the standard model is that the MSSM can more naturally support the electroweak scale. Quadratic corrections to the Higgs potential parameter μ cancel [117–122]. While this prevents Λ_{UV}^2 corrections from the unbroken MSSM Lagrangian, the supersymmetry-breaking terms must be limited to relevant terms in order to avoid reintroducing the problem. The terms generated by PMSB and GMSB both meet this criterion and yield corrections quadratic in m_{soft}. Note that μ does still

suffer from the same problem as the strong θ parameter in that there does not to appear to be a good reason for it to be similar to or smaller than m_{soft}, even when quantum corrections are not considered. Typical solutions to this "μ problem" involve the complete suppression of the μ term in the absence of the supersymmetry-breaking terms such as Refs. [100, 123, 124]. The scale of the Higgs VEV is then set by just m_{soft}, which might arise, for example, from the running of a dimensionless parameter in the supersymmetry-breaking sector.

The second advantage of the MSSM is that the gauge couplings unify when run to 10^{16} GeV [48]. In SU(5) and larger grand unified theories, the Higgs in the $5/\bar{5}$ representation come with additional color triplet scalars that cause baryon and lepton number violation in excess of experimental bounds if their masses are not kept extremely large. Supersymmetry removes quadratic corrections, allowing a large splitting between the Higgs doublet and the color triplet scalars, though the large difference in the tree-level couplings remains an issue similar to the μ problem.

The third advantage of the MSSM is that it naturally provides a dark matter candidate [125, 126]. The lightest R-parity odd particle, typically called the lightest supersymmetric particle (LSP), is stable and can be a dark matter candidate if it is a neutral and long lived. In GMSB models, the LSP is typically the gravitino and has a mass well below the TeV scale. TeV scale LSPs in particular can be thermal dark matter candidates and naturally generate the required dark matter density.

Additionally, supersymmetry is required in any scenarios where string theory provides

the UV completion to the laws of physics. Supersymmetry may also be connected to the baryon asymmetry problem if the mechanism responsible for the baryon asymmetry of the universe is a first-order electroweak phase transition. Such theories of electroweak baryogenesis can occur in the presence of new physics at the TeV scale, though current bounds on supersymmetry make this primarily appealing only for nonminimal models [127].

Phenomenology of the MSSM

The particle mass eigenstates of the MSSM typically include, in addition to the SM fermions and gauge bosons, five Higgs scalars, pairs of squarks $\widetilde{\mathrm{q}}$ and sleptons $\widetilde{\ell}$ for each quark and lepton, eight gluinos $\widetilde{\mathrm{g}}$, and eight electroweakinos $\widetilde{\chi}$. The Higgs scalars include 3 neutral scalars, the lightest of which is identified as the known Higgs boson H, and a pair of charged scalars. The electroweakinos are general mixtures of the higgsinos, winos, and binos consisting of four neutralinos $\widetilde{\chi}^0$ and two pairs of charginos $\widetilde{\chi}^{\pm}$. The exact properties of these particles are model dependent.

R-parity conservation predicts that collisions of standard model particles must produce supersymmetric particles in pairs. The assumption that the LSP is dark matter then means that heavier supersymmetric particles will tend to undergo decay chains that result in some collection of standard model particles plus the LSP. This yields a canonical missing mass or missing transverse momentum signature; see Section 1.2.3. The assumption that the MSSM does not have excessive fine tuning also suggests the unobserved superpartners to have a mass on the 100 GeV scale.

While the probability of the existence of supersymmetry is hard to quantify objectively, the nondiscovery of the Higgs or any superpartners at the experiments at the LEP collider is found to rule out about 95% of CMSSM space by one metric [128]. The exclusion for GMSB models is even stronger. The discovery of a Higgs boson with a mass of about 125 GeV also tends to favor top squarks with masses above 1 TeV, straining naturalness [129]. Finally, the nondiscovery of dark matter in direct searches rules out sneutrino dark matter [130] as well as purely thermal bino-higgsino mixture dark matter [131] though this latter bound can be avoided with more complicated mechanisms for generating the relic abundance.

To avoid large fine tuning, it is not necessary that all superpartners be at the 100 GeV scale. With only the requirement that the Higgs potential is not too fine tuned, one expects that in a natural model of supersymmetry, the four higgsinos have masses of a few hundred GeV, the two top squarks and one bottom squark have masses below about 1 TeV, and the gluinos have mass near or a bit above 1 TeV [132–134]. At the LHC experiments, the strongest bounds come from searches for gluinos and squarks since these particles are charged under the strong interaction and thus are produced in larger numbers as shown in Figure 1.8. In simplified models with light LSPs, the gluino mass is bounded to be above about 2.2 TeV while the top squark mass is bounded to be above about 1.2 TeV [135,136]. These constraints already disfavor natural RPC supersymmetry, but it is also of interest to consider searches for higgsinos as the higgsino mass is most constrained by naturalness. The main topic of this thesis is a search for higgsinos at the

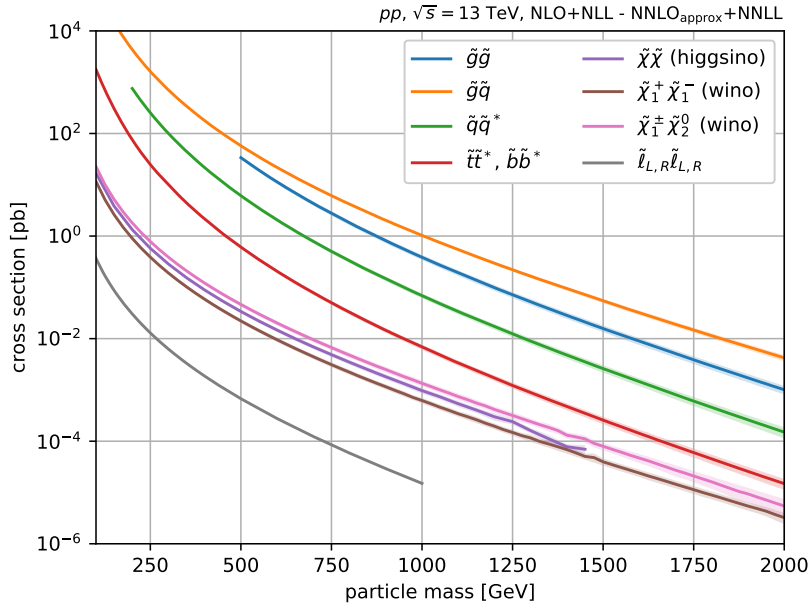

Figure 1.8: Cross sections for pair production of supersymmetric particles in proton-proton collisions at 13 TeV from Ref. [137]. The cross section is directly proportional to the production probability, see Section 1.2.1. Here, $\widetilde{\mathrm{q}}$ refers to any squark except for the top squark. In each scenario, supersymmetric particles other than the ones being produced are assumed to be too heavy to contribute significantly to the production mechanism.

CMS experiment at the LHC.

1.2 Phenomenological background

1.2.1 Kinematics and experimental observables

Experiments typically measure the four-momentum of particles. The four-momentum p of a particle consists of its energy E together with the three components of its spatial momentum $\vec{p}$, which are given by

$$p = (E, \vec{p})\,. \tag{1.39}$$

For a massive particle, the four-momentum can also be expressed

$$\left(m\gamma, m\vec{\beta}\gamma\right), \tag{1.40}$$

where m is the mass of the particle, $\vec{\beta}$ is the three-dimensional velocity vector, and γ is the Lorentz factor $\frac{1}{\sqrt{1-\beta^2}}$. The above formula implies that the energy of a particle at rest is just the mass m. Similarly, the Lorentz invariant magnitude $p_\mu p^\mu$ of the four-momentum can be shown to be equal to the mass squared of the particle m^2:

$$p_\mu p^\mu = m^2 = E^2 - |\vec{p}|^2. \tag{1.41}$$

Due to spacetime translational symmetry, each component of the four-momentum is separately conserved. Thus, if a particle of mass m decays into a set of child particles, the invariant magnitude of the sum of the child particles' four-momenta will still be the mass of the parent particle. The invariant magnitude of the total four-momentum of a system of particles is called the invariant mass, even if the particles did not originate from the decay of a single particle. This is also equal to the total energy of the system in the center-of-momentum (CM) frame, called $\sqrt{s}$. The easiest way to determine if a process is kinematically possible is by examining the total energy in the CM frame. In the decay of a particle with mass m, the sum of the masses of the child particles must be less than $m = \sqrt{s}$ to conserve energy since the total energy of the child particles must be at least the sum of their masses. Similarly the sum of the masses of the particles

produced in a scattering must be less than $\sqrt{s}$.

It is worth noting that the invariant mass of a particle that is not an initial- or final-state particle such as a decaying heavy particle may not match the nominal particle mass. At the level of Feynman diagrams, internal lines are associated to a factor proportional to $1/(p_\mu p^\mu - m^2_{\text{on-shell}})$ that causes distributions to peak when the particle mass m is near its nominal value m_{nominal}, but allows for different masses with some small probability. Particles whose mass is near the nominal value are typically referred to as "on-shell" or "real" while those whose mass is far from the nominal value are referred to as "off-shell" or "virtual". Off-shell particles may be denoted with an asterisk such as W*. When the invariant mass distribution of some final state particles are plotted in a histogram, heavy decaying particles can appear as an enhancement at a particular value of invariant mass. This enhancement is commonly called a resonance, and has a width that is proportional to the decay rate of the heavy particle. Figure 1.9 gives an example showing two resonances in the invariant mass distribution for four-lepton events from Ref. [138]. The resonance near 90 GeV corresponds to events with a Z boson decaying into four leptons, while the resonance near 125 GeV corresponds to events with a Higgs boson decaying into four leptons. The widths of the resonances are mainly determined by experimental resolution.

If the mean lifetime of a unstable particle in the CM frame is τ, then the mean lifetime in another frame is $\gamma\tau$ so that the mean distance a particle travels before decaying, $\langle\Delta x\rangle$, is, restoring a factor of c, $\Delta x = \gamma\beta\tau c$.

Scattering processes are sometimes classified into elastic and inelastic collisions. In

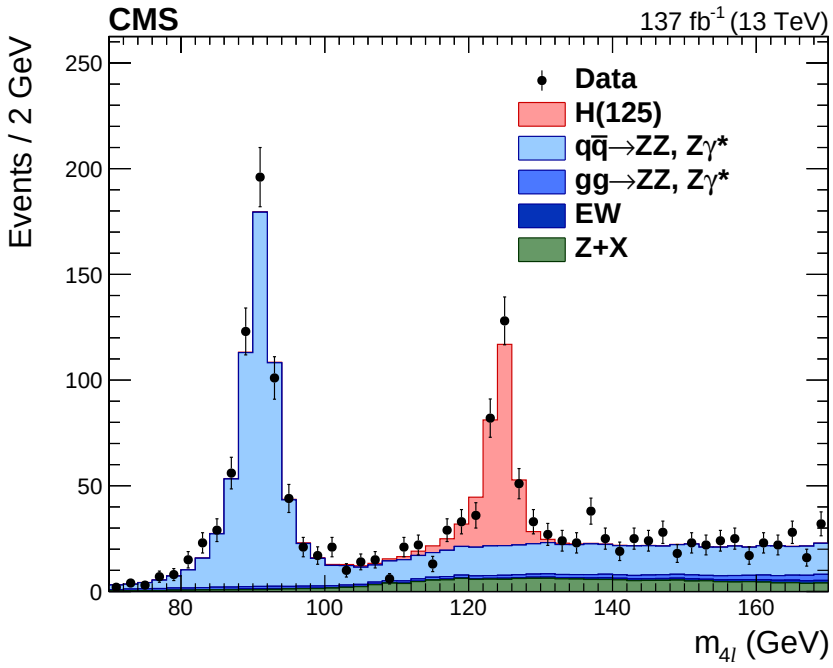

Figure 1.9: Distribution in invariant mass of four lepton events showing two resonance peaks. Experimental data is shown as black points while simulated events are displayed as a stacked histograms whose colors represent the contribution of simulated events from different categories. The 90 GeV peak corresponds to decays of a Z boson to four leptons while the 125 GeV peak corresponds to decays of a Higgs boson to four leptons. Figure from Ref. [138].

elastic collisions, the initial- and final-state particles are the same species and there is merely an exchange of four-momentum. In inelastic collisions, the initial- and final-state particles are not the same species.

A particular case of interest is collisions involving hadrons. Due to the fact the strong interaction coupling strength runs to zero at short distances/high energies, short-distance physics can be well described in terms of partons, the fundamental particles such as quarks and gluons. At long distances, one observes hadrons, which can be related back to the partons in terms of the parton distribution functions mentioned in Section 1.1.5. Figure 1.10 shows the parton distribution functions for a proton evaluated at two values of μ^2 as calculated by the NNPDF collaboration [139]. In principle, there are also PDFs for other particles such as photons and leptons inside protons due to radiative corrections, but these are very small. Because the colliding partons carry only a fraction of the total proton momentum, the parton-parton CM frame is generally boosted relative to the proton-proton CM frame, and outgoing particles can often have large momentum along the beam axis even when $\sqrt{s}$ of the proton-proton collision is small. The high energy flux of particles scattered near the beamline can make this region, sometimes called the forward region, quite harsh for detectors and electronics.

In a typical collider experiment, the beam axis is taken to be the z axis. Although the parton CM frame is not known in hadron-hadron collisions, it is known that it differs from the rest frame of the experiment, the lab frame, only by a boost along the z axis. For this reason, the three-momentum of a particle is typically specified in terms of the

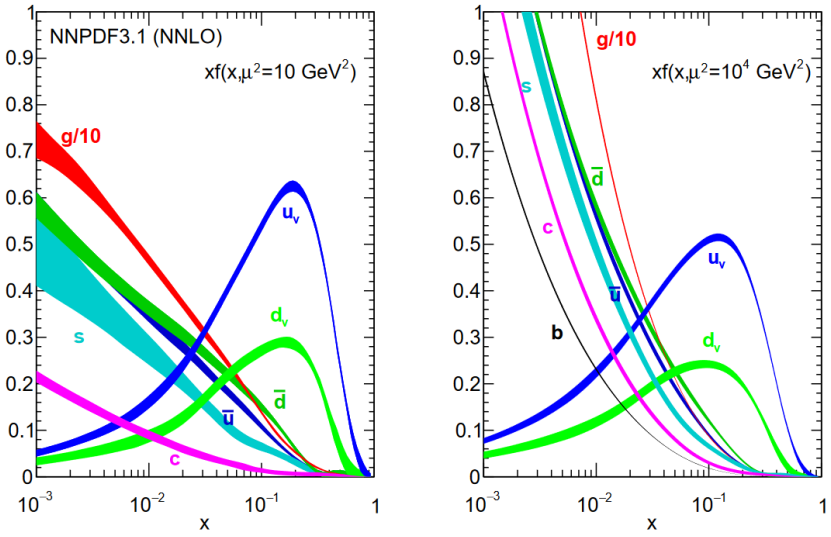

Figure 1.10: NNPDF3.1 parton distribution functions for protons used for some of the simulation in this thesis. Figure from Ref. [139].

transverse momentum p_{T}, the angle of the transverse momentum in the transverse plane ϕ, and a variable called pseudorapidity η. An illustration of these quantities is provided in Figure 1.11. The variable p_{T} is commonly used as a measure of particle momentum in hadron collisions since it is the same in the lab and CM frame and is thus not affected when the CM frame is boosted relative to the lab frame. The variable ϕ is equal to the standard azimuthal coordinate in spherical coordinates and is also common to the lab and CM frame. The rapidity y of a particle is defined as $\tanh^{-1}(p_Z/E)$, where p_Z is the momentum along the z axis. With this definition, boosting along the z axis by a speed β shifts y by a constant $\tanh^{-1}\beta$. In particular, this means that differences in y are exactly preserved under boosts between the CM frame and lab frame. In practice, y is typically replaced by the pseudorapidity $\eta = -\log\tan(\theta/2)$, where θ is the standard polar angle in spherical coordinates. For ultrarelativistic particles, η is a good approximation to y

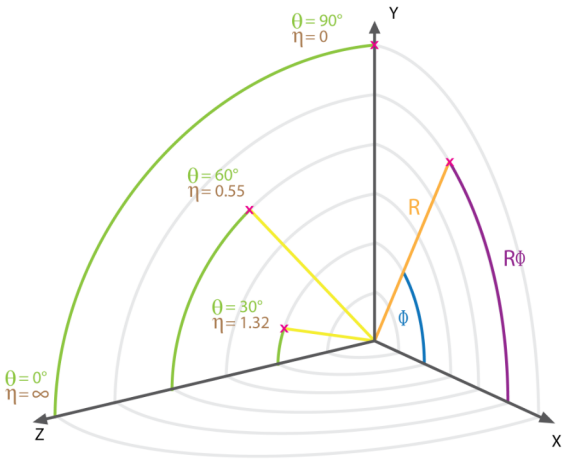

Figure 1.11: Coordinate system used in collider experiments in terms of the transverse length of a vector R, the azimuthal coordinate ϕ, and the pseudorapidity η. Figure from Ref. [140].

since the two are equal in the limit $p >> m$ and $\theta >> 1/\gamma$ [48]. Subsequently, the angular separation between two particles at a hadron collider is typically measured by $\Delta R = \sqrt{\Delta\eta^2 + \Delta\phi^2}$. In practical situations, when $\sqrt{s}$ is much larger than the mass m of some particle, the approximation $m = 0$ is often made, which makes the magnitude of momentum $|\vec{p}|$ and the energy equivalent.

Probabilities for different physical processes can be estimated from many experimental measurements. For example, the probability to measure a pair of muons in a proton-proton collision $P(\mathrm{pp} \rightarrow \mu^+\mu^- + \mathrm{X})$ can be estimated experimentally from the ratio of events where muon pairs were produced to the total number of collisions $N_{\mathrm{muon}}/N_{\mathrm{total}}$. However, rather than work directly with probabilities and total numbers of collisions, it is more convenient and physically meaningful to work in terms of quantities called luminosity and cross section. At a collider, instantaneous luminosity $\mathcal{L}_{\mathrm{inst}}$ is the flux of particles in a beam integrated over each particle in the colliding beam it passes. The

integrated luminosity $\mathcal{L}_{\text{int}}$ is the instantaneous luminosity $\mathcal{L}_{\text{inst}}(t)$ integrated over the time the collider was in operation, and thus can replace N_{total} as a metric of data gathered. The advantage of using $\mathcal{L}_{\text{int}}$ over the number of collisions is that $\mathcal{L}_{\text{int}}$ is more directly related to the beam parameters of the collider as described in Section 2.1.1. The cross section $\sigma(X)$ is the number of events of type X per integrated luminosity. The relation between probabilities and cross sections is summarized by

$$\sigma(pp \to X)\mathcal{L}_{\text{int}} = P(pp \to X)N_{\text{total}} = N_X. \tag{1.42}$$

Note that the cross section and the probability are simply proportional, as are the integrated luminosity and the number of collisions.

A probability density can be calculated in quantum field theory as the magnitude squared of an S-matrix element $|\mathcal{A}|^2$. With the conventions that the norm of a state is given by the product $2E_jV$ for each particle j with energy E_j and V is the total volume of space, the expression for a cross section is given by

$$\sigma = \int \frac{|\mathcal{A}|^2}{4|\vec{p_1}|_{\text{CM}}\sqrt{s}VT} \prod_{\text{final}j} \frac{d^3p_j}{(2\pi^3)2E_j}, \tag{1.43}$$

where $|\vec{p}_1|_{\text{CM}}$ is the magnitude of the spatial momentum of one of the initial particles in the center of momentum frame, and T is the total time [5]. The formally infinite factors of V and T will cancel against similar factors in $|\mathcal{A}|^2$.

1.2.2 Interactions of particles with matter

The fundamental particles of the SM that typically travel on the order of a meter or more and thus are commonly subject to direct detection by particle detectors are the electron, muon, photon, and neutrinos. The composite hadrons that typically travel at least a meter are the charged pion, proton, charged kaon, neutron, and the neutral K-long meson. This can be seen from the lifetimes of the particles in Figure 1.6. The interactions of these particles as they pass through matter determine how particle detectors must operate in order to detect them. This section details these interactions, largely following the treatment in the reviews in Ref. [48] as well as Ref. [141].

As electrically charged particles pass through matter, one mechanism through which they deposit energy in the material is through collisions with atomic electrons. This can result in ionization of an atom due to the loss of an electron or the excitation of the electron into an excited band in a semiconductor. This mechanism is generally referred to as energy loss by ionization. 90% of particle-electron collisions result in energy loss less than 100 eV, energy losses that are very small compared to the typical scales of particle physics experiments. Although the typical energy loss per distance $\frac{dE}{dx}$ is quite small, the probability distribution for ionization energy loss in materials of moderate thickness is well described by a Landau distribution, which features a significant tail of high energy loss events [142, 143]. For charged particles with $\beta\gamma(= p/m)$ between about 0.1 and 1000, ionization is the primary electromagnetic energy loss mechanism. In particular, particles with $\beta\gamma$ from about 1 to several hundred are called minimally ionizing particles

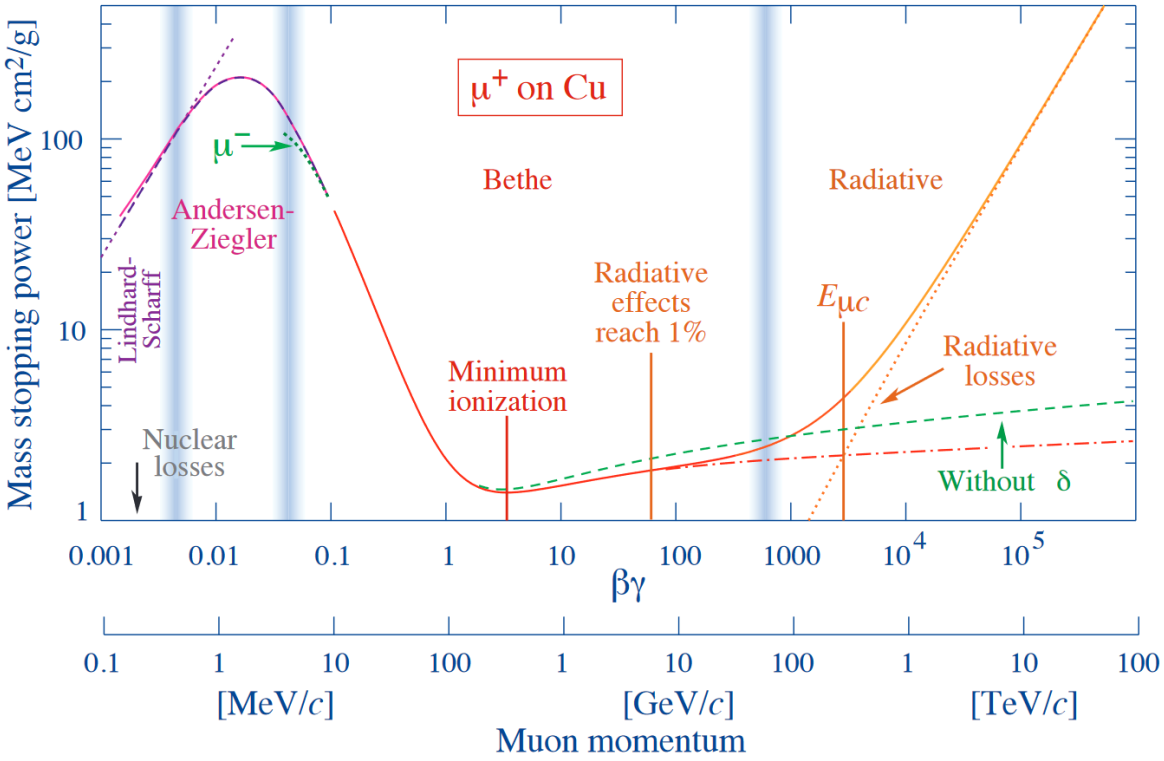

Figure 1.12: Mean energy loss per distance per density of muons passing through copper showing the region in which energy loss by ionization is dominant in red. The region in which energy loss from radiation becomes dominant is shown in orange, while energy loss from other mechanisms at low $\beta\gamma$ is shown in violet/pink. This mean is not a good measure of energy loss per distance through a real material as the real energy loss per distance approximately follows a Landau distribution. Figure from Ref. [48].

(MIPs) since this is when the most probable energy loss is approximately at a minimum. Figure 1.12 shows mean energy loss for muons passing through copper as a function of $\beta\gamma$ with the ionization-dominated regime shown in red.

Various detector technologies employ ionization energy for particle detection. In semiconductor detectors, particles traversing thin semiconductor sensors knock a small number of electrons into the semiconductor's conduction band. A bias voltage applied to the sensor causes the freed electrons and holes to produce a small current, which can

be detected by connected electronics. In gaseous ionization detectors, electrons freed by an incident particle are drifted toward an anode. To induce a measurable current at the anode, a large electric field is typically employed to cause the freed electrons to free additional electrons in an avalanche. The ionized atoms may also induce a measurable current at the cathode(s). In scintillation detectors, charged particles are detected using light emitted from the deexcitation of electrons or ionization and recomination following energy deposition from the particle. Scintillators are typically used in conjunction with a high-gain photon detector such as photomultiplier tubes or photodiodes, which can convert the resulting light into an electrical signal.

There are several other relevant electromagnetic mechanisms through which particles interact with matter. For charged particles with very high $\beta\gamma$ passing through matter, the primary method of electromagnetic energy loss is not ionization but rather bremsstrahlung, emission of photons caused by deceleration of the charged particle as it experiences the electric fields of atomic nuclei. This is the primary energy loss mechanism for electrons at collider experiment energy scales and becomes relevant for particles like muons and pions at energies of hundreds of GeV. The radiation length per density X_0/ρ is the mean distance over which an ultrarelativistic particle deposits all but $\frac{1}{e}$ of its energy via bremsstrahlung. A particle moving faster than the local phase speed of light in a medium also emits Cherenkov radiation, which is a negligible source of energy loss but can be used in conjunction with photon detectors as a particle detection mechanism. Finally, GeV scale photons primarily interact with matter through pair production of

electrons in the electric fields of nuclei. The typical scale over which photons deposit energy by pair production is also the radiation length per density.

The strong and weak interactions can also be relevant for particles passing through matter. Hadrons passing through matter can interact with atomic nuclei through the residual effects of the strong interaction. Of greatest interest are inelastic particle-nuclear collisions; the mean distance traveled by a hadron before an inelastic nuclear collision is the nuclear interaction length per density λ_I/ρ. Although negligible for other particles, neutrinos must be detected using charged (W-mediated) or neutral current (Z-mediated) weak interactions. Typical cross sections for GeV scale neutrinos are on the order of 10^{-38} cm^2 [48], which makes neutrinos effectively undetectable for typical collider experiments.

High energy electrons incident on a thick absorber will tend to emit high energy photons through bremsstrahlung while high energy photons will tend to pair produce into electron-positron pairs. These processes can repeat, resulting in a cascade of electrons, positrons, and photons called an electromagnetic shower. An electromagnetic shower typically develops on the scale of the radiation length of the material in the longitudinal direction while possessing a transverse size characterized by a property of the material called the Molière radius. Analogously, high energy hadrons incident on a thick absorber will undergo inelastic nuclear collisions, resulting in additional hadrons that again collide with other hadrons resulting in a hadronic shower on the scale of the nuclear interaction length. Neutral pions and eta mesons produced in the hadronic shower can decay

into pairs of photons, which then induce an electromagnetic component in the hadronic shower. Additionally, some of the shower energy of a hadronic shower goes into so-called invisible energy in the form of low energy neutrons, hard-to-detect delayed photons, and nuclear binding energy. Schematic diagrams and simulated showers are shown for electromagnetic showers in Figure 1.13 and hadronic showers in Figure 1.14.

Calorimeters are detectors that measure the shower generated by an incident particle, generally by measuring the ionization energy of charged particles in the shower, and then using this to estimate the energy of the original particle. The intrinsic stochasticity of showering can limit calorimeter resolution, but this relative intrinsic uncertainty tends to decrease as $1/\sqrt{E}$. Calorimeter resolution also tends to have contributions from noise and detector nonuniformities, which contribute to the relative uncertainty as $1/E$ and a constant respectively. When measuring hadronic showers, the calorimeter response to the electromagnetic and hadronic parts of the shower can in general differ due to the invisible energy in the hadronic part. If the ratio of the response to the electromagnetic part to that of the hadronic part, e/h, is not one and the fraction of the shower that is electromagnetic/hadronic is not directly measured, then there will be an additional loss in energy resolution due to the uncertainty in electromagnetic/hadronic fraction.

1.2.3 Physics objects

To compare between theories such as the SM or MSSM and experimental data, it is necessary to have a way to relate the two. Section 1.1 showed how to calculate cross

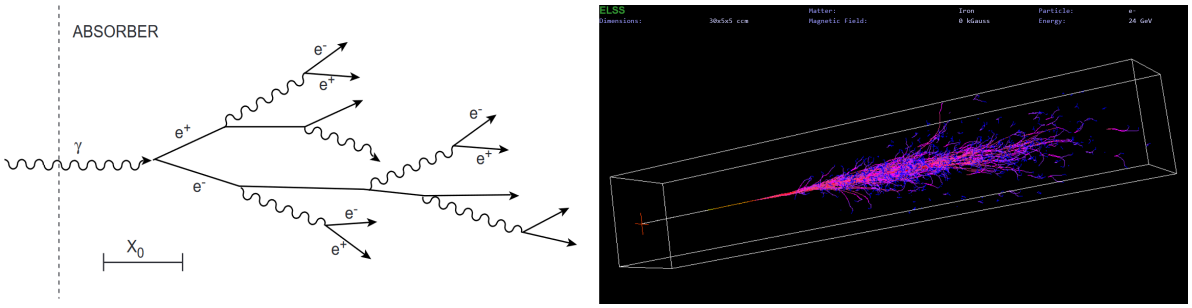

Figure 1.13: Diagram showing mechanism of EM shower development from an incident photon (left) and simulation of electromagnetic shower of a 20 GeV electron on Iron (right). Left image from Ref. [144], right image from Ref. [145].

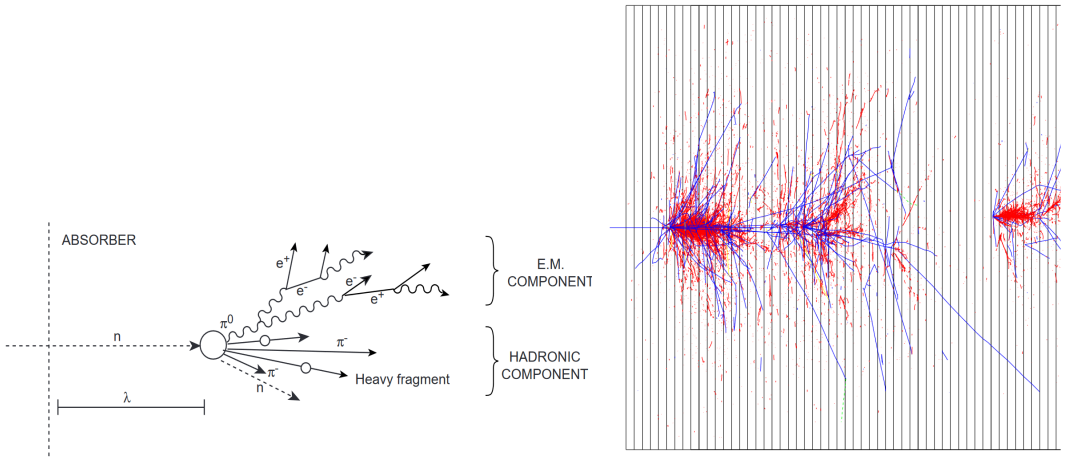

Figure 1.14: Schematic diagram showing mechanism of hadronic shower development from an incident neutron (left) and simulation of charged particles in a hadronic shower in copper (right). In the simulated shower, electrons are shown in red while charged hadrons are shown in blue. Images from Ref. [144].

Table 1.5: Typical correspondance between SM particles and hadron collider physics objects. $p_{\mathrm{T}}^{\mathrm{miss}}$ stands for missing transverse momentum.

Particle	Physics objects
Up quark	Jet
Down quark	Jet
Strange quark	Jet
Charm quark	(c-)Jet
Bottom quark	(b-)Jet
Top quark	Prompt decay
Electron	Electron
Muon	Muon
Tau	Electron, muon, or hadronic tau
Electron neutrino	$p_{\mathrm{T}}^{\mathrm{miss}}$
Muon neutrino	$p_{\mathrm{T}}^{\mathrm{miss}}$
Tau neutrino	$p_{\mathrm{T}}^{\mathrm{miss}}$
Gluon	Jet
Photon	Photon
W boson	Prompt Decay
Z boson	Prompt Decay
Higgs boson	Prompt Decay

sections for the sorts of scattering processes observed in collider experiments with the caveat discussed in Section 1.1.5 that only sufficiently inclusive initial and final states can be considered. "Physics objects" are the inclusive experimental signatures that are in rough correspondance with high-p_{T} fundamental particles at the level of Feynman diagrams. Table 1.5 shows the typical correspondance between SM particles and the physics objects seen at hadron colliders. The rest of this section describes each of the observed physics objects in more detail while detailed accounts of the reconstruction algorithms used by the CMS experiment are given in Section 2.3.

Photons, electrons, and muons

As shown in Table 1.2, electrons, photons, and muons are stable or long-lived on the timescales required to traverse a typical experiment. The electron, photon, and muon physics objects thus typically correspond to a high p_{T} electron, photon, or muon together with possible additional nearby low-p_{T} particles such radiated photons. Photons may also convert into $\mathrm{e}^{+}\,\mathrm{e}^{-}$ pairs when traversing a detector. These physics objects are also called prompt electrons/photons/muons to contrast them with nonprompt electrons, photons, and muons created as secondary particles in hadron decays as well as spurious electrons, photons, and muons that are actually other misidentified particles.

Jets

High p_{T} strongly interacting particles such as quarks and gluons give rise to more complicated final states. In addition to showering due to processes such as $\mathrm{q} \to \mathrm{qg}$, $\mathrm{q} \to \mathrm{q}\gamma$, $\mathrm{g} \to \mathrm{q}\overline{\mathrm{q}}$, and $\mathrm{g} \to \mathrm{gg}$, the confining nature of the strong interaction induces additional nonperturbative interactions. These include fragmentation and hadronization, in which additional quarks and gluons are produced and coalesce into hadrons. The long-distance dynamics of these strong interaction processes are not currently understood quantitatively from first principles, but are instead typically described with phenomenological models such as the string fragmentation model used in the simulation in this thesis [146]. Some of the resulting hadrons are unstable and subsequently decay. The cluster of particles generated from a final state quark or gluon is called a (QCD) jet, and can be thought

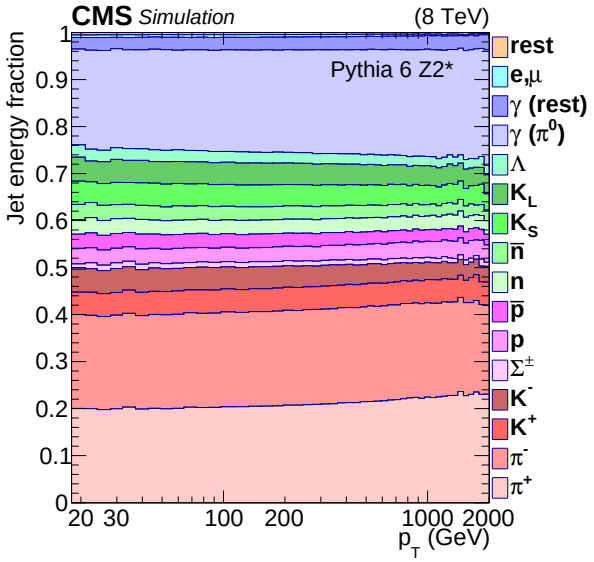

Figure 1.15: Average fraction of jet energy carried by each particle species as a function of jet p_{T}. Figure from Ref. [148].

of as a proxy to the quark/gluon at the parton level. Figure 1.15 shows the simulated average particle content of jets clustered with the anti-k_{T} algorithm as a function of jet p_{T} in a proton-proton collision dijet sample. Charged pions ($\pi^{\pm}$), which are long-lived and directly detected, carry on average 40% of the jet energy while neutral pions (π^{0}), which almost exclusively decay into pairs of photons, carry another 20%. Other long-lived charged hadrons, protons ($\mathrm{p}/\overline{\mathrm{p}}$) and kaons ($\mathrm{K}^{\pm}$) carry an average of about 15% of jet energy and long-lived neutral hadrons, neutrons ($\mathrm{n}/\overline{\mathrm{n}}$) and K long mesons ($\mathrm{K}^{0}_{\mathrm{L}}$) carry about 10%. The remaining energy is carried by hadrons with intermediate lifetimes (Λ, $\Sigma^{\pm}$, $\mathrm{K}^{0}_{\mathrm{S}}$), photons ($\gamma$), charged leptons (e, μ), and others. The typical multiplicity of charged particles with p_{T} >0.5 GeV is around 8 for jets with a p_{T} of 50 GeV and increases nonlinearly with p_{T} [147].

Jet flavor, the flavor of the particle initiating the jet, is not in general an infrared safe

variable since splittings like $q \to qg$ and $g \to q\overline{q}$ can occur in the parton shower. However, since one typically thinks of jets as associated to the partons at the matrix element level, it is still useful in practice to try to associate the flavor of this parton to the jet. This is referred to as jet tagging. In general, jets corresponding to light quarks and gluons (u, d, s, g) are difficult to distinguish while jets initiated by charm and bottom quarks, called c jets and b jets respectively, are more easily identified [149]. High p_{T} hadrons containing charm and bottom quarks are usually indicative of c and b jets; the properties of these hadrons are used to tag c and b jets. Most notably, these hadrons have mean lifetimes on the order of 1 ps, which means that they can travel hundreds of micrometers or even millimeters before decaying, giving rise to particles emerging from displaced secondary vertices. Additional useful properties of hadrons with bottom or charm quarks include their large mass, hard fragmentation functions, and relatively high probability to produce leptons in their decay [150]. These properties are utilized to tag c jets and b-jets.

Missing transverse momentum

As discussed in the previous section, neutrinos have extremely small interaction cross sections and are not detected in typical proton-proton collider experiments. Instead, one applies conservation of momentum along the transverse axes. The initial momentum of the colliding particles is typically nearly 0 along these axes, and thus the negative vector sum of the transverse momentum of all measured particles gives the missing transverse momentum $p_{\mathrm{T}}^{\mathrm{miss}}$, which is a proxy to the net transverse momentum carried by undetected

particles such as neutrinos. Since longitundinal boost of the CM frame is unknown in proton-proton collisions, the z component of the missing momentum is typically not measurable. However, in other experimental configurations such as electron-positron collisions, the total missing three-momentum as well as the missing energy can be determined.

Tau leptons

Taus have a lifetime of about 0.3 ps and thus generally decay before reaching a typical collider experiment detector. About one third of taus decay into two neutrinos plus a muon or electron, in which case the tau can be reconstructed as an electron or muon physics object. The other two thirds of taus predominantly decay into a neutrino, one or three charged hadrons, and possibly additional neutral pions. A hadronic tau physics object is thus reconstructed as one or three charged hadrons with possible additional photons. Hadronic tau decays are thus similar to QCD jets, but are distinguished by features such as lower particle multiplicity and smaller radius.

Heavy particles

As shown in Table 1.2, the heaviest SM particles, W, Z, t, and H have very short lifetimes and thus decay so fast that their decay products effectively originate from the same vertex at which the heavy particle originates. These particles must be reconstructed from the physics objects corresponding to their decay products. Decay modes are typically described as "hadronic" if they involve only quarks and gluons and "leptonic" if they

Table 1.6: Common decays of W, Z, t, and H with associated measured (W, Z, t) and theoretical (H) branching fractions [48, 151]. Here ℓ stands for a charged lepton, ν for a neutrino, $q\bar{q}$ for any quark-antiquark pair, and $q\bar{q}'$ for either $u\bar{d}$ or $c\bar{s}$.

Decay mode	Branching fraction [%]
$W^+ \to \ell^+\nu$	33
$W^+ \to q\bar{q}'$	67
$Z \to \ell^+\ell^-$	10
$Z \to \nu\bar{\nu}$	20
$Z \to q\bar{q}$	70
$t \to W^+(\to \ell^+\nu)b$	33
$t \to W^+(\to q\bar{q}')b$	67
$H \to b\bar{b}$	58
$H \to W^+W^-$	21
$H \to gg$	8.2
$H \to \tau^+\tau^-$	6.3
$H \to c\bar{c}$	2.9
$H \to ZZ$	2.6
$H \to \gamma\gamma$	0.23
$H \to Z\gamma$	0.15
$H \to \mu^+\mu^-$	0.022

involve charged leptons. If the decay products are measured by an experiment, one may also require that the invariant mass of the decay products matches the mass of the heavy particle. Table 1.6 shows the branching fractions for most common decays of the heavy SM particles.

Hadronic decays of the heavy particles are often particularly difficult to observe due to the large background from QCD multijet processes (see next section). One scenario in which this becomes easier is when the heavy particle has a large momentum, in which case its decay products become collimated and the resulting jets may merge into a single "fat jet." With an appropriate definition of jet mass (see Section 2.3.5), fat jets from

boosted particles will have a mass near the parent particle mass, which provides strong discrimination against QCD jets with masses near 0. The substructure of fat jets can also aid in separation. As a rough rule of thumb, the decay products of a heavy particle with mass m will lie within a fat jet of radius ΔR when $p_{\mathrm{T}} \gtrsim 2m/\Delta R$. One thus needs a p_{T} of about 200–320 GeV for the decay products of a W, Z, t, or H to be contained in a fat jet with a typical radius of 0.8.

1.2.4 Processes in proton-proton collisions

It is often useful to classify the types of proton-proton collisions into several categories. In particular, Monte Carlo simulation is typically generated process-by-process. The total cross section for proton-proton collisions at $\sqrt{s} = 13\,\mathrm{TeV}$ is approximately 110 mb where the elastic cross section is approximately 30 mb and the inelastic cross section is approximately 80 mb [152]. In the context of typical experiments, inelastic events are also called minimum bias events since detecting elastic collisions often requires specialized detectors near the beam line.

Within the category of inelastic collisions, the vast majority are "soft" collisions with small momentum transfer. This results in no high p_{T} physics objects of the type discussed in Section 1.2.3. The vast majority of "hard" collisions are QCD multijet events, which feature jets from final state quarks and gluons. Using the MadGraph5_aMC@NLO event generetor [153,154] at LO with the NNPDF2.3LO PDF set [155], one can estimate the QCD multijet cross section to be on the order of 170 µb for typical LHC requirements

of jet $p_{\mathrm{T}} > 30$ GeV and separation of $\Delta R > 0.4$.

Figure 1.16 shows theoretical and experimentally measured cross sections for a number of SM processes. A first order classification that is often used is based on the presence of the heavy SM particles: W, Z (sometimes together with γ^*), H, and t. The most common non-QCD multijet processes include W +jets production at about 180 nb, Z +jets production at about 56 nb, t $\bar{\mathrm{t}}$ production at 890 pb, and t-channel single t production at about 230 pb. The decay of a Z to charged leptons inherently interferes with a similar process involving an off-shell (nonzero mass) photon; as such, the process $\mathrm{q\overline{q}} \to \mathrm{Z}/\gamma^* \to \ell^+\ell^-$ is treated as a single process called the Drell-Yan process. Some rarer processes include Higgs production, multiboson production, and production of a top or top pair with additional heavy particles. One other class of rare processes is vector boson fusion(VBF)/vector boson scattering(VBS) in which vector bosons radiated by quarks in the colliding protons interact to produce one or more final state particles.

The cross sections and thus probabilities for processes studied at proton-proton colliders vary by more than 13 orders of magnitude. For this reason, it is imperative that searches for rare processes have ways to remove the potentially enormous backgrounds from more common processes. The presence of high p_{T} physics objects provides strong discrimination between hard scattering events and soft events. Similarly, the presence of prompt charged leptons or significant amounts of missing transverse momentum from prompt neutrinos provides a way to separate rare processes from common QCD multijet events.

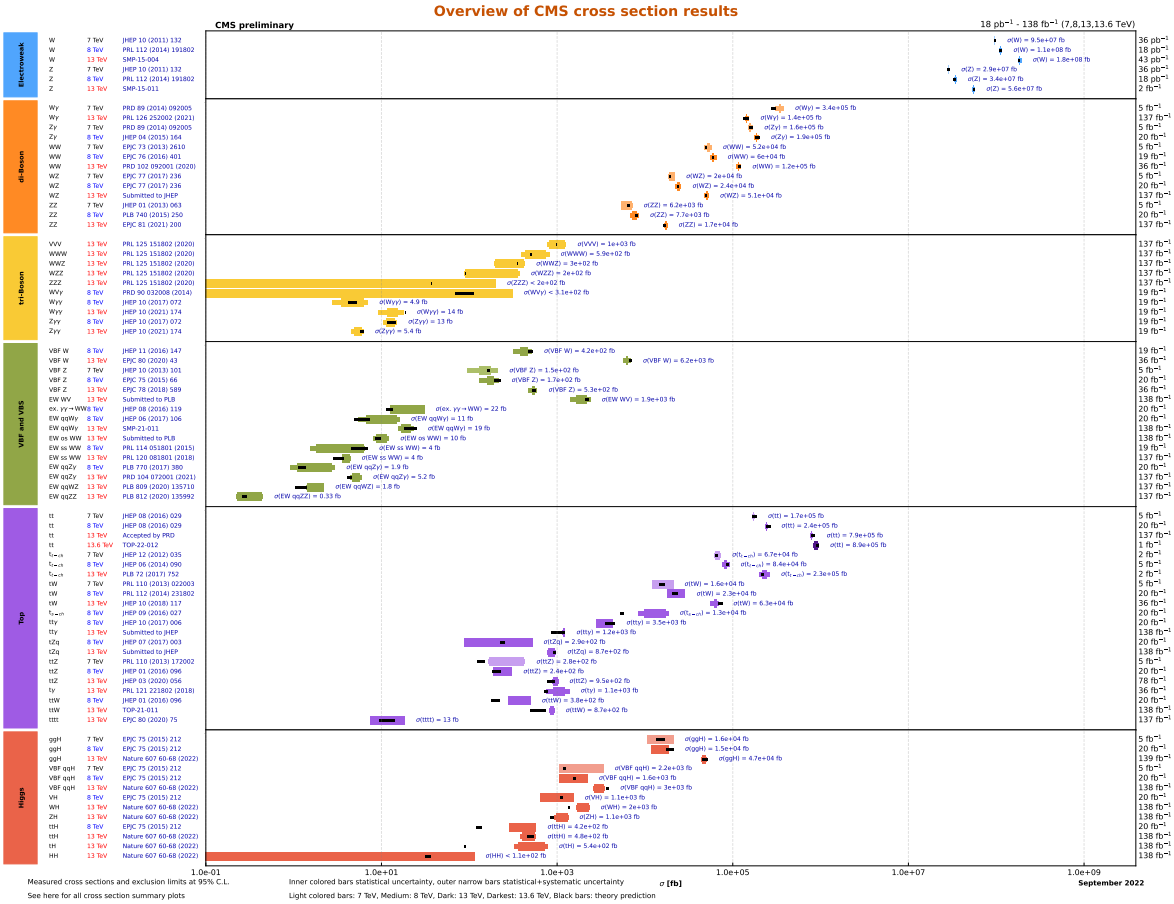

Figure 1.16: Measurements of cross sections for standard model processes made by the CMS experiment and comparison to theoretical predictions showing excellent agreement. Figure from Ref. [156].

1.2.5 Event generation

Simulation of particle physics processes is performed using programs called event generators. The process of generating a simulated event can be computationally quite intensive and involves various programs working in tandem. Numerically, event generators use a sampling and integration method known as Markov-Chain Monte Carlo (MCMC) and for this reason, simulated samples are also known as Monte Carlo (MC) samples. The following description roughly follows that of Ref. [157].

Event generation begins with matrix element calculations in perturbation theory, which are typically performed at LO or NLO. Figure 1.17 shows the (QCD) LO Feynman diagram for the processes $q\bar{q} \to t\bar{t}$ and $gg \to t\bar{t}$, which would evaluated by the event generator. Typically, electroweak Feynman diagrams contribute at a similar to NLO QCD diagrams. All of the matrix-level processes shown must be considered for proton-proton collisions, as both quarks and gluons are present in proton PDFs such as those shown in Figure 1.10. Matrix element calculations depend on the fundamental parameters of the theory, as well renormalization and factorization scales; phenomena softer than the factorization scale are added in a subsequent step. Short-lived resonances like Z or H are typically decayed in the matrix-element step.

After the matrix element level, the event is often handed to secondary event generator that deals with subsequent effects. In particular, this secondary generator generates parton showers in which initial state radiation (ISR) and final state radiation (FSR) of soft particles before and after the process described at the matrix element level occurs.

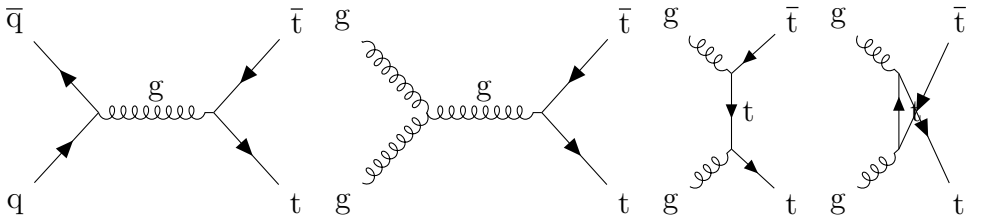

Figure 1.17: The QCD Feynman diagrams that contribute to $q\bar{q} \to t\bar{t}$ and $gg \to t\bar{t}$ (and thus $pp \to t\bar{t}$) at LO.

As described in Section 1.1.5, the parton shower gives a leading-log accurate description of physics that is valid in the soft and collinear limit. An accurate description of both hard and soft radiation thus requires use of both matrix element calculations with additional radiation and parton showering. Procedures known as matching and merging are then used to remove or subtract overlap created by these two descriptions. At the same time, additional multiparton interactions may arise between other fundamental particles in the colliding system. The multiparton interactions and other remnants of the colliding particles are commonly referred to as the underlying event. After matrix element calculation, parton showering and multiparton interactions, nonperturbative interactions between strongly charged particles are simulated with phenomenological models such as the string fragmentation model, which results in their combination into color neutral hadrons. After this, other effects such as Bose-Einstein enhancements, Fermi-Dirac suppressions, decays of unstable hadrons, and additional rescattering are simulated. Simulation of all of the complex post-matrix element phenomena are based on models with hundreds of parameters. These parameters are determined by experimental measurements in what is referred to as a tune. A schematic picture of post-matrix element simulation is shown in

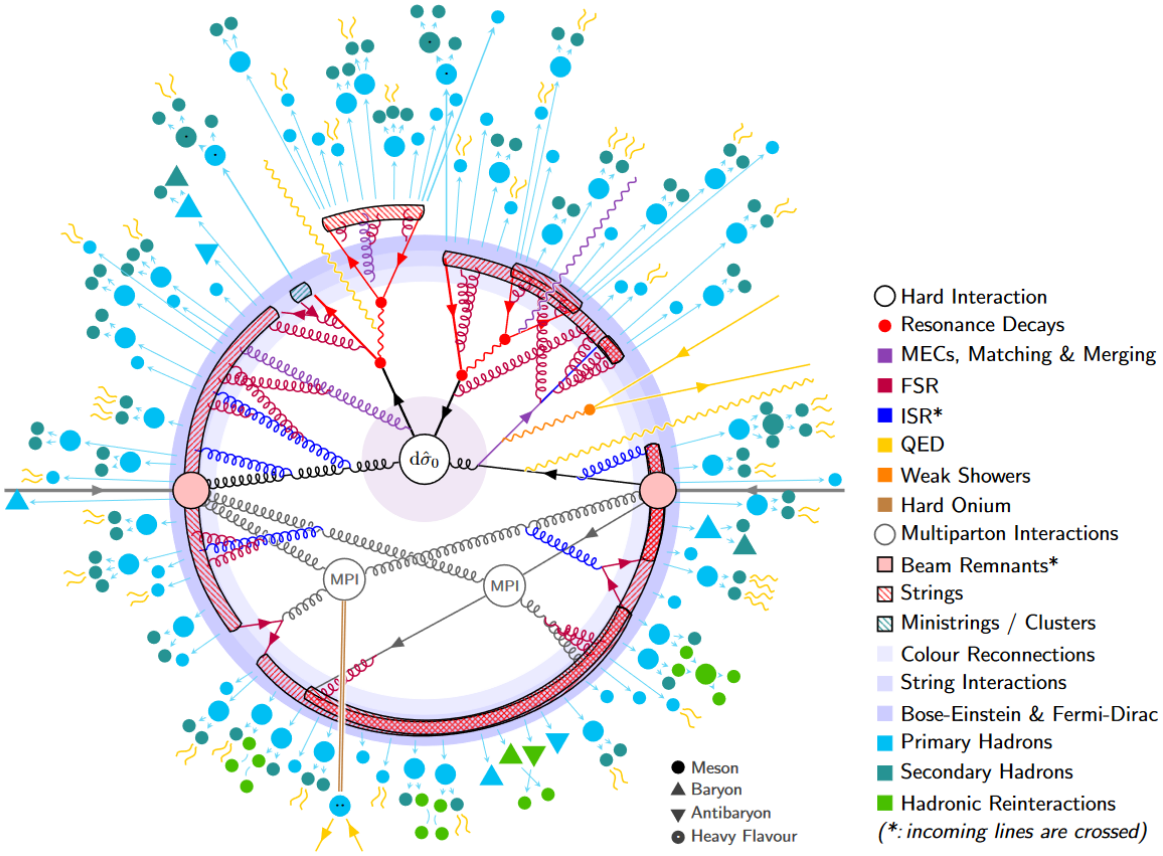

Figure 1.18: Schematic diagram of event simulation process ($pp \rightarrow t\bar{t}$) from Ref. [157].

Figure 1.18.

The final outgoing particles can then be provided to a simulation of the experimental detector to simulate the interaction of particles with matter and subsequent recorded electrical signals. The simulated events can then be compared to real data collected using the detector. The next chapter describes the general purpose particle collider experiment CMS used for this study as well as the collider that provides it with collisions.

Chapter 2

Experimental setup and reconstruction

To perform a search for heavy new particles such as the ones considered here, much experimental machinery is required. First, the particles need to be created using a particle collider, which transforms the energy of colliding particles into other forms of energy such as the new particles of interest. Next, an experiment consisting of many particle detectors needs to be installed near the collision point to detect the outgoing particles produced in the collision. Finally, the data from the experiment has to be used to reconstruct the processes that occurred in the collision.

This chapter covers the experimental setup used for the HH(4b)+$p_{\mathrm{T}}^{\mathrm{miss}}$ analysis described in this thesis. The first section describes the basics of accelerator physics and the LHC, the accelerator used to generate the collisions studied. The second section details the CMS detector, which is the general purpose experiment at the LHC used to detect the collisions. The final section explains how event reconstruction is performed using the data from the CMS experiment.

2.1 The Large Hadron Collider

2.1.1 Particle accelerators

This section provides a basic sketch of selected concepts in accelerator physics. A more comprehensive treatment can be found in texts such as Ref. [158]. A particle accelerator is a machine that accelerates beams of particles using electromagnetic fields. A beam from an accelerator can be directed into a fixed target to produce collisions for experiments. However, there are also accelerators called colliders that are capable of accelerating two beams of particles and colliding these beams with each other. Colliders can provide collisions that have much higher usable energy than a fixed-target setup since conservation of momentum constrains some of the energy of fixed-target experiment to be in the form of kinetic energy.

Accelerating particles requires electric fields, but simply using electrostatic fields to accelerate particles quickly becomes impractical due to the high voltages required. Instead, modern particle accelerators employ radio frequency (RF) cavities with electromagnetic waves timed so that particles passing through the cavities can be accelerated. A linear accelerator can be constructed by connecting many RF cavities with appropriate size so that particles will be accelerated as they pass through. Since particles only pass through the accelerator once, linear accelerators are limited in their energy reach by their length. For this reason, a class of modern accelerators called synchrotrons are often used to accelerate particle beams in a circle so that the accelerating element can be

reused every time a particle orbits the ring. The trajectory of the beams can be directed using the fields from dipole magnets, though as the particles accelerate, the strength of the dipole magnets must be increased to keep the orbit radius constant. The energy of a synchrotron is thus typically limited by the size of the ring and the corresponding maximum strength of the magnetic fields needed to direct the beam.

To keep a stable beam in orbit and accelerate it, synchrotrons also require various focusing mechanisms. In the longitudinal direction, particles in the beam are grouped into bunches so as to be accelerated by the RF cavities. The RF cavities are adjusted to provide extra acceleration to particles behind the center of the bunch bunch and less to those ahead of the center of the bunch in order to produce phase focusing in the longitudinal direction. To focus beams in the transverse directions, modern synchrotrons employ strong focusing. In this scheme, two quadrupole magnets are used, one that focuses in the horizontal plane and defocuses in the vertical plane, and one that focuses in the vertical plane and defocuses in the horizontal plane. These combine to produce an overall focusing effect in both directions. Higher multipole magnets are then typically used for small corrections and tuning.

The result of this focusing scheme is that particles that are offset from the center of a bunch will experience oscillations in the longitudinal or transverse directions. The transverse oscillations are called betatron oscillations. An accelerator must be designed to avoid resonant betatron oscillations by setting the beam tune, the number of oscillations per revolution, to be a non-integer. The path of the beams must also be wide enough so

that particles with very large betatron oscillations, the so-called beam halo, do not hit any components of the accelerator. The betatron oscillations are often described in terms of Twiss parameters, the most important of which are the emittance ϵ and the beta function $\beta(s)$. The emittance ϵ is a property of the beam describing its spread in oscillation phase space. In general ϵ decreases with beam energy, though using standard relativistic β_{rel} and γ_{rel} factors, one can define the normalized emittance $\epsilon_n = \beta_{\text{rel}}\gamma_{\text{rel}}\epsilon$, which does not decrease with beam energy. Emittance is roughly conserved, though second-order effects such as interactions between beam particles can cause it to grow over time. In contrast to the emittance, the beta function $\beta(s)$ is a property of the focusing magnets that can be made larger or smaller at different points around the synchrotron by using different magnet configurations.

As discussed in Section 1.2.1, the rate of collisions in a particle collider is proportional to the instantaneous luminosity of the collider. Thus, colliders are often built to maximize the luminosity provided to experiments. The instantaneous luminosity for a typical synchrotron collider is [159]

$$\mathcal{L}_{\text{inst}} = \frac{N_p^2 n_b f_{\text{rev}} \gamma_r}{4\pi\epsilon_n \beta^*} F, \tag{2.1}$$

where N_p is the number of particles per bunch, n_b is the number of bunches in the beam, f_{rev} is the revolution frequency, γ_r is the relativistic factor E/m, F is a geometric factor related to the crossing angle and bunch sizes, ϵ_n is the normalized emittance, and β^* is the beta function evaluated at the collision point. To optimize luminosity, the emittance of the bunches injected into a collider should be minimized and the focusing magnets

should be configured to minimize β^* at the collision points. To measure the geometric factor F, machines may use van der Meer scans whereby two beams are moved across each other and the measured rate of particles by a detector can be used to derive the overlap width [160]. The area in space in which collisions occur is called the beam spot.

Particle colliders can collide different types of particles. Different particle species offer different advantages and disadvantages. Electron-positron (e^--e^+) colliders provide clean and well controlled collisions since electrons are fundamental particles. On the other hand, electrons accelerated by circular accelerators radiate much of their energy away as synchrotron radiation due to their small mass, limiting the energy of e^--e^+ colliders. Proton-proton (p-p) and proton-antiproton (p-$\overline{p}$) colliders can reach higher energies due to lower synchrotron radiation and often feature higher cross sections and thus collision rates. The downsides of p-p and p-$\overline{p}$ collisions are the complications that come with (anti)protons not being fundamental particles discussed in Section 1.2.1 including messy collisions and lack of control of parton collision energy. Due to the larger PDFs for $\overline{u}$ and $\overline{d}$ quarks in antiprotons, p-$\overline{p}$ colliders offer some advantage for studying processes involving interactions of light quarks and antiquarks, but the use of an antiproton beam also somewhat limits the luminosity of the collider. Proton-electron (p-e) collisions, heavy ion collisions (X-X), and proton-heavy ion collisions (p-X) have been and are used for studying the strong interaction and strongly interacting matter. Finally, the possibility of a muon-antimuon (μ^--μ^+) collider is currently being investigated as a method to reach even higher energies, but this idea has not yet been realized due to the difficulty of

reducing muon emittance to create a beam given the constraint of the muon lifetime [161].

2.1.2 The LHC complex

The Large Hadron Collider is a 26.7 km circumference particle accelerator and collider at CERN, the European Laboratory for Particle Physics. A comprehensive description of the LHC can be found in Ref. [159], but some of the most relevant features of the LHC are discussed here.

The LHC is a two-ring-superconducting hadron collider designed to reach center-of-momentum collision energies of 14 TeV and a luminosity of 10^{34} $\mathrm{cm}^{-1}\mathrm{s}^{-1}$ to satisfy the needs of experiments at the highest energy scales and luminosities. The LHC can create p-p, p-X, and X-X collisions, though this document focuses on only p-p collisions. To direct the high energy beams, the LHC requires powerful 8.3 T dipole magnets. The magnets used in the LHC are superconducting electromagnets that rely on Nb-Ti cables cooled to 1.9 K by the LHC cryogenics system. These magnets are twin-bore magnets in which there are two sets of coils, one for each beam direction, contained in the same structure and cooling system. This is necessary due to the size constraints of the tunnel. Since even a small energy deposit can cause an increase in temperature that would cause the superconducting magnets to quench, the LHC has precise beam-loss monitoring and control systems.

The LHC is not completely circular, but rather is divided into eight curved segments called arcs equipped with the dipole magnets and eight largely straight segments called

insertion regions (IRs). Locations around the LHC are usually described in terms of 8 octants centered on the IRs. IRs 1, 2, 5, and 8 have at their center interaction points around which LHC experiments operate. These IRs are equipped with magnets that direct the two beams to cross each other, as well as magnets to reduce β^* and increase luminosity provided to the experiments. In particular, the insertions at IR1 and IR5 are optimized for the highest luminosity experiments, ATLAS and CMS. IR2 and IR8 also contain the beam injection systems. IR4 contains the LHC RF systems. IR3 and IR7 contain the LHC beam cleaning insertions. These insertions remove beam halo particles by placing targets called collimator jaws that block off-axis particles. There are several layers of these collimators at increasingly wide angles to block beam halo as well as secondary beam halo produced by collisions of the primary beam halo and the initial collimators from reaching critical accelerator components. Despite the many precautions, some secondary beam halo particles produced by either collisions with the collimators or collisions with gas in the beam pipe can reach the experiments, creating a source of machine-induced background. IR3 contains the momentum collimation system, which utilizes the transverse offset caused by particles with longitudinal offsets to to remove them, while IR7 contains the betatron collimation system to remove particles with large transverse oscillations. Finally, IR6 contains the beam dump system, which uses kicker magnets to deflect beams towards the beam dump lines where they can be safely collided with the beam stop block. This is shown schematically in Figure 2.1.

Synchrotrons such as the LHC can not accelerate particles from rest but instead

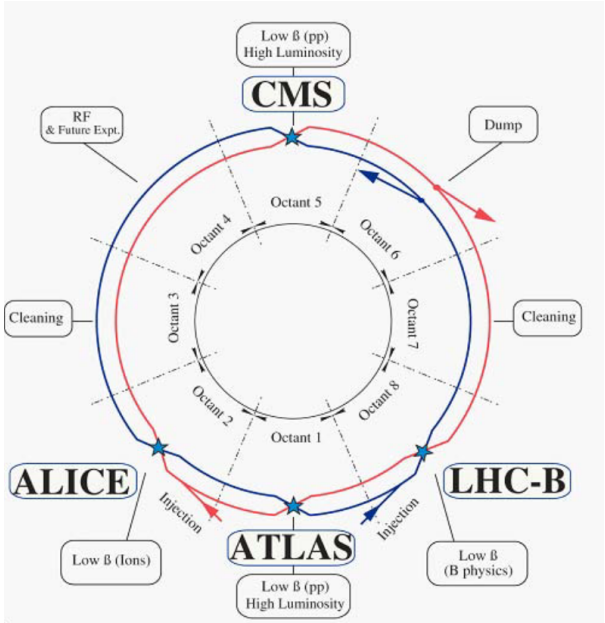

Figure 2.1: Schematic layout of the LHC showing the 8 octants and the function(s) performed in each IR, from Ref. [159].

require beams to be injected. The initial stages of acceleration are performed using other machines in the CERN accelerator complex. During Run 2 of the LHC (2015–2018), the acceleration chain began with ionized hydrogen gas being put into the LINAC 2. From LINAC 2, the beam was injected into the Proton Synchroton Booster (PSB), the Proton Synchrotron (PS), and the Super Proton Synchrotron (SPS), in this order, before being injected into the LHC. These machines accelerated protons to maximum energies of 50 MeV, 1.4 GeV, 25 GeV, 450 GeV, and 6.5 TeV respectively. For the Run 3 of the LHC (2022–present), the LINAC 2 has been replaced by the LINAC 4, which accelerates negative hydrogen ions to 160 MeV before they are stripped of their electrons and provided to the PSB. The LHC acceleration energy has also been increased to a maximum of 6.8 TeV.

The LHC begins to accelerate the beam bunches to their final energy once all the bunches have been injected from the other accelerators of CERN's accelerator complex. This period is referred to as the energy ramp. After the ramp, the size of the bunches is compressed at the collision points to increase luminosity in a phase called squeeze. After this, stable beams provide collision data to the experiments. The time period for which the LHC has circulating beams is called a fill. The instantaneous luminosity is highest at the start of a fill, but decreases because of both proton collisions and other mechanisms such as increase in emittance, beam-beam interactions, and RF noise. After several hours, the luminosity decreases to a low enough rate that it is beneficial to dump the beam and refill the LHC.

At the LHC, each proton bunch has about 10^{11} protons. During Run 2 of the LHC, the bunches in the LHC beam were typically 7.5 m apart, producing bunch crossings every 25 ns. However, not every 25 ns bucket necessarily has a bunch since bunches are typically injected in trains of 48 bunches with a gap between trains as well as a gap of about 3 µs used to provide time for the abort kicker magnet to reach full strength. During 2017, interactions between the beam and an electron cloud formed by frozen gas in the beam pipe led to the use of mini-trains with 8 bunches followed by 4 empty buckets. By 2018, fills largely returned to the nominal structure. During 2016–2018, fills provided up to 2556 bunches per beam, 2544 of which collided at interaction point 5 [162, 163].

The LHC has previously had two operational runs of data taking, referred to as Run 1 (2009–2013) and Run 2 (2015–2018). During Run 1, the LHC operated up to a maximum

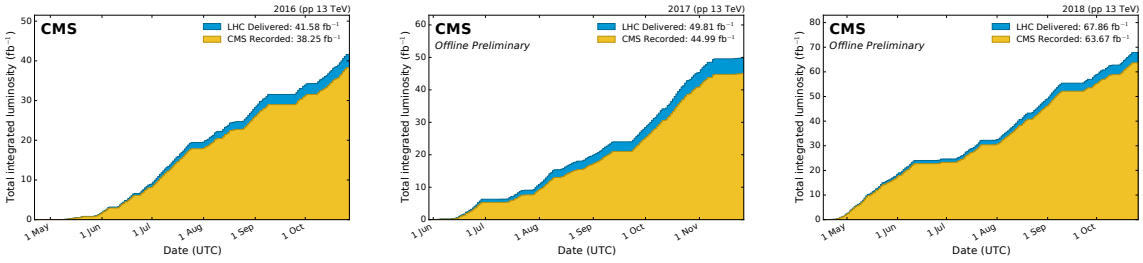

Figure 2.2: Integrated luminosity of p-p collisions provided to the CMS experiment by the LHC (blue) and recorded by the experiment (yellow) plotted as a function of time in 2016 (left), 2017 (center), and 2018 (right). Note that not all recorded data are necessarily usable for all analyses. Figure from Ref. [165].

energy of 8 TeV and maximum instantaneous luminosity of about 8×10^{33} $\text{cm}^{-1}\text{s}^{-1}$, delivering about 30 fb^{-1} to the high luminosity experiments. During Run 2, the LHC operated at a maximum energy of 13 TeV and a maximum instantaneous luminosity of 2×10^{34} cm^{-2} s^{-1}, delivering about 160 fb^{-1} to the high luminosity experiments. Run 1 and Run 2 were followed by long shutdown 1 (LS1) and long shutdown 2 (LS2) respectively. Run 3 data taking began in 2022 and is currently ongoing. There is also currently a large program of upgrades to the LHC, the CERN accelerator complex, and the LHC experiments to allow luminosities as high as 5.0×10^{34} $\text{cm}^{-1}\text{s}^{-1}$. The upgraded High-Luminosity Large Hadron Collider (HL-LHC) is planned to begin operation with the beginning of Run 4 in 2029 and continue until the end of Run 5 in 2038 [164]. During a data taking run, most time is devoted to proton-proton collisions, though some time is reserved for heavy ion collisions and special low luminosity runs. Figure 2.2 shows the integrated luminosity of p-p collisions provided by the LHC to the CMS experiment over time as well as the integrated luminosity recorded by the experiment in 2016–2018.

2.2 The CMS experiment

The Compact Muon Solenoid experiment is one of the two general purpose particle physics experiments at the LHC. It is located at LHC interaction point 5 together with the smaller total elastic and diffractive cross section measurement (TOTEM) experiment. CMS consists of many layers of particle detector systems designed to address a broad physics program by precisely measuring and robustly identifying physics objects such as the jets, electrons, muons, photons, and hadronic tau lepton decays described in Section 1.2.3. Furthermore, the detector operates in units of 25 ns "events" synchronized with the LHC bunch crossing frequency. In each bunch crossing, many proton-proton interactions can occur. When studying rare phenomena, there is typically one collision of interest per bunch crossing; the other collisions in a given event are referred to as "pileup." Separating pileup from the collision of interest poses an additional challenge for CMS. A comprehensive description of the experiment as it was initially constructed is given in Ref. [166]. This section gives an overview and identifies highlights of the CMS detector design.

The general layout of CMS is similar to that of other general purpose collider experiments, pioneered by the Mark I detector at the SPEAR e^+ e^- storage ring at SLAC National Accelerator Laboratory [167]. The CMS experiment is made of various subsystems constructed in concentric cylinders. The tubular portion of these cylinders is called the barrel while the disks on either end are called the endcaps. Figure 2.3 shows one quadrant of the CMS detector in the y-z plane as it appeared during Run 2. The

innermost layer of the CMS experiment outside of the LHC beam pipe, the inner tracker, measures the tracks of charged particles, and, by measuring their curvature in a magnetic field, provides a measurement of their momenta. The high energies of LHC collisions can produce very high momentum particles. To produce sufficient curvature to measure the momentum of such particles, the inner portion of the CMS experiment is contained within a large 4 T superconducting solenoid magnet. The innermost portion of the tracker features pixel detectors to improve vertex resolution, which aids in identifying both displaced particles such as those in b jets as well as charged particles produced in pileup collisions. The calorimeters, capable of measuring the energies of all long-lived particles except muons and neutrinos, are located outside of the tracker, but within the solenoid magnet to avoid degredation in energy resolution caused by showering in the magnet. Muon detectors are embedded in the flux-return yoke of the magnet outside the main solenoid and are able to provide additional identification and momentum measurements for muons. The CMS detector systems produce immense volumes of data. As such, the CMS trigger system performs real-time reconstruction and selects the data that are saved by the data acquisition (DAQ) system. The CMS detctor is located underground in the experimental cavern containing LHC interaction point 5, some of the electronics are located the adjacent service cavern, and the DAQ server farm is located in buildings at surface level.

CMS uses a coordinate system which is centered at the collision point and for which the z-axis is along the beam-line toward the Jura mountains, the x-axis points toward

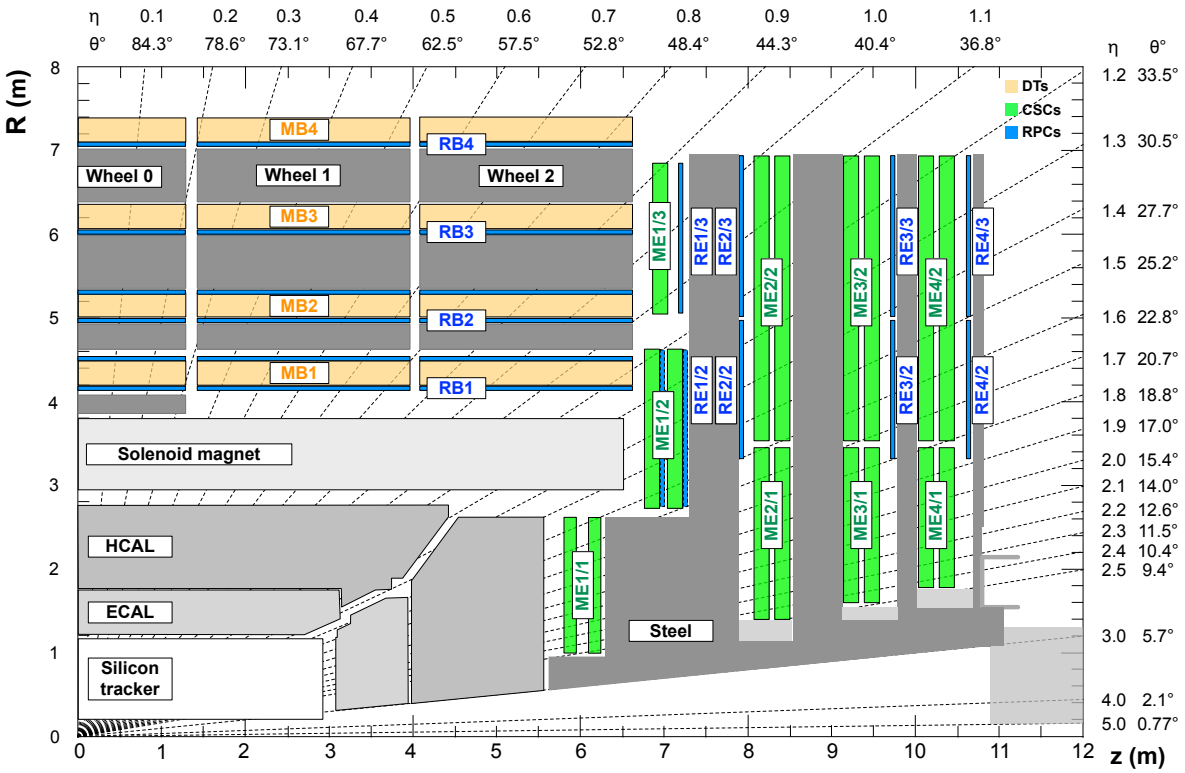

Figure 2.3: One quadrant of the CMS detector in the y-z plane as it appeared during Run 2 showing the tracker, the calorimeters, the solenoid magnet, and the muon detectors (colored) embedded in the magnet return-flux yoke.

the center of the LHC ring, and the y axis points vertically upward. Typically, vectors are expressed in (R, η, ϕ) coordinates discussed in Section 1.2.1.

2.2.1 Inner detectors

The innermost detector subsystem of CMS is the inner tracker, which is responsible for reconstructing the tracks of charged particles. At the original LHC design luminosity, each bunch crossing generates an average of 1000 particles that traverse the tracker. For this reason, the CMS tracker was designed to have high granularity and fast response. The innermost layers of the tracker comprise silicon pixel detectors in order to keep occupancy, the probability a given sensor is hit, below 1% per event. At larger radii where the particle flux per area is lower, CMS uses silicon micro-strip detectors. The strip pitch as well as the length and thickness of the detectors increases with radius to avoid an unserviceable number of readout channels while keeping the occupancy per event at the percent level. A layout of the original CMS tracker is shown in Figure 2.4. The innermost pixel detector system extends to a radius of 10.2 cm and is surrounded by the strip detectors, which are grouped into several subsystems called the tracker inner barrel (TIB), tracker inner disks (TID), tracker outer barrel (TOB), and tracker endcaps (TEC). For particle tracks with $|\eta| < 2.5$, the pixel detectors typically provide 3 two-dimensional measurements (4 after the 2016/2017 upgrade) while the strip detectors provide approximately 9 measurements of which 4 are two-dimensional.

The original CMS pixel detector consists of 3 barrel layers and 2 endcap disks with a

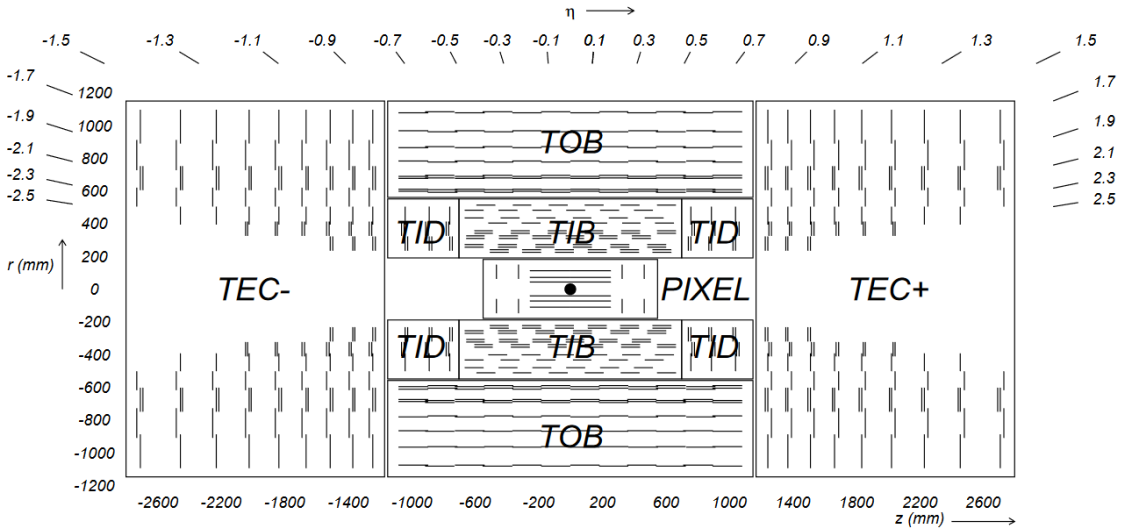

Figure 2.4: Cross section of the original CMS tracker in the z-y plane showing the various submodules and layers. Figure from Ref. [166].

total of about 66 million 100×150 µm^2 pixels. By interpolating charge between adjacent pixels, sub-pixel spatial resolution of as low as 15–20 µm can be achieved. The sensors are implemented as $n+$ pixel on n-substrate detectors, which allows for radiation hardness at moderate bias voltages. Groups of 52×80 pixels are bump-bonded to a read out chip (ROC), which amplifies and reads out the signals from the connected pixels into a buffer when the signals pass a programmable threshold. Several ROCs are controlled by a token bit manager (TBM) chip, which distributes signals to the ROCs and manages trigger accept signals. Trigger and clock signals from the CMS timing and control distribution system (TCDS) (formerly timing trigger and control (TTC)), as well as fast control signals to configure front-end board settings, are sent via optical fiber from pixel front-end controller boards located in the service cavern. Front-end controller (FEC) boards provide slo–control functionality to auxiliary components in the pixel system. Upon

receiving an trigger accept, a TBM initiates a token pass that traverses the ROCs in series in order to generate a data packet, which is sent via optical fiber to pixel front-end driver (pxFED) boards in the service cavern, which then digitize and transmit the pixel data to the central DAQ system.

During the year-end technical stop (YETS) in 2016/2017, the pixel system was replaced with an upgraded system called the phase-1 pixel detector [168]. The upgraded version features 4 barrel layers, the innermost of which has since been replaced after Run 2, and 3 endcap disks containing about 124 million pixels. The sensor technology is similar to that used in the original system, however the front-end ROC and TBM chips feature design changes to enable faster readout. Notably, the optical links to the back end of the new system allow higher frequency digital transmission in contrast to the original analog transmission. The off-detector VME-based DAQ system was replaced by a MicroTCA (µTCA)-based system containing new front-end driver modules for receiving data, tracker front-end controller modules for providing slow control, and pixel front-end controller modules for fast control, clock, and trigger distribution.

The silicon-strip detectors are divided into four subsystems: 4 inner barrel (TIB) layers, 3 inner disks (TID), 6 outer barrel (TOB) layers, and 9 endcap (TEC) disks. The first two layers/rings of the TIB, TID, and TOB as well as rings one, two, and five of the TECs each have a second layer of modules mounted at a different angle to provide a two-dimensional measurement. The sensor elements used in the silicon-strip detectors are AC-coupled single sided p-on-n type silicon microstrip sensors. The sensors are wire-

bonded via a pitch adapter to a custom integrated circuit called an APV25, which reads out and buffers data from the sensors. Trigger, clock, and control signals are distributed to the strip detector modules from FEC boards. Upon receiving a trigger, the data from the front-end APV25 chips is transmitted via optical fiber to front-end driver boards (FED), which are responsible for digitizing the data and transmitting it to the central DAQ system. Like the pixel read-out system, the FEC and FED boards are located in the service cavern.

Optimally, a tracking system would be able to measure the trajectories of particles without significantly affecting their momenta. However, CMS uses a silicon tracker in order to deal with the high flux of particles near LHC collisions. This leads to a substantial probability for inelastic collisions to occur within the detector, even with optimizations to minimize the material budget and thus the rate of inelastic interactions. Figure 2.5 shows the integrated thickness of the original CMS tracker as well as just the pixel layers before and after the 2016/2017 upgrade in units of radiation lengths and nuclear interaction lengths. At some values of $|\eta|$, particles may traverse as much as 2 radiation lengths or 0.5 nuclear interaction lengths, resulting in a high probability for particle interactions. The track reconstruction algorithms described in Section 2.3.2 are designed to mitigate the impact of such interactions by reconstructing nuclear interactions in the tracker, photon conversion, and electron bremsstrahlung. With the standard algorithms, CMS is able to reconstruct up to about 90% of tracks at intermediate momentum with a percent-level p_{T} resolution and impact parameter resolution on the order of 1–10 µm.

Tracks are reconstructed for particles with momentum as low as 200 MeV, which is well below the 700 MeV required for charged particles to reach the barrel calorimeters. Inefficiencies in track reconstruction for higher momentum tracks stem primarily from inelastic interactions within the tracker volume.

It is planned that the entire CMS tracker will be replaced before Run 4, the beginning of HL-LHC operation. The upgraded tracker will consist of an inner tracker based on silicon pixels and an outer tracker made of silicon strips and macropixels [170]. The upgraded detectors and electronics will feature increased acceptance, increased radiation hardness, better granularity, as well as higher data transfer rates and buffer space to accommodate the upgraded trigger parameters. The new outer tracker will also provide tracking information to the upgraded level-1 trigger system to improve muon momentum resolution, provide electron-photon discrimination, and aid in particle isolation measurements. In addition to the new tracker, CMS will be upgraded with a MIP timing detector consisting of a barrel timing layer employing scintillating crystals and silicon photomultipliers and an endcap layer that will employ silicon low-gain avalanche detectors [171]. These detectors are designed to be able to measure particles with a timing resolution of 30–40 ps upon installation, which will aid in rejecting pileup that cannot be rejected based upon track information alone.

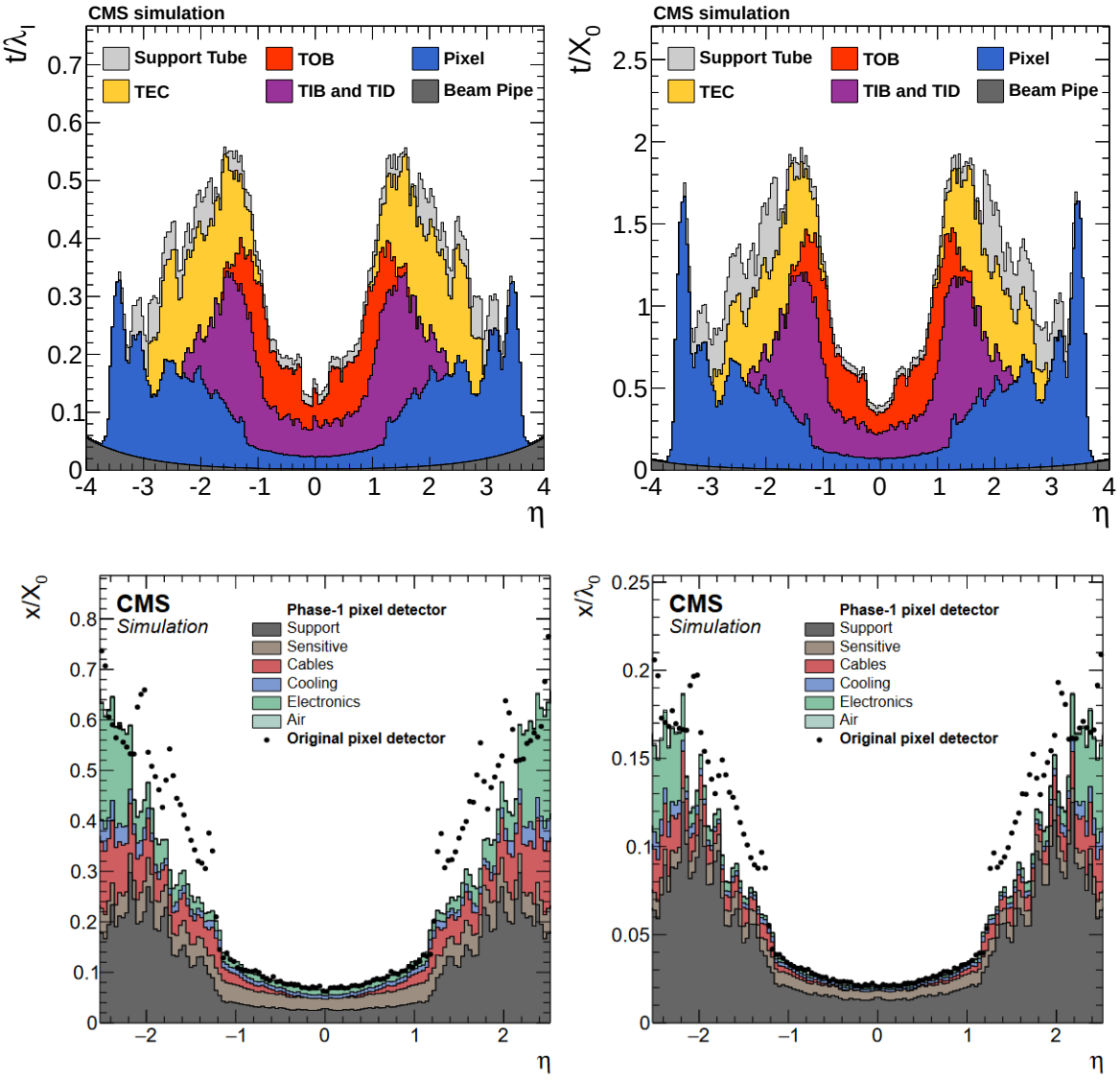

Figure 2.5: (Top) The integrated thickness of the original inner tracker as a function of η expressed in nuclear interaction lengths (left) and radiation lengths (right) from Ref. [169]. (Bottom) The integrated thickness of the pixel detector before (dots) and after (stacked histogram) the 2016/2017 YETS upgrade expressed in radiation lengths (left) and nuclear interaction lengths (right) from Ref. [168]. Although the tracker was designed to have a low material budget, there is still significant probability for particles to undergo inelastic collisions in the tracker volume, particularly at higher $|\eta|$.

2.2.2 Calorimeters and forward detectors

The main CMS calorimeters are divided into an inner electromagnetic calorimeter (ECAL) system and an outer hadronic calorimeter (HCAL) system. The ECAL provides at least 24 electromagnetic interaction lengths, ensuring it contains almost all the energy of electromagnetic showers, providing granular and very accurate measurements for showers initiated by electrons and photons up to an $|\eta|$ of 3.0 [169]. The HCAL provides measurements of hadronic showers with approximately 11 hadronic interaction lengths in order to provide inclusive energy measurements of deeper hadronic showers up to an $|\eta|$ of 3.0. Some coverage up to an $|\eta|$ of 5.0 is provided using radiation hard technologies. Additional calorimeters systems (CASTOR, ZDC) provide even further forward coverage. A specialized detector shared with the TOTEM experiment called the CMS-TOTEM precision proton spectrometer (CT-PPS) provides information about protons that remain intact after interacting.

Electromagnetic calorimeter

The CMS ECAL is a homogeneous calorimeter made of about 68 thousand lead tungstate ($PbWO_4$) crystals. The short interaction length and short scintillation decay time of $PbWO_4$ allows for a detector that is compact and can distinguish events on the time scale of LHC bunch crossings. $PbWO_4$ also has a Molière radius of 2.2 cm, which combined with the narrow width of the crystals, 2.2 cm in the barrel and 2.9 cm in the endcap, allows for resolving energy deposits as close together as 5 cm. The light

from the $PbWO_4$ crystals is detected by avalanche photodiodes in the barrel and vacuum phototriodes in the endcap. The signals from the photodetectors are given to very front-end (VFE) boards, which shape and digitize the pulses before handing the information to front-end (FE) boards, which buffer data from the VFE boards and transmit the energy sum of the trigger tower and a fine-grain bit to the trigger concentrator card (TCC) via optical links. The TCCs are off-detector boards responsible for transmitting trigger primitives to the level-1 trigger. TCDS signals such as the clock and trigger accept signals as well as control signals are provided to the front-end boards by off-detector clock and control system boards. Upon receiving a trigger accept, the FE boards and TCC transmit data to off-detector data concentrator card (DCC) boards. The DCCs are also connected to selective read-out processor boards, which implement the selective read-out system. The selective read-out system uses level-1 trigger primitives to select channels to be read out based on energy deposits in the vicinity. This provides a 20-fold reduction in data needed to fit within the data budget.

A finer grained preshower detector is installed in front of the ECAL endcap disks. The preshower detector consists of two layers of lead target and silicon strip detectors providing a total of about 3 radiation lengths. The high granularity of this detector was intended to help resolve photons produced in neutral pion decays from prompt photons and identify photons/electrons, but the large number of neutral pions produced by hadronic interactions in the tracker severely hinder the preshower detector so that the energy recorded in the preshower is simply considered together with that of the main

endcap ECAL disks.

Using a test beam, the intrinsic energy resolution of the ECAL for particles was measured to be

$$\left(\frac{\sigma_E}{E}\right)^2 = \left(\frac{2.8\%}{\sqrt{E/(1\ \text{GeV})}}\right)^2 + \left(\frac{0.12}{E/(1\ \text{GeV})}\right)^2 + (0.30\%)^2, \tag{2.2}$$

where E is the energy of the incident electron or photon and σ_E is the resolution. This results in percent-level resolution for electrons and photons with p_{T} greater than 20 GeV. The three terms are called the stochastic term, the noise term, and the constant term, and are respectively primarily due to the intrinsic stochasticity in showering, electronics or digitization noise, and detector non-uniformities. Additional contribution from leakage of showers from the rear of the ECAL becomes relevant at energies near about 500 GeV. Particles directly ionizing the avalanche photodiodes can also create large spikes that are rejected by requiring measurements from neighboring crystals to be compatible with a shower. More information about the reconstruction algorithms that use ECAL information is provided in Section 2.3.1. The cell threshold for energy deposits in the ECAL is 80 MeV in the barrel, 300 MeV in the endcaps and 0.06 MeV for the preshower detector, which is 2–3 times the electronic noise for the system [172]. The reconstruction efficiency for particles reaching the ECAL with momenta well above these thresholds is nearly 100%.

Hadronic calorimeter

The CMS HCAL consists of four distinct components, asshown in Figure 2.6. The HCAL barrel (HB) is a sampling calorimeter located inside of the CMS solenoid magnet constructed from 16 layers of absorbers, the first and last of which are made of steel and the others of brass, with 17 plastic scintillator interleaved. The first scintillator layer is located in front of the first absorber to sample hadronic showers developing between the ECAL and HCAL while the last scintillator layer is extra thick in order to correct for late showers leaking out the back of the HB. The light from the scintillators is read out by hybrid photodiodes connected to the scintillator trays by inserted wavelength shifting fibers spliced to clear fibers. Unfortunately, the HB does not provide satisfactory containment for hadronic showers of high momentum particles and as such is supplemented by an outer HCAL tail-catcher (HO) located outside of the CMS solenoid. The HO uses the solenoid coil itself as an additional absorber and consists of 5 rings, each consisting of one layer of scintillating tile except for the central ring, which uses two layers of scintillating tiles separated by an additional steel absorber. The HCAL endcap (HE) features a similar design to the HB with 19 layers of scintillators interleaved with absorbers providing about 10 hadronic interaction lengths up to an $|\eta|$ of 3.0 [173]. The detector technology employed in the HO and HE is similar to that of the HB. Finally, the forward HCAL (HF) extends coverage up to $|\eta|$ of 5.0 and features radiation hard technologies in order to operate in the harsh environment of the forward region. The HF is made of grooved steel scintillators with quartz fibers inserted into the groves, running parallel to the beam

line. The Cherenkov radiation of particles passing through the fibers is measured using photomultiplier tubes, which yields an estimate for the electromagnetic energy component of showers. Furthermore, the quartz fibers alternate between long fibers covering the whole length of the HF and short fibers that end 22 cm before the front face. By reading out these fibers separately, the electromagnetic and hadronic components of the shower can be separately measured. HCAL front-end modules sport integrated circuits that take signals from the hybrid photodiodes (HB/HO/HE) or photomultiplier tubes (HF), digitize them, and transmit them to the service cavern via optical fiber. In the service cavern, the signals are received by HCAL trigger and readout (HTR) boards that calculate trigger primitives and provide them to the regional calorimeter trigger. Upon receipt of a trigger accept, the HTRs provide their data to the data concentration card, which controls transmission of data to the central DAQ system.

Since the end of LHC Run 1, various upgrades to the HCAL front-end electronics have been performed [174]. During LS1, the HO hybrid photodiodes were replaced by silicon photomultipliers to mitigate problems with discharge and improve detection efficiency. Also, during LS1, the photomultiplier tubes in the HF were replaced with a more radiation-hard photomultiplier tube design, and during the 2016/2017 YETS, the HF front-end electronics were upgraded. During the 2017/2018 YETS, the HE hybrid photodiodes were replaced by new silicon photomultipliers and the HE front-end electronics were upgraded to allow for increased depth segmentation, better timing, and compensation for radiation damage. During LS2, a similar upgrade was also performed for the

HB. Finally, the back-end electronics were upgraded to a µTCA-based system with new µTCA HCAL trigger and readout boards, which operate together with a commercial AMC13 board that is responsible for distributing TCDS signals as well as transmission to the DAQ system. The new back-end electronics for the HF were installed during LS1 while the back-end electronics for the HE and HB were installed during the 2017/2018 YETS and LS2 respectively in conjunction with the front-end upgrades

Using a test beam, the intrinsic resolution of the barrel ECAL+HCAL for single pions between 20 and 300 GeV was measured to be

$$\left(\frac{\sigma_E}{E}\right)^2 = \left(\frac{115\%}{\sqrt{E/(1\ \text{GeV})}}\right)^2 + (5.5\%)^2, \tag{2.3}$$

where E is the energy of the incident pion and σ_E is the resolution [175]. The stochastic and noise terms have largely the same origins as those for ECAL resolution, but the stochastic term coefficient is much larger since the ECAL+HCAL system has values of e/h that are both markedly nonunity and different for the ECAL and HCAL separately. Although this strongly limits calorimeter jet energy resolution, CMS uses the particle-flow reconstruction algorithm, which only uses HCAL information for the 10% of jet energy carried by neutral hadrons. For this reason, hadronic energy resolution in the calorimeters is not the limiting factor in jet energy resolution, as discussed in Section 2.3.5. The cell threshold for energy deposits in the HCAL is 800 MeV [148] and the intrinsic noise in the electronics is about 180 MeV. Section 2.3.1 provides more information about how HCAL information is used in reconstruction.

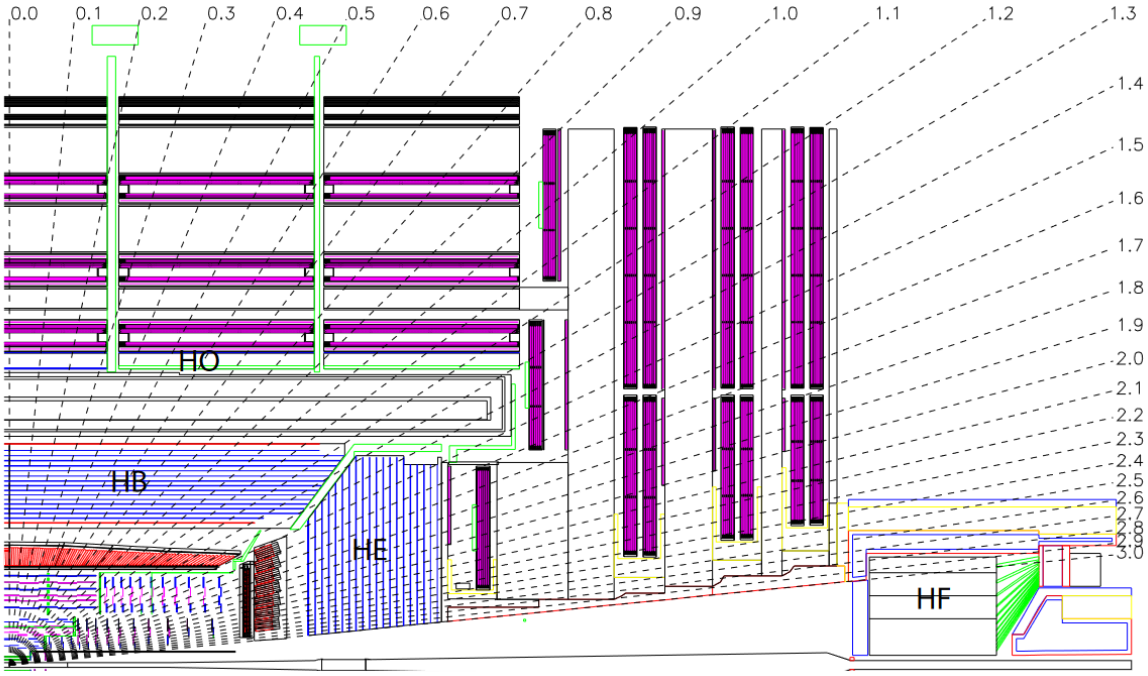

Figure 2.6: One quadrant of the CMS detector in the z-y plane showing in particular the location of the CMS HCAL subsystems (HB, HO, HE, HF). Figure from Ref. [166].

Forward detectors

For heavy-ion collisions, diffractive or low-x QCD studies, and searches for exotic particles, two very forward calorimeter systems, Centauro And Strange Object Research (CASTOR) and the Zero Degree Calorimeter (ZDC), are incorporated into the CMS experiment. CASTOR is a Cherenkov-based calorimeter made of layers of fused silica quartz and tungsten absorber covering the $5.2 < |\eta| < 6.6$ region. The ZDC also uses quartz Cherenkov detectors and tungsten absorbers with rapidity coverage in the region $|\eta| > 8.3$. CASTOR was upgraded with radiation hard PMTs in 2012 and later decomissioned during LS2 [176, 177].

Since data taking in 2016, a new detector system called the CMS-TOTEM precision proton spectrometer (CT-PPS) consisting of tracking and timing detectors in "roman pots," movable devices inserted directly into the beam pipe, at 200 m on either side of the interaction point has been operational. The CT-PPS can measure protons that have lost a small amount of momentum during collisions and diverge from the beam envelope. This allows the study of rare processes such as central exclusive production in which new particles are made while the colliding protons remain intact. The detectors were upgraded over the course of Run 2 and included silicon strip and pixel detectors for tracking as well as silicon and diamond detectors for precision timing. Since the end of Run 2, the precision proton spectrometer has been integrated into CMS as a regular subsystem [178, 179].

Future upgrades

Before HL-LHC operation, additional upgrades will be required. First, the EB VFE and FE boards will need to be upgraded. Additionally, a new barrel calorimeter processor (BCP) board will replace the legacy TCC and DCC boards for the EB, implement some of the buffering and clustering functionality previously performed by the FE boards, and replace the µHTR boards for the HB [180]. These upgrades allow for compliance with the larger data rate and trigger latency, suppression of avalanche photodiode spikes in the EB, more granular ECAL readout, and precision timing information that can aid in determining photon vertices. The HO and HF detectors will continue using Run 3 configuration with only an increase to the number of back-end cards used to read out the HF.

In addition, HL-LHC conditions will also require the EE and HE to be completely replaced with a new endcap calorimeter design called the high granularity calorimeter (HGCAL) [181]. The HGCAL features an electromagnetic compartment consisting of 28 layers silicon detector modules interleaved with stainless steel absorber as well as a hadronic compartment consisting of 24 layers of silicon modules (inner region) or scintillator tileboards (outer region) interleaved with stainless steel absorber. The signals from the silicon detectors and scintillator modules will be read out by HGCAL readout chips and subsequently transmitted by motherboards via optical fiber to the back-end electronics. The HGCAL will provide high radiation tolerance, high granularity and timing information to aid in pileup rejection, and the ability to interface with the upgraded

level-1 trigger.

2.2.3 Muon systems

The original CMS muon system is divided into three subsystems of gaseous ionization chambers using different detector designs. Muons in the region $|\eta| < 1.2$ are detected by drift tube (DT) chambers. In contrast, the higher neutron background and stronger magnetic fields of the endcap region $0.9 < |\eta| < 2.4$ require the use of cathode strip chambers (CSCs). The DTs and CSCs are complemented by resistive plate chambers (RPCs) in the region $|\eta| < 1.6$ in order to aid in identifying the correct bunch crossing for triggering purposes. The DTs, CSCs, and RPCs are shown in beige, green, and blue respectively in Figure 2.3.

The DTs are organized into four layers or "stations" integrated into the magnet flux return yokes. The first three stations each contain four chambers that measure the $r-\phi$ coordinate of the muons and four that measure the η component while the last station has only four $r-\phi$ oriented chambers. The individual cells in each chamber have a transverse length of 21 mm with 2.4 m long wires running down the chamber, which is sufficient to produce negligible occupancy with a serviceable number of readout channels. Muons that pass through a cell ionize argon in the DT gas mixture and the freed electrons will drift toward the central anode. When the electrons approach the anode wire, they produce a Townshend avalanche, which induces an electrical signal that is amplified by application specific integrated circuits on the DT front-end boards and transmitted to

readout boards (ROBs) that perform time digitization. The measured drift time of the muon can be used to determine the distance between the muon track and the anode wire. The ROBs provide input to the trigger boards (TRBs), which generate track segments that are transmitted to the muon trigger via server boards and sector collectors. Upon a level-1 trigger accept, the ROB also provides data to the readout server, which in turn provides data to the detector dependent units (DDUs), which are the DT interface to the central DAQ system. DT spatial resolution is better than 300 µm in the ϕ layers and about 250–600 µm in the θ layers except in inner stations in the outer wheels, and DT time intrinsic resolution is about 2 ns [182].

The CSCs are multiwire proportional chambers made of interleaved layers of cathode strips and anode wires. The chambers are organized into four layers or stations on the endcap disks, providing up to four $\eta-\phi$ measurements of muons. The outer portion of the fourth station was not installed until LS1 due to budget constraints. Each chamber has seven cathode planes providing $r-\phi$ measurements and six anode wire planes providing η and timing measurements. Muons passing through CSCs ionize the argon in the gas mixture, which in turn generates avalanches that induce pulses on nearby anode wires and cathode strips. By comparing the signals on adjacent strips, the muon track location can be determined to within half a strip. The anode wires are read out by anode front-end boards and aggregated by the anode local charged track (ALCT) board while the cathode strips are read out by cathode front-end boards (CFEBs). The ALCT board also forms anode local charged tracks, which are provided to the timing motherboards

(TMBs) together with data from the CFEBs in order to form 2D local charged track trigger primitives provided to the muon trigger through a muon port card (MPC). The data acquisition motherboard (DMB) manages aggregation of CSC data and transmission to the front-end driver DDUs and data concentration cards that interface with the central DAQ system. CSC spatial resolution varies from about 50–150 µm depending on the station and ring and an intrinsic timing resolution of about 3 ns.

The RPCs supplement the DTs and CSCs in both the barrel and outer endcap. Each DT station has additional RPCs with the inner two stations having RPCs on either side of the DTs and the outer stations featuring RPCs on one side of the DTs. The $|\eta| < 1.6$ portions of the endcap muon stations also have RPCs integrated, though the fourth station was not installed until LS1. The RPCs are made from double-gap modules with common pickup readout strips in between the gaps. Muons traversing the RPCs will generate avalanches in the two gaps, which are picked up by the readout strips. The strips are read out by front-end boards, which then transfer the data from link boards through optical fibers to trigger boards in the service cavern. The RPC data record is also transferred from the trigger boards. Before the trigger upgrade that concluded during the 2015/2016 YETS, the RPCs also had electronics for a cosmic ray muon technical trigger. Although RPCs provide only cm scale position resolution, they have an intrinsic time resolution of about 3 ns, which improves bunch crossing assignment relative to only DT and CSC reconstruction. Only 0.5% of level-1 RPC hits are associated to the wrong bunch crossing, which can be compared to the 2% for the DTs and CSCs.

During LS1, the outer portion of the fourth endcap muon station was completed with additional CSC and RPC detectors [183]. Furthermore, the electronics of the innermost CSC stations were upgraded and the cathode strip read-outs were unganged to cope with the high detection rates. The CSC MPCs were upgraded with a new mezzanine for compatibility with the level-1 trigger upgrade. Also during LS1, the θ TRBs of the innermost DT stations were replaced and the sector collector and read-out servers were relocated outside of the experimental hall where the boards will not receive a significant radiation dose. Then, during the 2015/2016 YETS, installation of the new level-1 trigger was finalized including the new TwinMux board, which replaces the DT sector collector and receives data from the DTs, RPCs, and the HO for the barrel muon trigger [184]. During the 2017/2018 YETS, the DT data acquisition system was also upgraded with new µTCA read-out servers that replace the previous ROSs and DDUs [185].

Section 2.3.2 details how information from the muon detectors is used in reconstructing muons and Section 2.3.8 provides more information on muon reconstruction. The average efficiency for reconstructing muon track segments across the DT stations is 99.0%, while that for the CSCs is 97.4% [182,186]. The average hit efficiency for RPCs is 94.2% in the barrel and 96.4% in the endcap. Most of the remaining inefficiency is due to faulty electronics boards and other hardware issues. This aids in the overall muon reconstruction efficiency, which is well over 99% for prompt muons with $p_{\mathrm{T}} > 3$ GeV and around 99% for muons from heavy flavor with $p_{\mathrm{T}} > 3$ GeV, as detailed below. The high spatial resolution of the muon detectors allows for stand-alone measurement of muon transverse

momentum at approximately the 10% level for muons under 100 GeV. The time resolution of the muon system allows for determination of the correct bunch crossing at the level-1 trigger with more than 99.8% accuracy.

In preparation for HL-LHC operation, many additional upgrades are planned or have been performed. For the DTs, a new on-board electronics for DTs (OBDT) board will replace the current minicrate electronics such as the ROBs and TRBs. Hit information will be streamed to new back-end boards, which will perform trigger primitive generation and buffering for readout. During LS2, many of the CSC electronics boards were upgraded including the CFEBs on the inner portions of all four stations, the ALCTs on all stations except those upgraded during LS1, and the TMBs on the inner portions of stations two through four. The CSC DMBs on inner rings and the front-end drivers will also be upgraded as will the RPC link and slow control boards. In addition to electronics upgrades for existing muon detectors, a new muon subsystem, the gas electron multipliers (GEMs) along with improved RPCs (iRPCs) will be installed in the forward region to provide additional redundancy and more accurate measurements up to $|\eta| = 2.4$ and some coverage up to $|\eta|$ as high as 2.8 [187]. GEMs are a micropattern gas detector capable of detecting high rates of muons as are present in the forward region of CMS. The first GEM detectors were installed in the forward region of station 1 during LS2 with additional detectors in station 2 and a new station 0 to be installed in the future. The iRPCs will be similar to the previous RPCs but with thinner electrodes and a narrower gas gap to shorten the recovery time to allow for higher rates. iRPCs will be added to

the forward region of endcap stations three and four.

ODMB7/5 Upgrade

Part of the remaining CSC electronics upgrade project is the upgrade of the DMBs for the inner rings of chambers in the CSC stations. The inner ring of the first station will be equipped with the new Optical Data Acquisition Motherboard 7 (ODMB7) model while the inner rings of stations two through four will be equipped with the ODMB5 model. The 7 and 5 refer to the number of CFEBs present on the respective chambers. The primary purpose of these boards, as with previous DMBs, is to aggregate the data from CFEBs, ALCT, and TMBs and build data packets to send to the back-end electronics. New boards are needed to accommodate the higher rates of particle detection and trigger accepts expected during HL-LHC operation. Additional functionalities of the ODMB7/5 include the distribution of clock, trigger, and slow control signals to the CFEBs; receiving slow control signals from a Versa Module Eurocard bus crate controller (VCC) ; controlling and monitoring the low voltage distribution on the chambers; and distributing field-programmable gate array (FPGA) configuration data to the first station CFEBs and ALCTs in the case the on-board memory fails. Figure 2.7 shows the connections between different boards in the CSC system showing the ODMBs' connections to the other off-chamber and on-chamber boards. Figure 2.8 shows the primary data flow for data acquisition and on-chamber FPGA programming data for the ODMB7 and ODMB5 boards.

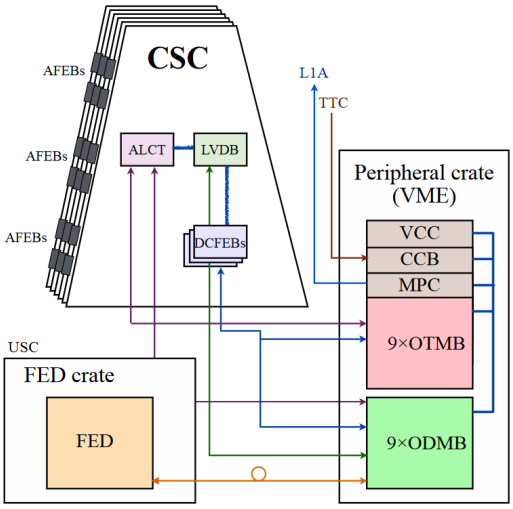

Figure 2.7: Schematic diagram of the electronics and connections used for the the inner CSC stations. The on-chamber boards include the AFEBs, the upgraded digital cathode front-end boards (DCFEBs), the upgraded ALCTs, and the upgraded low voltage distribution boards (LVDBs). The off-chamber peripheral crate electronics include the VCC, MPC, clock and control baord (CCB), upgraded optical timing motherboards (OTMBs), and upgraded ODMBs. In the CMS service cavern will be the upgraded front-end driver (FED) boards.

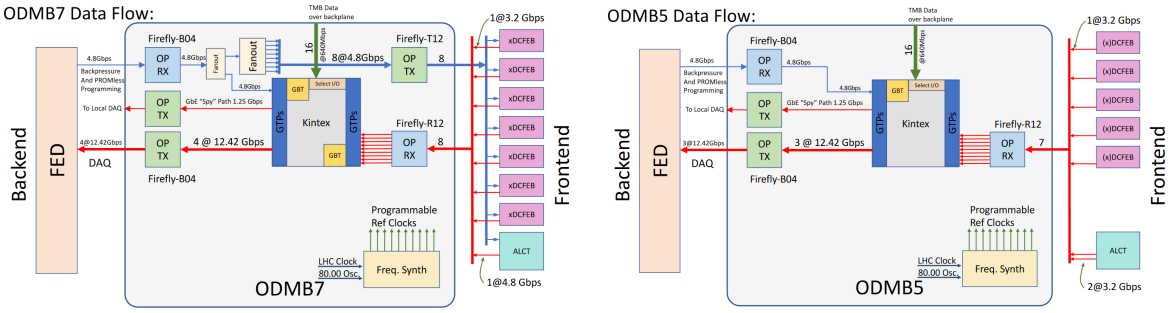

Figure 2.8: Schematic diagram showing the data flow for data acquisition and on-chamber board remote FPGA programming for the ODMB7 (left) and ODMB5 (right). In addition to other CSC electronics boards, the FPGA, optical transceivers, signal fanout, and frequency synthesizer on the ODMBs are shown.

Prototype ODMB7/5 boards have been designed and tested by a team from the Ohio State University and the University of California, Santa Barbara. The boards are Versa Module Eurocard (VME) bus cards equipped with commercial Xilinx Kintex Ultrascale FPGAs and Samtec Firefly high-speed optical transceivers that can provide up to 50 Gb/s data transfer rate to the CSC backend compared to the 4.25 Gb/s afforded by the legacy boards. A first round of prototype ODMB7 boards were designed and produced in 2020 while a first round of ODMB5 prototype boards were designed in 2021 and produced in 2022. A second round of ODMB7 prototype boards were also produced at the end of 2022. Figure 2.9 shows photographs of a second round ODMB7 prototype and an ODMB5 prototype. To test the boards, a test stand with other CSC electronics was constructed at UCSB, FPGA firmware implementing both the data acquisition packet building protocol as well as the miscellaneous slow control functionalities of the ODMB7/5 was developed, and testing software used to test the previous DMB upgrade was updated. All interfaces with other boards were tested, and with minor modifications to the prototypes, all tests succeeded. A full system test was also performed using a CSC chamber at CERN, which was used to successfully take cosmic ray data with an ODMB7 prototype. Several radiation tests were also performed to confirm that the integrated circuits used on the ODMB7/5 will continue to function after being exposed to the radiation doses expected during HL-LHC operation.

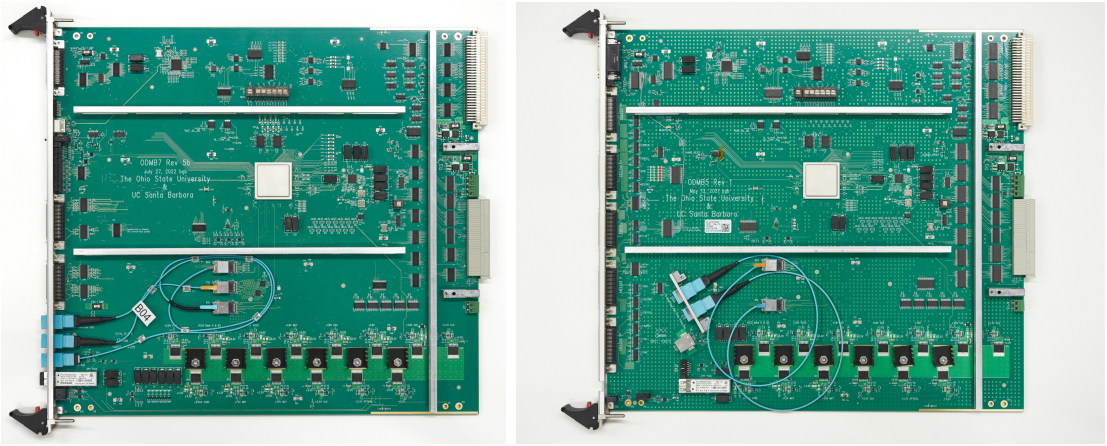

Figure 2.9: Photographs of a second round ODMB7 prototype board (left) and an ODMB5 prototype board (right).

2.2.4 Trigger, data acquisition, electronics, and monitoring systems

The detector systems of CMS produce an enormous amount of data. Typically, zero suppression is applied and detector channels are only read out if the signals are well above some baseline. Even with zero suppression, the data saved to disk is about 1 MB/event at LHC design luminosity. The current DAQ system installed during LS1 is capable of saving only a few GB/s of data, which means that an event rate of only 1 kHz out of the total 40 MHz event rate can be saved. For this reason, CMS incorporates a two level trigger system to determine which events should be saved for further analysis. The level-1 trigger system is implemented in custom electronics and uses a coarse-grained reconstruction from information in the ECAL, HCAL (including HF), and the muon detectors to reduce the event rate to about 100 kHz of events to be passed to the DAQ system. The high resolution data passed to the DAQ system are then used for reconstruction by

the software-based high-level trigger (HLT), which implements reconstruction algorithms similar to those used offline in order to make a final selection of a few kHz of events to save for further analysis.

Level-1 trigger

During LS1 and the 2015/2016 YETS, the CMS level-1 trigger system was upgraded to be able to handle the increased luminosity and pileup of Run 2. The trigger processing is performed on μTCA cards. Three cards called the CTP7, MP7, and MTF7 were designed to meet the different needs of the level-1 trigger system. The overall architecture of the upgraded trigger is shown in Figure 2.10 [163, 188]. Trigger primitives, energy deposits in the calorimeter or muon track segments and hit patterns, are the inputs to the level-1 trigger. The layer 1 calorimeter calibrates and sorts the energy deposits before handing them to the layer 2 calorimeter trigger, which reconstructs physics objects like electrons/photons, jets, and hadronic tau lepton decays. A single layer 2 calorimeter trigger board processes the physics objects for an entire event. This is in contrast to the original trigger architecture, which first reconstructed physics objects in individual detector regions in the regional calorimeter trigger before handing the best objects to the global calorimeter trigger. Muon reconstruction is performed by three track finders for different rapidity regions: the barrel muon track finder (BMTF), the overlap muon track finder (OMTF), and the endcap muon track finder (EMTF). This architecture can be compared to the original muon trigger design, which was split by subsystem into a

DT track finder, a CSC track finder, and an RPC trigger. The three muon track finders receive muon trigger primitives and generate muon tracks that are provided to the μTCA global muon trigger (μGMT) for final selection. The μTCA global trigger (μGT) then receives information from the calorimeter and muon triggers in order to make a final decision to accept or reject an event. This selection occurs with a latency of about 4 μs. When a trigger accept occurs, the level-1 trigger also provides its data to the DAQ system through AMC13 cards.

Trigger primitives from the ECAL, HCAL, and HF are sent to the trigger system via optical synchronization and link mezzanine boards mounted on the TCC and (μ)HTR. Sections of the CMS calorimeters are grouped into trigger towers (TTs). The layer 1 calorimeter trigger is implemented on 18 CTP7s, each of which is responsible for a subset of TTs. These boards apply corrections to the energy sums and transmit the energy sum, ratio, and additional flags to the layer 2 calorimeter trigger through an optical patch panel. The layer 2 calorimeter, which is responsible for reconstructing calorimeter-based physics objects, is implemented on 9 MP7 boards with time multiplexing so that the entire calorimeter data for each event is processed by a single card. Electron/photon candidates are built by clustering energy deposits around a seed TT, then selected based on compactness of showers in the seed TT, the relative distribution of energy in the HCAL and ECAL, and isolation. Hadronic tau lepton decays are reconstructed by using a clustering algorithm similar to that for electrons/photons but with some merging of nearby clusters to reconstruct tau lepton decays to multiple hadrons. A dynamic isolation

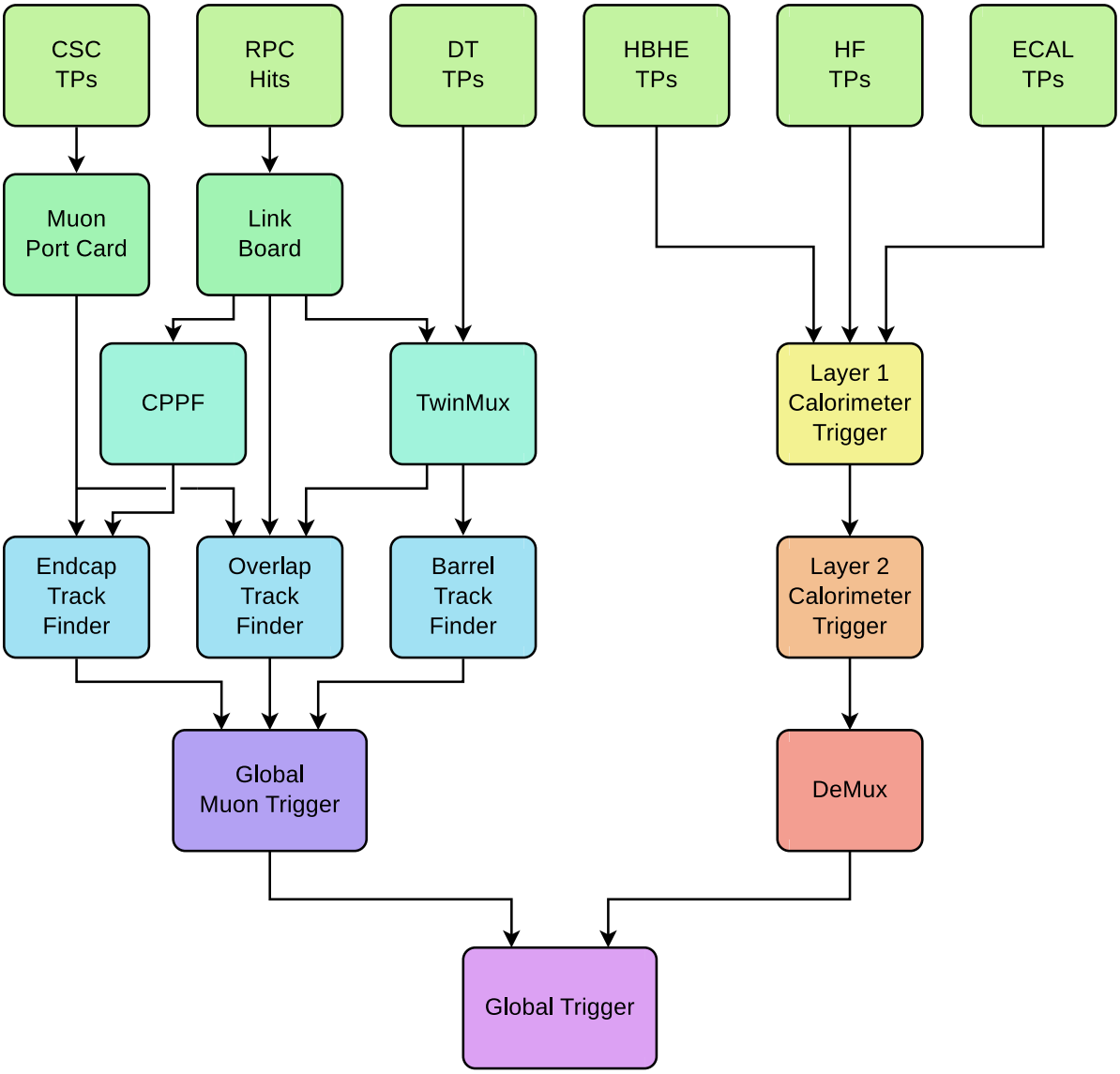

Figure 2.10: Architecture of the CMS level-1 trigger since 2016. Figure from Ref. [163].

threshold is used to differentiate hadronic taus from QCD jets. Jets are reconstructed as energy clusters in a 9×9 TT window, roughly corresponding to $\Delta R = 0.4$ with additional criteria to avoid double counting. Energy detected in an area around the jet window is used to estimate pileup, which is subtracted before energy response corrections are applied. The scalar-summed transverse energy E_{T} is calculated as the scalar sum of all TT energies while $E_{\mathrm{T}}^{\mathrm{miss}}$ is calculated as the vector sum of all TT energies. The scalar-summed jet transverse energy H_{T} and the negative vector-summed jet transverse energy $H_{\mathrm{T}}^{\mathrm{miss}}$ are respectively calculated as the scalar and negative vector sum of jet energies. In 2017 and 2018, a pileup correction was applied to $E_{\mathrm{T}}^{\mathrm{miss}}$. The physics objects produced by the layer 2 calorimeter processors are then given to an MP7 demultiplexer, which provides the objects to the µGT.

The muon trigger begins by receiving trigger primitives from the DTs, CSCs, and RPCs. DT and RPC trigger primitives are combined into superprimitives by the TwinMux, which provides the superprimitives to the BMTF and the separate primitives to the overlap muon track finder OMTF. The OMTF also receives trigger primitives from the RPC link boards and CSC MPCs. The EMTF receives trigger primitives from the MPCs and concentration preprocessing and fan-out boards installed during the 2016/2017 YETS that provide RPC hits. The BMTF is implemented on 12 MP7 cards and reconstructs muons in the region $|\eta| < 0.83$. It uses a lookup table to extrapolate superprimitives from inner stations to outer stations and assembles the superprimitives into a track to which p_{T}, ϕ, and η are assigned using another lookup table. The best tracks from each

BMTF card are provided to the µGMT. The OTMF reconstructs muons in the region $0.8 < |\eta| < 1.2$ and is implemented on 12 MTF7 boards. The OMTF begins reconstruction by identifying high quality reference hits, which are then extrapolated using patterns. The best matched patterns are provided as muon candidates to the µGMT. The EMTF is responsible for muons in the region $1.2 < |\eta| < 2.4$ and is implemented on 12 MTF7s. The EMTF constructs tracks by looking for patterns of trigger primitives in multiple stations. The bending angles of the track are provided to a boosted decision tree, which provides an estimate of the track p_{T}. The reconstructed muons are then sent to the µGMT. The µGMT is implemented in a MP7 and is responsible for receiving up to 108 muon candidates from the track finders, sorting the muon tracks and removing duplicates, correcting muon spatial coordinates, and sending the eight best muons together with quality information to the µGT.

In 2016, the µGT was initially implemented on one MP7, which was then expanded to a total of six boards by the beginning of 2017. The µGT receives physics objects from the layer 2 calorimeter trigger and µGMT and implements trigger algorithms that make a decision on whether or not to save each event. Most algorithms in the trigger menu are based on the presence of physics objects passing various quality, p_{T}, and $|\eta|$ thresholds. There also exist more complex algorithms such as those for selecting vector boson fusion events, low mass dimuon resonances, and leptonically tagged b jets. Triggers may also be prescaled, which means that only a fixed fraction of events passing the criteria are retained. The thresholds and prescale values for all triggers are determined

Table 2.1: Some representative unprescaled triggers of the CMS level-1 menu and corresponding thresholds. Each trigger has additional quality criteria that are not listed including isolation for leptons and photons. Threshold values from Ref. [163].

Trigger objects	Typical (p_{T}) threshold [GeV]
Single muon	22
Double muon	15, 7
Single electron/photon	28
Double electron/photon	22, 12
Single muon + single electron/photon	20, 10 or 7, 20
Single hadronic tau	120
Double hadronic tau	32, 32
Single muon + Single hadronic tau	18, 24
Single electron/photon + Single hadronic tau	22, 26
Single jet	180
Double jet	150, 150
Triple jet	95, 75, 65
$E_{\mathrm{T}}^{\mathrm{miss}}$	100
H_{T}	360
E_{T}	2000

in order to fit within the maximum 100 kHz level-1 trigger rate. By the end of 2018, the trigger menu included about 50 unprescaled triggers used for analysis, 100 unprescaled triggers with tighter criteria for backup, and 250 prescaled triggers used for monitoring, calibration, and other technical measurements. Table 2.1 lists some of the level-1 triggers and corresponding thresholds, while Figure 2.11 shows the approximate proportion of the level-1 100 kHz rate devoted to the highest rate triggers. The final level-1 trigger decision is provided to the TCDS system, which handles distribution of the trigger accept signal to all detector subsystems.

Several plots showing trigger efficiency for common physics objects are shown in

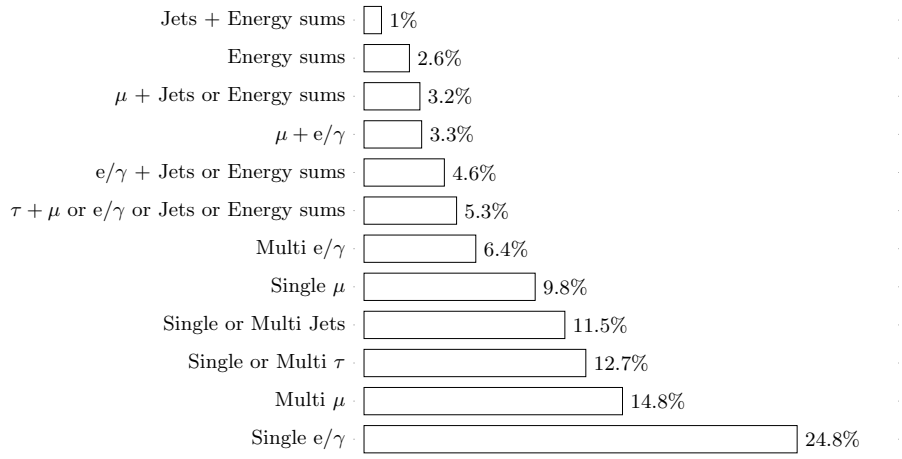

Figure 2.11: Fractions of the 100 kHz level-1 trigger rate allocated for different categories of triggers during typical Run 2 operation. Figure from Ref. [163].

Figure 2.12. Because the level-1 trigger uses a coarse reconstruction, the resolution is somewhat worse than for offline physics, which results in turn-on curves that are not very sharp in the corresponding offline values. The isolated muon and electron trigger plateau efficiencies are somewhat less than unity, though there exist additional triggers not shown in the figure that don't have the isolation requirements and instead have higher p_{T} thresholds in order to recover most of the remaining inefficiency at high p_{T}.

To maintain performance in the high pileup environment of the HL-LHC, the CMS level-1 trigger system is planned to be replaced before Run 4. Improvements to the detectors allow some tracking information as well as high granularity calorimeter information from both the barrel and endcap calorimeters to be provided as inputs to the level-1 trigger. Logic implemented on FPGAs on ATCA cards will be used to perform reconstruction, incorporating more complex algorithms including machine learning and

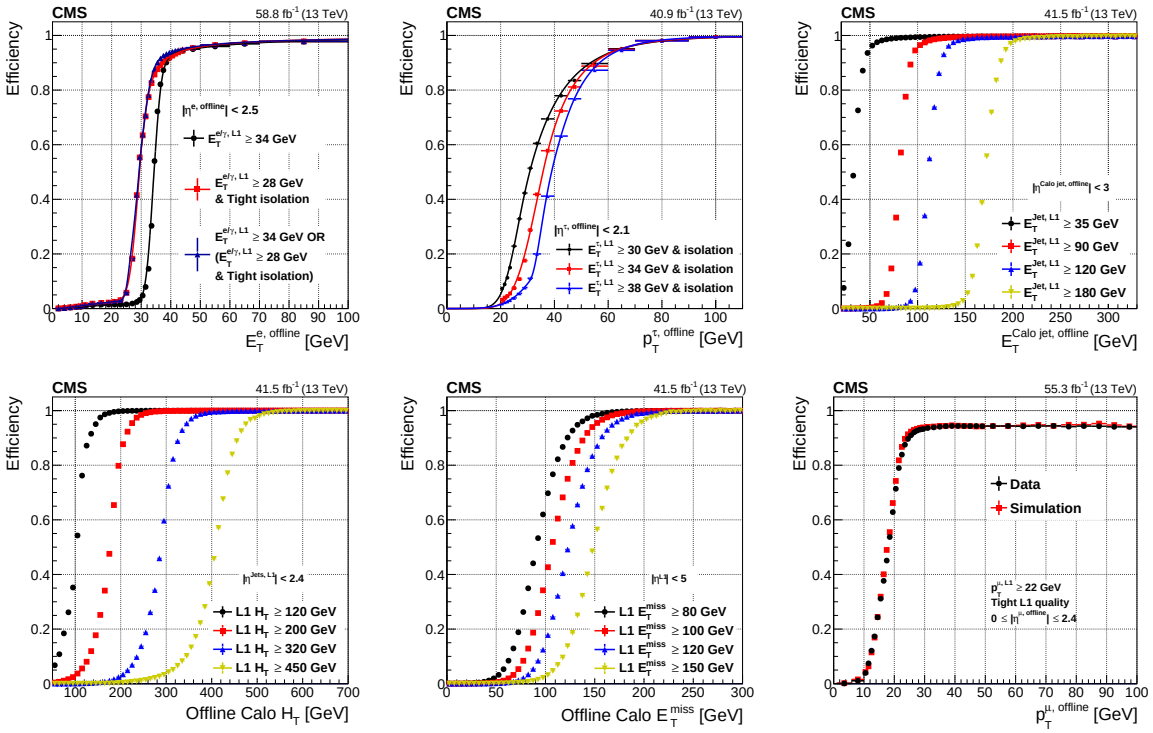

Figure 2.12: Level-1 trigger efficiency plotted against offline p_{T} or equivalent for isolated electrons/photons (top left), isolated hadronic taus (top middle), jets (top right), H_{T} (bottom left), $E_{\mathrm{T}}^{\mathrm{miss}}$ (bottom center), and isolated muons (bottom right). Figure from Ref. [163].

a version of the particle flow algorithm described in Section 2.3.3. Together with the increased allowed level-1 accept rate of 750 kHz and latency of 12.5 µs, the upgraded level-1 trigger will be able to maintain similar physics performance to the existing trigger in considerably more adverse pileup conditions.

Data acquisition system and HLT

The CMS DAQ system is responsible for receiving the data from all the subsystems when a level-1 accept is initiated, aggregating the data from all subsystems for a single event, reconstructing the event, implementing the software-based high-level trigger, and sending the resulting data to the CERN data center [189]. The original DAQ system was upgraded during LS1. The overall architecture of the current CMS DAQ system is shown in Figure 2.13. The DAQ system receives data from various front-end driver boards discussed previously such as the ECAL DCC and the AMC13. The data from the front-end drivers are received by front-end readout link cards and front-end readout optical link cards, and the data are transmitted through ethernet links with the TCP/IP protocol from the CMS service cavern to the counting room on the surface. The ethernet links are received by ethernet switches and subsequently by readout unit PCs. The readout units provide merged event fragments to builder unit PCs by way of a 56 Gb/s FDR Infiniband network that links all readout and builder units. This allows the second stage of event building to be performed with a single network, unlike the Run 1 DAQ system. A single builder unit receives all the fragments for a given event and writes the

assembled raw event data as files into its 250 GB RAM. Each builder unit is assigned several filter unit PCs, which are connected to the builder unit via an ethernet network and mount the builder unit RAM and hard drive via a network file system. This also differs from the original architecture, which combined builder and filter units into a single machine. The filter units run processes using the CMS software (CMSSW) framework that are used to perform event reconstruction in a manner similar but not identical to offline reconstruction. The new file-based interface between builder and filter units allows CMSSW to be decoupled from the online software. The filter units implement the high-level trigger and save events passing trigger criteria to their hard drives. The files on filter unit hard drives are copied back to builder unit hard drives and merged. Finally, the data are transferred to the CERN computing center for storage. The DAQ system can receive data at 200 GB/s in order to accommodate a 100 kHz level-1 trigger rate and event sizes up to 2 MB. The total data output that can be received and reconstructed at the CERN data center is about 1 GB/s, and subsequently, HLT thresholds are chosen to accept a total event rate for prompt reconstruction of about 1 kHz.

The reconstruction algorithms used by the HLT are described in Section 2.3 and provide physics objects such as electrons, photons, muons, hadronic taus, QCD jets, H_{T}, and $p_{\mathrm{T}}^{\mathrm{miss}}$. Table 2.2 shows thresholds for a few representative HLT triggers in 2018. Figure 2.14 shows HLT+L1 efficiency as a function of physics object p_{T} or equivalent for a few representative physics objects and triggers. Trigger efficiency is typically measured for each analysis as a function of the offline selection criteria used in that specific analysis. A

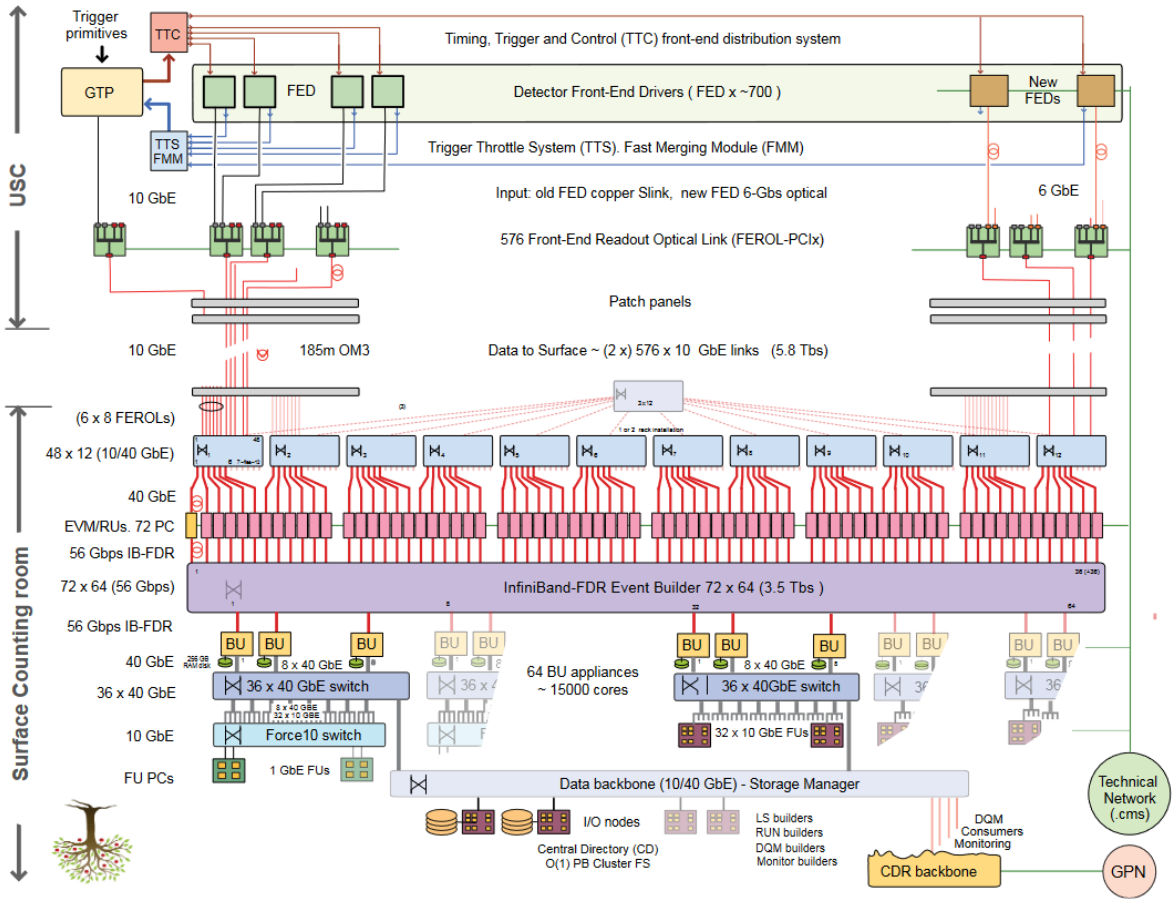

Figure 2.13: Architecture of the Run 2 CMS DAQ system described in the text. Figure from Ref. [189].

Table 2.2: Some representative unprescaled triggers of the CMS HLT menu and corresponding thresholds. Each trigger has additional quality criteria that are not listed including isolation for leptons and photons.

Trigger objects	Typical HLT (p_{T}) threshold
Single muon	27
Double muon	17, 8
Single electron	32
Double electron	23, 12
Single photon	110
Double photon	30, 18
Muon + electron	23, 12 or 12, 23
Single tau	180
Double tau	35, 35
Single jet	500
Single jet with substructure	400
Quad jet with 3b	75, 60, 45, 40
$p_{\mathrm{T}}^{\mathrm{miss}}$	120
H_{T}	1050

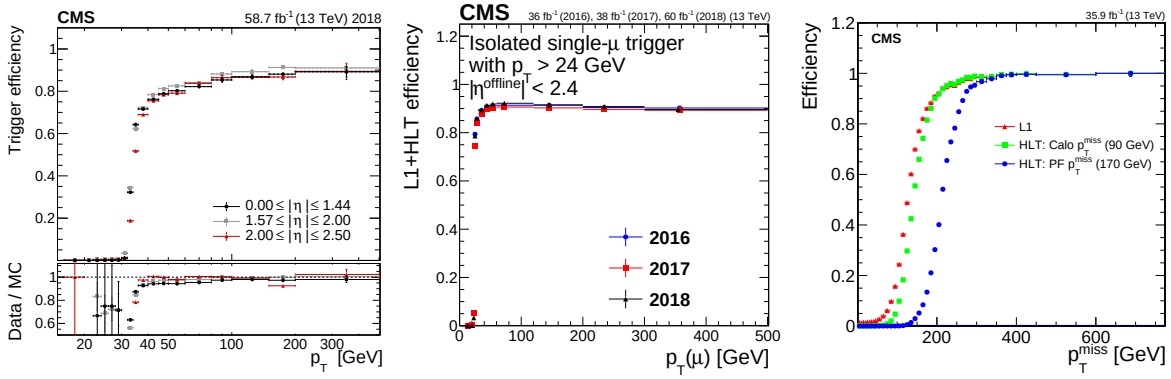

Figure 2.14: Combined level-1 and HLT efficiency plotted against offline p_{T} or $p_{\mathrm{T}}^{\mathrm{miss}}$ for the isolated single electron trigger with a threshold at 32 GeV (left) the isolated single muon trigger with a a threshold at 24 GeV (center) and $p_{\mathrm{T}}^{\mathrm{miss}}$ triggers including the level-1 trigger, a calorimeter $p_{\mathrm{T}}^{\mathrm{miss}}$ trigger with a threshold at 90 GeV, and a particle flow $p_{\mathrm{T}}^{\mathrm{miss}}$ trigger at 170 GeV. Figures from Refs. [172], [190], and [191] respectively.

description of trigger efficiency measurement for this analysis is provided in Section 3.3.4.

In addition to the normal data saved by the HLT, CMS employs two specialized

trigger strategies called data scouting and data parking. Data scouting allows analyses to target high rate final states by saving only high-level physics object information and discarding the raw detector data to reduce the size per event from around 1 MB to only a few kB. Data parking addresses the 1 GB/s limit of standard triggers set by the speed at which prompt reconstruction can be performed by not promptly reconstructing events. Data parking allows up to 5 kHz of additional events to be saved [192, 193].

For the HL-LHC, the CMS DAQ system will be completely replaced [194]. The new DAQ system will accept events at rates of up to 750 kHz to accommodate the level-1 trigger upgrades and maintain performance. The maximum output rate of the upgraded DAQ system is set to be 7.5 kHz. To meet this rate, the HLT reconstruction and selection will need to be improved, possibly using technologies such as heterogeneous computing with GPUs.

Other electronics and monitoring systems

The CMS TCDS system is responsible for distribution of clock and trigger signals and replaces the previous TTC system used before LS1. The central partition manager receives level-1 trigger accept signals as well as LHC clock signals. These signals are then distributed amongst local partition manager boards that translate the signals into the formats needed by each CMS subsystem, then provided to each subsystem via partition interface boards that fans out the signals to the subsystems. In addition, a trigger throttling mechanism is implemented whereby subsystems can provide trigger readiness

signals to the other TCDS boards via the partition interface boards [195].

The beam radiation, instrumentation and luminosity (BRIL) subsystems provide CMS with important information about the instantaneously luminosity, the radiation environment in the CMS cavern, and the status of LHC beams. The BRIL subsystem consists of many different detectors providing various information about beam and radiation conditions.

CMS features three detector systems for providing online measurements of luminosity: the fast beam conditions monitoring system (BCM1F), the pixel luminosity telescope (PLT), and the HF luminosity readout. The BCM1F was implemented as 24 single-crystal diamond sensors within the pixel volume. Before data taking in 2017, it was upgraded to 10 silicon sensors, 10 polycrystalline diamond sensors, and 4 single-crystal diamond sensors. The high time resolution of 6.25 ns is used to distinguish hits from collision products, machine-induced background, and collision-induced activation in order to provide luminosity measurements. The afterglow caused by collision-induced activation is measured and corrected [196, 197]. The Run 2 PLT was made of the silicon pixel sensors arranged into 16 three-layer telescopes outside the pixel endcap oriented so that tracks from the interaction point pass through the three layers. An online luminosity measurement is derived by assuming a Poisson distribution for the rate of triple coincidences [198]. Corrections for efficiency loss from radiation damage were applied offline [197]. The HF (μ)HTR boards also have a dedicated luminosity readout that is used for two HF rings in order to generate online and offline luminosity measurements. Either the fraction of

occupied towers or the sum of transverse energy is used to estimate the luminosity, after corrections for afterglow, noise, and aging. The HF luminosity readout is taken as the primary online luminometer. These three luminometers provide data to a special BRILDAQ system separate from the main CMS DAQ system to provide unbiased online luminosity measurements. They are calibrated using LHC van der Meer scans. Additionally, counting pixel clusters, primary vertices, or DT muon stubs detected by standard CMS subsystems can also provide luminosity estimates. The RAMSES radiation detector of the REMUS system described below also functions as a luminometer. The primary offline luminosity measurement was based on pixel clusters in 2016, and a combination of the luminometers in 2017 and 2018.

BRIL also operates a number of other detectors including the beam halo monitor (BHM), the beam conditions monitor for losses (BCML), the beam pickup timing for experiments (BPTX) system, and the HF radiation monitors. The BHM system uses quartz rods with PMTs situated on either side of CMS that detect the Cherenkov radiation produced by machine-induced background to measure the per-bunch crossing rate of beam halo particles. The BCML detectors are also located very close to the LHC beam line within the pixel volume and in the forward region near the TOTEM T2 detectors. During Run 1 and 2, the current produced by the BCML poly-crystalline diamond sensors was used to measure particle fluxes. Fluxes indicative of excessive beam loss trigger a beam abort signal to the LHC. The BPTX system uses button-electrode based detectors to provide precise measurements of incoming bunch timing. The HF radiation

monitors are a set of proportional chambers located at the periphery of the HF that monitor possible radiation damage to the detector. BRIL also previously operated the beam scintillation counter (BSC) during Run 1. Additionally, information from central LHC systems including the RadMon system that monitors radiation dose around the LHC ring, and the REMUS system that measures radiation dose in experimental areas are used by BRIL [199].

2.2.5 Offline computing

Once data have been recorded by the CMS experiment, the CMS offline computing systems must deal with manipulating the data samples and making them available to analyzers. The primary software framework used by the collaboration is called CMSSW and manipulates event data in the form of C++ objects. The CERN ROOT framework is used to write these objects into compressed binary files for storage [200]. Non-event data are stored in a separate CMSSW calibrations database. CMS event data are stored in several formats detailed below and managed by the worldwide LHC computing Grid (WLCG). The computing centers that make up the grid are organized in a hierarchical fashion into a Tier-0 computing center at CERN, a small collection of Tier-1 centers at national computing facilities in several countries, and additional Tier-2 and Tier-3 centers at member institutions. The total size of the event data stored by CMS, including both real and simulated samples, is about 500 PB [201].

Events selected by the HLT are sent to the Tier-0 CERN data center in several data

streams, including the physics data stream used for standard analysis, an express stream used for calibration and monitoring, and specialized streams such as a scouting stream and a parking stream. Most data provided to the Tier-0 are in RAW format, which consists of about 1 MB per event of raw detector data and some HLT information. At the Tier-0, the RAW data are written to tape, a copy is provided to a Tier-1 for backup, and prompt reconstruction is performed using the algorithms detailed in the next section. Each Tier-1 is responsible for holding a backup of part of the CMS data set and may also perform later reconstruction with improved algorithms or calibrations. The data format holding both raw detector data and reconstructed objects is called RAW/RECO and is about 2 MB per event.

Most analyses do not make use of raw detector data and as such, a smaller format without the raw data called analysis object data (AOD) consisting of about 500 kB per event was envisioned for analysis use. However, this size proved to be unwieldy and before Run 2, another format called MiniAOD was introduced. MiniAOD contains only particle-flow candidates (see Section 2.3.3), high-level physics objects, metadata, and selected truth information in the case of simulation in order to reduce the size per event to about 30 kB [202]. The NanoAOD format is smaller still, retaining only high-level physics objects, some metadata, and selected truth information in order to fit in a size of 1-2 kB per event. About 95% of analyses performed with Run 2 data used the MiniAOD or NanoAOD formats, and the NanoAOD format is envisioned to be usable by about 50-70% of analyses [203, 204]. A data certification process specifies which subsets of the

recorded data are usable for analysis. The samples used in this thesis were derived from the MiniAOD and NanoAOD formats.

In addition to real data, nearly all CMS analyses also use simulated samples. Monte Carlo generators are used to simulate proton-proton collisions and generate the outgoing particles, as detailed in Section 1.2.5. For most samples, the simulated particles are then translated into hits in the detector using a simulation of the CMS experiment in the GEANT4 program [205]. The hits are provided to a simulation of the CMS electronics, which then produces raw data like that recorded by the experiment. Pileup is addressed using a method called premixing, whereby separate pileup collisions are simulated in the same way, then the resulting electronics signals are combined with those of the event of interest [206]. The resulting raw data can then be reconstructed with the normal reconstruction algorithms. For some SUSY simulation, including some of the samples used in this analysis, the CMS custom FASTSIM program is used. The FASTSIM program accepts Monte Carlo generated particles as input, simulates physical effects such as curvature in the magnetic field, decays in flight, and particle-matter interactions, and builds reconstructed hits that are used in a modified version of the reconstruction algorithms described below [207, 208].

2.3 Object reconstruction

This section details the reconstruction of high-level physics objects from the basic information recorded by the CMS detector systems. The reconstruction used offline and

that used for the high-level trigger are very similar, though the differences are noted below. An important feature of CMS reconstruction is that the usage of the particle-flow (PF) algorithm, which performs reconstruction at the level of individual detected particles rather than composite physics objects such as jets [169].

2.3.1 Calorimeter clusters

When an electromagnetic shower is detected in the ECAL, the electrical pulse produced by the ECAL photosensors is shaped, amplified, digitized, and sampled. The sampled data are then read out if the digitized signal passes a zero suppression threshold or is selected for full readout by the ECAL selective readout. In software, pedestal-subtracted ADC counts are transformed into an amplitude by the multifit method described in Ref. [209] to mitigate the effects of pileup. For high amplitude signals in the EB, the effects of pileup are negligible, and a simple maximum amplitude method is used. The ADC amplitude is converted into an energy by a conversion factor and various correction factors [210]. Another algorithm reconstructs the arrival time of the energy deposit using an assumed pulse shape [211]. Spikes caused by particles interacting with the photodiodes are rejected based on topological criteria and timing [212], and an energy threshold is applied to reduce noise. Finally, the energy and timing information are stored as an ECAL reconstructed hit. For the endcap preshower, the ADC counts in three time samples are summed with predetermined weights to extract the amplitudes, which are then similarly used to build reconstructed hits [213]. Nonlinearities in calorimeter response

are corrected at the physics object level.

The output of the HCAL photodiodes in the HB and HE is similarly digitized using a charge integrator and encoder chip that provides ten (prior to 2018) or eight (in 2018) time samples to be read out. Readout is only performed for channels with two samples above a fixed threshold. In 2016 and 2017, reconstruction of pulse amplitude was performed differently at HLT and offline. After subtracting the electronic pedestal, both algorithms performed a fit of three pulses to the shape, but the HLT algorithm assumed fixed arrival times and used only three time samples [214]. Starting in 2018, the same algorithm was used for both HLT and offline. This algorithm is similar to the previous offline algorithm except that it supports more pulses and uses the faster non-negative least squares algorithm to perform the fit [215]. In the HF, the entire digitized pulse from the photomultiplier tubes is contained in one time sample and the amplitude is directly extracted. In the HO, the effects of pileup are minimal and the amplitude is extracted assuming a single pulse. The amplitude is then converted to an energy, noise from spurious electronics signals are subtracted, and corrections are applied to generate an HCAL energy, which is stored with timing information as a reconstructed hit [214]. Nonlinearities in calorimeter response are again corrected at the physics object level.

Calorimeter reconstructed hits are grouped into topological clusters by identifying cells with energy above the seed threshold and all adjacent cells, then iteratively adding cells adjacent to the cluster with energy above the cell thresholds discussed in Section 2.2.2. The seed threshold energy, which sets the minimum topological cluster energy,

is 230 MeV for the EB, 600 MeV for the EE (with an additional requirement of 150 MeV of transverse energy), 800 MeV for the HB, 1100 MeV for the HE, and 0.12 MeV for the endcap preshower system. From the topological cluster, individual clusters are formed by fitting a Gaussian-mixture model that assumes the topological cluster is formed from some number of overlapping Gaussian energy deposits. This procedure is used for ECAL and HCAL deposits excluding HF, for which each cell is directly turned into an electromagnetic or hadronic cluster. The energy of purely electromagnetic clusters is calibrated based on simulated photons, and the mean reconstructed energy reaches an accuracy of $\pm 1\%$ measured in data. The energy of hadronic energy deposits in both the ECAL and HCAL are similarly calibrated using simulated K_L^0's, and the mean reconstructed energy reaches an accuracy of about 10–25% that is worst for hadrons with momenta near 10 GeV [169].

Electromagnetic clusters with energy above about 1 GeV are then used as potential seeds for superclusters, which are formed by aggregating clusters in an extended ϕ window around the seed. These superclusters are used to account for the large spread of photons produced by electron bremsstrahlung as the electron's trajectory is curved by the CMS solenoid [172].

2.3.2 Tracking

Muon detectors

The electrical pulse produced by a muon traversing a DT cell is digitized by a time-to-digital converter and read out. The time can be corrected for various delays in the detector system and combined with the drift velocity to determine the distance between the anode wire and the point at which the muon passed through the cell, which is saved as a reconstructed hit [182].

A muon passing through a CSC induces current pulses on both the anode wires and cathode strips, which are respectively transformed into step pulses and digitized samples by the anode and cathode front-end boards. All AFEB data for an appropriate time window as well as CFEB data from CFEBs corresponding to local charged tracks is read out upon a level-1 trigger accept. In software, the digitized cathode pulses are corrected for electronic pedestal, noise, cross-talk, and gain and combined with anode data to build reconstructed hits containing both position and timing data [186].

Pulses on RPC strips produced by muons are amplified and a simple zero-crossing discriminator is used to generate a fixed pulse, which is recorded upon data read out. Adjacent strips with pulses are clustered together and the centroid of the strips is used to generate a reconstructed hits.

In DTs and CSCs, reconstructed hits are fit with straight lines to form muon track segments. For DTs segments, the time associated with reconstructed hits is also used to reject reconstructed hits created by muons from other bunch crossings and non-muon

background. Groups of CSC or DT segments are then used as seeds for a Kalman-filter based fit that builds tracks in the muon system called standalone-muon tracks [182].

Inner tracker

In the inner tracker, tracking begins with the zero-suppressed measurements from the pixel readout chips, which are digitized by the pxFED, and the measurements from the silicon strip front-end ASICs, which are digitized and filtered for zero-suppression by the silicon strip FED. These measurements are part of the raw data collected by the DAQ system. In software, adjacent pixels and strips with charges well above background levels are then grouped together to form clusters. Pixel clusters are translated into reconstructed hits using the charge measured the ends of the cluster when performing track finding or using a more accurate template based method for the final track fit. Strip clusters are translated into reconstructed hits using the charge weighted average of strip positions, subject to corrections. The efficiency for a hit being generated by a charged particle away from detector boundaries is well over 99% excluding defective pixels and strips, though efficiency decreases with luminosity [216].

Initially, the CMS tracker was designed primarily for measuring the momentum of isolated tracks such as muons, identifying hadronic tau decays, and tagging b-jets [217]. However, with the adoption of the particle-flow algorithm, the scope was expanded to the reconstruction of all charged particles. To efficiently reconstruct real particle tracks while keeping spurious tracks to a minimum, CMS iteratively applies a combinatorial track

finding algorithm, where each iteration relaxes quality requirements but employs more complex tracking procedures based on the Kalman Filter (KF) algorithm [216,218]. After each iteration, hits used to construct tracks are masked, which reduces the combinatorics sufficiently for later iterations. The first three iterations are seeded with triplets in the pixel detector, which results in high quality tracks. The fourth and fifth iterations focus on tracks with missing hits in the pixel detector, while the sixth and seventh focus on highly displaced tracks. The eighth iteration focuses on tracks inside jets, and the ninth and tenth iterations focus on muons using muon detector information for seeding. Displaced tracks with a common secondary vertex are linked for later use. The offline algorithm provides an efficiency of above 90% for tracks between 1 and 10 GeV and a misreconstruction rate below 3.5% in the same range, as shown in red in Figure 2.15. The algorithm can reconstruct tracks down to a p_{T} of about 200 MeV, well below the 700 MeV threshold required to reach the barrel calorimeters. The remaining inefficiencies stem primarily from particles that undergo interactions within the tracker volume, which are expected to occur somewhat regularly, as shown in Figure 2.5. The high rate of misreconstructed tracks with high p_{T} is addressed in the particle-flow algorithm described below with calorimeter and muon system information. The impact parameters d_{xy} and d_z of a track are the distance between a track and a vertex in the x-y plane and along the z axis, respectively. The reconstructed tracks have a typical p_{T} resolution of 1–2% and typical d_{xy} and d_z resolutions of 100-200 µm for central tracks, as shown in Figure 2.16.

Electron tracking is performed by a dedicated algorithm. Tracking seeds are first

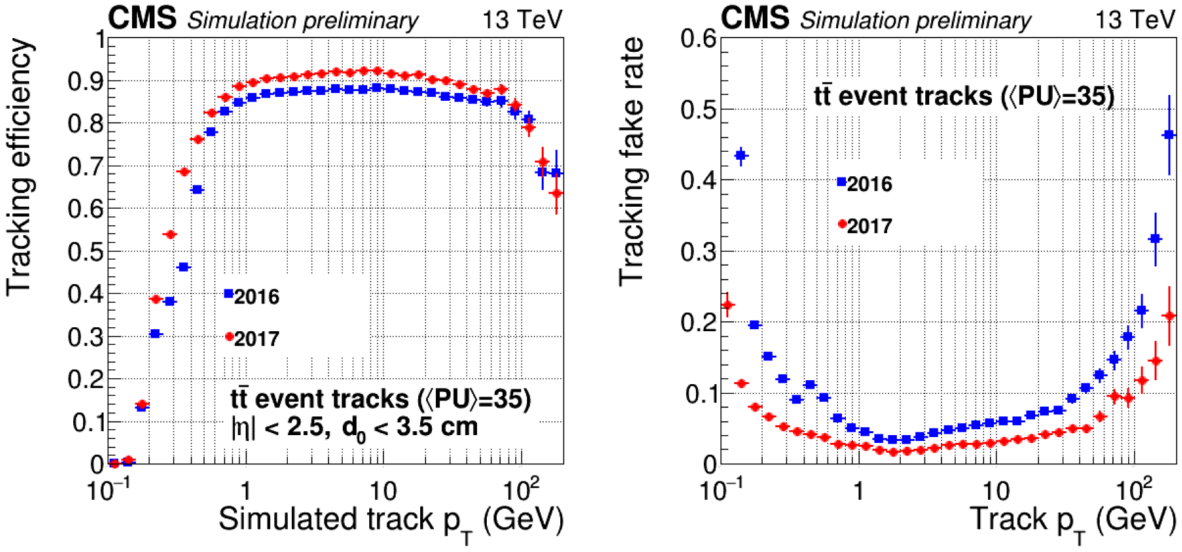

Figure 2.15: Simulated efficiency (left) and misreconstruction rate (right) of the CMS tracking algorithm as a function of track p_{T} for a relatively inclusive set of tracks with $|\eta| < 2.5$. Performance for the original tracker is shown in blue, while that after the 2016/2017 pixel upgrade is shown in red. Figure from Ref. [219].

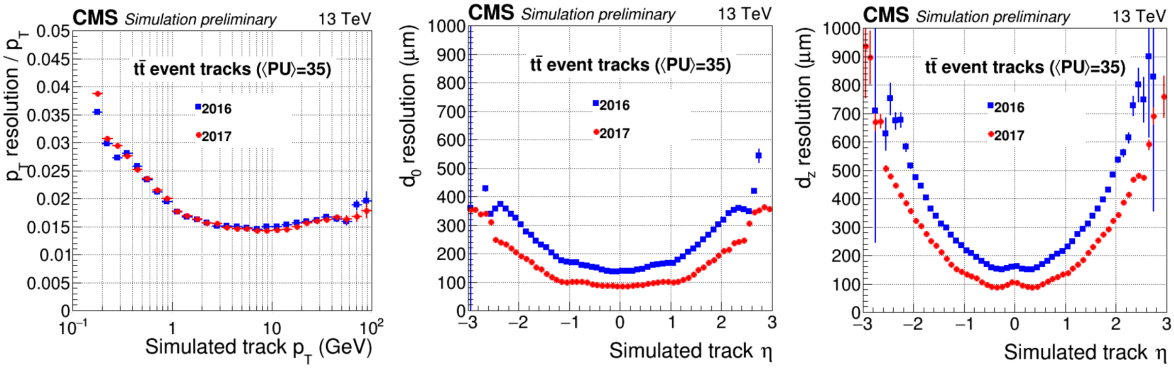

Figure 2.16: Track p_{T}, d_{xy} (denoted d_0), and d_z resolution as a function of track p_{T}, η, and η respectively. Performance for the original tracker is shown in blue, while that after the 2016/2017 pixel upgrade is shown in red. Figure from Ref. [219].

selected, either by inferring the location of pixel hits from an ECAL supercluster, by finding a track constructed with the normal tracking algorithm together with an ECAL cluster of compatible energy, or by selecting tracks with poor fits or missing hits that are considerably improved using a five component Gaussian sum filter (GSF) [220] fit that can better account for bremsstrahlung. These seeds are then refit with a more complex twelve component GSF track. This procedure drastically improves electron track reconstruction efficiency from about 50% to over 80% for 30 GeV electrons. For isolated electrons, the efficiency is about 96%, as shown in Figure 2.22. At the HLT level, electron tracking is based only on seeding from an ECAL supercluster with compatible pixel hits. Furthermore, the HLT electron GSF tracks are not provided to the particle-flow algorithm detailed below and electrons are instead reconstructed independently as described in Section 2.3.8 [172].

Muon tracks are classified into three types. The standalone muon tracks discussed above are compared with tracks in the inner tracker, and compatible tracks are combined into global muons. Standalone muons with no compatible track in the inner tracker are left as is. Finally, tracks in the inner tracker with $p > 2.5$ GeV and $p_{\mathrm{T}} > 0.5$ GeV are extrapolated to the muon system, and promoted to tracker muon tracks if at least one matching muon segment is found, which improves the acceptance for low momentum muons. Only global and tracker muons are directly passed on to the link algorithm described below. About 99% of muons produced in geometrical acceptance of the muon system are reconstructed as a global or tracker muon [169]. Muons with $p_{\mathrm{T}} \gtrsim 200$ GeV

will start to have significant energy loss through radiation, causing showers that can confound standard muon reconstruction. Three special algorithms for fitting high momentum muons that can omit stations with poor or inconsistent reconstruction are employed, and the best fit is selected [221].

Since tracking is by far the most time consuming part of reconstruction, a modified version of the iterative tracking is performed at HLT where only three iterations are used and low p_{T} and highly displaced tracks from nuclear interactions are not considered. Furthermore, tracking is only performed on demand, typically in the vicinity of a physics object reconstructed with other subsystems. This allows particle-flow style tracking to be used in HLT reconstruction while meeting the stringent time constraints.

2.3.3 Particle flow candidates

After reconstructing tracks and calorimeter clusters, these elements are combined to reconstruct individual particles, also called particle-flow (PF) candidates. This process begins with a link algorithm, which associates nearby elements into PF blocks. A track is extrapolated to the calorimeters and linked with calorimeter deposits if it is inside or near the cells containing the calorimeter deposit. If multiple tracks are linked to a single calorimeter deposit or multiple calorimeter deposits are linked to a single track, only the shortest link is considered. For GSF tracks, calorimeter clusters compatible with bremsstrahlung photons as well as pairs of tracks consistent with converted bremsstrahlung photons are linked to the GSF track. Preshower, ECAL, and HCAL

clusters are linked when the more granular cluster is within the envelope of the less granular one, again subject to the constraint that only one preshower-ECAL or ECAL-HCAL cluster link is retained per preshower and ECAL cluster respectively. ECAL clusters are linked with superclusters if they contain at least one cell in common. Finally, tracks can be linked together if they share a common secondary vertex, at most one of the tracks is incoming, and the invariant mass of the outgoing tracks is at least 0.2 GeV. Once the link algorithm has formed PF blocks, the particle-flow algorithm iteratively attempts to form PF candidates from the blocks until all blocks have been processed by sequentially following the steps below.

First, the PF algorithm attempts to build muons from PF blocks. Isolated muons whose p_{T} exceeds ten times that of the p_{T} and E_{T} of tracks and calorimeter clusters within ΔR of 0.3 are selected with no further requirements. For nonisolated muons, candidates are first selected if they possess at least three segments in the muon chambers or the linked calorimeter deposits are consistent with muon energy deposition. The muons that fail this selection can still be selected if the standalone muon track is high quality or the inner tracker track is high quality and the calorimeter deposit is relatively consistent with muon energy deposition. The momentum for the muon candidates is taken to be the inner track momentum if the muon p_{T} is less than 200 GeV, or the refit momentum described above for higher momentum muons. After muons are built, the associated elements are masked from the PF blocks.

Next, the PF algorithm attempts to construct electrons and isolated photons. Elec-

trons are seeded by GSF tracks while photons are seeded by ECAL superclusters with $E_{\mathrm{T}} > 10$ GeV and no associated GSF track. The seeds are expanded by including ECAL clusters linked to the associated supercluster, ECAL deposits and photon conversion tracks tangent to the GSF track, and tracks linked to these ECAL deposits that are consistent with the electron hypothesis. The total energy measured in HCAL cells within ΔR of 0.15 of such a candidate is required to be less than 10% of the supercluster energy. A multivariate discriminator and requirements on shower shape and HCAL to ECAL energy ratio are respectively used to determine whether or not retain the electron and photon PF candidates. After applying a correction, the energy of all associated clusters is taken as the energy of a photon candidate, and this corrected total energy is combined with GSF track information to derive the four-momentum of the electron candidate. All tracks and clusters used in electron and isolated photon reconstruction are then masked against further use. For reconstruction at the HLT, electrons and isolated photons are reconstructed independently of the particle flow algorithm. Nonisolated HLT electrons are reconstructed in the same way as nonisolated photons as detailed below.

Remaining calorimeter clusters that are not linked to tracks are processed next. First, all such ECAL clusters within tracker acceptance are promoted to photon candidates and then all unlinked HCAL clusters within tracker acceptance are promoted to neutral hadron candidates. Outside of tracker acceptance in the endcap, HCAL cluster and any linked ECAL clusters are promoted to hadron candidates, while unlinked ECAL clusters are promoted to photon candidates. In the HF, electromagnetic clusters and

hadronic clusters are directly added as HF photons and HF hadrons. After the clusters with no track links are masked, only HCAL clusters with track links and possibly ECAL cluster links remain. If the combined calorimetric energy is compatible with the track momentum, the clusters and tracks are promoted to a charged hadron candidate whose momentum are determined by a fit to tracker and calorimeter measurements. If the calorimetric energy significantly exceeds the track momentum, the linked elements are split into a charged hadron candidate with a momentum determined by the track, and a photon candidate with momentum set by the excess energy and the measured ECAL cluster energy. Any remaining excess, if greater than 1 GeV, is added as a neutral hadron candidate. If the track momentum significantly exceeds the calorimetric energy measurement, remaining global muons with a momentum uncertainty of 25% or less are promoted to muon candidates and masked, then tracks are sorted in order of p_{T} uncertainty and masked until the tracker momentum is compatible with or less than the calorimetric energy.

When two PF candidates are linked by creation at a secondary vertex in the detector, they are replaced by a single hadron PF candidate whose momentum is set by the secondary particles or a combination of the secondary particles and an incoming track if one exists. This step is skipped for HLT reconstruction as tracks from nuclear interactions are not reconstructed.

Finally, a post processing step is performed with the constructed PF candidates. First, cosmic ray muons are rejected by removing muons whose trajectories are more

than 1 cm from the beam axis if the $p_{\mathrm{T}}^{\mathrm{miss}}$ is reduced by at least half when the muon is removed. Second, muons with $p_{\mathrm{T}} > 20$ GeV are reviewed if the available estimates of their momentum show a large discrepancy. If there is an estimate that reduces the $p_{\mathrm{T}}^{\mathrm{miss}}$ by at least half, then the lowest estimate of the muon momentum is taken. Next, charged hadron punch through misidentified as muons is corrected by combining nearby muons and neutral hadrons if their energy and momentum are each greater than 100 GeV and the $p_{\mathrm{T}}^{\mathrm{miss}}$ is decreased by at least half. Finally, muons and nearby neutral hadrons that are misreconstructed as a single charged hadron are restored by changing charged hadrons into a muon and a neutral hadron if the $p_{\mathrm{T}}^{\mathrm{miss}}$ is reduced by half [169].

2.3.4 Vertex reconstruction

CMS data taking runs are split into "lumi sections" during which the LHC beam conditions are approximately constant. For a given lumi section, the center of the beam spot in the transverse plane and its slope are first determined using a fit that exploits the correlation between the transverse impact parameter d_{xy} and the azimuthal angle ϕ of tracks in the lumi section. After primary vertices are reconstructed as described below, primary vertices and associated tracks are used to determine to the position of the beam spot along the z axis and its spread. The size of the beam spot is typically on the order of 20 µm in the transverse directions and 5 cm in the z direction and grows over time for a given fill.

Reconstruction of the primary vertices of proton-proton collisions begins with select-

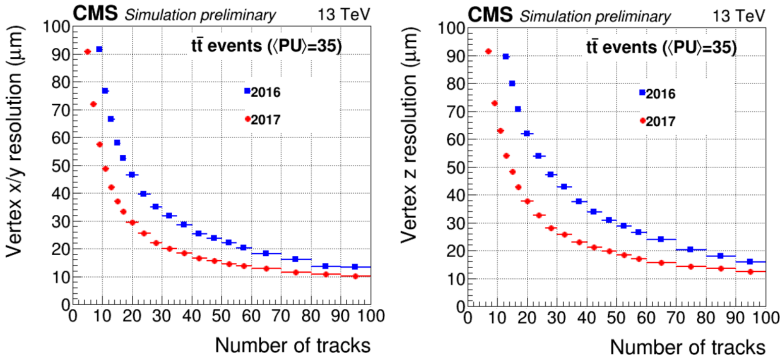

Figure 2.17: Vertex resolution in the x-y plane (left) and along the z axis (right) as a function of associated track multiplicity. Performance for the original CMS tracker is shown in blue and that for the tracker after the 2016/2017 pixel upgrade in red. Figure from Ref. [219].

ing tracks whose transverse impact parameter is consistent with the beam spot and pass a number of quality criteria. The z coordinate of each track is computed at the closest point of the track to the center of the beam spot, then a deterministic annealing algorithm is used to cluster tracks together into vertices based on their z positions. After the vertices are determined, another fit is performed to associated tracks in order to extract the position of the vertex in three-dimensional space. Reconstruction efficiency is near 99.9% for vertices with at least 3 tracks. Vertex spatial resolution is highly dependent on track multiplicity, and decreases from being on the order of 100 μm to less than 50 μm in each coordinate as the track multiplicity is raised from 5 to 20 as shown in Figure 2.17. At the HLT level, primary vertices are reconstructed using tracks constructed from pixel triplets and grouped based on their z-coordinate using a simpler gap clustering algorithm [216].

After the jet clustering described in the next section is performed, the primary vertex with highest sum of jet p_{T}^2 is taken as the primary vertex of interest for the collision and additional requirements on the displacement of this primary vertex from the center of

the detector are typically imposed.

2.3.5 Jet reconstruction

As described in Section 1.2.3, a jet is a cluster of high energy particles created by the hadronization of a quark or gluon from the hard scattering process. The CMS experiment most commonly reconstructs jets by clustering particle-flow candidates using the anti-k_{T} algorithm [222], as implemented in the FASTJET package [223] with a radius parameter of $R = 0.4$ or $R = 0.8$ [149]. Jets clustered with $R = 0.4$ will be referred to as "jets" or "AK4 jets," while jets clustered with $R = 0.8$ will be referred to as "fat jets" or "AK8 jets."

The anti-k_{T} algorithm belongs to the generalized k_{T} class of jet-clustering algorithms that combine a set of physics objects into aggregate jets as follows. First, all charged particle-flow candidates associated to the primary vertex of interest as well as all neutral particle flow candidates are considered in the set of objects to cluster. Distance measures d_{ij} and d_{iB} are defined for each pair of objects as well as for each object by itself. The algorithm then recursively selects the objects i and j (particle flow candidates or aggregate objects) with the lowest distance measure d_{ij} and combines them into a single aggregate object. If d_{iB} is the lowest distance measure, object i is considered a jet and

removed from further combination. The equation

$$\begin{aligned} d_{ij} &= \min(p_{\mathrm{T}i}^{2p}, p_{\mathrm{T}j}^{2p}) \frac{(y_i - y_j)^2 + (\phi_i - \phi_j)^2}{R^2} \\ d_{iB} &= p_{\mathrm{T}i}^{2p} \end{aligned} \tag{2.4}$$

gives the distance measures used by generalized k_{T} algorithm family, where $p_{\mathrm{T}i}$, y_i, and ϕ_i are the transverse momentum, rapidity, and azimuthal angle of particle i. The anti-k_{T} algorithm corresponds to $p = -1$ and thus aggregates harder particles first. This makes it less susceptible to contributions from pileup and underlying event than the Aachen-Cambridge algorithm ($p = 0$) and the k_{T} algorithm ($p = 1$). The efficiency for reconstruction a 30 GeV QCD jet within detector acceptance as an AK4 jet is essentially unity.

Within CMS, there are two commonly used algorithms to deal with possible contamination of jets from pileup and underlying event. The first is called charged hadron subtraction (CHS), which entails explicitly excluding charged particle flow candidates associated to other primary vertices and then applying a momentum correction determined using the jet area and average energy density in the event to cancel the contribution of other pileup and the underlying event [148, 224]. Specifically, the offset energy density ρ is calculated as the median energy per η–ϕ area in a grid of η–ϕ cells while the jet area A is calculated as the η–ϕ area in which infinitely soft "ghost" particles would be clustered into a given jet. The multiplicative correction factor applied to the uncorrected energy

is then

$$C(p_{\mathrm{T,uncorr}}, \eta, A, \rho) = 1 - \frac{[\rho_0(\eta) + \rho\beta(\eta)(1 - \gamma(\eta)\log(p_{\mathrm{T,uncorr}}))]A}{p_{\mathrm{T,uncorr}}}, \tag{2.5}$$

the form of which is chosen to match the known η and p_{T} dependence of pileup energy corrections. The coefficients $\rho_0(\eta)$, $\beta(\eta)$, and $\gamma(\eta)$ are set so that the average difference in p_{T} of jets in simulation with and without pileup overlaid is 0. The average pileup contribution to jet energy in simulation and data is also estimated by taking zero-bias data consisting of soft collisions and clustering jets in randomly placed cones covering η–ϕ space. The energy in these cones is another estimate of pileup energy and the ratio of the average offset correction with this random cone method in data to simulation parametrized in η is used as an additional correction for data. The uncertainty from pileup subtraction is taken as 30% of the difference between the simulated particle-level correction and the random cone-based correction, though this is indirectly used after being propagated through other corrections as detailed below.

In contrast, the pileup per particle identification (PUPPI) [225,226] algorithm consists of assigning a shape α_i defined by

$$\alpha_i = \log \sum_{j \neq i, \Delta R_{ij} \leq 0.4} \left(\frac{p_{\mathrm{T}j}}{\Delta R_{ij}}\right)^2 \begin{cases} |\eta_i| < 2.5 & j \text{ are charged particles from the primary vertex} \\ |\eta_i| > 2.5 & j \text{ are all particles} \end{cases} \tag{2.6}$$

to each neutral particle flow candidate i. Particles with smaller α_i are more pileup-like.

Neutral particles are weighted by calculating an approximate χ^2 using the distribution of α for charged pileup and evaluating the cumulative distribution function for a one degree of freedom χ^2 distribution. No further correction is made, though an uncertainty is derived by comparing the truth energy without pileup and the reconstructed energy of PUPPI jets in simulation. In this analysis, AK4 jets are constructed using the CHS algorithm while AK8 jets are constructed using the PUPPI algorithm.

After CHS/PUPPI corrections, additional jet energy corrections (JECs) are applied to calibrate the jet energy scale (JES) and jet energy resolution (JER) [148]. The JES corrections attempt to compensate for bias in the measurement of jet energy. Corrections for detector response parametrized in p_{T} and η are derived by comparing the true jet energy with the reconstructed energy in a QCD multijet simulated sample.

After the simulated response corrections are applied, small residual corrections for data are derived in data samples. First, corrections to make response uniform in η are derived by using QCD dijet events and assuming that any average observed $\vec{p}_{\mathrm{T}}^{\,\mathrm{miss}}$ aligned with the tag jet's p_{T} comes from a bias in jet energy scale. This is called the missing transverse momentum projection fraction (MPF) method. Corrections for the presence of other soft ISR and FSR jets and simulated jet energy resolution, which enters in the soft jet correction, are applied, and the η-dependent corrections are extracted with the assumption of possible logarithmic p_{T} dependence. Second, η-independent or absolute jet energy scale corrections are derived from $\mathrm{Z} \to \mathrm{e}^{+}\mathrm{e}^{-}$+jet, $\mathrm{Z} \to \mu^{+}\mu^{-}$+jet, γ +jet, and QCD multijet events. The QCD multijet sample is used in order to derive corrections for

high p_{T} jets recoiling against several lower p_{T} jets. A p_{T} balance method in which the probed jet's p_{T} is assumed to match that of the recoiling system, the Z, γ, or other jets is used along with the MPF method. A correction is applied to account for ISR and FSR jets not considered in the recoiling system and both the p_{T} balance and MPF methods are fit simultaneously to constrain biases from underlying event and out-of-cone showering that affect the two methods differently. The final fit allows a p_{T} dependence proportional to the single pion response of the calorimeters and includes systematic uncertainties from the uncertainties on the momentum of the recoiling system, residual ISR and FSR contributions, pileup, and possible double counting of corrections applied to electron and photon physics objects for the MPF method.

After jet energy calibration, the following sources of systematic uncertainty [148, 227] are taken and propagated to the analysis level as described in Section 4.3.

- The pileup uncertainties discussed above are propagated through the η-dependent correction using the dijet sample and the result is taken as a JES uncertainty.

- The pileup uncertainties are also propagated through the absolute correction using Z +jet, γ +jet, and multijet samples and the result is taken as another JES uncertainty.

- The data/simulation scale disagreement for pileup corrections is taken as a JES uncertainty.

- Uncertainties on the ISR+FSR correction process for the η-dependent corrections

are evaluated using a HERWIG++ simulated sample and comparing the reconstructed and true responses.

- The statistical uncertainty on the ISR+FSR correction is also propagated to a jet energy scale uncertainty.

- Uncertainties on jet energy resolution on the η-dependent corrections are propagated from the jet energy resolution uncertainties discussed below.

- Uncertainties on the parametrization of p_{T} dependence in the η-dependent corrections are taken by taking half the difference between the nominal corrections and p_{T}-independent ones.

- The statistical uncertainty in determining the η-dependent corrections are propagated to uncertainties in the JES.

- In addition to the nominal MPF method for determining η-dependent corrections, a p_{T}-balance method is also used and the difference between the two is taken as an uncertainty.

- η-dependent corrections are also evaluated in Z +jet and $\boldsymbol{\gamma}$ +jet samples and compared to the nominal dijet derived correction to produce an uncertainty.

- Uncertainties in the p_{T} scale of the Z or $\boldsymbol{\gamma}$ reference system are propagated to JES uncertainties.

- Since the absolute corrections allow p_{T} dependence proportional to the single pion calorimeter response, a $\pm 3\%$ difference in ECAL single pion response is propagated to the JES uncertainties.

- Similarly, a $\pm 3\%$ difference in HCAL single pion response is propagated to the JES uncertainties.

- The statistical uncertainties on the samples used to derive the absolute corrections are also taken as a source of JES uncertainty.

- Bias in the MPF absolute corrections from neutrino production are evaluated from the electron and muon energies in jets while bias from activity outside detector acceptance is evaluated from phase space constraints on particles outside detector acceptance.

- JES uncertainty from jet fragmentation are taken from a comparison of Pythia and Herwig++ simulation.

- The change in detector response over time is encoded in an uncertainty by comparing the corrections derived per data-taking epoch and that across an entire year of data taking.

- Finally, uncertainties due to different responses for different jet flavors are evaluated by comparing Pythia and Herwig++ simulated samples. The uncertainties for each flavor weighted to the flavor composition of QCD multijet events are combined to yield an overall uncertainty.

After JES corrections are applied, it is observed that simulated jets have better resolution than those in data. The jet energy resolution is measured in simulation and data using momentum balance in dijet and γ +jet events as for the JES corrections. Rather than the average response, the targeted variable is instead the width of the response distribution, which has contributions from jet energy resolution as well as soft FSR and ISR, out-of-cone radiation, underlying event, and photon energy resolution for γ +jets events. The JER is measured in data and simulation with other effects corrected and propagated as systematic uncertainties along with those from pileup, parametrization, non-Gaussian tales, event contamination, flavor uncertainties, and jet energy resolution. The jet four-momentum in simulation for jets matched to truth jets is multiplied by a correction factor $1-(s-1)(p_{\mathrm{T}}-p_{\mathrm{T,truth}})/p_{\mathrm{T}}$ where s is the data over simulation resolution scale factor. For jets not matched to truth jets, the four-momentum is multiplied by a factor $1+N\sqrt{\max(s^2-1)}$ where N is a random number sampled from a Gaussian distribution with zero mean and variance equal to that of simulated p_{T} resolution. Uncertainties in jet energy resolution are propagated to the final analysis as detailed in Section 4.3.

Typical jet energy resolution is on the order of 15–25% for jets with p_{T} of 30 GeV and decreases with increasing p_{T} as shown in Figure 2.18, which shows jet energy resolution in simulation. Jet energy resolution can be expressed in the form

$$\left(\frac{\sigma_{p_{\mathrm{T}}}}{p_{\mathrm{T}}}\right)^2=\left(\frac{N}{p_{\mathrm{T}}/(1\ \mathrm{GeV})}\right)^2+\left(\frac{S}{\sqrt{p_{\mathrm{T}}/(1\ \mathrm{GeV})}}\right)^2+C^2, \tag{2.7}$$

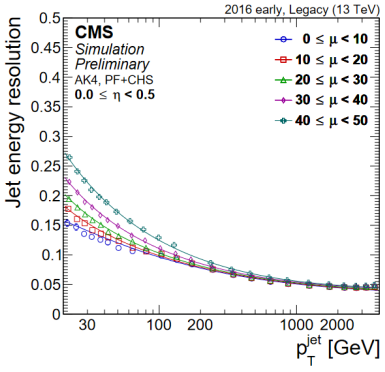

Figure 2.18: Jet energy resolution in simulation for CHS particle flow jets in the central region as a function of jet p_{T}. The different colors correspond to different levels of pileup, which affects jet energy resolution at low p_{T}. Figure from Ref. [229].

with coefficients N, S, and C for the noise, stochastic, and constant terms in analogy with calorimeter energy parametrization. The dominant contribution to N is pileup, which yields a coefficient of about 400% for AK4 jets at pileup 50, thus dominating resolution at jet p_{T} below about 30 GeV. The S coefficient is about 80%, much larger than the 40% energy resolution of the jet constituents, because it is dominated by particle flow confusion [228]. Above about 400 GeV, the constant coefficient C, which is set by detector resolution, becomes dominant. Neither S nor C have large dependence on pileup [169].

The mass of a jet can be defined as the invariant mass of its components. In contrast to light quark and gluon jets, whose mass arises primarily from parton branching, single jets formed from the decay of a heavy particle typically have a mass near that of the decaying particle due to kinematics [230, 231]. For this reason, an alternative definition of jet mass called the "soft-drop" mass is employed [230, 232]. The soft-drop mass is calculated by removing soft particles from the jet using the soft-drop algorithm with $\beta = 0$, also known as the modified mass drop tagger. The jet in question is recursively

declustered using the Cambridge-Aachen algorithm and the softer of the two declustered objects is removed until the condition

$$\frac{\min(p_{\mathrm{T}1}, p_{\mathrm{T}2})}{p_{\mathrm{T}1} + p_{\mathrm{T}2}} < z_{\mathrm{cut}}, \tag{2.8}$$

with $z_{\mathrm{cut}} = 0.1$, is no longer fulfilled [149]. This procedure has the effect of enhancing the heavy resonance mass peak relative to jets from single quarks and gluons and also removes some contribution from pileup and underlying event. In the analysis described in this thesis, the soft-drop mass will be used for AK8 jets.

At HLT, jets are first reconstructed as calorimeter jets by clustering energy deposits in the calorimeter. PF reconstruction with the caveats mentioned in previous sections is then performed in the vicinity of reconstructed calorimeter jets to form the PF jets used in trigger decisions.

2.3.6 b and double-b tagging

As described in Section 1.2.3, algorithms called jet flavor taggers are often used to identify jets generated by specific parton flavors. This analysis will focus on jets generated by bottom quarks, either in isolation, or in pairs from the decay of a Higgs boson. The most distinguishing feature of b jets is the presence of displaced secondary vertices (SVs) on the order of a few mm to 1 cm caused by the b hadrons. This section describes the b-tagging and double-b-tagging algorithms used to identify b jets and double-b jets. The primary inputs to these algorithms are tracks and secondary vertices.

There are various variables that are commonly used in b tagging. In addition to the longitudinal impact parameter d_z and the transverse impact parameter d_{xy} defined previously, the flight distance of SVs, the impact parameter significance, and the SV corrected mass are also frequently used. The flight distance of a SV, the distance between the primary vertex and the SV, is another common variable. The significance of an impact parameter or flight distance is the quantity divided by its uncertainty. The corrected mass of a SV is given by $\sqrt{M_{\mathrm{SV}}^2 + p^2 \sin^2\theta} + p \sin\theta$, where M_{SV} is the invariant mass of the tracks associated with an SV, p is the magnitude of their net three momentum, and θ is the angle between their momentum and the direction of flight. This provides an approximation for the mass of the decaying particle accounting for particles that were not reconstructed as tracks.

The primary algorithm in CMS Run 2 for reconstructing secondary vertices is the inclusive vertex finding (IVF) algorithm. The algorithm begins by considering all tracks with $p_{\mathrm{T}} > 0.8$ GeV and longitudinal impact parameter less than 0.3 cm. Tracks with sufficiently large impact parameters and impact parameter significance are identified as seeds. Other tracks that are sufficiently close to the seed and are more compatible with a shared secondary vertex with the seed track that the primary vertex are clustered together to form groups of tracks from SVs. The adaptive vertex fitter algorithm is then used to determine the properties of each SV, and SVs that are not significantly separated from the primary vertex or from another SV are removed. SVs that share a large portion of their tracks with another SV are also removed. Next, tracks shared between the

primary vertex and a SV are assigned to one or the other based on relative compatibility. Finally, a refit of remaining secondary vertices with at least 2 tracks is performed and nearby vertices or those sharing 20% of tracks in common are merged. The number of SVs, the flight distance significance, the corrected SV mass, the SV track multiplicity, the SV energy ratio to that of the tracks selected below, and the ΔR between the SV flight direction and jet momentum direction are provided to the b-tagging algorithm described below.

For a given jet, all tracks from clustered PF candidates that meet a set of baseline quality criteria are considered. Additional requirements on track proximity to the primary vertex of interest and the jet axis are used to reject very displaced tracks that are likely from pileup, nuclear interactions in the tracker, and Λ or K^0_S decays. Tracks are also required to be within ΔR of 0.3 of the center of the jet and pairs of tracks compatible with the K^0_S mass are rejected. The track η relative to the jet axis, the 3D impact parameter significance of the first 4 tracks, the relative track p_T from the jet axis, the distance between the track and jet axis at point of closest approach, the distance between the track and the primary vertex at point of closest approach to the jet axis, the ratio of the summed p_T of the tracks to the jet p_T, the ΔR between the summed tracks momenta and the jet axis, the 2D impact parameter significance for the first track that raises the combined invariant mass above 1.5 GeV, and the number of selected tracks are provided to the b-tagging algorithm below.

The DeepCSV algorithm [150] is one common b-tagging algorithm used by the CMS

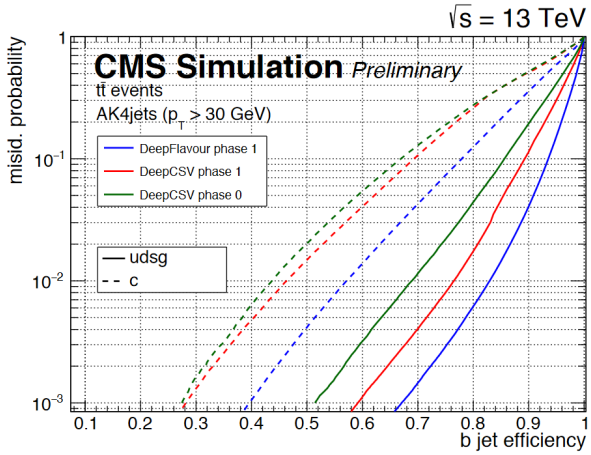

Figure 2.19: Efficiency for correctly identifying b jets plotted against the probability to misidentify a usdg jet (solid) or c jet (dashed) in simulation for the DeepCSV algorithm with the original CMS tracker (green), the DeepCSV algorithm with the tracker after the 2016/2017 pixel upgrade (red), and the deepFlavour/deepJet algorithm after the 2016/2017 upgrade (blue). Figure from [233].

collaboration. In this algorithm, the p_{T} and η of each jet together with the properties of the associated secondary vertices and tracks described above are provided as input to a deep neural network with four fully connected hidden layers with 100 nodes each. The deep neural net is trained in simulation where the true presence of b and c hadrons is known, and regression is performed to generate estimators for the probability of a jet to contain exactly 1 b hadron, at least 2 b hadrons, exactly 1 c hadron and no b hadrons, at least 2 c hadrons and no b hadrons, or none of the above. For b tagging in physics analyses, the sum of the probabilities for having exactly 1 or at least 2 b hadrons are summed to provide a b-tagging discriminant. The loose, medium, and tight working points of the DeepCSV algorithm provide 85%, 70%, and 50% efficiency respectively, while having mistag rates of 10% (40%), 1% (12%), and 0.1% (2.5%) for usdg (c) jets [3].

Jets formed from two nearby b quarks have additional information that can aid in

tagging. The N-subjettiness of a jet τ_{N} [234] is defined by

$$\tau_{\mathrm{N}} = \frac{\sum_{k \in \mathrm{constituents}} p_{\mathrm{T}}^{k} \min(\Delta R_{1,k}, ..., \Delta R_{N,k})}{\sum_{k \in \mathrm{constituents}} p_{\mathrm{T}}^{k} R_0} \tag{2.9}$$

where there are N subjet axes, $\Delta R_{i,k}$ is the distance between a PF candidate and the nearest subjet axis, and R_0 is the radius of the jet [234]. First, τ_{N} is minimized for $\mathrm{N} = 2$ over the subjet axes. Information about tracks and secondary vertices analogous to the properties used as input to the DeepCSV algorithm are computed for each subjet axis. Then, the four tracks with the highest impact parameter significance, the impact parameter significance for the top 2 tracks for each subjet axis, the 2D impact parameter significance for the first two tracks that raise the mass above 5.2/1.5 GeV, the SV energy ratio for each subjet axis relative to the total jet energy, the total number of SVs, the 2D flight distance significance for the SV with the lowest flight distance uncertainty for each subjet axis, the ΔR for the SV with the lowest flight distance uncertainty to its subjet axis, the relative η for the top three tracks for each subjet axis, the total SV mass for each subjet axis, and the variable $z = \Delta R(\mathrm{SV}_0, \mathrm{SV}_1) p_{\mathrm{T}}(\mathrm{SV}_1)/m(\mathrm{SV}_0, \mathrm{SV}_1)$ where SV_0 and SV_1 are the SVs with the lowest flight distance uncertainty for each subjet axis are considered. These properties together with properties of the PF jet constituents and the secondary vertices associated to the jet are provided as input to a neural network. Each collection of charged particles and vertices are provided to a 1x1 convolutional layer with 2 hidden layers of 32 filters each. The output of these layers are supplied to two gated recurrent units, each with 50 outputs. The outputs of the gated recurrent units

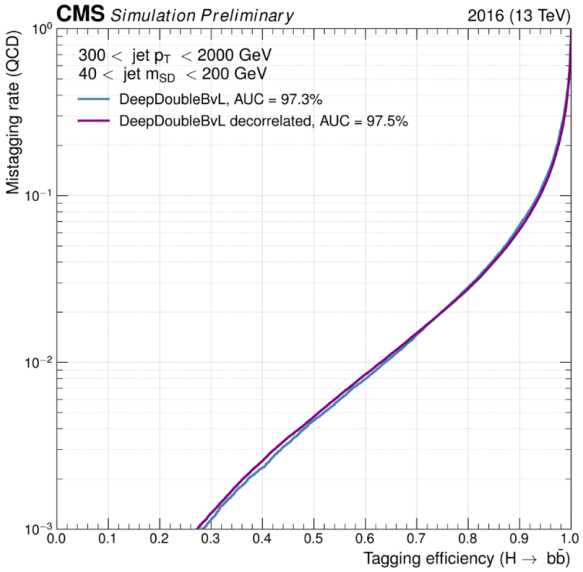

Figure 2.20: Efficiency for correctly identifying double-b jets plotted against the probability to misidentify a usdg jet in simulation for the DeepDoubleBvL algorithm with (violet) and without (blue) mass decorrelation. Mass decorrelation has little effect on tagging performance. Figure from Ref. [235].

are combined with the global properties specified above and fed to one dense layer of 1000 nodes. The neural net is trained to identify jets formed by the decay of a heavy resonance into a pair of b quarks while simultaneously penalizing any differences between the mass distributions between tagged and untagged jets to decorrelate the output with jet mass. This algorithm is called the DeepDoubleBvL decorrelated tagger [150, 235].

The performance of the DeepDoubleBvL tagger plotted as efficiency for selecting double-b jets versus the misidentification probability for udsg jets is shown in Figure 2.20. This analysis uses the loose working point of the DeepDoubleBvL decorrelated tagger, which provides 90% efficiency for selecting jets built from $H \to b\bar{b}$ decays and 5% mistag rate for selecting jets with only u, d, s, and g partons.

2.3.7 Missing transverse momentum reconstruction

Missing transverse momentum is used to characterize the net transverse momentum carried by undetected particles such as neutrinos or new particles that are not directly detected. In CMS, the raw missing transverse momentum $\vec{p}_{\mathrm{T}}^{\,\mathrm{miss,raw}}$ associated to a given event is calculated as the negative vector sum of the transverse momenta of all particle flow candidates in the event as given by

$$\vec{p}_{\mathrm{T}}^{\,\mathrm{miss,raw}} = -\sum_{i \in \mathrm{PF\ Cands}} \vec{p}_{\mathrm{T},i}. \tag{2.10}$$

A correction is then applied to the raw $\vec{p}_{\mathrm{T}}^{\,\mathrm{miss}}$ by subtracting the corrections to jet transverse momenta from the previous section as described by

$$\vec{p}_{\mathrm{T}}^{\,\mathrm{miss}} = \vec{p}_{\mathrm{T}}^{\,\mathrm{miss,raw}} - \sum_{i \in \mathrm{jets}} (\vec{p}_{\mathrm{T},i}^{\,\mathrm{corr}} - \vec{p}_{\mathrm{T},i}). \tag{2.11}$$

All jets with $p_{\mathrm{T}} > 15\,\mathrm{GeV}$ and less than 90% of their energy in the ECAL are considered for this correction, and jets that include muons have the muons removed prior to the correction. The uncertainty on $p_{\mathrm{T}}^{\mathrm{miss}}$ is propagated from the uncertainties in the particle flow candidates' p_{T} and the JECs [191].

To provide a cross-check against particle-flow failures, another version of $\vec{p}_{\mathrm{T}}^{\,\mathrm{miss}}$, called calorimeter $\vec{p}_{\mathrm{T}}^{\,\mathrm{miss}}$ or $\vec{p}_{\mathrm{T,calo}}^{\,\mathrm{miss}}$, is calculated as the negative vector sum of calorimeter cell

energies and muon momenta corrected by the JECs for calorimeter jets as given by

$$\vec{p}_{\mathrm{T,calo}}^{\,\mathrm{miss}} = -\sum_{i\in\mathrm{cells}} \vec{p}_{\mathrm{T},i} - \sum_{i\in\mathrm{muons}} \vec{p}_{\mathrm{T},i} - \sum_{i\in\mathrm{calo\ jets}} (\vec{p}_{\mathrm{T},i}^{\,\mathrm{corr}} - \vec{p}_{\mathrm{T},i}). \tag{2.12}$$

The resolution of the $p_{\mathrm{T}}^{\mathrm{miss}}$ is dominated by the momentum resolution of hadronic activity in the form of jets or unclustered energy. The momentum resolution of hadronic activity is measured using events with a leptonic decay of a Z or an isolated $\boldsymbol{\gamma}$ for which real $p_{\mathrm{T}}^{\mathrm{miss}}$ is negligible. Figure 2.21 shows the hadronic activity resolution parallel to ($u_{\parallel}$) and perpendicular to ($u_{\perp}$) the Z/$\boldsymbol{\gamma}$ as a function of number of pileup vertices and total transverse energy in the event. Typical uncertainties are on the order of 15–30 GeV, increasing with pileup and energy scale.

At the HLT level, the missing transverse momentum is first computed using the variable $p_{\mathrm{T,calo}}^{\mathrm{miss}}$. If $p_{\mathrm{T,calo}}^{\mathrm{miss}}$ is sufficiently large, the full PF $p_{\mathrm{T}}^{\mathrm{miss}}$ is computed from PF jets with jet energy corrections propagated for jets with $p_{\mathrm{T}} > 35$ GeV. In contrast to offline reconstruction, a set of filters are used to remove energy deposits consistent with calorimeter noise or beam halo when computing $p_{\mathrm{T}}^{\mathrm{miss}}$ [191]. For offline reconstruction, application of these filters is left to the analysis level; the filters used in the HH(4b)+$p_{\mathrm{T}}^{\mathrm{miss}}$ analysis are detailed in Section 3.3.2.

2.3.8 Lepton and photon reconstruction

Offline, isolated electron and photon physics objects correspond to isolated superclusters as described in Section 2.3.3. Superclusters with an associated track are taken as

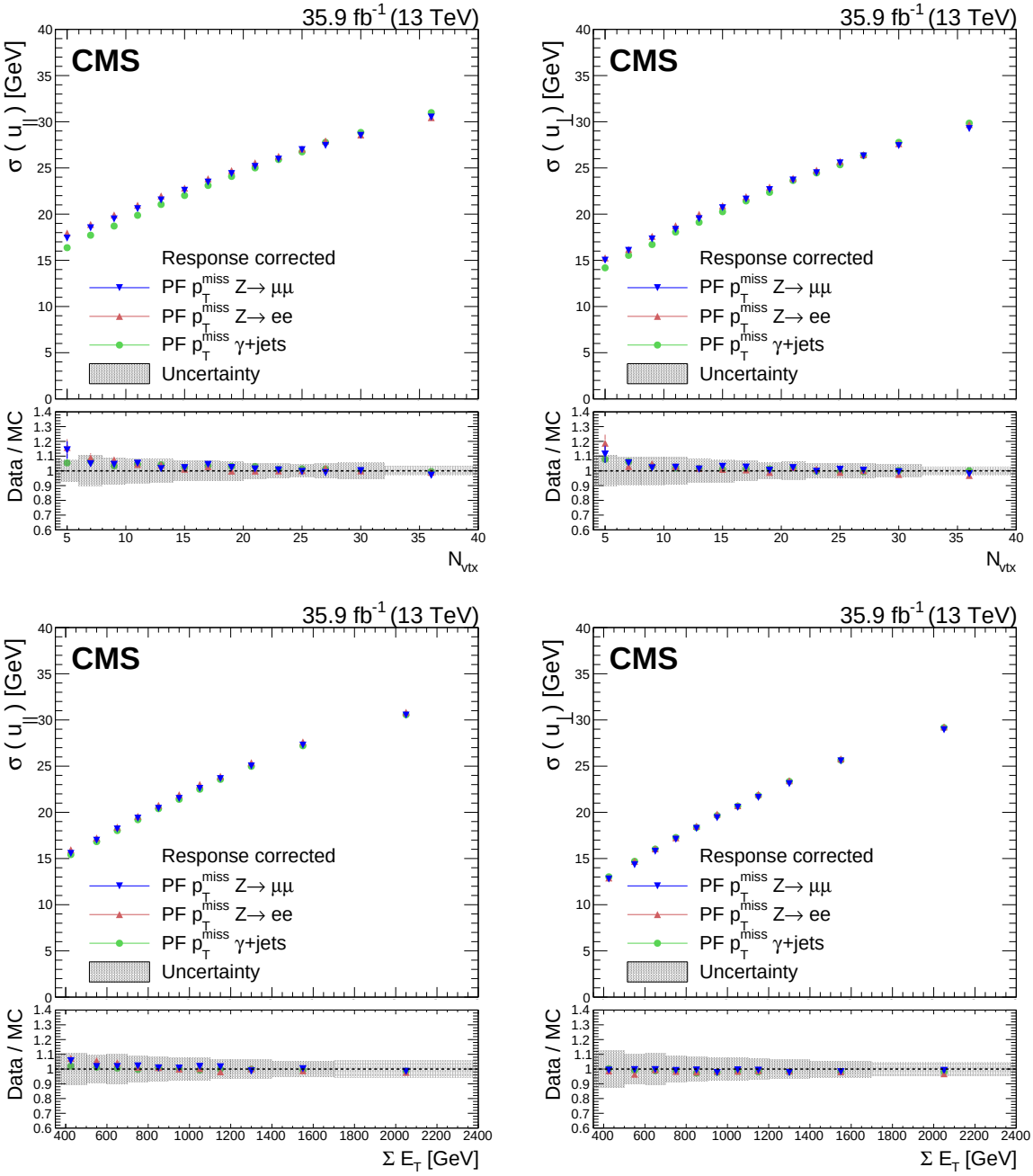

Figure 2.21: Resolution of hadronic activity transverse energy (a proxy for $p_{\mathrm{T}}^{\mathrm{miss}}$) parallel to (left) and perpendicular to (right) to a Z/γ as a function of number of vertices (top) and total transverse energy (bottom) measured in Z and γ events. Figure from Ref. [191].

electron objects while a track veto is typically used to define photon objects. Since the reconstruction efficiency for energetic superclusters is nearly unity, the reconstruction efficiency for photons with $p_{\mathrm{T}} > 10$ GeV is essentially unity while the efficiency for isolated electrons with $p_{\mathrm{T}} > 20$ GeV is over 95% as shown in Figure 2.22 and is dependent only on track reconstruction efficiency. After reconstruction, corrections are applied to the electron and photon energy scale and resolution by performing a series of regressions in simulation. After this, residual corrections are derived using data-simulation comparison. The final energy resolution is typically 1–5% for electrons and photons, and is dominated by calorimeter thresholds and resolution for electrons and photons with $p_{\mathrm{T}} > 20$ GeV, as shown in Figure 2.23 [172]. Although not used in this analysis, multivariate techniques are used to discriminate between real electrons and photons and fake electrons and photons. The performance of these algorithms are shown in Figure 2.24.

At the HLT level, isolated electron and photon reconstruction begins by clustering energy deposits adjacent to L1 electron/photon candidates into superclusters similarly to what is done offline. The algorithm then searches for pixel seeds that could correspond to an electron that would generate the supercluster and fits any found track seeds using GSF tracking. Nearby tracks are also reconstructed using the normal procedure in order to calculate track isolation. Quality criteria for the shower shape, the energy deposited in the HCAL, the isolation, and track compatibility in the case of electrons are then applied to generate online electron and photon candidates.

Muon physics objects directly correspond to muon PF candidates. The efficiency for

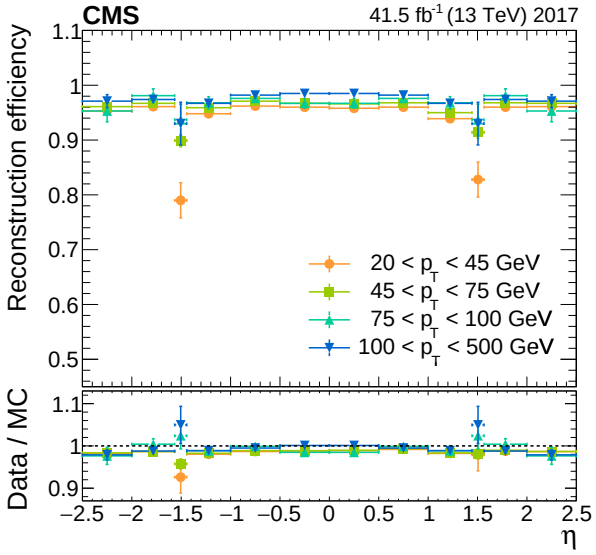

Figure 2.22: Reconstruction efficiency for isolated electrons as a function of p_{T} and $|\eta|$. Noticeable drops can be seen between the barrel and endcap regions, but the integrated efficiency for electrons with $p_{\mathrm{T}} > 20$ GeV is over 95%. Figure from Ref. [172].

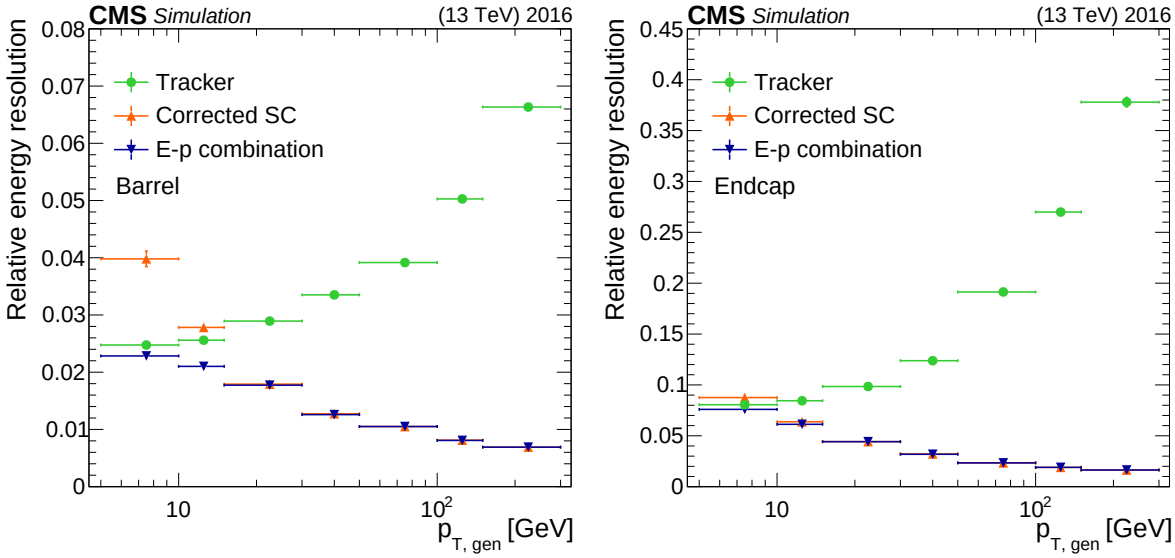

Figure 2.23: Electron energy resolution using only the corrected supercluster energy (orange), only the track momentum (green) and the combination of the two (blue) as a function of electron p_{T} in the barrel (left) and endcap (right). Figure from Ref. [172].

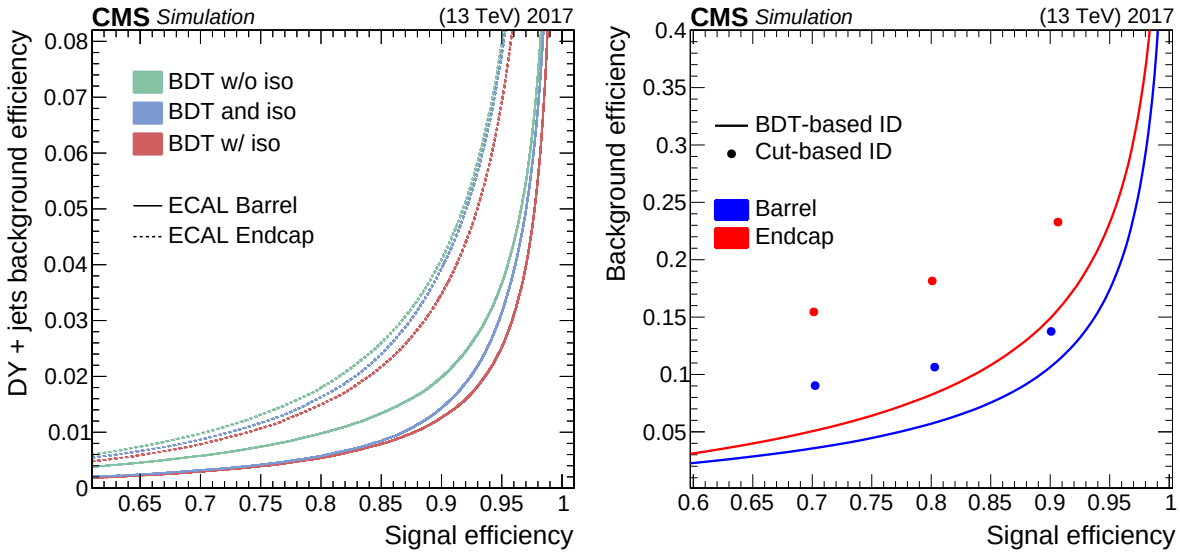

Figure 2.24: Identification efficiency for isolated electrons (left) and photons (right) versus misidentification efficiency. Figure from Ref. [172].

reconstructing PF muons, also referred to as the loose ID, is over 99% for isolated muons as previously mentioned and shown in Figure 2.25. Corrections to the muon momentum scale and resolution are derived from data and applied to the muon objects. The final momentum resolution for muons is on the order of 1–2% for muons with $p_{\mathrm{T}} < 100$ GeV as shown in Figure 2.26. The probability for pions to be misidentified as loose muons is measured to be about 0.2% in data, although such particles will be typically be contained in jets and will not be used as isolated physics objects. Additional sets of ID criteria can be used to reduce the rate of fake muons and select muons from prompt production or heavy flavor decay. At the HLT level, muon reconstruction is only performed in the vicinity of a level-1 muon candidate, which can either seed a more complete standalone muon that is then propagated inward to the tracker or can be used to select a region in the tracker from which tracker muons can be built [182].

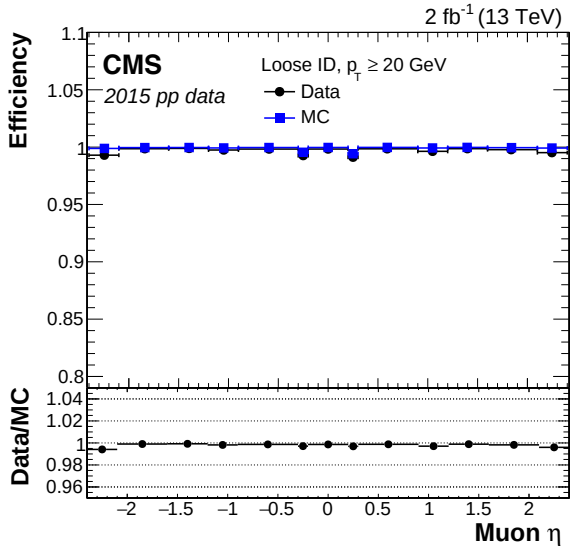

Figure 2.25: Muon reconstruction efficiency in simulation and data as a function of η. Figure from Ref. [182].

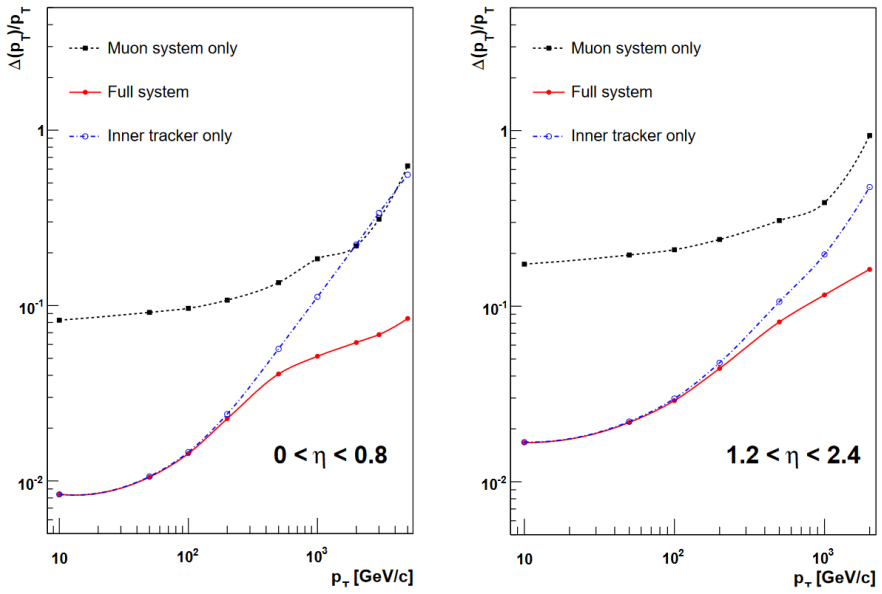

Figure 2.26: Muon momentum resolution as a function of p_{T} using just muon system information, just tracker information, and the combination of the two in the barrel (left) and endcap (right) regions. Figure from [166].

Although hadronic tau physics objects are not directly used in the analysis described in this thesis, it is of possible interest to consider hadronic taus to reduce lost lepton background in future analyses. In CMS, hadronic taus are reconstructed by the hadrons-plus-strips (HPS) algorithm. Given a reconstructed jet, the algorithm first dynamically clusters groups of nearby electrons and photon PF candidates into "strips" that could correspond to the decay products of neutral pions. The algorithm then considers the strips together with charged hadrons ($h^{\pm}$) in the jet in all possible combinations of the following: $h^{\pm}$, $h^{\pm}\pi^0$, $h^{\pm}\pi^0\pi^0$, and $h^{\pm}h^{\pm}h^{\mp}$. For the latter three possibilities, the mass of the system is required to be consistent with the $\rho(770)$, the $\rho(770)$ or the $a_1(1260)$ respectively. These reconstructed decay modes account for about 88% of hadronic tau decays. Finally, taus with charge other than ± 1 and those spread over too large an area are rejected. Only the highest p_{T} hadronic tau candidate is kept for each jet. Discrimination between taus and jets can then be performed, typically by using isolation of the tau candidate. Additional discriminators between taus and jets as well as taus and electrons are also commonly used. Figure 2.27 shows the efficiency of tau reconstruction plotted against misidentification probability for jets. As with other physics objects, corrections to energy scale are derived and applied. After corrections, the resolution for the visible energy in the hadronic tau is on the order of 4% as shown in Figure 2.28. At the HLT, tau reconstruction begins by first generating simple tau candidates by clustering calorimeter deposits near level-1 tau candidates. If these calorimeter cluster tau candidates pass a basic track isolation criterion or if the primary vertex cannot be

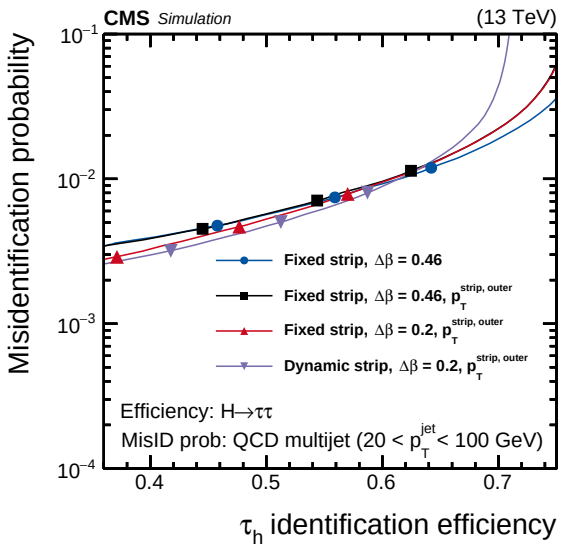

Figure 2.27: Selection efficiency for hadronic taus versus jet misidentification probability. The nominal HPS algorithm is shown in violet while older algorithms with fixed strips sizes are shown in other colors. The markers correspond to the standard loose, medium, and tight working points. Figure from Ref. [236].

reconstructed, a version of the PF algorithm and a much simplified version of the HPS algorithm is used to reconstruct hadronic tau candidates [236].

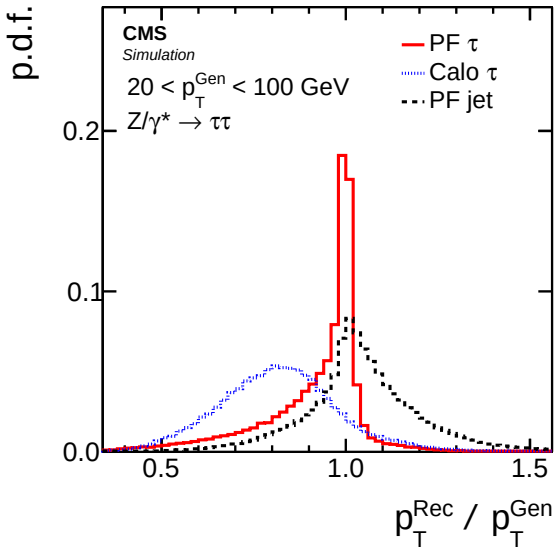

Figure 2.28: Calibrated visible energy resolution for hadronic taus produced in the Drell-Yan process with p_{T} between 20 and 100 GeV in simulation without pileup. Resolution for standard (PF) hadronic taus shown in red, taus reconstructed with only calorimeter information in blue, and the energy of the jet containing the tau in a black dashed line. Figure from Ref. [169].

Chapter 3

Signal model, physics objects, and data sets

This chapter describes the signal models, physics objects, and data sets used in the HH(4b)+$p_{\mathrm{T}}^{\mathrm{miss}}$ analysis. The supersymmetry scenarios targeted by this analysis involving pairs of higgsinos together with the simplified models used for interpretation are briefly described in Section 3.1. These models all share a final state with two Higgs bosons decaying to pairs of bottom quarks and $p_{\mathrm{T}}^{\mathrm{miss}}$ created by the lightest supersymmetric particle. Section 3.2 then describes the analysis specific selection on physics objects following the general reconstruction described in Section 2.3. Selection on jets, $p_{\mathrm{T}}^{\mathrm{miss}}$, b tagging, and bb tagging are used to identify objects in the signal topology, while selections on leptons, photons, and isolated tracks are used both for defining control regions, as well as for removing events with prompt leptons from the primary search region. This section also describes the method used to reconstruct and select Higgs boson candidates. Finally, Section 3.3 describes the data and simulated event samples used in the analysis, along with related items including the triggers used to select the events and filters and

corrections that are applied to the data sets to correct for known detector issues as well as differences between simulation and real data.

3.1 Signal models

As described in Refs. [132–134], one expects higgsinos to be among the lightest superpartners in natural models of supersymmetry. The electroweak superpartner mass states can in general be a mixture of winos, binos, and higgsinos, but we will restrict ourselves to the simplifying assumption that this mixing is small so that we can identify nearly pure winos, binos, and higgsinos separately. If the lightest higgsino is the LSP, then the experimental signatures of higgsino production can be very difficult to search for. Collider analyses targeting signatures such as disappearing tracks [237–246], long-lived charged particles [247–255], soft displaced tracks, $p_{\mathrm{T}}^{\mathrm{miss}}$ recoiling against a jet [256–270], or low-p_{T} leptons or tracks [271–276] are needed to search for higgsino LSP models, which means that such models possess a large area of parameter space to which current measurements are not sensitive. Similarly, as the gaugino component of the LSP approaches 0, a higgsino LSP is a simple $\mathrm{SU}(2)_{\mathrm{L}}$ doublet and direct detection cross sections are pushed below that of coherent neutrino scattering [277], making direct detection currently infeasible.

On the other hand, if the LSP is not a higgsino but rather another superpartner such as a bino or the gravitino, then higgsino production can yield signatures such as vector bosons or charged leptons together with $p_{\mathrm{T}}^{\mathrm{miss}}$. In this case, current data may provide much higher sensitivity. Other ATLAS and CMS analyses that have searched for

electroweakino production with large mass splitting include Refs. [271, 278–336]. These analyses target different final states depending on the decay mode of the higgsinos as well as the decay modes of any SM particles produced in higgsino decay. Many other searches also have sensitivity to higgsino production, even if a direct interpretation is not given. The search described in this thesis targets pairs of higgsinos, each decaying to the LSP and a Higgs boson, which subsequently decays into a pair of bottom quarks. The decay $\mathrm{H} \to \mathrm{b\bar{b}}$ is the most common decay of the Higgs boson, occurring with a predicted probability of $58.2^{+1.2}_{-1.3}\%$ [337, 338]. Although the measurement of this decay channel of this Higgs is considered more difficult in isolation due to the large background from QCD multijet events, the presence of substantial $p_{\mathrm{T}}^{\mathrm{miss}}$ removes most of the QCD multijet background, making this decay channel the most appealing for signal models with large $p_{\mathrm{T}}^{\mathrm{miss}}$. The combination of this search and with other searches sensitive to other higgsino and Higgs decay modes is described in Chapter 5. In this analysis, three different simplified models of supersymmetry [339–342] are considered and described in the following paragraphs. In the simplified models, most supersymmetric partners are assumed to have masses that are above LHC reach and thus are "integrated out" leaving only effective interactions in the effective field theory sense.

TChiHH-G

The first simplified model, called TChiHH-G, is motivated by theories of gauge-mediated supersymmetry breaking [343–345]. In this simplified model, the only relevant

particles are the four higgsinos, $\widetilde{\chi}_1^0$, $\widetilde{\chi}_1^\pm$, and $\widetilde{\chi}_2^0$, which are assumed to be nearly degenerate around an unknown mass $m(\widetilde{\chi}_1^0)$, and the gravitino $\widetilde{\mathrm{G}}$, whose mass is constrained to be 1 GeV. Because the gravitino couplings are dominated by the couplings to its goldstino component, which are in turn suppressed by the SUSY breaking scale, the heavier three higgsinos $\widetilde{\chi}_1^\pm$ and $\widetilde{\chi}_2^0$ are assumed to decay entirely to the lightest higgsino $\widetilde{\chi}_1^0$ plus additional soft particles. Since the higgsinos are expected to be nearly degenerate, the soft particles are typically not in detector acceptance and are thus ignored. The decay of the lightest higgsino is in general dependent on the parameters of the supersymmetry model, but the simplified model considered here assumes a branching ratio of 100% to a Higgs boson together with a gravitino. Higgsinos can be produced in the pairs $\widetilde{\chi}_1^0\widetilde{\chi}_2^0$, $\widetilde{\chi}_1^0\widetilde{\chi}_1^\pm$, $\widetilde{\chi}_2^0\widetilde{\chi}_1^\pm$, and $\widetilde{\chi}_1^\pm\widetilde{\chi}_1^\mp$, all of which eventually decay down to $\widetilde{\chi}_1^0\widetilde{\chi}_1^0$ and soft particles. This gives an effective total cross section for $\widetilde{\chi}_1^0\widetilde{\chi}_1^0$ production shown in red in Figure 3.4 that is substantially larger than any individual higgsino pair. At the LHC, the primary production mechanism for higgsinos is s-channel Z, W, or γ exchange. Representative Feynman diagrams for the TChiHH-G model are shown in Figure 3.1.

Note that the lifetimes of the heavier higgsinos become long in the limit that all the higgsinos have exactly the same mass. Additionally, the lifetime of the lightest higgsino becomes long in the limit that the supersymmetry breaking scale is large. In the simplified model considered, all particles are assumed to decay promptly in the detector, which technically limits the sensitivity to parameter space of supersymmetry models in which the higgsinos are not too degenerate and the supersymmetry breaking scale is not too

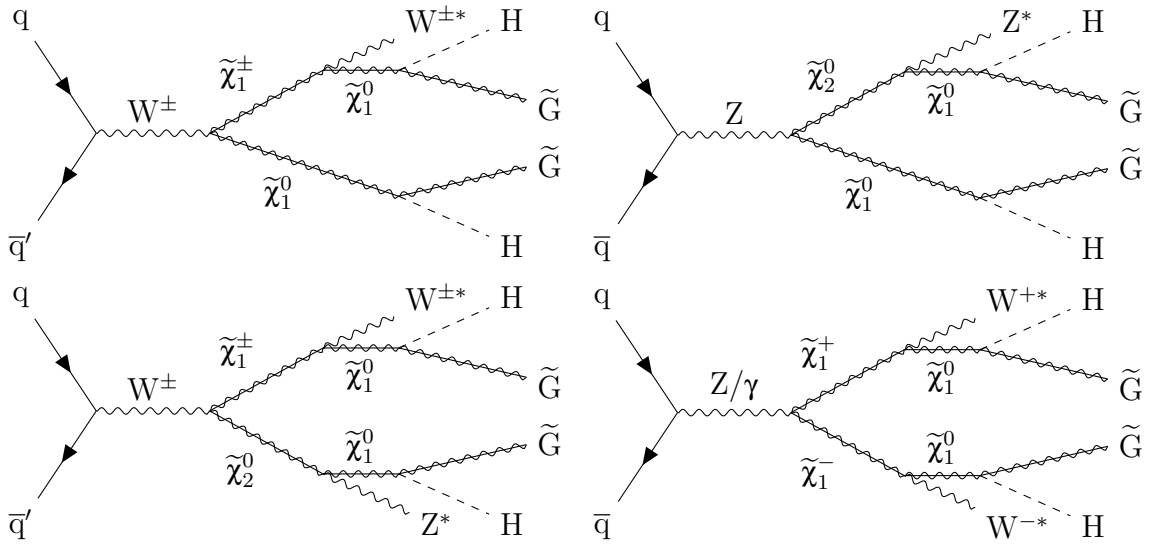

Figure 3.1: Feynman diagrams representing the TChiHH-G simplified model with production of higgsinos $\widetilde{\chi}_1^0$, $\widetilde{\chi}_1^{\pm}$, and $\widetilde{\chi}_2^0$, the heavier of which decay to soft particles represented as W^* or Z^* and the lightest higgsino, which then decays into a Higgs boson H and a gravitino $\widetilde{G}$, which is the LSP.

large. This analysis does not attempt to quantitatively describe these limitations.

TChiHH

The second model considered, TChiHH, is one in which the LSP is not a gravitino, but rather a bino-like neutralino. In this case, each of the higgsinos, $\widetilde{\chi}_2^0$, $\widetilde{\chi}_1^{\pm}$, and $\widetilde{\chi}_3^0$, decays directly to the bino LSP $\widetilde{\chi}_1^0$ plus an SM particle, so that the $\mathrm{HH} + p_{\mathrm{T}}^{\mathrm{miss}}$ signature can only occur from production of the neutral higgsinos, $\widetilde{\chi}_2^0\widetilde{\chi}_3^0$. Note that production of pairs of the same neutral higgsino does not occur at tree level and is thus neglected for this analysis. The TChiHH simplified models consists of two degenerate higgsinos $\widetilde{\chi}_2^0$ and $\widetilde{\chi}_3^0$ with an unknown mass of $m(\widetilde{\chi}_2^0)$, together with a bino LSP $\widetilde{\chi}_1^0$ with an unknown mass of $m(\widetilde{\chi}_1^0)$. The cross section for $\widetilde{\chi}_2^0\widetilde{\chi}_3^0$ production as a function of $m(\widetilde{\chi}_2^0)$ is shown

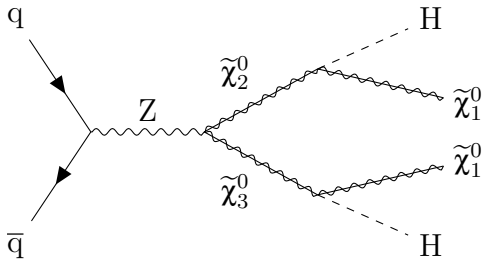

Figure 3.2: Feynman diagram representing the TChiHH simplified model with production of higgsinos $\widetilde{\chi}_2^0$ and $\widetilde{\chi}_3^0$ decaying into a Higgs boson H and a bino $\widetilde{\chi}_1^0$, which is the LSP.

in violet in Figure 3.4. The TChiHH simplified model also assumes that both neutral higgsinos decay with a branching ratio of 100% to a Higgs and the LSP, though it should be noted that this scenario does not typically occur in realistic models of supersymmetry. Figure 3.2 shows the representative Feynman diagram for this model.

T5HH

The final model considered, T5HH, does not target direct higgsino pair production but rather higgsinos produced in gluino decays. In this case, pairs of gluinos $\widetilde{g}$ with unknown mass $m(\widetilde{g})$ are produced and then decay each into two quarks and a higgsino $\widetilde{\chi}_2^0$ with a mass $m(\widetilde{\chi}_2^0)$ equal to $m(\widetilde{g}) - 50$ GeV. This decay is made possible by the effective interaction obtained by integrating out high-mass squarks. Each higgsino then decays to a bino-like LSP $\widetilde{\chi}_1^0$, whose mass $m(\widetilde{\chi}_1^0)$ is set to be 1 GeV. The choice of a 50 GeV mass splitting between the gluino and higgsino as well as the choice of a nearly massless LSP is an arbitrary feature of the simplified model, and the analysis has sensitivity to a wide range of mass splittings and LSP masses. The cross section for gluino production as a function of $m(\widetilde{g})$ is shown in orange in Figure 3.4. Figure 3.3 shows representative

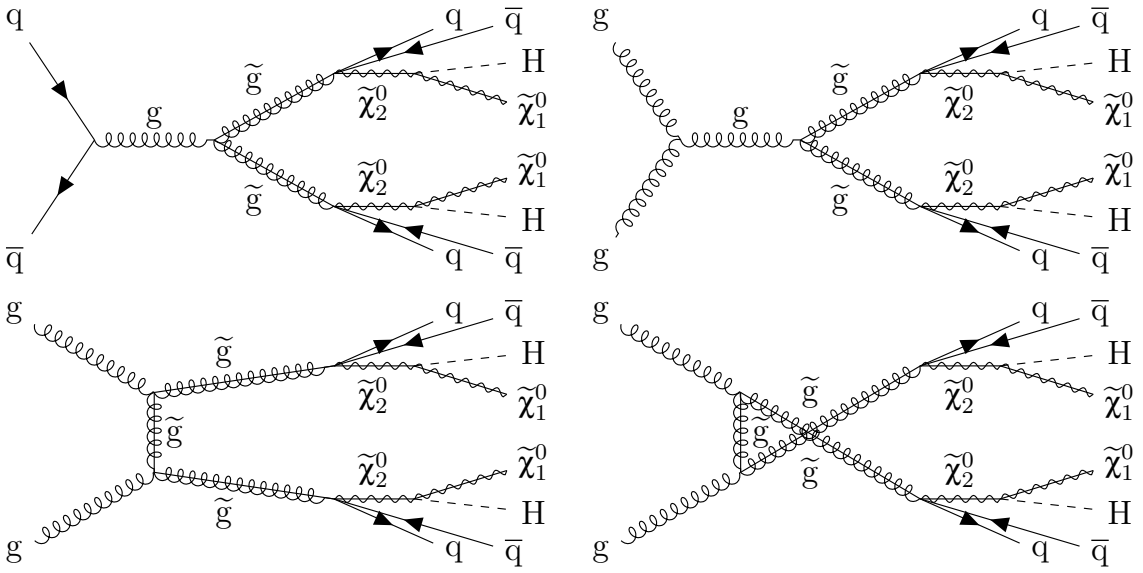

Figure 3.3: Feynman diagrams representing the T5HH simplified model with production of pairs of gluinos $\widetilde{g}$ through any of the modes shown. The gluinos then decay into jets together with a neutral higgsino $\widetilde{\chi}_2^0$, which then decays into a Higgs boson H and a bino $\widetilde{\chi}_1^0$, which is the LSP.

Feynman diagrams for this model including the four primary gluino production diagrams at a p-p collider.

3.2 Physics object selection

3.2.1 Leptons, photons, and tracks

In this analysis, the presence of prompt electrons, muons, and photons is used to define control regions and validation regions used to evaluate systematic uncertainties described in Section 4.3. The criteria used to select these objects for these control regions are described in this section. Furthermore, the signal region selection features veto criteria designed to reject prompt leptons since the considered signal models do not contain

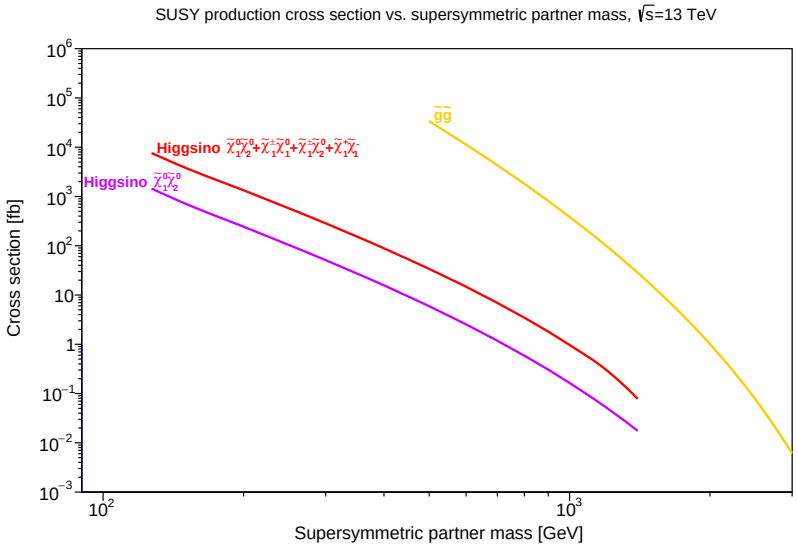

Figure 3.4: Cross section for gluino pair production (orange) used for the T5HH model, integrated higgsino pair production (red) used for the TChiHH-G model, and neutral higgsino pair production (violet) used for the TChiHH model as a function of sparticle mass. Cross sections for higgsino production are calculated with the Resummino program [346–353] to NLO+NLL precision while those for gluino pair production are calculated with the NNLL-fast program [354–361] to approximately NNLO+NNL precision.

prompt leptons while some of the largest backgrounds do. It is worth noting, however, that signal events may have nonprompt leptons produced in the decays of b and c hadrons commonly found in b jets. The criteria used to veto prompt electrons and muons as well as isolated tracks, which are used as a proxy for prompt single-pronged hadronic taus, are also described in this section.

There are a number of variables commonly used to identify prompt electrons, photons, muons, and isolated tracks and reject nonprompt or fake objects.

- Previously discussed kinetic and spatial variables include the transverse momentum p_{T}, the pseudorapidity η, and the impact parameters d_z and d_{xy}. Nonprompt leptons may have nonzero d_z and d_{xy} while both nonprompt and spurious leptons and photons tend to have lower p_{T} than prompt particles.

- The absolute isolation I with a cone size ΔR of a particle is defined to be the scalar sum of the p_{T} of other particles within a radius ΔR from the particle being considered after subtracting the pileup ρEA where ρ is the median transverse energy and per area and EA is the effective area of the physics object. In this analysis, I_γ, I_n, and I_c, the isolation with respect to photons, neutral hadron, and charged hadron PF candidates within a ΔR of 0.3 are used for photon selection. I_{chg}, the isolation with respect to all other charged PF candidates with $\Delta R = 0.3$, is also used for isolated track selection. Isolation variables tend to be smaller for prompt leptons and photons as nonprompt and spurious leptons and photons are generally produced in jets.

- The relative isolation I_{rel} for a cone size ΔR is the isolation divided by the p_{T} of the particle being considered. The relative isolation I_{relchg} with respect to charged hadrons where $\Delta R = 0.3$ is used in the isolated track selection.

- The mini isolation I_{mini} is the relative isolation where the cone size is $\Delta R = 0.2$ when the considered particle's momentum is under 50 GeV, $\Delta R = 10 \text{ GeV}/p_{\text{T}}$ for p_{T} between 50 and 200 GeV, and $\Delta R = 0.05$ for p_{T} over 200 GeV. This is used in the electron and muon selections.

- Measurements of the compatibility of electron properties between its track and its supercluster include $\Delta\eta_{\text{in}}^{\text{seed}}$, the difference in pseudorapidity between an electron's seed supercluster and the associated track near the interaction point, $\Delta\phi_{\text{in}}$, the difference in azimuthal angle between an electron's seed supercluster and track near the interaction point, and $\left|1/E_{\text{SC}} - 1/p\right|$, the difference between an electron's supercluster energy and the track momentum near the interaction point. These variable aid in discriminating between true and spurious electrons.

- $\sigma_{i\eta i\eta}$ is a function of the crystal energies in the 5x5 ECAL crystals surrounding the most energetic crystal defined as:

$$\begin{aligned} \sigma_{i\eta i\eta} &= \sqrt{\frac{\sum_i^{5\times5} w_i(\eta_i - \bar{\eta}_{5\times5})^2}{\sigma_i^{5\times5} w_i}} \\ w_i &= \max(0, 4.7 + \log(E_i/E_{5\times5})) \end{aligned} \tag{3.1}$$

this variable is typically smaller for real electron and photon showers and larger for

two photon showers such as those produced by π^0 decays.

- H/E is the ratio of energy deposited in the CMS HCAL to that deposited in the CMS ECAL and is used to discriminate between real electrons or photons and early showering hadrons.

In addition, the selection for isolated tracks also utilizes the transverse mass m_{T}, which is defined as $\sqrt{2p_{\mathrm{T}}p_{\mathrm{T}}^{\mathrm{miss}}(1-\cos\Delta\phi)}$, where p_{T} is the transverse momentum of the object under consideration and $\Delta\phi$ is the azimuthal angular separation between the object and the $p_{\mathrm{T}}^{\mathrm{miss}}$. In the case where a heavy particle decays into a visible system and an undetected system that gives rise to the observed $p_{\mathrm{T}}^{\mathrm{miss}}$, the transverse mass of the visible system provides a lower bound on the mass of the heavy particle. The variable m_{T} is used to only veto isolated tracks consistent with the decay of a W boson, which should have an m_{T} less than m_{W}.

Table 3.1 lists the criteria applied to electron physics objects reconstructed by CMS that define the electrons used in the control regions of this analysis. The criteria below the horizontal line are part of the CMS medium quality electron identification, which is designed to select prompt electrons with about 80% efficiency and reject most spurious and nonprompt electrons. The identification criteria together with the p_{T} and isolation cuts are intended to reject spurious electrons while the impact parameter cuts are intended to reject nonprompt electrons. The conversion-safe electron veto criteria select only electrons with tracks that have a hit in the innermost layer of the pixel layer and are not linked to a conversion vertex in order to remove electrons from photon pair produc-

Table 3.1: Selections applied to the control region electrons. Some selection criteria differ between barrel and endcap in which case $|\eta| = 1.479$ is considered the division between the two. Selections below the horizontal line are part of the standard CMS Fall17v2 cut-based medium electron identification criteria.

Variable	Barrel selection	Endcap selection
p_{T}	> 30 GeV (leading), > 20 GeV (subleading)	
Supercluster $\lvert\eta\rvert$	< 1.479	> 1.479 and < 2.5
I_{mini}	< 0.1	
$\lvert d_{xy}\rvert$	< 0.05 cm	< 0.1 cm
$\lvert d_z\rvert$	< 0.1 cm	< 0.2 cm
$\lvert\Delta\eta_{\mathrm{in}}^{\mathrm{seed}}\rvert$	< 0.0032	< 0.00632
$\lvert\Delta\phi_{\mathrm{in}}\rvert$	< 0.0547	< 0.0394
$\sigma_{i\eta i\eta}$	< 0.0106	< 0.0387
H/E	$< 0.046 + 1.16/E_{\mathrm{SC}} + 0.032$ GeV $\times\, \rho/E_{\mathrm{SC}}$	$< 0.0275 + 2.52$ GeV$/E_{\mathrm{SC}} + 0.183 \times \rho/E_{\mathrm{SC}}$
$\lvert 1/E_{\mathrm{SC}} - 1/p\rvert$	$< 0.184/$ GeV	$< 0.0721/$ GeV
Conversion-safe electron veto	true	
Missing pixel hits	≤ 1	

tion in the detector. The criteria used to select electrons for the lepton veto in the signal region are shown in Table 3.2. These selections are looser in order to more completely remove events with prompt leptons from the signal region, and are designed to reject about 95% of prompt electrons. The efficiency to reconstruct electrons and to pass the veto criteria and medium identification criteria was measured in data using the tag-and-probe technique on $\mathrm{Z} \to \mathrm{e}^{+}\mathrm{e}^{-}$ events introduced in Ref. [362]. In this type of measurement, one selects events with a tag electron passing a tight working point and a probe electron candidate consisting of an isolated supercluster, then constructs the distribution of lepton pair invariant mass m_{ee} with and without imposing the restriction that the electron be reconstructed or pass the appropriate identification working point. By fitting the Z peak in the m_{ee} distribution before and after imposing reconstruction or identification requirements, one measures the probability for electrons to be reconstructed and pass the quality requirements as a function of p_{T} and $|\eta|$ [172].

Table 3.2: Selections applied to veto electrons used to remove leptonic events from the signal region. Some selection criteria differ between barrel and endcap in which case $|\eta| = 1.479$ is the considered the division between the two. Selections below the horizontal line are part of the standard CMS Fall17v2 cut-based veto electron identification criteria.

Variable	Barrel selection	Endcap selection
p_{T}	> 10 GeV	
Supercluster $\lvert\eta\rvert$	< 1.479	> 1.479 and < 2.5
I_{mini}	< 0.1	
$\lvert d_{xy}\rvert$	< 0.05 cm	< 0.1 cm
$\lvert d_z\rvert$	< 0.1 cm	< 0.2 cm
$\lvert\Delta\eta_{\mathrm{in}}^{\mathrm{seed}}\rvert$	< 0.00463	< 0.00814
$\lvert\Delta\phi_{\mathrm{in}}\rvert$	< 0.148	< 0.19
$\sigma_{i\eta i\eta}$	< 0.0126	< 0.0457
H/E	$< (0.05 + 1.16/E_{\mathrm{SC}} + 0.032\ \mathrm{GeV} \times \rho/E_{\mathrm{SC}})$	$< (0.05 + 2.54\ \mathrm{GeV}/E_{\mathrm{SC}} + 0.183 \times \rho/E_{\mathrm{SC}})$
$\lvert 1/E_{\mathrm{SC}} - 1/p\rvert$	$< 0.209/\mathrm{GeV}$	$< 0.132/\mathrm{GeV}$
Conversion-safe electron veto	pass	
Missing pixel hits	≤ 2	≤ 3

Muons used in this analysis are muon physics objects with the selections detailed in Table 3.3 applied. The only difference between muons used in the control region and those used to veto leptonic events from the signal region is the p_{T} threshold. The medium muon identification criteria require hits in at least 80% of the inner tracker layers traversed by the muon and a compatibility score between the inner track and muon detectors of at least 0.451 or greater than 0.303 if the muon is additionally a global muon with a global fit chi-squared per degree of freedom less than 3, a position compatibility chi-squared of less than 12, and a kink-finding algorithm chi-squared less than 20. The medium muon identification criteria are designed to have an efficiency of about 99.5% for prompt muons. The efficiency for muon reconstruction and identification was measured using the tag-and-probe technique in a sample of $\mathrm{Z} \to \mu^+\mu^-$ events with a tight tag muon and a tracker track probe and is parametrized by muon p_{T} and $|\eta|$ [182].

The isolated track veto criteria target singled-pronged hadronic taus as well as elec-

Table 3.3: Selections applied to control region muons and those used to veto muons from the signal region in this analysis.

Variable	Control region selection	Veto selection
p_{T}	> 30 GeV (leading), > 20 GeV (subleading)	> 10 GeV
$\lvert\eta\rvert$	< 2.4	
I_{mini}	< 0.2	
$\lvert d_{xy}\rvert$	< 0.2 cm	
$\lvert d_z\rvert$	< 0.5 cm	
medium ID	pass	

Table 3.4: Selections applied to define the isolated tracks used to reject events with isolated tracks from the signal region. Electron, muon, and charged hadron PF candidates are taken as the possible candidates for isolated tracks and the criteria in the middle row (right row) are applied to electron and muon (charged hadron) candidates.

Variable	Lepton track selection	Charge hadron track selection
p_{T}	> 5 GeV	> 10 GeV
$\lvert\eta\rvert$	< 2.5	
Isolation	($p_{\mathrm{T}} < 25$ GeV and $I_{\mathrm{chg}} < 5$ GeV) or $I_{\mathrm{relchg}} < 0.2$)	($p_{\mathrm{T}} < 25$ GeV and $I_{\mathrm{chg}} < 5$ GeV) or $I_{\mathrm{relchg}} < 0.1$)
$\lvert d_{xy}\rvert$	< 0.2 cm	
$\lvert d_z\rvert$	< 0.1 cm	
m_{T}	< 100 GeV	

trons and muons not rejected by the dedicated electron and muon veto criteria. All electron, muon, and charged hadron PF candidates associated to the primary vertex are taken and those passing the selections detailed in Table 3.4 are taken as isolated tracks. Events with any isolated tracks are removed from the analysis signal regions. To limit the veto to tracks likely to have come from the decay of a W, which is the case for the dominant backgrounds, the transverse mass m_{T} of the isolated track is limited to be less than 100 GeV.

The photons used in the photon control sample were selected from general photon physics objects using the criteria shown in Table 3.5. This analysis uses the standard

Table 3.5: Selections applied to control region photons in this analysis where $|\eta| = 1.479$ is taken to be the cutoff between barrel and endcap photons. The criteria under the horizontal line correspond to the standard CMS Fall17v2 loose cut-based photon ID.

Variable	Barrel selection	Endcap selection
p_{T}	> 100 GeV	
$\lvert\eta\rvert$	< 1.4442	> 1.566 and < 2.5
Pixel seed veto	fail	
H/E	< 0.04596	< 0.0590
$\sigma_{i\eta i\eta}$	< 0.0106	< 0.0272
I_c	< 1.694 GeV	< 2.089 GeV
I_n	$< (24.032\ \mathrm{GeV} + 0.01512 p_{\mathrm{T}} + 0.00002259 p_{\mathrm{T}}^2/\ \mathrm{GeV})$	$< (19.722\,\mathrm{GeV} + 0.0117 p_{\mathrm{T}} + 0.000023 p_{\mathrm{T}}^2/\ \mathrm{GeV})$
I_γ	$< (2.876\ \mathrm{GeV} + 0.004017 p_{\mathrm{T}})$	$< (4.162\ \mathrm{GeV} + 0.0037 p_{\mathrm{T}})$

CMS loose cut-based identification criteria, which have a selection efficiency of about 90%, together with a pixel seed veto that rejects any photons that have a track seed in the pixel detector consisting of at least 2 hits within a window around the supercluster. Photons are not considered for veto purposes in the signal region since the primary backgrounds do not typically include photons and furthermore, true photons can be radiated in the targeted signal process by the incoming or outgoing partons. The efficiency for photon reconstruction and identification was measured as a function of p_{T} and η using the tag-and-probe technique on a sample of $\mathrm{Z} \to \mathrm{e}^+\mathrm{e}^-$ events where the pixel seed veto was not applied and the electrons were treated as photon physics objects [172].

3.2.2 Jets and missing transverse momentum

The primary physics objects used in this analysis are b jets and double-b jets from Higgs decays as well as $p_{\mathrm{T}}^{\mathrm{miss}}$. This section describes the selection criteria for radius $\Delta R = 0.4$ and $\Delta R = 0.8$ jets, which may in general overlap, as well as energy sum

Table 3.6: Selections applied to AK4 jets in this analysis. The selections below the horizontal line are the standard CMS loose (2016) and tight (2017/2018) noise jet identification criteria.

Variable	Selection (2016)	Selection (2017/18)
p_{T}	> 30 GeV	
$\lvert\eta\rvert$	< 2.4	
ΔR (jet,control lepton)	> 0.4 for all leptons with $\frac{\lvert p_{\mathrm{Tjet}} - p_{\mathrm{Tlep}}\rvert}{p_{\mathrm{Tlep}}} < 1$	
Neutral hadron energy fraction	< 0.99	< 0.9
Photon energy fraction	< 0.99	< 0.9
Charged hadron energy fraction	> 0	> 0
Electron energy fraction	< 0.99	-
Constituents	≥ 2	≥ 2
Charged particle multiplicity	≥ 1	≥ 1

related variables including $p_{\mathrm{T}}^{\mathrm{miss}}$, H_{T}, H_{T5}, $H_{\mathrm{T}}^{\mathrm{miss}}$, and $p_{\mathrm{T,calo}}^{\mathrm{miss}}$.

The AK4 jets used in this analysis are corrected with the CHS algorithm and selected using the criteria given in Table 3.6. Only jets that do not overlap with control region leptons, whose transverse momentum is at least 30 GeV, and whose $|\eta|$ is less than 2.4 are considered as jet objects. Additionally, for data and standard simulated samples, noise jet identification criteria are applied to remove spurious jets originating from instrumental noise or mis-reconstruction [149]. These criteria are more than 99% efficient for true QCD jets. The noise jet identification criteria are not applied to the FastSim signal samples.

The AK8 jets are corrected with the PUPPI algorithm and then selected with the criteria given in Table 3.7. Only jets with $p_{\mathrm{T}} > 300$ GeV and $|\eta| < 2.4$ are used. As with AK4 jets, noise jet identification criteria are used to reject spurious jets in data and standard simulation samples, but not in FastSim samples. Furthermore, there is

Table 3.7: Selections applied to AK8 jets in this analysis. The selections below the horizontal line are the standard CMS loose (2016) and tight (2017/2018) noise jet identification criteria.

Variable	Selection (2016)	Selection (2017/18)
p_{T}	> 300 GeV	
$\lvert\eta\rvert$	< 2.4	
Neutral hadron energy fraction	< 0.99	< 0.9
Photon energy fraction	< 0.99	< 0.9
Charged hadron energy fraction	> 0	> 0
Electron energy fraction	< 0.99	-
Constituents	≥ 2	≥ 2
Charged particle multiplicity	≥ 1	≥ 1

a correction to the jet soft-drop mass derived by comparing the mean and width of the peak created by boosted W bosons in data and simulation. The widths are found to be consistent, and a 2.6 GeV upward correction is applied to simulation to match the distribution observed in data.

This analysis also uses the scalar sum of jet transverse momenta, H_{T}, the scalar sum of jet transverse momenta of jets up to an $|\eta|$ of 5, H_{T5}, the negative vector sum of jet transverse momenta, $H_{\mathrm{T}}^{\mathrm{miss}}$, the particle-flow missing momentum, $\vec{p}_{\mathrm{T}}^{\,\mathrm{miss}}$, and the calorimeter-level missing transverse momentum $\vec{p}_{\mathrm{T,calo}}^{\,\mathrm{miss}}$. H_{T} is calculated by simply summing the magnitude of the transverse momenta of the AK4 jet objects used in the analysis. H_{T5} is calculated by summing the magnitude of the transverse momenta of AK4 jets with the looser psuedorapidity selection $|\eta| < 5$ and without the noise jet identification requirements. $H_{\mathrm{T}}^{\mathrm{miss}}$ is the negative vector sum of AK4 jet momenta for all AK4 jets with $p_{\mathrm{T}} > 30$ GeV and $|\eta| < 5$ without any lepton overlap removal or noise jet identification requirements. $\vec{p}_{\mathrm{T}}^{\,\mathrm{miss}}$ is the particle-flow level missing transverse momentum with

jet energy corrections as described in Section 2.3.7. $\vec{p}_{\mathrm{T,calo}}^{\,\mathrm{miss}}$ is similarly the calorimeter level missing transverse momentum with jet energy corrections, also described in Section 2.3.7. In 2017, increased noise in the $2.65 < |\eta| < 3.139$ region of the CMS endcap electromagnetic calorimeter was not taken into account during the first rounds of offline reconstruction. This can lead to spurious $\vec{p}_{\mathrm{T}}^{\,\mathrm{miss}}$. For this reason, jets and unclustered PF candidates in this $|\eta|$ region are not included in particle flow $p_{\mathrm{T}}^{\mathrm{miss}}$ calculation for 2017 samples.

3.2.3 b tagging

In this analysis, b jets as well as double-b fat jets from the decay $\mathrm{H} \to \mathrm{b\bar{b}}$ are selecting using the DeepCSV and DeepDoubleBvL b- and double-b-tagging algorithms described in Section 2.3.6. For the resolved topology in which each b quark is associated with a b jet, a variable N_{b} is defined as a measure of the number of b jets in an event. N_{b} is defined as

$$N_{\mathrm{b}} = \begin{cases} 2 & N_{\mathrm{b,T}} = 2 \text{ and } N_{\mathrm{b,M}} = 2 \\ 3 & N_{\mathrm{b,T}} \geq 2 \text{ and } N_{\mathrm{b,M}} = 3 \text{ and } N_{\mathrm{b,L}} = 3 \\ 4 & N_{\mathrm{b,T}} \geq 2 \text{ and } N_{\mathrm{b,M}} = 3 \text{ and } N_{\mathrm{b,L}} \geq 4 \end{cases} \tag{3.2}$$

where $N_{\mathrm{b,L}}$, $N_{\mathrm{b,M}}$, and $N_{\mathrm{b,T}}$ are the number of AK4 jets passing the loose, medium, and tight working points of the DeepCSV discriminant respectively. This particular choice

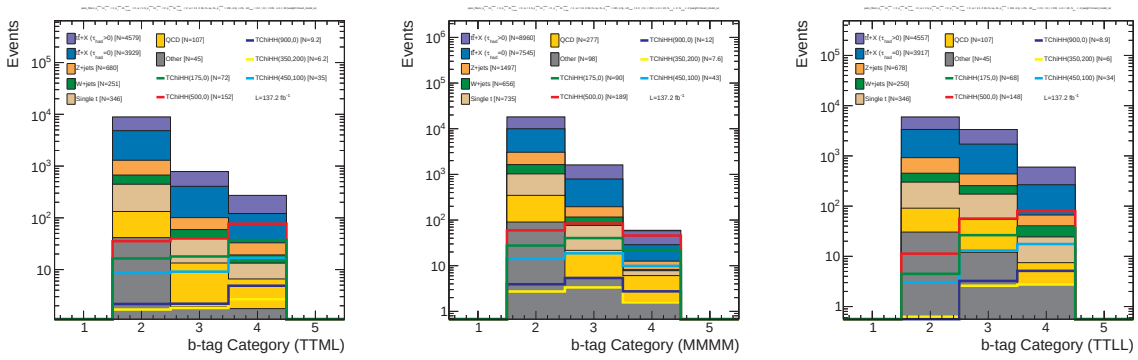

Figure 3.5: Simulated signal and background distributions of three possible definitions of N_{b} after the resolved topology baseline selection described in Section 4.1.2 except for the selection on N_{b}. Background is shown as stacked colored histogram while the colored outlines represent a selection of signal models. L, M, and T stand for the loose, medium, and tight DeepCSV working points respectively. The left plot shows the final definition using the TTML working points while the center plot shows N_{b} defined using the MMMM working points and the right plot shows N_{b} defined with the TTLL working points. The TTML definition is found to provide the highest sensitivity.

of working points has been chosen to optimize sensitivity to signal, taking into account the background passing each working point. A comparison between this choice and two others is shown in Figure 3.5. The chosen definition of N_{b} can be seen to significantly reduce background relative to the considered signal models. Note that N_{b} is only defined for events with at least 2 tight b-tagged jets. In control samples with fewer than 2 b-tagged jets, the number of medium b-tagged jets, $N_{\mathrm{b,M}}$, is used instead. For the boosted topology in which pairs of b quarks are merged into double-b jets, the number of double-b jets is quantified by N_{H}, the number of AK8 jets passing the loose working point of the DeepDoubleBvL algorithm. The identification and misidentification efficiency of these algorithms were measured in data as described in Ref. [3,150] and elaborated upon in the following paragraphs.

The DeepCSV mistag rate for light (u s d g) jets is measured in data and simulation using a QCD multijet sample and negative-tagged jets, jets that are tagged with a sign-agnostic version of the DeepCSV algorithm provided with only tracks with negative impact parameters and secondary vertices with negative flight distance. For light flavor jets that do not have nonprompt decays, detector resolution and misreconstruction contribute to a nearly symmetric distribution of tracks and secondary vertices with positive and negative displacement. Nonprompt decays of K^0_S and Λ can cause a slight asymmetry. The efficiency for mistagging light jets is derived from the number of negative-tagged jets with a slight correction factor from simulation.

The efficiency for DeepCSV charm jet mistagging is evaluated in CMS in two samples. A $\mathrm{W} + \mathrm{c}$ sample is selected using events with an isolated lepton and large m_T along with a jet containing a soft muon. For $\mathrm{W} + \mathrm{c}$ events, the muon has predominantly the opposite sign of the lepton from the W while for background events, the signs are largely uncorrelated. The same-sign selection can then be subtracted from the opposite sign selection to largely cancel out contributions from background events. The efficiency for selecting charm jets with the DeepCSV algorithm is then evaluated. An additional measurement is performed in a single-lepton $\mathrm{t\bar{t}}$ sample with a lepton, substantial m_T, and four jets, which are assigned to the two b jets and the partons from the W decay using the likelihood of the invariant masses of the W candidate and the hadronic t candidate. The jets assigned as the b jets by the mass-based assignment are then required to pass b-tagging requirements. A maximum likelihood fit including various nuisance parame-

ters is then performed to extract the charm mistag rate and associated uncertainties. A weighted average of the charm mistag rates from the two samples with shared uncertainties correlated is used to derive final charm mistag rates and subsequently scale factors and uncertainties.

The DeepCSV b-tagging efficiency is measured in several ways. In a muon-enriched jet sample, the shape of $p_{\mathrm{T}}^{\mathrm{rel}}$, the p_{T} of the muon relative to the jet axis, as well as the jet probability discriminant based only on the probability the jet tracks originate at the primary vertex are fit with shapes from simulation to subtract the background contribution and the jet that contains the muon is used to measure the b-tagging efficiency. An alternative to the template method that involves solving a system of equations for tagging efficiencies in 8 categories split by DeepCSV, a version of the jet probability discriminant based on tracks, and $p_{\mathrm{T}}^{\mathrm{rel}}$ is also used to derive tagging efficiencies. A simultaneous fit to data and simulation of a kinematic b jet discriminant in a dilepton $\mathrm{t\bar{t}}$ sample with opposite flavor leptons is used to derive another measurement of b-tagging efficiency from this sample. A single lepton $\mathrm{t\bar{t}}$ sample is also used with a mass-based likelihood assignment of partons to jets where one b jet is required to pass the tight working point of the CSVv2 b-tagging algorithm and the other is used to measure the efficiency of the DeepCSV algorithm. The b-tagging efficiencies measured in the muon-jet sample, the dilepton $\mathrm{t\bar{t}}$ sample, and the single lepton $\mathrm{t\bar{t}}$ samples are combined to produce final b-tagging efficiency measurements with associated uncertainties.

The tagging efficiencies for the DeepDoubleBvL tagger are derived from QCD

multijet and $Z \to b\bar{b}$ samples. One method uses a boosted decision tree (BDT) trained to select $g \to b\bar{b}$ and $g \to c\bar{c}$ gluon splitting jets in the QCD multijet sample that are similar to the target heavy resonance $b\ \bar{b}$ in order to measure efficiencies in data and simulation. The second method similarly targets gluon splitting using jets containing soft muons rather a multivariate selector. The final method measures the efficiency for $Z \to b\bar{b}$ in a sample with AK8 jets with mass near the Z, which has a considerable background from QCD multijet events that must be subtracted. The combination of these three methods is used to determine the final efficiencies for the DeepDoubleBvL tagger and the associated uncertainties. The DeepDoubleBvL mistag efficiencies are measured specifically for this analysis using a region with two AK8 jets with $p_T > 300$ GeV, soft-drop mass between 60 and 260 GeV, $H_T > 600$ GeV, $200 < p_T^{miss} < 300$ GeV, and various quality cuts to remove events with spurious p_T^{miss}. This selection is identical to the boosted topology baseline selection described in Section 4.1.3 but with the p_T^{miss} requirement changed to be in the range 200–300 GeV. In this region the background is dominated by leptonically decaying W or Z bosons with jets and $t\bar{t}$ events. The mistag efficiency is measured in bins of p_T and the number of AK4 b jets identified with the medium working point of the DeepCSV tagger. The difference between mistag rates in simulation with the baseline selection and the low p_T^{miss} sideband is taken as a systematic uncertainty.

3.2.4 Higgs candidates

For low momentum Higgs bosons, the b jets generated in the Higgs boson decay are typically reconstructed as two separate b-tagged AK4 jets. For high momentum Higgs bosons, the two b jets from the decay of the Higgs boson may overlap and instead be reconstructed as a single double-b AK8 jet. To maximize sensitivity to different physics scenarios, this analysis considers both a "boosted" topology in which each Higgs boson is reconstructed as a single AK8 jet, and a resolved topology in which each Higgs boson is reconstructed as two AK4 jets. Let ΔR_{bb} be the angular separation between the b jets produced in a single Higgs decay as shown in Figure 3.6. Figure 3.7 illustrates the regions of ΔR_{bb} space to which the resolved and boosted methods are sensitive, as well as the distribution of the $m(\widetilde{\chi}_1^0) = 950$ GeV TChiHH-G signal model in ΔR_{bb} space. The resolved topology reconstruction method is sensitive to the case both Higgs boson candidates have $\Delta R_{\mathrm{bb}} > 0.4$ while the boosted topology reconstruction method is sensitive when both Higgs boson candidates have $\Delta R_{\mathrm{bb}} < 0.8$. There is some overlap of these two phase space regions in which the resolved reconstruction method is prioritized as studies showed this slightly improved sensitivity.

In the resolved topology, the four AK4 jets with the highest DeepCSV score are selected to reconstruct the Higgs boson candidates. There are three possible ways to make two disjoint pairs from the four selected jets. If $m_{(\mathrm{bb})_1}$ and $m_{(\mathrm{bb})_2}$ are the invariant masses of the first and second pair of jets respectively, the pairing that minimizes $\Delta m_{\mathrm{bb}} = |m_{(\mathrm{bb})_1} - m_{(\mathrm{bb})_2}|$ is chosen to be the reconstructed Higgs boson candidates. Because this

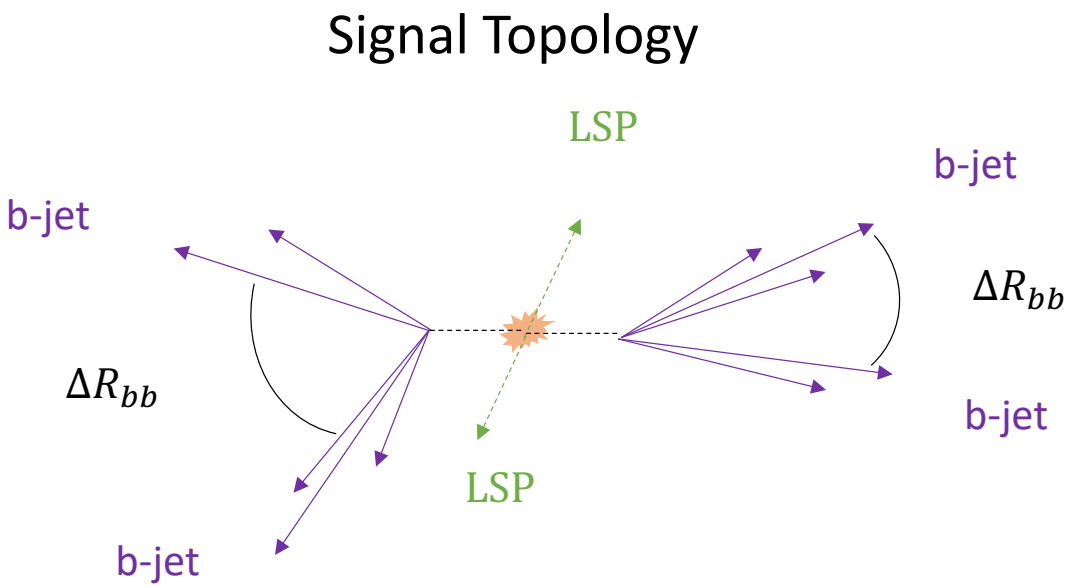

Figure 3.6: Signal event topology in the TChiHH and TChiHH-G models. One typically observes two pairs of b jets and missing transverse momentum in the final state. The angle between b jets in a pair tends to decrease as the momentum of the parent Higgs increases.

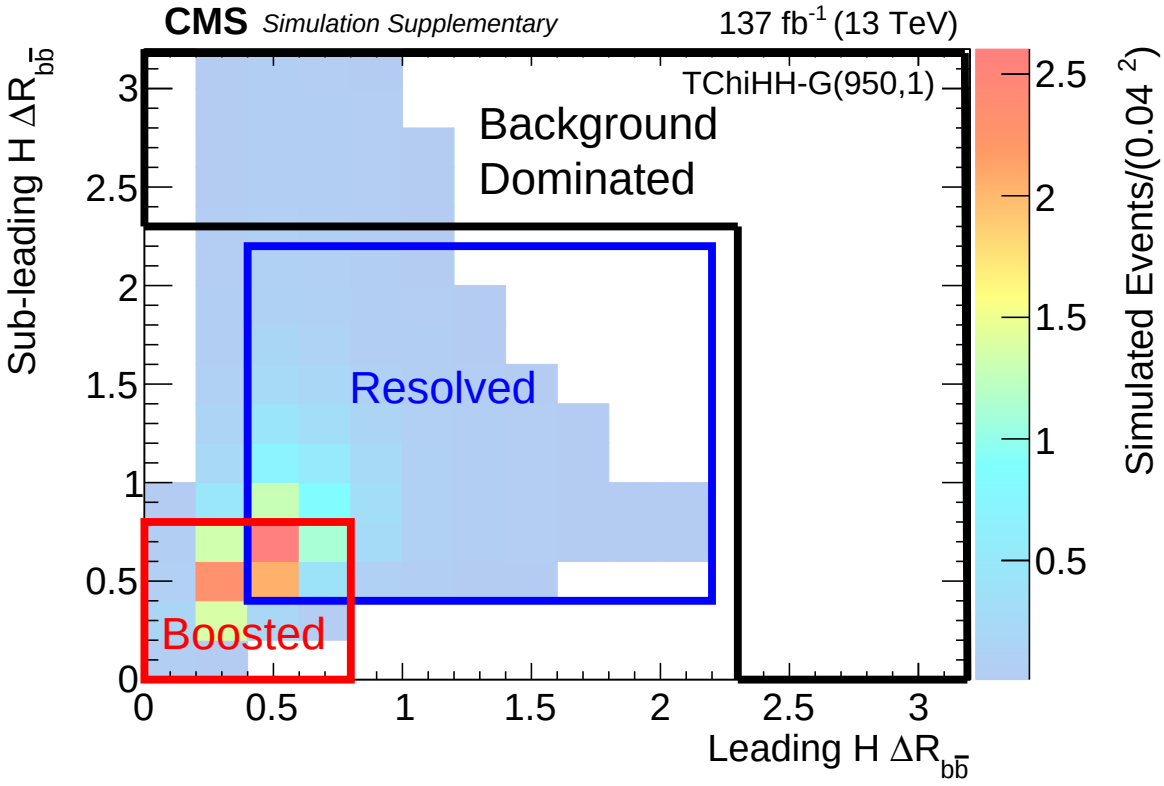

Figure 3.7: Two dimensional distribution in ΔR_{bb} of the leading and subleading Higgs boson candidates for simulated ($m(\widetilde{\chi}_1^0) = 950\,\mathrm{GeV}$) TChiHH-G events, showing the approximate phase space coverage of the resolved and boosted topologies. The resolved topology extends from $\Delta R_{\mathrm{bb}} = 0.4$ up to 2.2, corresponding to the middle of the histogram, while the lower left region from $\Delta R_{\mathrm{bb}} = 0$ to 0.8 corresponds to the boosted topology.

method generates the Higgs boson candidates solely based the difference between their masses, the average mass of the Higgs candidates $\langle m_{\mathrm{bb}} \rangle = \frac{m_{(\mathrm{bb})_1} + m_{(\mathrm{bb})_2}}{2}$ is unbiased and can be used as an analysis variable in the background estimation method as detailed in Section 4.2. The variable ΔR_{max}, the greater of the ΔR_{bb} between the two Higgs boson candidates is also used the analysis to aid in signal-background discrimination.

For the boosted topology, the two AK8 jets with the highest p_{T} are considered to be the Higgs boson candidates.

3.3 Data samples

3.3.1 Event samples

The data samples used in this analysis consist of 13 TeV proton-proton collision data recorded by the CMS experiment in Run 2 between 2016 and 2018. CMS data are split into primary data sets based on the triggers passed by each event. Events that pass multiple triggers may appear in multiple data sets. This analysis primarily uses $p_{\mathrm{T}}^{\mathrm{miss}}$ triggers, though single-electron, single-muon, single-photon, and jet/H_{T} triggers are used for control samples, validation samples, and auxiliary measurements. Section 3.3.4 describes the trigger efficiency measurements for the triggers used in this analysis. Events passing $p_{\mathrm{T}}^{\mathrm{miss}}$ triggers are included in the `MET` data set, those passing single-muon triggers are included in the `SingleMuon` data set, and those passing jet or H_{T} triggers are included in the `JetHT` data set. Events passing single-electron and single-photon triggers are included in the

Table 3.8: Primary data sets used in this analysis and total certified luminosity in fb^{-1} of each data set for each era.

		Luminosity [fb^{-1}]								
Year	Primary Data set	A	B	C	D	E	F	G	H	Total
2016	MET	–	5.75	2.57	4.24	3.92	3.10	7.58	8.65	35.82
	SingleElectron	–	5.75	2.57	4.24	4.03	3.10	7.58	8.65	35.92
	SinglePhoton	–	5.75	2.57	4.24	4.03	3.10	7.58	8.65	35.92
	SingleMuon	–	5.75	2.57	4.24	4.03	3.10	7.58	8.65	35.92
	JetHT	–	5.75	2.57	4.24	4.02	3.10	7.58	8.65	35.92
2017	MET	–	4.79	9.63	4.25	9.31	13.50	–	–	41.49
	SingleElectron	–	4.79	9.63	4.25	9.31	13.54	–	–	41.53
	SinglePhoton	–	4.79	9.63	4.25	9.31	13.54	–	–	41.53
	SingleMuon	–	4.79	9.63	4.25	9.31	13.54	–	–	41.53
	JetHT	–	4.79	9.63	4.25	9.31	13.53	–	–	41.52
2018	MET	14.02	6.91	6.89	31.72	–	–	–	–	59.55
	EGamma	13.95	7.06	6.89	31.74	–	–	–	–	59.64
	SingleMuon	14.03	7.06	6.89	31.74	–	–	–	–	59.73
	JetHT	14.03	7.06	6.89	31.71	–	–	–	–	59.69

`SingleElectron` and `SinglePhoton` data sets respectively in 2016 and 2017, but both put into the `EGamma` data set in 2018. To avoid double-counting events, the data sets are ordered and events that are already contained in a prior data set are removed from subsequent data sets. The ordering used is: `MET`, `SingleElectron`/`SinglePhoton`/`EGamma`, `SingleMuon`, and `JetHT`. Only data where all CMS subsystems were operating acceptably is certified by CMS for analysis use. Table 3.8 shows the primary data sets used in the analysis together with the integrated luminosity of used data certified good during each era of each year of data taking. The total integrated luminosity of 13 TeV data used in the MET data set is approximately 137 fb^{-1}.

Simulated samples are generated following the procedure outlined in Section 1.2.5.

The simulated background samples used in this analysis are listed in Tables 3.9 and 3.10. The generator used to generate the matrix elements are listed next to each sample. These include MadGraph5_aMC@NLO [153, 154] 2.2.2 (2016 background samples) and 2.4.2 (2017/2018 background samples and all signal samples) in leading and next-to-leading order modes, Powheg v2.0 [363–367], JHUGen 7.0.11 [368, 369], and Pythia 8.205 [370]. Samples generated with Powheg use NLO precision while those generated with JHUGen and Pythia use LO precision. The samples generated using MadGraph5_aMC@NLO at LO employ MLM parton matching [153,371], while those generated using MadGraph5_aMC@NLO at NLO employ FXFX matching [372]. The W+jets and Z+jets samples include up to four additional partons at the matrix element level while the $t\bar{t}$+jets samples include up to three additional partons at the matrix element level.

The simulated signal samples used in this analysis corresponding to the simplified SUSY models described in Section 3.1 are given in Table 3.11. They were generated with MadGraph5_aMC@NLO in leading-order mode with up to two additional partons at the matrix-element level. The TChiHH-G model samples were generated by scanning over values of $m(\widetilde{\chi}_1^0)$ from 127 to 1500 GeV while keeping $m(\widetilde{\mathrm{G}})$ fixed at 1 GeV. The TChiHH model samples were generated by scanning over values of $m(\widetilde{\chi}_2^0) = m(\widetilde{\chi}_3^0)$ from 127 to 1200 GeV and simultaneous scanning over values of $m(\widetilde{\chi}_1^0)$ from 1 to $m(\widetilde{\chi}_2^0) - 125$ GeV. Finally, the T5HH model samples were generated by scanning over values of $m(\widetilde{\mathrm{g}})$ from 1000 to 2500 GeV while fixing $m(\widetilde{\chi}_2^0)$ fixed to $m(\widetilde{\mathrm{g}}) - 50$ GeV and $m(\widetilde{\chi}_1^0)$ fixed

to 1 GeV. For the TChiHH-G and TChiHH samples, only $H \to b\bar{b}$ decays are generated; auxiliary simulations indicate that inclusion of other decays modes could slightly boost the sensitivity of the analysis, but are not considered here. All simulated SUSY particles are decayed promptly. The decays of all particles in the signal samples are handled by PYTHIA using a simple n-body phase space model [370], which neglects polarization effects.

After the matrix elements are generated, all samples use PYTHIA 8.205 to simulate parton showering and hadronization. The CUETP8M1 tune [373] tune derived from measurements in CMS data is used in all 2016 simulated samples while the CP5 and CP2 tunes [374], again derived from from CMS measurements, are used for 2017 and 2018 simulated samples for the background and signal samples respectively. Samples generated with the CUETP8M1 tune use the NNPDF3.0LO or NNPLDF3.0NLO families of parton distribution functions [155] for LO and NLO samples respectively while samples generated with the CP5 and CP2 tunes use the NNPDF3.1LO and NNPDF3.1NLO families of parton distribution functions [139] for LO and NLO samples respectively.

As described in Section 2.2.5, the detector response for background samples is modeled with the GEANT4 program [205] while the detector response for signal samples is modeled with the CMS FASTSIM software [207, 208] in order to minimize the time needed to scan over many different mass points. Pileup collisions are simulated with PYTHIA and are added to simulated events using the premixing technique described in Section 2.2.5.

Since the number of simulated events generated does not in general match the num-

ber of events expected from the integrated luminosity of the collected data, simulated events are multiplied by a weighting factor so that the weighted number of events in simulation is equal to the number of expected events in data, the cross section σ times the luminosity $\mathcal{L}$. This is done separately for each year. The cross sections used in this weighting are approximately those given in Tables 3.9–3.11. The exact cross sections vary slightly by year and generator settings. The total cross section for $\mathrm{t\bar{t}}$+jets production is calculated at NNLO+NNLL precision in Ref. [375] using the Top++ program [376] while branching fractions are taken from Ref. [377] and the fraction passing $p_{\mathrm{T}}^{\mathrm{miss}}$ cuts is determined with MadGraph5_aMC@NLO at LO. Cross sections for $\mathrm{t\bar{t}}\gamma$, $\mathrm{t\bar{t}Z}$, $\mathrm{t\bar{t}W}$, and $\mathrm{t\bar{t}t\bar{t}}$ are derived from MadGraph5_aMC@NLO with NLO precision, and that for $\mathrm{t\bar{t}H}$ is calculated in Ref. [151] with NNLO precision. The total cross sections for Drell-Yan+jets, $\mathrm{Z} \to \nu\bar{\nu}$+jets, and W+jets events are derived at NNLO with the FEWZ 3.1 program [378–380] with H_{T} fractions determined by the generator at LO. The cross sections for γ+jets events as well as those for QCD multijet events are derived at LO with MadGraph5_aMC@NLO. The cross sections for single top samples including tW are evaluated at NLO with Powheg for all processes except for the s-channel process, which is evaluated instead with MadGraph5_aMC@NLO. The cross section for WW production is taken from the NNLO calculation in Ref. [381], the cross section for WZ production is evaluated with MadGraph5_aMC@NLO or Powheg at NLO, and the cross section for ZZ production is taken from the NNLO calculation in Ref. [382]. WH and ZH sample cross sections are based the NNLO calculation in Ref. [151] together

with branching fractions from the same reference as well as Ref. [377]. Cross sections for pure higgsino production for the two neutral states (N1N2), the two charged states (C1C2), and the combination of a charged state and a neutral state (CN) are calculated with the Resummino program [348, 349] to NLO+NLL precision and are a function of the higgsino mass. Cross sections for gluino production are calculated to approximately NNLO+NNLL precision with the NNLL-fast program [354–361] and are a function of the gluino mass. The higgsino and gluino cross sections used for the TChiHH-G, TChiHH, and T5HH samples as a function of higgsino or gluino mass are shown in Figure 3.4 in red, violet, and orange respectively.

Some of the phase space simulated in different simulation samples overlaps, and events from one sample must be removed to avoid double counting. Events in the inclusive $\mathrm{t\bar{t}}$+jets samples are removed if the generator-level $p_{\mathrm{T}}^{\mathrm{miss}}$ is greater than that of the dedicated high $p_{\mathrm{T}}^{\mathrm{miss}}$ samples. Events in the inclusive and high $p_{\mathrm{T}}^{\mathrm{miss}}\mathrm{t\bar{t}}$+jets samples are removed if there is a generator-level photon that would have been generated by MadGraph5_aMC@NLO in the $\mathrm{t\bar{t}\gamma}$+jets sample. Finally, events in the inclusive Drell-Yan+jets and W+jets samples are removed if the generator-level H_{T} is greater than 70 GeV to avoid overlap with the H_{T}-binned samples.

3.3.2 Filters

Additional filters are applied to reject events with well-defined spurious sources of missing transverse momentum. Some of these filters are standard for data analysis within

Table 3.9: Simulated background samples used in this analysis from the $t\bar{t}+X$ and Z+jets categories as well as γ +jets samples.

Sample	Generator	Cross Section [pb]	Plotting Category
$t\bar{t}$+jets with 1 lepton from t	MadGraph5_aMC@NLO (LO)	182	$t\bar{t}+X$
$t\bar{t}$+jets with 1 lepton from $\bar{t}$	MadGraph5_aMC@NLO (LO)	182	$t\bar{t}+X$
$t\bar{t}$+jets with 2 leptons	MadGraph5_aMC@NLO (LO)	87.3	$t\bar{t}+X$
$t\bar{t}$+jets with 1 lepton from t and $p_T^{miss} > 150$ GeV (2016/2017)	MadGraph5_aMC@NLO (LO)	10.4	$t\bar{t}+X$
$t\bar{t}$+jets with 1 lepton from $\bar{t}$ and $p_T^{miss} > 150$ GeV (2016/2017)	MadGraph5_aMC@NLO (LO)	10.4	$t\bar{t}+X$
$t\bar{t}$+jets with 2 leptons and $p_T^{miss} > 150$ GeV (2016/2017)	MadGraph5_aMC@NLO (LO)	6.14	$t\bar{t}+X$
$t\bar{t}$+jets with 1 lepton from t and $p_T^{miss} > 80$ GeV (2018)	MadGraph5_aMC@NLO (LO)	54.0	$t\bar{t}+X$
$t\bar{t}$+jets with 1 lepton from $\bar{t}$ and $p_T^{miss} > 80$ GeV (2018)	MadGraph5_aMC@NLO (LO)	54.0	$t\bar{t}+X$
$t\bar{t}$+jets with 2 leptons and $p_T^{miss} > 80$ GeV (2018)	MadGraph5_aMC@NLO (LO)	37.7	$t\bar{t}+X$
$t\bar{t}\gamma$+jets	MadGraph5_aMC@NLO (NLO)	3.70	$t\bar{t}+X$
$t\bar{t}Z$, $Z \to \ell^+\ell^-/\nu\nu$	MadGraph5_aMC@NLO (NLO)	0.243	$t\bar{t}+X$
$t\bar{t}Z$, $Z \to q\bar{q}$	MadGraph5_aMC@NLO (NLO)	0.510	$t\bar{t}+X$
$t\bar{t}W$, $W \to \ell\nu$	MadGraph5_aMC@NLO (NLO)	0.204	$t\bar{t}+X$
$t\bar{t}W$, $W \to q\bar{q}'$	MadGraph5_aMC@NLO (NLO)	0.406	$t\bar{t}+X$
$t\bar{t}t\bar{t}$	MadGraph5_aMC@NLO (NLO)	0.00821	$t\bar{t}+X$
$t\bar{t}H$, $H \to b\bar{b}$	Powheg	0.293	$t\bar{t}+X$
$Z/\gamma* \to \ell^+\ell^-$+jets, $m_{\ell\ell} > 50$ GeV	MadGraph5_aMC@NLO (LO)	6230	Z+jets
$Z/\gamma* \to \ell^+\ell^-$+jets, $m_{\ell\ell} > 50$ GeV $70 < H_T < 100$ GeV	MadGraph5_aMC@NLO (LO)	171	Z+jets
$Z/\gamma* \to \ell^+\ell^-$+jets, $m_{\ell\ell} > 50$ GeV $100 < H_T < 200$ GeV	MadGraph5_aMC@NLO (LO)	188	Z+jets
$Z/\gamma* \to \ell^+\ell^-$+jets, $m_{\ell\ell} > 50$ GeV $200 < H_T < 400$ GeV	MadGraph5_aMC@NLO (LO)	56.5	Z+jets
$Z/\gamma* \to \ell^+\ell^-$+jets, $m_{\ell\ell} > 50$ GeV $400 < H_T < 600$ GeV	MadGraph5_aMC@NLO (LO)	8.05	Z+jets
$Z/\gamma* \to \ell^+\ell^-$+jets, $m_{\ell\ell} > 50$ GeV $600 < H_T < 800$ GeV	MadGraph5_aMC@NLO (LO)	1.97	Z+jets
$Z/\gamma* \to \ell^+\ell^-$+jets, $m_{\ell\ell} > 50$ GeV $800 < H_T < 1200$ GeV	MadGraph5_aMC@NLO (LO)	0.856	Z+jets
$Z/\gamma* \to \ell^+\ell^-$+jets, $m_{\ell\ell} > 50$ GeV $1200 < H_T < 2500$ GeV	MadGraph5_aMC@NLO (LO)	0.193	Z+jets
$Z/\gamma* \to \ell^+\ell^-$+jets, $m_{\ell\ell} > 50$ GeV $H_T > 2500$ GeV	MadGraph5_aMC@NLO (LO)	0.00274	Z+jets
$Z \to \nu\bar{\nu}$+jets, $m_{\ell\ell} > 50$ GeV $100 < H_T < 200$ GeV	MadGraph5_aMC@NLO (LO)	345	Z+jets
$Z \to \nu\bar{\nu}$+jets, $m_{\ell\ell} > 50$ GeV $200 < H_T < 400$ GeV	MadGraph5_aMC@NLO (LO)	103	Z+jets
$Z \to \nu\bar{\nu}$+jets, $m_{\ell\ell} > 50$ GeV $400 < H_T < 600$ GeV	MadGraph5_aMC@NLO (LO)	14.6	Z+jets
$Z \to \nu\bar{\nu}$+jets, $m_{\ell\ell} > 50$ GeV $600 < H_T < 800$ GeV	MadGraph5_aMC@NLO (LO)	3.61	Z+jets
$Z \to \nu\bar{\nu}$+jets, $m_{\ell\ell} > 50$ GeV $800 < H_T < 1200$ GeV	MadGraph5_aMC@NLO (LO)	1.57	Z+jets
$Z \to \nu\bar{\nu}$+jets, $m_{\ell\ell} > 50$ GeV $1200 < H_T < 2500$ GeV	MadGraph5_aMC@NLO (LO)	0.344	Z+jets
$Z \to \nu\bar{\nu}$+jets, $m_{\ell\ell} > 50$ GeV $H_T > 2500$ GeV	MadGraph5_aMC@NLO (LO)	0.00767	Z+jets
γ+jets, $100 < H_T < 200$ GeV	MadGraph5_aMC@NLO (LO)	5030	N/A
γ+jets, $200 < H_T < 400$ GeV	MadGraph5_aMC@NLO (LO)	1130	N/A
γ+jets, $400 < H_T < 600$ GeV	MadGraph5_aMC@NLO (LO)	125	N/A
γ+jets, $H_T > 600$ GeV	MadGraph5_aMC@NLO (LO)	40.5	N/A

Table 3.10: Simulated background samples used in this analysis from the W+jets, QCD, Single t, and other categories.

Sample	Generator	Cross Section [pb]	Plotting Category
W+jets	MadGraph5_aMC@NLO (LO)	61500	W+jets
W+jets, $70 < H_T < 100$ GeV	MadGraph5_aMC@NLO (LO)	1500	W+jets
W+jets, $100 < H_T < 200$ GeV	MadGraph5_aMC@NLO (LO)	1610	W+jets
W+jets, $200 < H_T < 400$ GeV	MadGraph5_aMC@NLO (LO)	478	W+jets
W+jets, $400 < H_T < 600$ GeV	MadGraph5_aMC@NLO (LO)	67.9	W+jets
W+jets, $600 < H_T < 800$ GeV	MadGraph5_aMC@NLO (LO)	16.9	W+jets
W+jets, $800 < H_T < 1200$ GeV	MadGraph5_aMC@NLO (LO)	7.63	W+jets
W+jets, $1200 < H_T < 2500$ GeV	MadGraph5_aMC@NLO (LO)	1.66	W+jets
W+jets, $H_T > 2500$ GeV	MadGraph5_aMC@NLO (LO)	0.0394	W+jets
QCD multijet $100 < H_T < 200$ GeV	MadGraph5_aMC@NLO (LO)	23700000	QCD
QCD multijet $200 < H_T < 300$ GeV	MadGraph5_aMC@NLO (LO)	1560000	QCD
QCD multijet $300 < H_T < 500$ GeV	MadGraph5_aMC@NLO (LO)	323000	QCD
QCD multijet $500 < H_T < 700$ GeV	MadGraph5_aMC@NLO (LO)	30100	QCD
QCD multijet $700 < H_T < 1000$ GeV	MadGraph5_aMC@NLO (LO)	6310	QCD
QCD multijet $1000 < H_T < 1500$ GeV	MadGraph5_aMC@NLO (LO)	1090	QCD
QCD multijet $1500 < H_T < 2000$ GeV	MadGraph5_aMC@NLO (LO)	99.4	QCD
QCD multijet $H_T > 2000$ GeV	MadGraph5_aMC@NLO (LO)	20.2	QCD
tW^-, no fully hadronic decays	Powheg	18.6	Single t/Other
$\bar{t}W^+$, no fully hadronic decays	Powheg	18.5	Single t/Other
$\bar{t}$, t channel	Powheg	69.1	Single t/Other
t, t channel	Powheg	115	Single t/Other
$t/\bar{t} \to b\ell\nu$, s channel	MadGraph5_aMC@NLO (NLO)	3.74	Single t/Other
WH, $H \to b\bar{b}$	MadGraph5_aMC@NLO (NLO) (2016), JHUGen (2017/2018)	0.262	Other
$WW \to \ell\ell'\nu\nu'$	Powheg	12.2	Other
$WW \to \ell\nu q\bar{q}'$	Powheg	50.0	Other
$WZ \to \ell\nu q\bar{q}$	MadGraph5_aMC@NLO (NLO)	11.8	Other
$WZ \to \ell\nu\nu'\bar{\nu}'$	MadGraph5_aMC@NLO (NLO)	3.32	Other
$WZ \to q\bar{q}'\ell^+\ell^-$	MadGraph5_aMC@NLO (NLO)	5.61	Other
$WZ \to \ell\nu\ell^+\ell^-$	Powheg (2016/2018) MadGraph5_aMC@NLO (2017)	4.43	Other
$ZH \to \nu\bar{\nu}b\bar{b}$	Powheg	0.103	Other
ZZ	Pythia	16.5	Other

Table 3.11: Signal samples used in this analysis.

Sample	Generator	Cross Section [pb]	Plotting Category
$\widetilde{\chi}_1^0\widetilde{\chi}_1^0 \to HH\widetilde{G}\widetilde{G}$, $H \to b\bar{b}$	MadGraph5_aMC@NLO (LO)	(Higgsino N1N2 + C1C2 + 2CN)×BR($H \to b\bar{b}$)^2	TChiHH-G
$\widetilde{\chi}_2^0\widetilde{\chi}_3^0 \to HH\widetilde{\chi}_1^0\widetilde{\chi}_1^0$, $H \to b\bar{b}$	MadGraph5_aMC@NLO (LO)	(Higgsino N1N2)×BR($H \to b\bar{b}$)^2	TChiHH
$\widetilde{g}\widetilde{g} \to q\bar{q}q\bar{q}\widetilde{\chi}_2^0\widetilde{\chi}_2^0$, $\widetilde{\chi}_2^0 \to H\widetilde{\chi}_1^0$	MadGraph5_aMC@NLO (LO)	Gluino pair production	T5HH

CMS [191], while others were specifically designed for a supersymmetry search in the jets+$p_{\mathrm{T}}^{\mathrm{miss}}$ channel [135].

- **HCAL noise filter** Events with anomalous energy deposits in the barrel and endcap HCAL are identified with a dedicated algorithm that uses pulse shape and timing information [191]. Such events are rejected and not used in this analysis.

- **HCAL track-based noise filter** An additional algorithm identifies anomalous HCAL energy deposits within tracker η acceptance by comparing energy deposits with tracker information [191]. Events that have identified anomalous energy deposits are rejected.

- **ECAL endcap supercrystal filter** Some sets of ECAL endcap supercrystals are observed to produce large anomalous pulses. Events with large energy deposits in these crystals are removed in data only [191].

- **ECAL dead cell filter** The readout electronics for certain ECAL towers are not functional. However, the energy deposited in the towers can be estimated from the trigger primitives since the level 1 trigger path is functional [191]. A filter removes events for which the cell energy is close to the trigger primitive saturation limit where the energy cannot be estimated.

- **Primary vertex filter** To reject events with misreconstructed vertices that can also lead to spurious $p_{\mathrm{T}}^{\mathrm{miss}}$, the primary vertex considered must lie within 24 cm of the center of the detector along the z axis, lie within 2 cm in the transverse plane,

and have at least 4 effective degrees of freedom used in the vertex fit described in Ref. [216].

- **Beam halo filter** Beam halo particles produced by the LHC can interact with the CMS detectors, most commonly the CSCs and calorimeters, producing spurious signals. A filter was designed to remove events that have calorimeter deposits and CSC hits consistent with beam halo particles [191]. This filter is not applied to samples generated with FastSim.

- **Reconstruction filters** High p_{T} but low quality tracks can also cause significant spurious $p_{\mathrm{T}}^{\mathrm{miss}}$. Events with tracks that have high p_{T} and high relative uncertainty evaluated from either the inner track or a combination of the inner track and muon detector tracks are rejected [191].

- **FastSIM jet filter** Signal events generated with FastSim can have spurious jets that are not observed in the full Geant4 simulation. Events with an AK4 jet with $|\eta| < 2.5$, $p_{\mathrm{T}} > 20$ GeV, and charged hadron fraction less than 0.1 that do not have a matching jet at generator level are rejected.

- **Muon jet filter** It is found that jets that originate from misreconstructed muons can have highly overestimated p_{T} and produce large spurious $p_{\mathrm{T}}^{\mathrm{miss}}$. To mitigate this effect, events containing a jet with $p_{\mathrm{T}} > 200$ GeV, muon energy fraction greater that 0.5, and $\Delta\phi(\mathrm{jet}, \vec{p}_{\mathrm{T}}^{\mathrm{miss}}) > \pi - 0.4$ are removed.

- **Low neutral jet filter** Similarly, events with anomalously low electromagnetic

energy fraction are found to often have overestimated p_{T}. Subsequently, events are removed if the leading p_{T} jet had neutral electromagnetic energy fraction less than 0.03 and $\Delta\phi(\mathrm{jet}, \vec{p}_{\mathrm{T}}^{\mathrm{miss}}) > \pi - 0.4$.

- **ECAL noise jet filter** Despite the correction described in Section 3.2.2, noise in the endcap and forward calorimeters in 2017 can produce events with anomalous $p_{\mathrm{T}}^{\mathrm{miss}}$. If either of the two leading p_{T} jets have $2.4 < |\eta| < 5$, $p_{\mathrm{T}} > 250$ GeV, and $\Delta\phi(\mathrm{jet}, \vec{p}_{\mathrm{T}}^{\mathrm{miss}}) > 2.6$ or $\Delta\phi(\mathrm{jet}, \vec{p}_{\mathrm{T}}^{\mathrm{miss}}) < 0.1$, then the event is removed.

- **HT ratio noise filter** To further mitigate the effect of endcap and forward calorimeter noise on $p_{\mathrm{T}}^{\mathrm{miss}}$, an additional requirement is imposed on events with large transverse momentum in the forward regions. H_{T} is the sum of jet p_{T} for jets with $|\eta| < 2.4$ while H_{T5} is the sum of jet p_{T} for jets with $|\eta| < 5$. Events for which $H_{\mathrm{T5}}/H_{\mathrm{T}} > 1.2$ and the leading jet satisfies $\Delta\phi(\mathrm{jet}, \vec{p}_{\mathrm{T}}^{\mathrm{miss}}) > 5.3 H_{\mathrm{T5}}/H_{\mathrm{T}} - 4.78$ are rejected.

- **HCAL dead sector filter** During the later portion of data taking in 2018, two endcap HCAL sectors were not operational, which can lead to various particle flow misreconstruction. For this reason, events containing electrons passing the veto criteria with $I_{\mathrm{mini}} < 0.1$ in the region $-3.0 < \eta < -1.4$ and $-1.57 < \phi < -0.87$, or AK4 jets in the region $-3.2 < \eta < -1.2$ and $-1.77 < \phi < -0.67$ are removed from both affected data samples and an equivalent portion of 2018 simulated samples.

- **MET misreconstruction rejection cuts** Additionally, events with problematic

$p_{\mathrm{T}}^{\mathrm{miss}}$ reconstruction may be removed at the analysis selection level. Events where the particle-flow $p_{\mathrm{T}}^{\mathrm{miss}}$ is much larger than the calorimeter-based $p_{\mathrm{T,calo}}^{\mathrm{miss}}$ or jet-level $H_{\mathrm{T}}^{\mathrm{miss}}$, which should agree with $p_{\mathrm{T}}^{\mathrm{miss}}$ up to soft unclustered energy, are removed as described in Section 4.1 since the $p_{\mathrm{T}}^{\mathrm{miss}}$ in such events may have arisen from particle flow reconstruction failures.

3.3.3 Corrections

Energy scale corrections used in this analysis include the standard reconstruction-level energy corrections described in Section 2.3, the $p_{\mathrm{T}}^{\mathrm{miss}}$ correction for the endcap noise issue described in Section 3.2.2, the correction to AK8 jet soft-drop mass described in the same section, a correction to $p_{\mathrm{T}}^{\mathrm{miss}}$ in FastSim samples, and a correction to b jets in FastSim samples in 2017 and 2018. In all FastSim samples, it is found that the $p_{\mathrm{T}}^{\mathrm{miss}}$ resolution is worse than that for the full Geant4 simulation and data. Subsequently, the value of reconstructed $p_{\mathrm{T}}^{\mathrm{miss}}$ used in the analysis is taken to be the average of the nominal reconstructed value and the generator-level value. It was also found that for high p_{T} b jets in the 2017 and 2018 FastSim samples, the reconstructed energy is biased to be about 3% higher than that of the generator level jets. For this reason, the energy of AK4 b jets and derived variables as well as the soft drop mass of AK8 jets containing AK4 b jets is scaled down by about 3% for the boosted topology. For the resolved topology, the typical b jet p_{T} is lower so no correction is applied.

In addition to energy scale corrections, additional corrections for simulated samples

are applied as scale factors in order to account for known problems in simulation and differences between the simulated detector and the real detector. Each event in simulation is assigned a weight, which is normalized so that the total event yields in simulation match those in data, yet incorporates different weights for different events in order to account for differences between simulation and data. This next part of this section describes these "scale factor" weights.

To correct event-level differences between simulation and data in n categories such as the number of hard partons, one can simply multiply the weight of each simulated event by a scale factor $p_{\text{data,cat}}/p_{\text{sim,cat}}$, where $p_{\text{data,cat}}$ is the fraction of events in category cat based on a measurement in data and $p_{\text{sim,cat}}$ is the fraction of events in category cat in simulation. These fractions are approximations to the probability of an event being in that category. Since $\sum_{\text{cat}} p_{\text{data,cat}} = \sum_{\text{cat}} p_{\text{sim,cat}} = 1$, the overall number of events is preserved, but the simulated events in each category are adjusted to match data. For corrections to individual objects such as corrections to b-tagging efficiencies, the same scheme is used, though the implementation is slightly more technically complex. We will consider the example of b-tag weighting and assume that the true parton-level distributions of quarks match between data and simulation or have been weighted to match. We again multiply the weight of each simulated event by a scale factor $p_{\text{data,cat}}/p_{\text{sim,cat}}$ where now, $p_{\text{data,cat}}$ and $p_{\text{sim,cat}}$ must be computed from the number of true jets and the probability of tagging or mistagging each jet as a b jet. For example, suppose we have an event with 2 jets arranged in in p_{T} order, which are both true b jets but only the first

of which is b-tagged. The appropriate scale factor would then be

$$p_{\text{data,cat}}/p_{\text{sim,cat}} = \frac{p_{\text{data}}(\text{jet 1 tagged}|\text{b}, p_{\text{T}}, \eta)p_{\text{data}}(\text{jet 2 untagged}|\text{b}, p_{\text{T}}, \eta)}{p_{\text{sim}}(\text{jet 1 tagged}|\text{b}, p_{\text{T}}, \eta)p_{\text{sim}}(\text{jet 2 untagged}|\text{b}, p_{\text{T}}, \eta)} \tag{3.3}$$

where each probability in data or simulation depends on the the true parton flavor, the p_{T} of the jet, and the $|\eta|$ of the jet.

The following scale factors are applied to simulated events in order to correct for known issues.

- For $\text{t}\bar{\text{t}}$+jets samples generated with the CUETP8M1 tune, the distribution of the number of ISR jets was found to differ between simulation and data. Measurements of the number of ISR jets were derived from a $\text{t}\bar{\text{t}}$+jets sample with 2 leptons and 2 b jets for both data and simulation, and from this, scale factors were derived. These scale factors are used to reweight CUETP8M1 $\text{t}\bar{\text{t}}$ events as well as the T5HH model signal events. It is additionally observed that the net p_{T} of ISR jets in Z+jets events does not match between data and simulation. The p_{T} spectrum was measured for both data and simulation in a 2 lepton on-Z 0 b jet sample [383] and this was used to derive scale factors that are used to re-weight all TChiHH and TChiHH-G samples since higgsino production primarily proceeds through off-shell Z diagrams. Associated uncertainties in the scale factors are propagated to the final analysis results.

- The reconstruction and identification efficiency for electrons, muons, and photons

is known to differ between the real detector and the GEANT4 simulated detector. As described in Section 3.2.1, efficiency measurements were performed with on-ZDrell-Yan+jets to $e^+ e^-$ and $\mu^+ \mu^-$ events in data, and these measurements are combined with the known efficiency in simulation to derive scale factors to correct for the difference between simulation and data. Furthermore, the full GEANT4 simulation and FASTSIM simulation of detector response do not match, so additional scale factors for FASTSIM samples are derived by comparing the reconstruction and identification efficiencies of the two.

- As described in Section 3.2.3, the probability for light, c, and b jets to pass the various DEEPCSV tagger working points in data is measured in dedicated samples. The mistag rate for light jets is evaluated in a negative flight distance region, the mistag rate for c jets is evaluated in $\mathrm{W}+\mathrm{c}$ and single lepton $\mathrm{t\bar{t}}$ regions, and the tag rate for b jets is evaluated in muon jet, single lepton $\mathrm{t\bar{t}}$, and dilepton $\mathrm{t\bar{t}}$ regions. Scale factors are derived based on the efficiencies in data and simulation. Because there are multiple working points, the probability ratios used to define the scale factors are evaluated in 4 exclusive categories: untagged, loose but not medium tagged, medium but not tight tagged, and tight tagged. Again, an additional set of scale factors for FASTSIM samples are derived by comparing b-tagging selection efficiencies for different categories of jets in FASTSIM and full simulation samples.

- Section 3.2.3 also describes how the efficiency for tagging double-b jets and mistagging non-double-b jets with the DEEPDOUBLEBVL tagger are measured in data

regions including a $g \to b\bar{b}/c\bar{c}$ region selected with a boosted decision tree, a similar region selected with soft muons in jets, a $Z \to b\bar{b}$ sample, and a region with at least two AK8 jets and 200–300 GeV of p_T^{miss}. The tag and mistag efficiencies measured in data are combined with the efficiencies in simulation to derive scale factors used to correct the simulated samples. Furthermore, additional scale factors are used to correct for the difference in double-b tagging efficiency between FastSim samples and full Geant4 simulation samples with the CP2 tune as well as between the Geant4 simulation with the CP2 tune and the CP5 tune.

- While the soft-drop mass in standard Geant4 simulation samples is corrected with an energy calibration described above, the soft-drop mass in FastSim samples is adjusted to match that of Geant4 samples by using scale factors derived from measurements made with CP2 tune FastSim and Geant4 T5HH simulated samples. A comparison between CP2 and CP5 tune Geant4 simulated samples showed no difference with respect to soft-drop mass, so no additional correction is applied.

- To account for differences in the number of pileup collisions per event in data and simulation, the distribution of number of pileup collisions in data is estimated using luminosity measurements described in Section 2.2.4 together with the measurement of total p-p inelastic cross section from Ref. [384]. From this measurement and the distribution of pileup collisions simulated, scale factors are derived to correct the pileup distribution in simulation to match that in data.

In addition to scale factors, there are also two overall weights applied to simulated events to correct for differences between simulation and data. Unlike scale factors, these weights do affect the total number of events in simulation, since they model data taking inefficiencies.

- In 2016 and 2017, an ECAL timing miscalibration resulted in some ECAL trigger primitives in the $2 < |\eta| < 3$ region being associated with a bunch crossing one earlier than intended. Since CMS did not allow triggering on subsequent bunch crossings during Run 2, this effectively causes some events to "self veto". To account for this effect in simulation, the probability for generating an early trigger primitive was measured in data for as a function of p_{T} and η for photons in events triggered on central electrons as well as for jets as a function of electromagnetic p_{T} and η in events triggered on muons. These probabilities are applied as overall weights to the simulated samples.

- The emulation of the trigger system in simulation is known to differ substantially from that in the real data. As described in Section 3.3.4, the efficiency for passing the analysis triggers were measured as a function of event-level variables. These efficiencies are directly applied as weights to simulation in order to emulate the trigger efficiency and no requirements are placed on the emulated triggers themselves.

3.3.4 Trigger

The HH(4b)+$p_{\mathrm{T}}^{\mathrm{miss}}$ analysis uses a series of triggers to select different samples for study including:

- The main search sample for both resolved and boosted topologies is selected with $p_{\mathrm{T}}^{\mathrm{miss}}$ triggers.
- The resolved topology single lepton control sample is selected with the OR of $p_{\mathrm{T}}^{\mathrm{miss}}$ and single lepton triggers.
- The resolved topology dilepton control sample is selected with single lepton triggers.
- The resolved topology low-$\Delta\phi$ control sample is selected with $p_{\mathrm{T}}^{\mathrm{miss}}$ triggers.
- The boosted topology single lepton control sample is selected with the OR of $p_{\mathrm{T}}^{\mathrm{miss}}$ and single lepton triggers.
- The boosted topology photon validation sample is selected with single photon triggers.
- Various trigger measurement samples described in this section are selected with single lepton or jet-H_{T} triggers depending on the sample.

The triggers used in this analysis are listed in Tables 3.12–3.16. In addition to the primary triggers for each category, there exist various triggers that were disabled for parts of data taking or prescaled in order to maintain acceptable data rates. These triggers

Table 3.12: Triggers used in this analysis from the MET data set. The logical OR of all triggers listed in this table is typically referred to as "$p_{\mathrm{T}}^{\mathrm{miss}}$ triggers", though the triggers have additional requirements on $H_{\mathrm{T}}^{\mathrm{miss}}$ calculated with jets passing the tight ID criteria and possibly other criteria. Not all triggers were enabled for all values of instantaneous luminosity, and some triggers were enabled but prescaled. The effective luminosity recorded in 2016, 2017, and 2018 based on trigger enablement and prescale is provided in the table. The primary triggers are the $p_{\mathrm{T}}^{\mathrm{miss}}$-$H_{\mathrm{T}}^{\mathrm{miss}}$ 120 triggers, though taking the OR with the other listed triggers increases the efficiency, particularly for 2016 where lower threshold triggers were enabled for much of the data taking.

Trigger	2016 Lumi.	2017 Lumi.	2018 Lumi.
HLT_PFMET(NoMu)90_PFMHT(NoMu)90_IDTight	14.16	0	0
HLT_PFMET(NoMu)100_PFMHT(NoMu)100_IDTight	17.89	0	0
HLT_PFMET(NoMu)110_PFMHT(NoMu)110_IDTight	35.83	5.12	0.025
HLT_PFMET(NoMu)120_PFMHT(NoMu)120_IDTight	36.47	40.67	59.96
HLT_PFMET(NoMu)130_PFMHT(NoMu)130_IDTight	0	40.67	59.96
HLT_PFMET(NoMu)140_PFMHT(NoMu)140_IDTight	0	41.54	59.96
HLT_PFMET(NoMu)100_PFMHT(NoMu)100_IDTight_PFHT60	0	3.83	1.11
HLT_PFMET(NoMu)120_PFMHT(NoMu)120_IDTight_PFHT60	0	36.75	59.96
HLT_PFMET(NoMu)120_PFMHT(NoMu)120_IDTight_HFCleaned	0	8.36	0
HLT_PFMET(NoMu)120_PFMHT(NoMu)120_IDTight_PFHT60_HFCleaned	0	8.36	0

may have lower thresholds so that the total efficiency of selected events can be improved by taking the logical OR of all triggers in each category.

The efficiency for the sets of triggers used in this analysis is measured in data as described in the paragraphs below. These measurements are used to derive scale factors for simulated samples as well as to evaluate the associated systematic uncertainty on signal acceptance. The effect of uncertainties in the trigger efficiency on the background estimation is found to be negligible due to the data-driven background estimation method.

Trigger efficiency in zero lepton samples with true $p_{\mathrm{T}}^{\mathrm{miss}}$

For samples with true $p_{\mathrm{T}}^{\mathrm{miss}}$, the efficiency of the $p_{\mathrm{T}}^{\mathrm{miss}}$ triggers is evaluated as a function of offline $p_{\mathrm{T}}^{\mathrm{miss}}$ and H_{T}. The efficiencies are measured in a dedicated trigger efficiency measurement region selected with single electron triggers and defined by the

Table 3.13: Single electron triggers used in this analysis from the `SingleElectron` data set (2016/2017) or the `EGamma` data set (2018). The logical OR of all triggers listed in this table together with those in Table 3.14 is typically referred to as the "single lepton triggers". Not all triggers were enabled for all values of instantaneous luminosity, and some triggers were enabled but prescaled. The effective luminosity recorded in 2016, 2017, and 2018 based on trigger enablement and prescale is provided in the table. The primary triggers are the tight working point isolated electron triggers with thresholds at 27 (2016) and 32 (2017/2018) GeV, though taking the OR with the other listed triggers slightly increases the efficiency.

Trigger	2016 Lumi.	2017 Lumi.	2018 Lumi.
HLT_Ele25_WPTight_Gsf	25.36	0	0
HLT_Ele27_WPTight_Gsf	36.47	31.72	1.11
HLT_Ele28_WPTight_Gsf	0	0	23.69
HLT_Ele32_WPTight_Gsf	8.76	27.13	59.96
HLT_Ele32_WPTight_Gsf_L1DoubleEG	0	41.54	59.96
HLT_Ele35_WPTight_Gsf	0	41.54	59.96
HLT_Ele45_WPLoose_Gsf	27.71	0	0
HLT_Ele105_CaloIdVT_GsfTrkIdT	24.64	0	0
HLT_Ele115_CaloIdVT_GsfTrkIdT	36.47	36.75	59.96
HLT_Ele135_CaloIdVT_GsfTrkIdT	0	36.75	59.96
HLT_Ele145_CaloIdVT_GsfTrkIdT	7.45	36.75	59.96
HLT_Ele25_eta2p1_WPTight_Gsf	36.47	0	0
HLT_Ele27_eta2p1_WPTight_Gsf	36.47	0	0
HLT_Ele27_eta2p1_WPLoose_Gsf	27.74	0	0
HLT_Ele15_IsoVVVL_PFHT350	0.0004	0	0
HLT_Ele15_IsoVVVL_PFHT400	0.001	0	0
HLT_Ele15_IsoVVVL_PFHT450	0.001	0	0
HLT_Ele15_IsoVVVL_PFHT600	0	0.0015	0.0011
HLT_Ele15_IsoVVVL_PFHT600	0.0011	0.0015	0.0011
HLT_Ele50_IsoVVVL_PFHT450	0	0.0015	0.0011

Table 3.14: Triggers used in this analysis from the `SingleMuon` data set. The logical OR of all triggers listed in this table together with those in Table 3.13 is typically referred to as the "single lepton triggers". Not all triggers were enabled for all values of instantaneous luminosity, and some triggers were enabled but prescaled. The effective luminosity recorded in 2016, 2017, and 2018 based on trigger enablement and prescale is provided in the table. The primary triggers are the isolated muon triggers with p_{T} thresholds at 24 and 27 GeV, though taking the OR with the other listed triggers slightly increases the efficiency.

Trigger	2016 Lumi.	2017 Lumi.	2018 Lumi.
`HLT_IsoMu20`	9.82	0.93	0.27
`HLT_IsoMu22`	28.99	0	0
`HLT_IsoMu24`	36.47	38.06	59.96
`HLT_IsoMu27`	36.47	41.54	59.96
`HLT_IsoTkMu20`	9.82	0	0
`HLT_IsoTkMu22`	28.99	0	0
`HLT_IsoTkMu24`	36.47	0	0
`HLT_Mu50`	36.47	41.54	59.96
`HLT_Mu55`	36.47	27.13	59.96
`HLT_TkMu50`	33.64	0	0
`HLT_IsoMu22_eta2p1`	33.64	0	0
`HLT_IsoMu24_eta2p1`	7.85	29.22	59.96
`HLT_Mu45_eta2p1`	24.64	0	0
`HLT_Mu15_IsoVVVL_PFHT350`	0.0011	0	0
`HLT_Mu15_IsoVVVL_PFHT400`	0.0027	0	0
`HLT_Mu15_IsoVVVL_PFHT450`	0	0.0012	0.001
`HLT_Mu15_IsoVVVL_PFHT600`	0.0031	0.0012	0.001
`HLT_Mu50_IsoVVVL_PFHT400`	0.0027	0.0012	0
`HLT_Mu50_IsoVVVL_PFHT450`	0	0	0.001

Table 3.15: Single photon triggers used in this analysis from the `SinglePhoton` data set (2016/2017) or the `EGamma` dat aset (2018). The logical OR of the two triggers listed in this table is typically referred to as the "single photon triggers". Not all triggers were enabled during all data taking. The effective luminosity recorded in 2016, 2017, and 2018 based on trigger enablement and prescale is provided in the table.

Trigger	2016 Lumi.	2017 Lumi.	2018 Lumi.
`HLT_Photon175`	36.47	41.54	59.96
`HLT_Photon200`	0	41.54	59.96

Table 3.16: Triggers used in this analysis from the `JetHT` data set. The logical OR of all triggers listed in this table is typically referred to as "jet-H_{T} triggers". Not all triggers were enabled for all values of instantaneous luminosity, and some triggers were enabled but prescaled. The effective luminosity recorded in 2016, 2017, and 2018 based on trigger enablement and prescale is provided in the table. The primary triggers are the 500 GeV jet trigger and the 900 (2016) or 1050 (2017/2018) GeV H_{T} triggers, though taking the OR with the other listed triggers is necessary in order to retain lower H_{T} events needed for trigger efficiency measurement.

Trigger	2016 Lumi.	2017 Lumi.	2018 Lumi.
HLT_PFJet500	36.47	41.54	59.96
HLT_PFHT125	0.0037	0	0
HLT_PFHT180	0	0.0102	0.0052
HLT_PFHT200	0.0065	0	0
HLT_PFHT250	0.0096	0.0147	0.0144
HLT_PFHT300	0.039	0	0
HLT_PFHT350	0.0779	0.17	0.23
HLT_PFHT370	0	0.0417	0.0368
HLT_PFHT400	0.16	0	0
HLT_PFHT430	0	0.13	0.12
HLT_PFHT475	0.31	0	0
HLT_PFHT510	0	0.22	0.23
HLT_PFHT590	0	0.44	0.47
HLT_PFHT600	1.25	0	0
HLT_PFHT650	1.67	0	0
HLT_PFHT680	0	0.78	0.92
HLT_PFHT780	0	1.45	1.84
HLT_PFHT800	27.71	0	0
HLT_PFHT900	36.47	0	0
HLT_PFHT1050	0	41.54	59.96

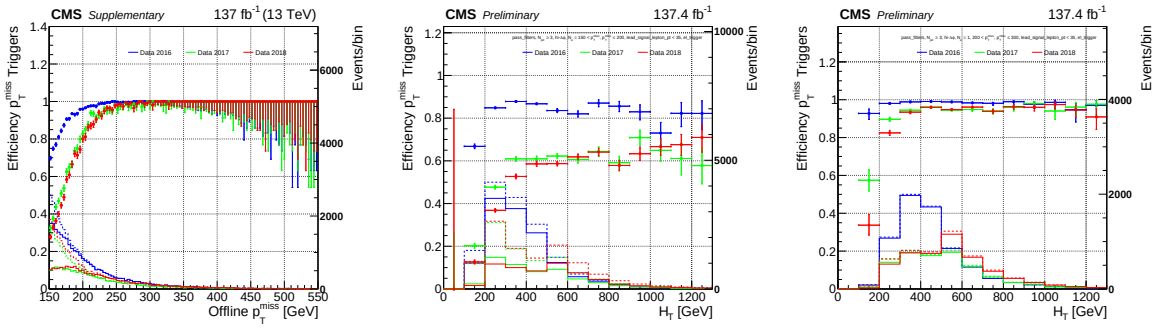

Figure 3.8: Total events in the true $p_{\mathrm{T}}^{\mathrm{miss}}$ trigger measurement region (dashed lines), events in the true $p_{\mathrm{T}}^{\mathrm{miss}}$ trigger measurement region passing the OR of the $p_{\mathrm{T}}^{\mathrm{miss}}$ triggers (solid lines), and their ratio, the trigger efficiency (data points) for 2016 (blue), 2017 (green), and 2018 (red) as a function of $p_{\mathrm{T}}^{\mathrm{miss}}$ integrated in H_{T} bins (left), as a function of H_{T} for events with $p_{\mathrm{T}}^{\mathrm{miss}} < 200$ GeV (center), and as a function of H_{T} for events with $p_{\mathrm{T}}^{\mathrm{miss}} > 200$ GeV (right).

requirements $p_{\mathrm{T}}^{\mathrm{miss}} > 150$ GeV, $N_{\mathrm{jets}} \geq 3$, 1 electron with $30 < p_{\mathrm{T}} < 35$ GeV, and $\Delta\phi$ of at least 0.5 (0.3) between $\vec{p}_{\mathrm{T}}^{\mathrm{miss}}$ the leading 2 (3rd-4th) jets ordered by p_{T}. Figure 3.8 shows a projections of the trigger efficiency onto $p_{\mathrm{T}}^{\mathrm{miss}}$ for each year as well as projections onto H_{T} for two different $p_{\mathrm{T}}^{\mathrm{miss}}$ ranges. The trigger efficiency increases with $p_{\mathrm{T}}^{\mathrm{miss}}$ and plateaus at around 99% efficiency for events with $p_{\mathrm{T}}^{\mathrm{miss}}$ above about 250 GeV. The measured efficiencies are applied as scale factors to all simulated samples in the search and low $\Delta\phi$ regions except for the simulated QCD multijet sample in order to emulate the effect of trigger acceptance.

In addition to the measurement of the nominal trigger efficiency, the uncertainty in the trigger efficiency is also measured. In the final statistical analysis described in Section 4.4, the trigger efficiency will be a nuisance parameter that is allowed to float with the constraint that its difference from the nominal value should not be much larger than the uncertainty scale. Four sources of uncertainty in the trigger measurement are

considered:

1. **Statistical uncertainty** The statistical uncertainty on the trigger efficiency in each $p_{\mathrm{T}}^{\mathrm{miss}} \times H_{\mathrm{T}}$ bin is used as one source of trigger efficiency uncertainty.

2. **Kinematic variations** Within statistical uncertainty, the trigger efficiency of the $p_{\mathrm{T}}^{\mathrm{miss}}$ triggers is captured entirely by $p_{\mathrm{T}}^{\mathrm{miss}}$ and H_{T}. Additional uncertainties due to kinematic differences between the trigger measurement region and the analysis search region are nonetheless assigned. First, in H_{T}-integrated coarse $p_{\mathrm{T}}^{\mathrm{miss}}$ bins, a series of additional selections on N_{jets}, N_{b}, and ΔR_{max} are applied and the maximum variation between the new efficiency and the nominal efficiency is taken as the scale of the systematic uncertainty. Then, the same is done for $\langle m_{\mathrm{bb}} \rangle$ except with H_{T} fixed between 300 and 400 GeV, which is needed since $\langle m_{\mathrm{bb}} \rangle$ is found to be highly correlated with H_{T}.

3. **Reference trigger** The uncertainty stemming from the use of the single electron reference trigger is evaluated by comparing the nominal efficiencies with those measured in a sample selected with the `HLT_PFJet500` trigger requiring at least 1 jet with $p_{\mathrm{T}} > 500$ GeV and otherwise identical selections in H_{T}-integrated coarse $p_{\mathrm{T}}^{\mathrm{miss}}$ bins.

4. **Electron energy scale** Due to the difference in energy scales and corrections between jets and electrons, the relation between offline and online $p_{\mathrm{T}}^{\mathrm{miss}}$ is in general different between events that only have jets and those that additionally have iso-

Table 3.17: Representative uncertainties for trigger efficiencies in different $p_{\mathrm{T}}^{\mathrm{miss}}$ ranges for $300 < H_{\mathrm{T}} < 400$ GeV. The uncertainties are expressed as in percent of the nominal efficiency.

	$p_{\mathrm{T}}^{\mathrm{miss}}$ range [GeV]						
Source	$[150, 160]$	$[160, 180]$	$[180, 200]$	$[200, 225]$	$[225, 250]$	$[250, 300]$	≥ 300
Statistical [%]	1.9	1.1	1.6	0.6	0.4	0.2	0.1
Kinematic variations [%]	10.6	8.2	4.4	3.8	2.1	1.3	2.6
Reference trigger [%]	3.1	7.2	3.1	2.3	0.8	0.5	0.1
Electron energy scale [%]	37.3	12.8	15.9	6.6	2.1	0.8	1.4
Total uncertainty [%]	38.9	16.9	16.9	8.0	3.1	1.6	3.0

lated electrons. In coarse $p_{\mathrm{T}}^{\mathrm{miss}} \times H_{\mathrm{T}}$ bins, the nominal trigger efficiency is compared to that with a linear extrapolation to an electron p_{T} of 0 and the difference is used as the scale of a systematic uncertainty.

The total uncertainty in each $p_{\mathrm{T}}^{\mathrm{miss}} \times H_{\mathrm{T}}$ bin is the sum in quadrature of these sources. Table 3.17 shows the uncertainties from each source for a representative H_{T} selection. At lower values of $p_{\mathrm{T}}^{\mathrm{miss}}$, the uncertainty can be as high as 50%, while for events with $p_{\mathrm{T}}^{\mathrm{miss}} > 250$ GeV, the uncertainty is typically on the order of 1%.

Trigger efficiency in zero lepton samples with fake $p_{\mathrm{T}}^{\mathrm{miss}}$

For QCD multijet events in which the $p_{\mathrm{T}}^{\mathrm{miss}}$ arises from mismeasurement, the relation between offline $p_{\mathrm{T}}^{\mathrm{miss}}$ and level-1/HLT $p_{\mathrm{T}}^{\mathrm{miss}}$ is different than that for events with genuine $p_{\mathrm{T}}^{\mathrm{miss}}$. For this reason, trigger efficiencies for fake $p_{\mathrm{T}}^{\mathrm{miss}}$ events are measured separately, again parametrized as a function of offline $p_{\mathrm{T}}^{\mathrm{miss}}$ and H_{T}. A dedicated trigger efficiency measurement region selected with the jet-H_{T} triggers is defined by the requirements that there be zero leptons, $p_{\mathrm{T}}^{\mathrm{miss}} > 150$ GeV, and that at least one of the leading four jets ordered by p_{T} be within $\Delta\phi$ of 0.5(0.3) of the $\vec{p}_{\mathrm{T}}^{\mathrm{miss}}$ where 0.5 is used for the leading two

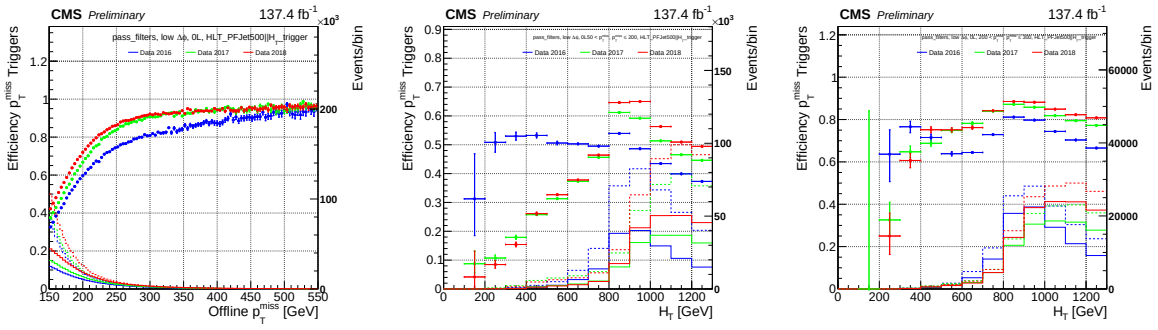

Figure 3.9: Total events in the fake $p_{\mathrm{T}}^{\mathrm{miss}}$ trigger measurement region (dashed lines), events in the fake $p_{\mathrm{T}}^{\mathrm{miss}}$ trigger measurement region passing the OR of the $p_{\mathrm{T}}^{\mathrm{miss}}$ triggers (solid lines), and their ratio, the trigger efficiency (data points) for 2016 (blue), 2017 (green), and 2018 (red) as a function of $p_{\mathrm{T}}^{\mathrm{miss}}$ integrated in H_{T} bins (left), as a function of H_{T} for events with $p_{\mathrm{T}}^{\mathrm{miss}} < 200$ GeV (center), and as a function of H_{T} for events with $p_{\mathrm{T}}^{\mathrm{miss}} > 200$ GeV (right).

jets and 0.3 for the third and fourth. Figure 3.9 shows the trigger efficiency measured in this region as a function of $p_{\mathrm{T}}^{\mathrm{miss}}$ and as a function of H_{T} for two $p_{\mathrm{T}}^{\mathrm{miss}}$ ranges. The trigger efficiency slowly increases with offline $p_{\mathrm{T}}^{\mathrm{miss}}$, but does not have the plateau behavior of true $p_{\mathrm{T}}^{\mathrm{miss}}$ events.

Trigger efficiency in single lepton samples

For the single lepton samples, the trigger efficiency for the OR of all $p_{\mathrm{T}}^{\mathrm{miss}}$ and single lepton triggers is measured as a three-dimensional function of offline $p_{\mathrm{T}}^{\mathrm{miss}}$, H_{T}, and lepton p_{T} separately for electron and muon events. This measurement is performed in single electron and muon samples selected with jet-H_{T} triggers that require $N_{\mathrm{jets}} \geq 2$ and one electron or muon respectively. Figure 3.10 shows the trigger efficiency as a function of offline $p_{\mathrm{T}}^{\mathrm{miss}}$ and lepton p_{T} for the electron and muon samples. The use of an OR between $p_{\mathrm{T}}^{\mathrm{miss}}$ and single lepton triggers provides substantial acceptance down to a $p_{\mathrm{T}}^{\mathrm{miss}}$ of 0.

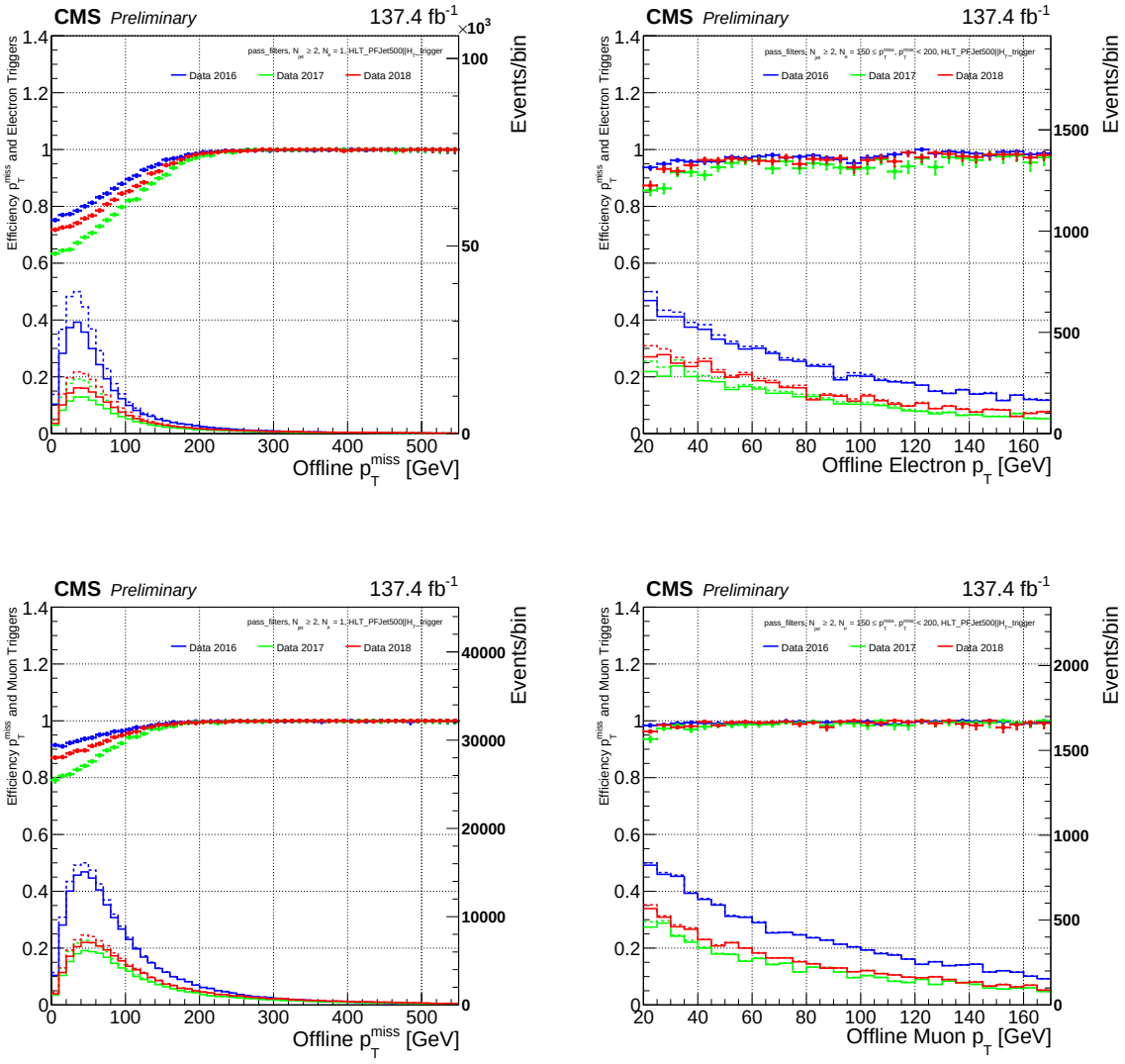

Figure 3.10: Total events in the single lepton trigger measurement region (dashed lines), events in the single lepton trigger measurement region passing the OR of the $p_{\mathrm{T}}^{\mathrm{miss}}$ and single lepton triggers (solid lines), and their ratio, the trigger efficiency (data points) for 2016 (blue), 2017 (green), and 2018 (red) as a function of $p_{\mathrm{T}}^{\mathrm{miss}}$ (left) and of lepton p_{T} (right) for single electron events (top) and single muon events (bottom).

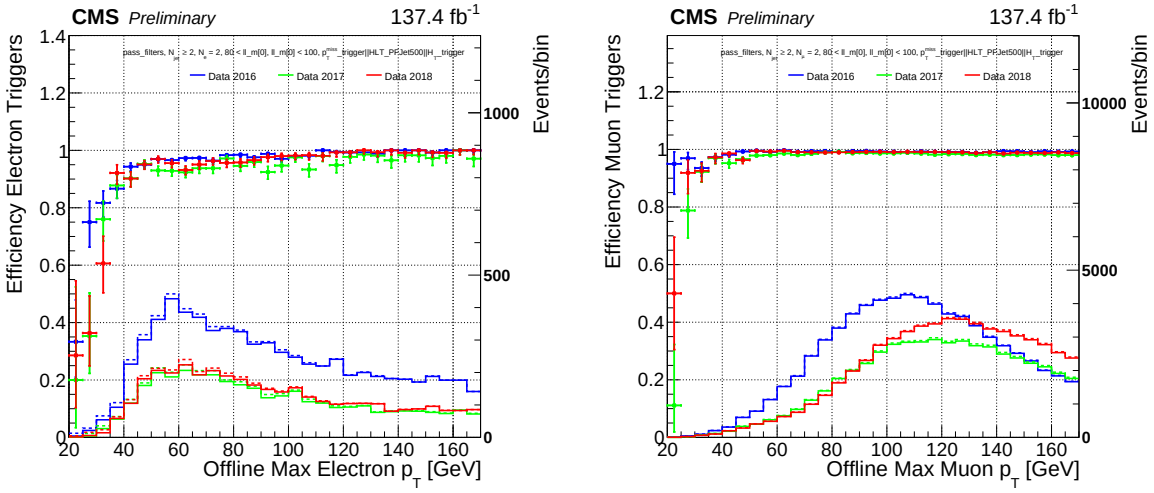

Figure 3.11: Total events in the dilepton trigger measurement region (dashed lines), events in the two lepton trigger measurement region passing the OR of the single lepton triggers (solid lines), and their ratio, the trigger efficiency (data points) for 2016 (blue), 2017 (green), and 2018 (red) as a function of lead lepton p_{T} for two electron events (left) and two muon events (right).

Trigger efficiency in dilepton samples

For the dilepton samples, the trigger efficiency for single lepton triggers is measured as function of lead lepton p_{T} for electron and muon events. This measurement is performed in two electron and two muon samples selected with the OR of $p_{\mathrm{T}}^{\mathrm{miss}}$ and jet-H_{T} triggers that requires $N_{\mathrm{jets}} \geq 2$ and two opposite sign same flavor leptons with an invariant mass between 80 and 100 GeV. Figure 3.11 shows the trigger efficiency as a function of lead lepton p_{T} for the electron and muon samples.

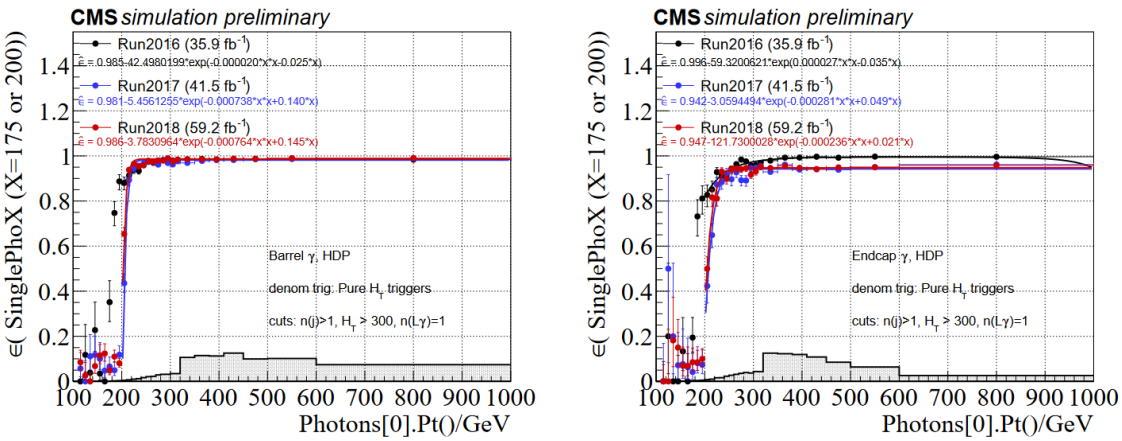

Figure 3.12: Total events in the photon trigger measurement region (shaded histogram) and the trigger efficiency (data points) for 2016 (black), 2017 (blue), and 2018 (red) as a function of photon p_{T} for photons in the CMS barrel (left) and endcap (right).

Trigger efficiency in photon sample

The trigger efficiency of the photon sample was measured for an inclusive supersymmetry search targeting the jets+$p_{\mathrm{T}}^{\mathrm{miss}}$ signature [135]. A trigger measurement sample passing jet-H_{T} triggers that has $H_{\mathrm{T}} > 300$ GeV and one photon passing the identification criteria in Section 3.2.1 was used to measure the single photon trigger efficiency as a function of photon p_{T} and $|\eta|$. Figure 3.12 shows the trigger efficiency for the photon triggers as a function of photon p_{T}. The trigger efficiency curve is fit with a Gaussian cumulative distribution function plus a constant, which is used to parametrize the trigger efficiencies for the single photon sample. This procedure is also cross checked using a sample collected with single muon triggers rather than jet-H_{T} triggers and the result is found to agree within 2%.

Chapter 4

Analysis strategy and methodology

This chapter gives an overview of the analysis strategy used to search for higgsinos in the HH(4b)+$p_{\mathrm{T}}^{\mathrm{miss}}$ topology, including the event selection, the background estimation method, the evaluation of systematic uncertainties, and the statistical model.

Section 4.1 outlines the baseline event selection and categorization for the resolved and boosted topologies. The resolved topology selects events with at least four jets that are paired into two Higgs boson candidates following the method described in Section 3.2.4, and $p_{\mathrm{T}}^{\mathrm{miss}} > 150$ GeV. The boosted topology selects events with at least two fat jets, which are the Higgs boson candidates, and $p_{\mathrm{T}}^{\mathrm{miss}} > 300$ GeV. A veto on leptons and charged tracks is used in both topologies to reject backgrounds in which the $p_{\mathrm{T}}^{\mathrm{miss}}$ is produced by the decay $\mathrm{W} \to \ell\nu$ such as W+jets and $\mathrm{t\bar{t}}$+jets events. Various quality criteria are also imposed on the missing transverse momentum to reduce events with spurious $p_{\mathrm{T}}^{\mathrm{miss}}$, which are mostly QCD multijet events. After the baseline selection, the primary backgrounds are $\mathrm{t\bar{t}}$+jets with at least one leptonically decaying W, W+jets with $\mathrm{W} \to \ell\nu$, and Z+jets with $\mathrm{Z} \to \nu\bar{\nu}$. To increase the sensitivity to signal models with large

mass splitting that tend to have larger $p_{\mathrm{T}}^{\mathrm{miss}}$ and more collimated Higgs decays without sacrificing sensitivity to low mass splitting signal models, both the resolved and boosted topologies organize events into categories based on $p_{\mathrm{T}}^{\mathrm{miss}}$, while the resolved topology also features two categories split by ΔR_{max}. Events passing the baseline selections are said to reside in the "search region".

Section 4.2 describes the background estimation method for the analysis. The baseline selection does not feature tight requirements on the number of b or double-b jets ($N_{\mathrm{b}}/N_{\mathrm{H}}$) nor on the mass of the Higgs boson candidates because these variables are the primary variables used in the background estimation method. The analysis signal regions are defined by the requirements that the Higgs boson candidates have a mass near the Higgs mass, 125 GeV, and that a number of b or double-b jets are present. The number of events inside and outside of the Higgs mass window is approximately independent of $N_{\mathrm{b}}/N_{\mathrm{H}}$ so that the number of events in the low $N_{\mathrm{b}}/N_{\mathrm{H}}$ categories and in the Higgs mass sideband categories can be used to predict the number of background events in the signal region.

Next, Section 4.3 explains how the systematic uncertainties in both the background estimation method as well as the expected signal yield in the simplified models are estimated.

Finally, Section 4.4 discusses the statistical model used to implement the analysis. The full statistical model provides a probability distribution function for the observed event yields as a function of various parameters. This section details the form of the

probability distribution function as well as the inference procedure used to quote limits on the rate of signal events.

4.1 Event selection and categorization

4.1.1 Primary backgrounds

The goal of the baseline event selection is to select events with properties consistent with the considered signals while minimizing the number of background events selected. Signal events in this analysis feature numerous b jets, large $p_{\mathrm{T}}^{\mathrm{miss}}$, and no prompt leptons. The primary standard model backgrounds thus include neutrinos, which generate genuine $p_{\mathrm{T}}^{\mathrm{miss}}$, along with jets. Figure 4.1 shows representative Feynman diagrams for the primary standard-model backgrounds: $\mathrm{t\bar{t}}$+jets, W+jets, and Z+jets. A representative Feynman diagram for QCD multijet events is also shown, though QCD multijet events are a subleading background as such events typically do not have large genuine $p_{\mathrm{T}}^{\mathrm{miss}}$ and must have large mismeasurement to pass the baseline selection. The $\mathrm{t\bar{t}}$+jets and W+jets events also have prompt leptons, which must missed during reconstructed in order to pass the lepton veto requirements in the baseline selection.

4.1.2 Resolved topology event selection and categorization

This section details the baseline selection for the resolved topology using variables defined in Section 3.2. The baseline selections include requirements on $p_{\mathrm{T}}^{\mathrm{miss}}$ and on the

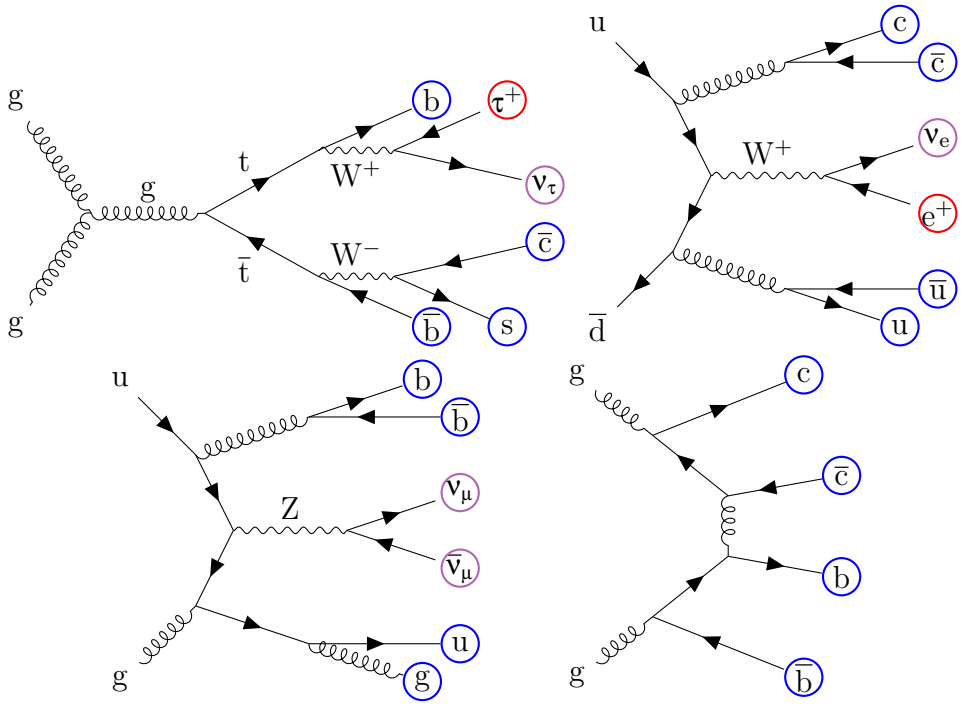

Figure 4.1: Representative Feynman diagrams for the three primary backgrounds in this analysis, $t\bar{t}$+jets (top left), W+jets (top right), and Z+jets (bottom left), as well as a representative Feynman diagram for QCD multijet background (bottom right), which is a smaller background. The first three categories feature b jets or other jets that may be misidentified as b jets, which are circled in blue, as well as $p_{\mathrm{T}}^{\mathrm{miss}}$ from neutrinos, which are circled in violet. The first two categories also feature prompt leptons, which are circled in red, and must be missed in order to enter the analysis baseline selection. QCD multijet events generally have low $p_{\mathrm{T}}^{\mathrm{miss}}$ since the only source of true $p_{\mathrm{T}}^{\mathrm{miss}}$ in such events are neutrinos produced in b and c hadron decays, which generally have low p_{T}. QCD multijet events are thus a subleading source of background. However, if there is large spurious $p_{\mathrm{T}}^{\mathrm{miss}}$ due to mismeasurement, QCD multijet events can enter the baseline selection.

number of jets N_{jets} and b jets N_{b}, a veto on prompt leptons and isolated tracks that are not present in signal events, and some basic selections on the Higgs boson candidates. Table 4.1 shows the number of simulated events in various background categories and for various signal models after various selections are sequentially applied. The following paragraphs describe the resolved baseline selections in more detail.

- $p_{\text{T}}^{\text{miss}}$ **selections** The resolved baseline selection requires a $p_{\text{T}}^{\text{miss}}$ of at least 150 GeV. This value is set to be near the around the lowest value for which reasonable trigger efficiency is achieved (see Section 3.3.4) in order to maximize sensitivity to signal models with lower $p_{\text{T}}^{\text{miss}}$. As discussed below, events are later categorized based on $p_{\text{T}}^{\text{miss}}$ so that additional discrimination is retained for signal models with larger mass splitting that may have much larger $p_{\text{T}}^{\text{miss}}$ than typical for backgrounds. Additionally, the filter criteria detailed in Section 3.3.2 are also used to reject events that are likely to have spurious $p_{\text{T}}^{\text{miss}}$. To further reject QCD multijet events with large $p_{\text{T}}^{\text{miss}}$ due to mismeasurement, additional requirements are imposed on $\Delta\phi_i$, the difference in azimuthal angle between the ith highest p_{T} jet and the $\vec{p}_{\text{T}}^{\text{miss}}$ as well as on the ratios between the nominal particle-flow $p_{\text{T}}^{\text{miss}}$ and the missing transverse momentum reconstructed from only calorimeter information, $p_{\text{T,calo}}^{\text{miss}}$, and the missing transverse momentum reconstructed neglecting unclustered energy, $H_{\text{T}}^{\text{miss}}$. Specifically, $\Delta\phi_1$ and $\Delta\phi_2$ are required to be greater than 0.5 while $\Delta\phi_3$ and $\Delta\phi_4$ are required to be greater than 0.3 since jet energy underestimation can produce $p_{\text{T}}^{\text{miss}}$ that is closely aligned with a jet. The $p_{\text{T}}^{\text{miss}}$ is required to not be larger than

twice $p_{\mathrm{T,calo}}^{\mathrm{miss}}$ or $H_{\mathrm{T}}^{\mathrm{miss}}$ since this could indicate a failure in the particle flow algorithm. These $p_{\mathrm{T}}^{\mathrm{miss}}$ quality criteria are included in Table 4.1 as "spurious $p_{\mathrm{T}}^{\mathrm{miss}}$ rejection". The top left plot in Figure 4.2 shows the distribution of $p_{\mathrm{T}}^{\mathrm{miss}}$ for signal and background after requiring the resolved topology baseline selection and $N_{\mathrm{b}} \geq 3$.

- **Jet selections** The top-center plot in Figure 4.2 shows the distribution in N_{jets} for the simulated samples and data events with $N_{\mathrm{b}} \geq 3$ and the resolved baseline selection except for the upper limit N_{jets}. The resolved topology baseline selection requires at least four jets in order to reconstruct the Higgs candidates. Furthermore, events with six or more jets are rejected since this region contains relatively less signal and substantially more background. This allows for up to one additional initial-state radiation or final-state radiation jet in addition to the four jets from the Higgs decays. The resolved baseline selection also includes a relatively loose requirement of two b jets passing the tight working point of the DeepCSV b tagger. The top-right plot of Figure 4.2 shows the distribution of events in the N_{b} variable defined in Section 3.2.3 after the resolved baseline selection. Tighter selections on the number of b jets are used to define the signal region as detailed below.

- **Leptons and track veto** The resolved baseline selection requires exactly zero leptons passing the veto criteria or isolated tracks as defined in Section 3.2.1. These selections are instrumental to removing the majority of background with neutrinos from W boson decays, though a large fraction of the background entering the final analysis does consist of "lost lepton" events with missed prompt leptons as shown

by the large fraction of $t\bar{t}$+jets and W+jets events in Figure 4.3.

- **Higgs boson candidate selections** Finally, the resolved baseline applies some basic selections to the Higgs boson candidates. The difference in mass between the Higgs boson candidates, Δm_{bb}, is required to be less than 40 GeV since the mass for both candidates in signal events is expected to be near 125 GeV, while it may be much larger in background. The distribution in Δm_{bb} for simulated and data events with $N_{\mathrm{b}} \geq 3$ and the resolved topology baseline selection applied except for the selection on Δm_{bb} is shown in the bottom-left plot in Figure 4.2. After the two Higgs boson candidates are required to be relatively similar in mass, a very loose requirement that the average of the Higgs boson candidate masses, $\langle m_{\mathrm{bb}} \rangle$, be less than 200 GeV is imposed. The distribution in $\langle m_{\mathrm{bb}} \rangle$ for simulated and data events with $N_{\mathrm{b}} \geq 3$ the resolved topology baseline selection applied is shown in the bottom-center plot of Figure 4.2. As with N_{b}, a tighter selection on $\langle m_{\mathrm{bb}} \rangle$ is used to define the signal region as detailed below. The resolved baseline also requires that ΔR_{max}, the larger of the angular separation between the jets in the Higgs boson candidates, be less than 2.2 since as shown in the bottom-right plot of Figure 4.2, the high ΔR_{max} region is strongly background dominated.

All events passing the baseline selection are used in the analysis, however only events with $N_{\mathrm{b}} \geq 3$ and $\langle m_{\mathrm{bb}} \rangle$ between 100 and 140 GeV are considered to be in the signal region (SR). Events are sorted into the SR, the mass sideband (SB), control signal region (CSR), or control mass sideband (CSB) based on the following conditions:

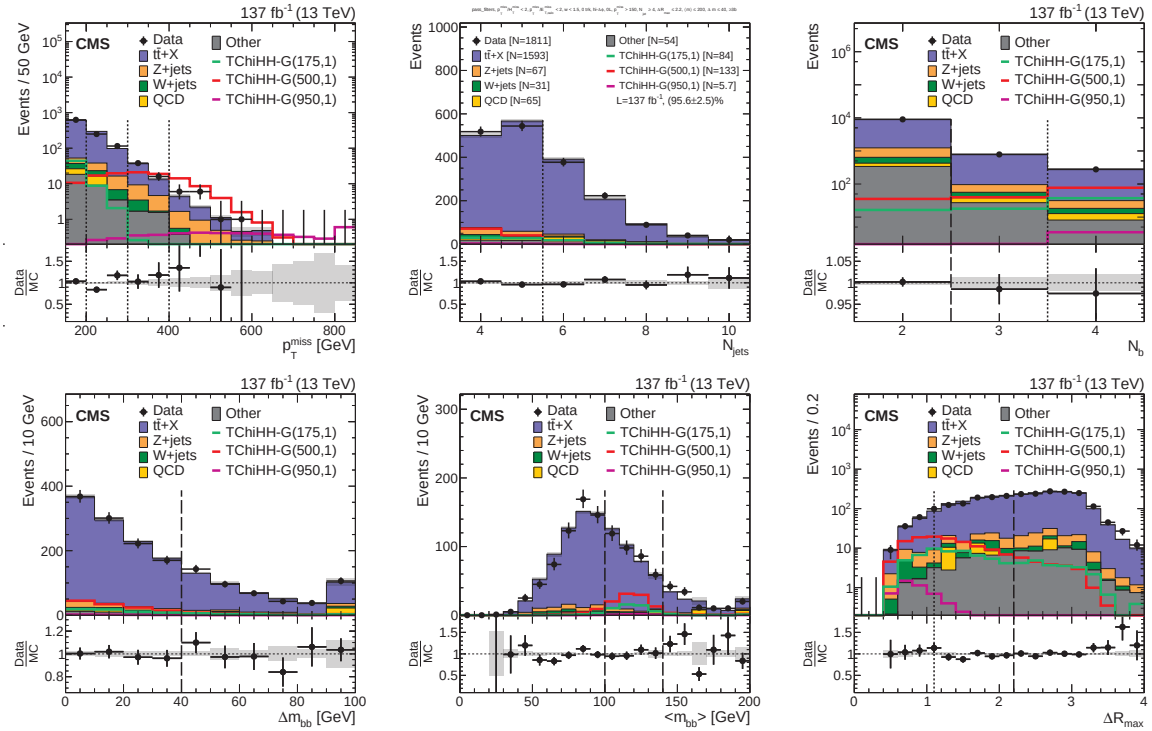

Figure 4.2: Distributions in the key analysis variables of the resolved topology after the baseline selection and an $N_{\mathrm{b}} \geq 3$ selection are applied, excepting any selection on the variable being plotted. The black data points represent the observed data, the stacked histograms represent the yield from background simulation, scaled by a factor of 0.93–0.97 to match the integral of the observed data, and the colored outlines represent expected yields from selected signal models. The dashed lines indicate the signal region selection while the dotted lines represent signal region categorization.

Table 4.1: Event yields obtained from simulated event samples as selection criteria are sequentially applied, weighted to correspond to the luminosity of the Run 2 data set. These can be taken as an estimate for the number of events one would expect in data, though the formal background estimate is obtained from a data-driven method detailed in the next section. The event selection requirements listed above the horizontal line in the middle of the table are defined as the *resolved topology baseline selection*. The selections below the horizontal line are only to give a sense to the relative number of signal and background events expected in the different signal region categories.

$\mathcal{L} = 137$ fb^{-1}	$\mathrm{t\bar{t}} + X$	V +jets	QCD	Other	Total SM Bkg.	TChiHH-G(175,0)	TChiHH-G(500,0)	TChiHH-G(900,0)
$p_{\mathrm{T}}^{\mathrm{miss}}$ Filters, $p_{\mathrm{T}}^{\mathrm{miss}} > 150$ GeV	2686501.24	13316613.37	6968252.21	624405.10	23595771.91	3520.41	1120.99	73.28
$N_{\mathrm{veto\ leptons}} = N_{\mathrm{iso.\ tracks}} = 0$	625309.52	6521644.32	6057386.05	156159.82	13360499.71	2829.81	989.51	68.35
$4 \leq N_{\mathrm{jets}} \leq 5$	314816.74	715097.98	2018030.28	42411.15	3090356.15	1588.79	548.40	36.06
$N_{\mathrm{b}} \geq 2$	49506.80	5808.71	29573.10	3204.54	88093.14	860.71	318.06	17.72
Spurious $p_{\mathrm{T}}^{\mathrm{miss}}$ rejection	34209.37	4342.03	1323.83	1976.46	41851.69	201.00	274.59	15.85
$\Delta m_{\mathrm{bb}} < 40$ GeV, $\langle m_{\mathrm{bb}} \rangle < 200$ GeV	19444.08	1774.61	178.09	848.06	22244.84	107.72	177.03	9.23
$\Delta R_{\mathrm{max}} < 2.2$	8190.11	916.70	127.70	385.73	9620.25	72.98	147.22	8.76
$100 \leq \langle m_{\mathrm{bb}} \rangle < 140$ GeV	2967.16	224.64	37.00	120.38	3349.19	57.26	115.91	7.40
$N_{\mathrm{b}} \geq 3$	328.84	19.21	8.55	11.59	368.19	47.00	90.03	5.63
$N_{\mathrm{b}} = 4$	85.71	4.89	3.79	2.44	96.84	34.59	64.55	4.18
$p_{\mathrm{T}}^{\mathrm{miss}} > 200$ GeV	37.18	3.38	0.00	1.24	41.79	6.58	58.49	4.04
$p_{\mathrm{T}}^{\mathrm{miss}} > 300$ GeV	4.64	1.28	0.00	0.86	6.78	0.26	38.37	3.53
$p_{\mathrm{T}}^{\mathrm{miss}} > 400$ GeV	0.54	0.53	0.00	0.03	1.10	0.00	17.08	2.92

- $N_{\mathrm{b}} = 4$ SR: $N_{\mathrm{b}} \geq 4$, $100 < \langle m_{\mathrm{bb}} \rangle < 140$ GeV
- $N_{\mathrm{b}} = 4$ SB: $N_{\mathrm{b}} \geq 4$, $\langle m_{\mathrm{bb}} \rangle < 100$ GeV or $\langle m_{\mathrm{bb}} \rangle > 140$ GeV
- $N_{\mathrm{b}} = 3$ SR: $N_{\mathrm{b}} = 3$, $100 < \langle m_{\mathrm{bb}} \rangle < 140$ GeV
- $N_{\mathrm{b}} = 3$ SB: $N_{\mathrm{b}} = 3$, $\langle m_{\mathrm{bb}} \rangle < 100$ GeV or $\langle m_{\mathrm{bb}} \rangle > 140$ GeV
- CSR: $N_{\mathrm{b}} = 2$, $100 < \langle m_{\mathrm{bb}} \rangle < 140$ GeV
- CSB: $N_{\mathrm{b}} = 2$, $\langle m_{\mathrm{bb}} \rangle < 100$ GeV or $\langle m_{\mathrm{bb}} \rangle > 140$ GeV

These regions are used in the background estimation detailed in Section 4.2.1.

Additionally, all events passing the baseline selection are categorized into different categories based on $p_{\mathrm{T}}^{\mathrm{miss}}$ and ΔR_{max}. Events are split into four categories of $p_{\mathrm{T}}^{\mathrm{miss}}$, 150–200 GeV, 200–300 GeV, 300-400 GeV, and above 400 GeV as shown by the dotted lines in the top-left plot of Figure 4.2. Events are also split into two categories of ΔR_{max}, 0–1.1 and 1.1–2.2 as shown by the dotted lines in the bottom-right plot of Figure 4.2. Note that the SRs and SBs are also divided into $N_{\mathrm{b}} = 3$ and $N_{\mathrm{b}} = 4$ categories, which are treated separately by the background estimation method discussed in Section 4.2.1. Figure 4.3 shows the expected background composition of different integrated N_{b}–$p_{\mathrm{T}}^{\mathrm{miss}}$ and N_{b}–ΔR_{max} regions as derived from simulation. As previously described, $\mathrm{t\bar{t}}$+jets, Z+jets, and W+jets form the largest sources of background.

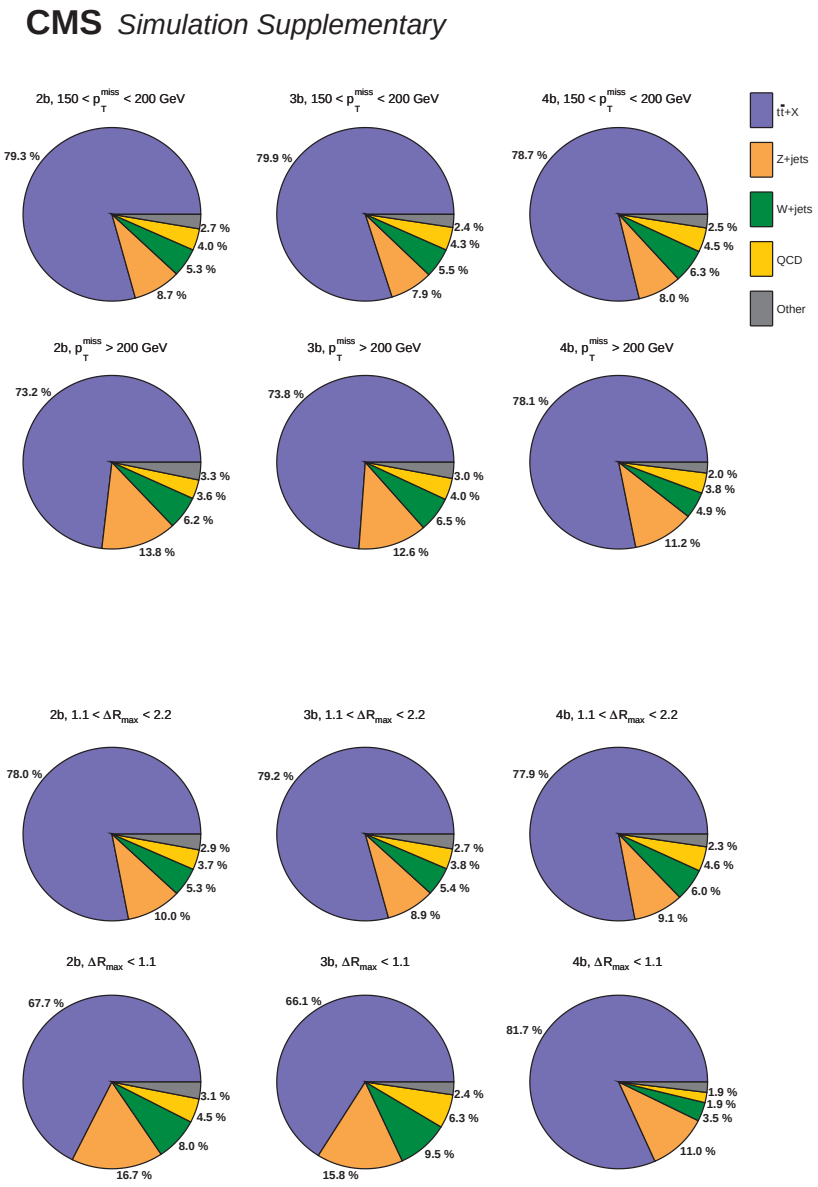

Figure 4.3: The background composition for different categories for the resolved topology. The columns correspond to N_{b} =2 (left), 3 (center), and 4 (right). Each row has one selection in addition to the baseline selection, $150 < p_{\mathrm{T}}^{\mathrm{miss}} < 200$ GeV (top row), $p_{\mathrm{T}}^{\mathrm{miss}} > 200$ GeV (second row), $1.1 < \Delta R_{\mathrm{max}} < 2.2$ (third row), and $\Delta R_{\mathrm{max}} < 1.1$ (bottom row).

4.1.3 Boosted topology event selection and categorization

The baseline selection for the boosted topology is similar to that for the resolved topology, featuring selections on $p_{\mathrm{T}}^{\mathrm{miss}}$, jets/Higgs boson candidates, leptons, and isolated tracks. The number of events in simulation passing different selections in the boosted baseline selection is shown in Table 4.2.

- $p_{\mathrm{T}}^{\mathrm{miss}}$ **selections** The boosted topology requires a $p_{\mathrm{T}}^{\mathrm{miss}} > 300$ GeV, a thresholda threshold which is higher than that for the resolved topology as the signal models targeted by the boosted topology have higher overall energy scales leading to higher momentum LSPs. As with the resolved topology, events are additionally categorized based on $p_{\mathrm{T}}^{\mathrm{miss}}$ to increase sensitivity for models with particularly large tails in their $p_{\mathrm{T}}^{\mathrm{miss}}$ distributions. As with the resolved topology, events likely to have spurious $p_{\mathrm{T}}^{\mathrm{miss}}$ are rejected using the filter criteria described in Section 3.3.2, the requirement $\Delta\phi_i > 0.3(0.5)$ for $i = 1, 2(3, 4)$, and the requirements $p_{\mathrm{T}}^{\mathrm{miss}}/p_{\mathrm{T,calo}}^{\mathrm{miss}} < 2$ and $p_{\mathrm{T}}^{\mathrm{miss}}/H_{\mathrm{T}}^{\mathrm{miss}} < 2$. If there are not four AK4 jets in an event, $\Delta\phi_i$ is only considered for i up to N_{jets}. The top-left plot of Figure 4.4 shows the distribution in $p_{\mathrm{T}}^{\mathrm{miss}}$ for events passing the boosted topology baseline selection.

- **Jet and Higgs boson candidate selections** At least two AK8 jets passing the selections described in Section 3.2.2 including a p_{T} requirement of at least 300 GeV must be present in boosted topology. The top-right plot of Figure 4.4 shows the p_{T} distribution for AK8 jets passing the boosted topology baseline selection. A loose selection is applied to the soft-drop mass of the two leading AK8 jets, requiring the

Table 4.2: Event yields obtained from simulated event samples as selection criteria are sequentially applied weighted to correspond to the luminosity of the Run 2 data set. These can be taken as an estimate for the number of events one would expect in data, though the formal background estimate is obtained from a data-driven method detailed in the next section. The event selection requirements listed above the horizontal line in the middle of the table are defined as the *boosted topology baseline selection*. The selections below the horizontal line are only to give a sense to the relative number of signal and background events expected in the different signal region categories.

$\mathcal{L} = 137$ fb^{-1}	$t\bar{t} + X$	Z +jets	W +jets	QCD	Other	Total SM Bkg.	TChiHH-G(500,0)	T5HH(1600,0)	T5HH(2000,0)
$p_T^{miss} > 250$ GeV, $H_T > 400$ GeV, $N_{veto\ leptons} = 0$, $N_{iso.\ tracks} = 0$, $N_{jets} \geq 2$, spurious p_T^{miss} rejection	219771.84	1220846.86	701764.09	1180276.47	22558.63	3345217.81	710.69	679.35	81.61
p_T^{miss} filters	194337.41	1136058.01	637884.34	32767.75	20022.70	2021070.24	701.12	655.18	78.77
$p_T^{miss} > 300$ GeV, $H_T > 600$ GeV	11022.84	68211.69	27892.49	728.94	1070.42	108926.38	204.37	620.10	76.20
2 AK8 jets	6355.74	41721.83	18416.62	580.64	694.27	67769.10	130.38	539.14	67.52
AK8 jet $p_T > 300$ GeV	1677.05	15763.63	6907.47	307.71	235.81	24891.67	58.86	465.02	61.30
$60 < m_J < 260$ GeV	424.59	1074.02	529.72	26.37	39.46	2094.04	27.93	268.44	35.64
$95 < m_J < 145$ GeV	53.69	149.82	74.75	2.22	3.31	283.81	16.97	155.07	21.28
$D_{bb} > 0.7$	2.57	0.42	0.07	0.00	0.88	3.95	12.58	60.73	8.42

jet mass to lie between 60 and 160 GeV. The bottom-left plot of Figure 4.4 shows the soft-drop mass distribution for AK8 jets after the boosted topology baseline selection. As discussed previously, these two jets are the Higgs boson candidates. Unlike the resolved topology baseline selection, no restriction on the maximum number of jets is imposed.

- **Leptons and track veto** The boosted baseline selection also requires exactly zero leptons passing the veto criteria or isolated tracks as defined in Section 3.2.1. This is identical to the resolved topology lepton and track veto, and removes a majority of the background from leptonically decaying W bosons.

All events passing the boosted topology baseline selection enter the final fit. However, events are only considered to be in the signal region (SR) if both Higgs boson candidate soft-drop masses are between 95 and 145 GeV and at least one of the Higgs boson candidates passes the loose working point of the DeepDoubleBvL double-b tagger. The bottom-right plot of Figure 4.4 shows the distribution in DeepDoubleBvL discriminant

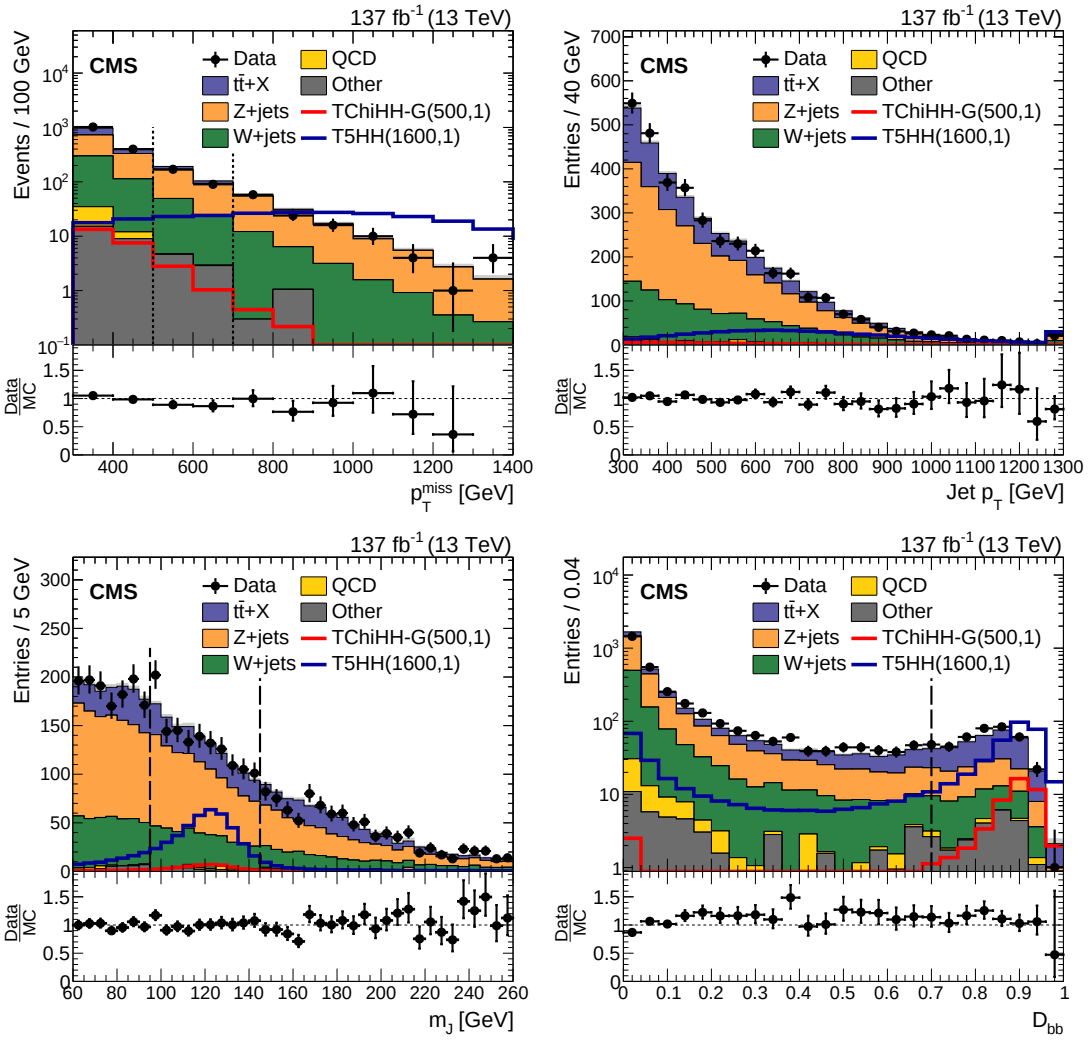

Figure 4.4: Distributions in the key analysis variables of the boosted topology after the baseline selection is applied. The black data points represent the observed data, the stacked histograms represent the yield from background simulation, scaled by a factor of 0.86 to match the integral of the observed data, and the colored outlines represent expected yields from selected signal models. The dashed lines indicate the signal region selection while the dotted lines represent signal region categorization (see Section 4.2).

for Higgs boson candidates and the loose-tagging threshold. Events are categorized into the SR, the sideband (SB), control region (CR), and control sideband (CSB) as follows:

- $N_{\mathrm{H}} = 2$ SR: $N_{\mathrm{H}} = 2$, $95 < m_{\mathrm{J}} < 145$ GeV for both Higgs boson candidates
- $N_{\mathrm{H}} = 2$ SB: $N_{\mathrm{H}} = 2$, not $95 < m_{\mathrm{J}} < 145$ GeV for both Higgs boson candidates
- $N_{\mathrm{H}} = 1$ SR: $N_{\mathrm{H}} = 1$, $95 < m_{\mathrm{J}} < 145$ GeV for both Higgs boson candidates
- $N_{\mathrm{H}} = 1$ SB: $N_{\mathrm{H}} = 1$, not $95 < m_{\mathrm{J}} < 145$ GeV for both Higgs boson candidates
- CSR: $N_{\mathrm{H}} = 0$, $95 < m_{\mathrm{J}} < 145$ GeV for both Higgs boson candidates
- CSB: $N_{\mathrm{H}} = 0$, not $95 < m_{\mathrm{J}} < 145$ GeV for both Higgs boson candidates

These regions are used in the background estimation detailed in Section 4.2.2.

Additionally, all events passing the baseline selection are categorized into different categories based on $p_{\mathrm{T}}^{\mathrm{miss}}$. Events are split into three categories of $p_{\mathrm{T}}^{\mathrm{miss}}$, 300–500 GeV, 500-700 GeV, and above 700 GeV as shown by the dotted lines in the top-left plot of Figure 4.4. Note that the SRs and SBs are also divided into $N_{\mathrm{H}} = 1$ and $N_{\mathrm{H}} = 2$ categories, which are treated separately by the background estimation method discussed in Section 4.2.2. Figure 4.5 shows the expected background composition from simulation in the SRs, the SBs, the CSR, the CSB, and the 0H+b SR described in Section 4.2.2. The largest sources of background are $\mathrm{t\bar{t}}$+jets, Z+jets, and W+jets events.

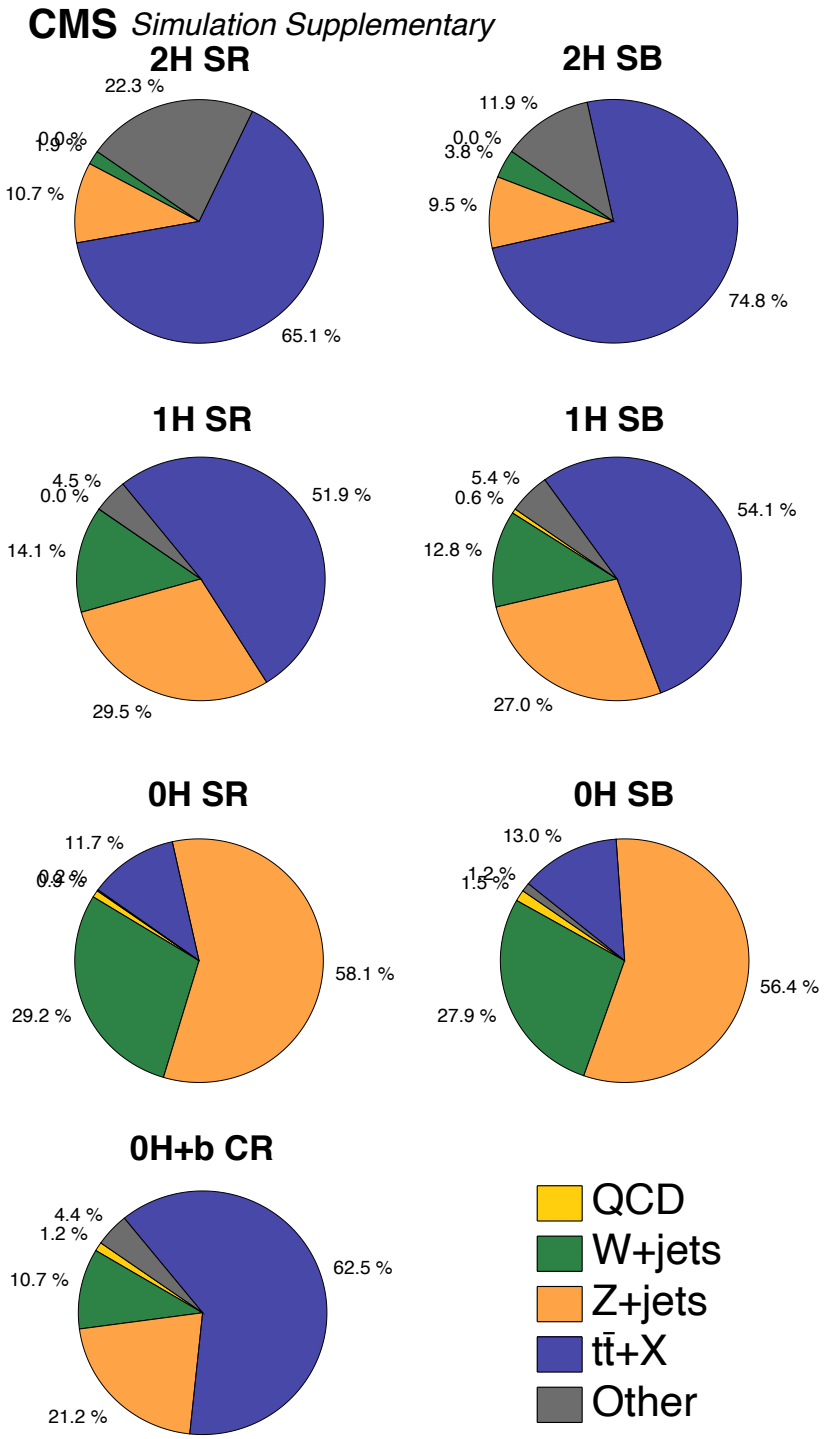

Figure 4.5: The background composition for different categories for the boosted topology.

4.2 Background estimation

If the considered higgsino signal models are true and produce HH(4b)+$p_{\mathrm{T}}^{\mathrm{miss}}$ events, these events would manifest as an excess over the SM background. The expected event yields of the SM backgrounds are predicted using a predominantly data-driven approach that exploits the minimal correlation between the mass of the Higgs boson candidates and the number of b- or double-b-tagged jets for background events. This section describes this background estimation method, which is sometimes called the "ABCD method".

4.2.1 Resolved topology background estimation

For the resolved topology, the HH(4b)+$p_{\mathrm{T}}^{\mathrm{miss}}$ signal is characterized by having $\langle m_{\mathrm{bb}} \rangle$ near the Higgs boson mass, 125 GeV, and by having a large number of b jets. Since the background is essentially entirely composed of fake Higgs bosons, it will only sometimes have both of these properties. Moreover, the distribution of background events in the variable $\langle m_{\mathrm{bb}} \rangle$ is approximately independent of N_{b} as shown in Figure 4.6. The left illustration in Figure 4.7 shows how the N_{b}-$\langle m_{\mathrm{bb}} \rangle$ plane is split into SRs, SBs, CSRs, and CSBs based on $\langle m_{\mathrm{bb}} \rangle$ and N_{b} as previously described. In the absence of any signal events, the yields in the four regions are related by

$$\frac{N_{n\text{b SR}}^{\text{background}}}{N_{n\text{b SB}}^{\text{background}}} = \kappa \frac{N_{\text{CSR}}^{\text{background}}}{N_{\text{CSB}}^{\text{background}}}, \tag{4.1}$$

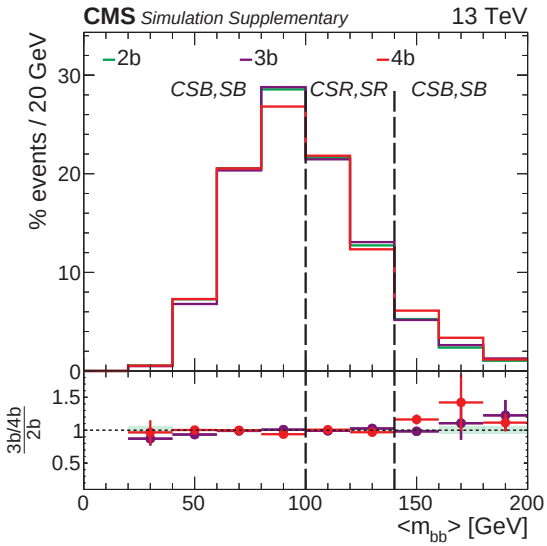

Figure 4.6: Normalized distributions in $\langle m_{\mathrm{bb}} \rangle$ for the $N_{\mathrm{b}} = 2$, 3, and 4 regions of the combined background simulated samples after the resolved topology baseline selection. The similarity of these shapes indicates that the ABCD method can be used to estimate the background in the SR region from the SB, CSR, and CSB regions.

where κ is a correction factor measured in simulation. In the case $\langle m_{\mathrm{bb}} \rangle$ and N_{b} are perfectly uncorrelated, κ is exactly one. As shown in Figure 4.8, the values of κ for the various categories of the resolved analysis are essentially all compatible with unity within statistical uncertainty. The quantity κ is thus mostly used to capture the uncertainty in possible correlation between N_{b} and $\langle m_{\mathrm{bb}} \rangle$ as described in Section 4.3.1.

While the full statistical methods take into account possible signal contamination in other regions, simulation suggests the signal should be largely negligible in all regions except the SRs. Equation 4.1 can thus be rearranged into

$$N^{\mathrm{pred}}_{n\mathrm{b}\ \mathrm{SR},i} = \kappa_{n\mathrm{b}} \frac{N_{\mathrm{CSR},i}}{N_{\mathrm{CSB},i}} N_{n\mathrm{b}\ \mathrm{SB}} \tag{4.2}$$

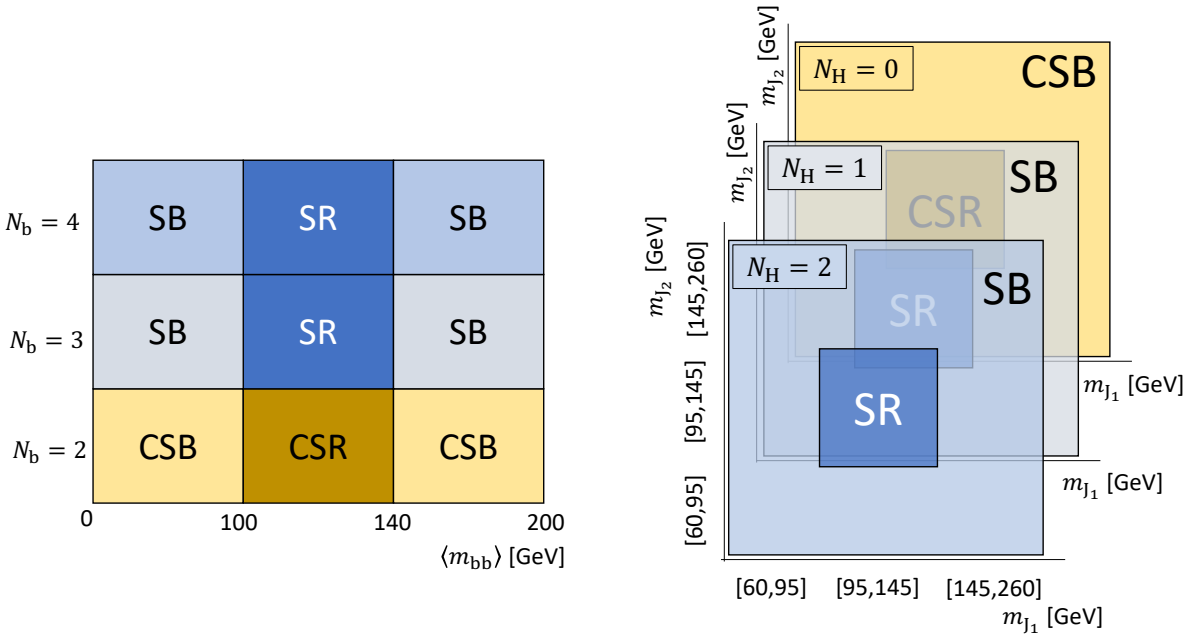

Figure 4.7: Configuration of SR, SB, CSR, and CSB regions for the resolved and boosted topologies.

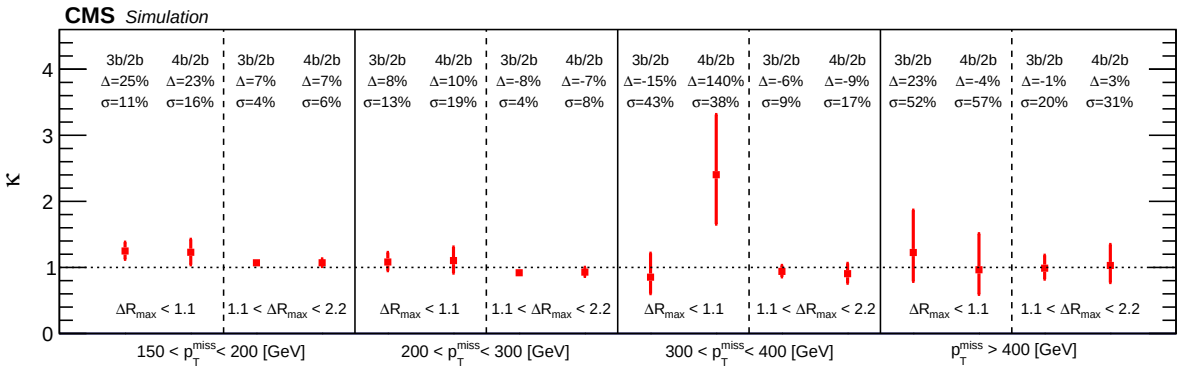

Figure 4.8: κ correction factors derived from simulation used for each category of the resolved topology along with their statistical uncertainty.

in order to make an approximate prediction for the number of events in the signal region.

This "ABCD method" is used to predict the SM event yields independently for each N_{b} region and in each of the $p_{\mathrm{T}}^{\mathrm{miss}}$ and ΔR_{max} categories for a total of 16 ABCD planes.

4.2.2 Boosted topology background estimation

The background estimation for the boosted topology is similar to that of the resolved topology, though with some key differences. Again, the HH(4b)+$p_{\mathrm{T}}^{\mathrm{miss}}$ signal is characterized by the two Higgs boson candidate jets having soft drop mass m_{J1} and m_{J2} near 125 GeV and having high DeepDoubleBvL discriminant score leading to high N_{H}. The right illustration of Figure 4.7 shows how the 3 dimensional space of m_{J1}, m_{J2}, and N_{H} is divided into SR, SB, CSR, and CSB regions in analogy with the resolved phase space. The left plot of Figure 4.9 shows the ratio of events in the (C)SR to those in the C(SB) as a function of N_{H}, again showing that this ratio of events in the Higgs boson mass window to those outside of it is roughly independent of N_{H}.

The key difference between the resolved and boosted topology background estimation methods is that the boosted topology does not have a sufficiently large statistical sample size in data to estimate the background independently in each $p_{\mathrm{T}}^{\mathrm{miss}}$ category. For this reason, the ABCD method is used only to estimate the total background in the SRs integrated across $p_{\mathrm{T}}^{\mathrm{miss}}$ categories. The fraction of background falling into each $p_{\mathrm{T}}^{\mathrm{miss}}$ category or "bin" is then estimated using a fraction f_i measured in a distinct 0H+b subregion that comprises events from both the CSR and CSB that have 0 double-b-tagged

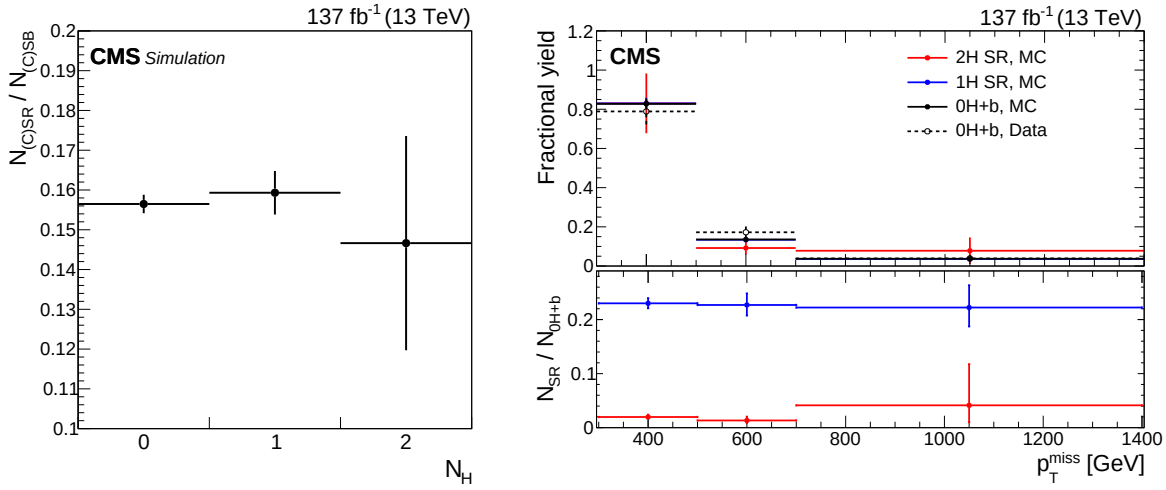

Figure 4.9: (left) The ratio of event yields in the Higgs boson mass window (C)SR to the event yields outside of the Higgs boson mass window (C)SB in simulation along with its uncertainty as a function of N_{H}. The ratio is relatively independent of N_{H}. (right) The normalized distribution of boosted topology events in $p_{\mathrm{T}}^{\mathrm{miss}}$ of $N_{\mathrm{H}} = 2$ category events from background simulation, $N_{\mathrm{H}} = 1$ category events from background simulation, 0H+b category events from background simulation, and 0H+b category events in data.

AK8 jets but 1 b-tagged AK4 jet. As shown in Figure 4.5, the background composition of this region is similar to that of the SRs and SBs. Furthermore, the right plot of Figure 4.9 shows that the normalized $p_{\mathrm{T}}^{\mathrm{miss}}$ distribution of the 0H+b region matches that of the $N_{\mathrm{H}} = 1$ and $N_{\mathrm{H}} = 2$ regions, justifying the use of the 0H+b region to determine the distribution of background across $p_{\mathrm{T}}^{\mathrm{miss}}$ categories.

Again assuming negligible signal contamination outside of the SRs, the background estimates for each boosted topology signal category are approximately given by

$$N^{\mathrm{pred}}_{n\mathrm{H\ SR},i} = f_i N^{\mathrm{pred}}_{n\mathrm{H\ SR,integrated}} = f_i \kappa_{n\mathrm{H}} \frac{N_{\mathrm{CSR}}}{N_{\mathrm{CSB}}} N_{n\mathrm{H\ SB}}, \tag{4.3}$$

where the κ are again correction factors for possible correlation between the Higgs boson

candidates masses and N_{H} and f_i for $i = 1, 2, 3$ are fraction of events in each $p_{\mathrm{T}}^{\mathrm{miss}}$ category in the 0H+b region. As seen in the left plot of Figure 4.9, both κ factors are consistent with 1 within uncertainties. Subsequently, the nominal value of κ is set to 1 and the factors are exclusively used to capture uncertainty in possible correlation as detailed in the next section.

4.3 Systematic uncertainties

This section outlines the measurement of systematic uncertainty in both the background prediction as well as the predicted signal yields for both the resolved and boosted topology. The analysis is designed so that the uncertainty in the background estimation is dominated by the statistical uncertainties of the SR, SB, CSR, and CSB regions as well as the 0H+b region of the boosted topology. The systematic uncertainties are nonetheless studied in order to demonstrate that the statistical uncertainty is in fact dominant.

4.3.1 Resolved topology background uncertainties

For the resolved topology, the uncertainty in any possible correlation between $\langle m_{\mathrm{bb}} \rangle$ and N_{b} and thus on the background estimation is entirely captured by the uncertainty in κ. In addition to the statistical uncertainty inherent to the derivation of κ in simulation, additional systematic uncertainties are taken from control samples in data to account for possible differences between simulation and actual data. In particular, the systematic uncertainty in κ is evaluated separately for the $\mathrm{t\bar{t}}$+jets, V+jets, and QCD

multijet background components. For each background source, the κ correction factors are evaluated in data and simulation across $p_{\mathrm{T}}^{\mathrm{miss}}$ categories in a data control sample. Since no $p_{\mathrm{T}}^{\mathrm{miss}}$ dependence is observed in the simulation-data agreement for any of the control samples, the κ factors are evaluated in a $p_{\mathrm{T}}^{\mathrm{miss}}$-integrated sample, and the larger of the data-simulation difference and the statistical uncertainty in simulation is taken as a measure of the systematic uncertainty in κ due to mismodeling of that particular background component.

κ systematic uncertainty for $\mathrm{t\bar{t}}$+jets events

A single-lepton control sample is used to measure the uncertainty in κ for $\mathrm{t\bar{t}}$ events. This control sample is similar to the baseline selection, but with the following modifications:

- $\boldsymbol{p_{\mathrm{T}}^{\mathrm{miss}}}$ **selections** To the increase the statistical sample size, the absolute $p_{\mathrm{T}}^{\mathrm{miss}}$ selection is loosened to 0 and events are instead categorized into three $p_{\mathrm{T}}^{\mathrm{miss}}$ categories: $p_{\mathrm{T}}^{\mathrm{miss}} < 75$ GeV, $75 < p_{\mathrm{T}}^{\mathrm{miss}} < 150$ GeV, and $p_{\mathrm{T}}^{\mathrm{miss}} > 150$ GeV. The $p_{\mathrm{T}}^{\mathrm{miss}}$ filters used in the baseline selection as well as the selections $p_{\mathrm{T}}^{\mathrm{miss}}/p_{\mathrm{T,calo}}^{\mathrm{miss}} < 5$ and $p_{\mathrm{T}}^{\mathrm{miss}}/H_{\mathrm{T}}^{\mathrm{miss}} < 5$ are applied. However, the presence of an isolated lepton makes contamination from mismeasured QCD multijet events minimal so the $\Delta\phi_i$ selections are not applied.

- **Jet selections** The requirements of four or five AK4 jets and at least two tight b-tagged jets are identical to the resolved topology baseline selection.

- **Lepton and isolated track selections** The lepton and isolated track veto requirements from the resolved topology baseline are removed and instead it is required that there is exactly one lepton passing the control sample lepton criteria outlined in Section 3.2.1 and no additional leptons passing the veto criteria. A requirement of $m_{\mathrm{T}} < 100$ GeV is imposed on the lepton to suppress signal contamination, though this is most relevant for removing contamination from other SUSY models that feature prompt leptons.

- **Higgs boson candidate selections** The selections on Higgs candidates are identical to the resolved topology baseline selection.

For $\mathrm{t\bar{t}}$+jets events, this control region is nearly identical to the search region except that the lepton that would be missed in the search region is instead reconstructed. The reconstruction status of the lepton has minimal correlation with the properties of the Higgs candidates, so the $\langle m_{\mathrm{bb}} \rangle$-$N_{\mathrm{b}}$ correlation measured in this control sample should accurately represent the correlation in the signal region. Figure 4.10 shows the distribution in $\langle m_{\mathrm{bb}} \rangle$ for $N_{\mathrm{b}} = 2$ and $3 \leq N_{\mathrm{b}} \leq 4$ events as well as the relative background contribution, which is dominated by $\mathrm{t\bar{t}}$+jets events. By comparing the yields in data and simulation between the SR, SB, CSR, and CSB, κ factors are calculated for each N_{b}, $p_{\mathrm{T}}^{\mathrm{miss}}$, and ΔR_{max} category. The κ factors are shown in Figure 4.11. Overall good agreement is observed and appears independent of $p_{\mathrm{T}}^{\mathrm{miss}}$. For this reason, final κ factors are evaluated by integrating $p_{\mathrm{T}}^{\mathrm{miss}}$ categories, and the larger of the data-simulation disagreement and the systematic uncertainty in simulation is taken as the scale of systematic uncertainty

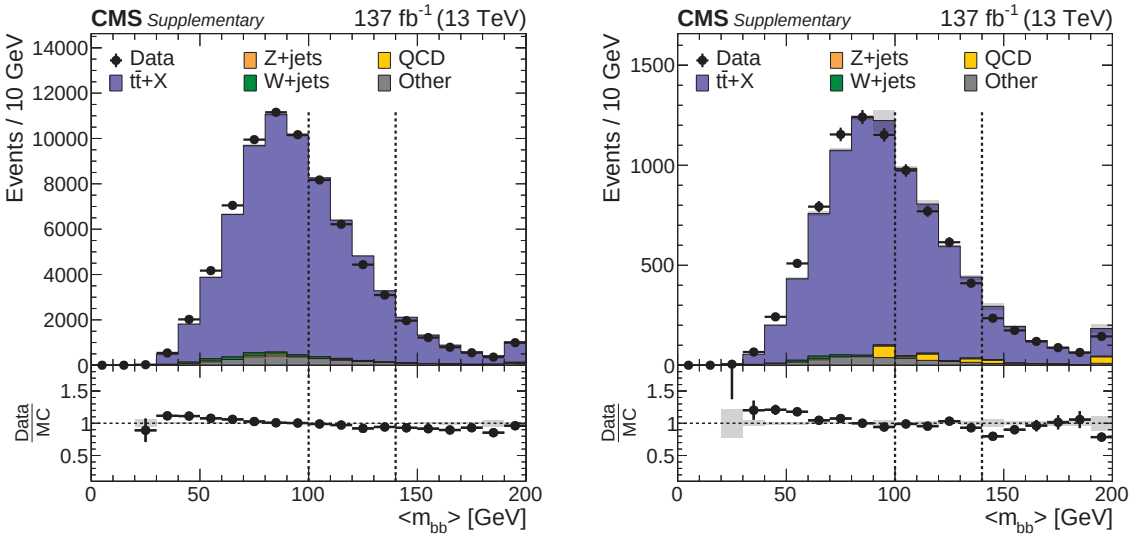

Figure 4.10: Distribution in $\langle m_{\mathrm{bb}} \rangle$ of events in the single-lepton control sample showing the data in black and the simulated events as a stacked histogram with colors corresponding to the background type in the $N_{\mathrm{b}} = 2$ category (left) and in the $N_{\mathrm{b}} = 3$ or $N_{\mathrm{b}} = 4$ categories (right). Any correlation between $\langle m_{\mathrm{bb}} \rangle$ and N_{b} should manifest as a difference in these $\langle m_{\mathrm{bb}} \rangle$ shapes.

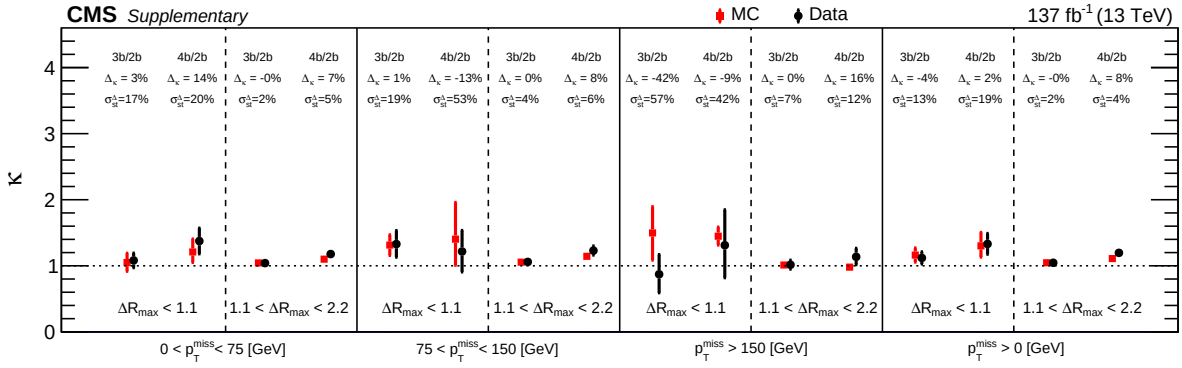

Figure 4.11: κ factors measured in data (black) and simulation (red) across N_{b}, $p_{\mathrm{T}}^{\mathrm{miss}}$, and ΔR_{max} categories in the single-lepton control sample.

in κ for $\mathrm{t\bar{t}}$+jets events. The final relative uncertainties are 13%, 19%, 2%, and 8% for the $(\Delta R_{\mathrm{max}} < 1.1, N_{\mathrm{b}} = 3)$, $(\Delta R_{\mathrm{max}} < 1.1, N_{\mathrm{b}} = 4)$, $(1.1 < \Delta R_{\mathrm{max}} < 2.2, N_{\mathrm{b}} = 3)$, and $(1.1 < \Delta R_{\mathrm{max}} < 2.2, N_{\mathrm{b}} = 4)$ categories, respectively.

κ systematic uncertainty for V+jets events

A Drell-Yan $Z \to \ell^+\ell^-$ dilepton control sample is used to measure the uncertainty in κ for V+jets events. The control sample is again similar to the baseline selection, but with the following modifications:

- $p_{\mathbf{T}}^{\mathbf{miss}}$ **selections** Since no true $p_{\mathrm{T}}^{\mathrm{miss}}$ is expected in such events, the $p_{\mathrm{T}}^{\mathrm{miss}}$ selection is inverted and events with $p_{\mathrm{T}}^{\mathrm{miss}} < 50$ GeV are selected. Furthermore, $\Delta\phi_i$ selections are not applied since contamination from QCD multijet events are negligible, though the standard $p_{\mathrm{T}}^{\mathrm{miss}}$ filters, the requirement $p_{\mathrm{T}}^{\mathrm{miss}}/p_{\mathrm{T,calo}}^{\mathrm{miss}} < 5$, and the requirement $p_{\mathrm{T}}^{\mathrm{miss}}/H_{\mathrm{T}}^{\mathrm{miss}} < 5$ are applied to remove events that may have particle-flow reconstruction failures.

- **Jet selections** The requirements of four or five AK4 jets is identical to the baseline selection, however no requirement is placed on the number of b jets since such a requirement causes significant contamination from $\mathrm{t\bar{t}}$+jets events.

- **Lepton and isolated track selections** Events in the dilepton control sample must have two leptons passing the control sample lepton criteria given in Section 3.2.1 and no additional leptons passing the veto criteria. The two leptons must have an invariant mass between 80 and 100 GeV in order to select events with leptons from Z boson decays.

- **Higgs boson candidate selections** The selections on Higgs candidates are identical to the resolved topology baseline selection.

Other than the decay of the Z boson, the topology of Z+jets events with a Z boson decaying into charged leptons should be identical to that of Z+jets events in which the Z boson decays into a pair of neutrinos. The leptonic events can then be used as a proxy for Z+jets with a Z boson decaying to neutrinos if the p_{T} of the dilepton system, $p_{\mathrm{T}}^{\mathrm{Z}}$, is identified with the $p_{\mathrm{T}}^{\mathrm{miss}}$. Events are thus categorized into five $p_{\mathrm{T}}^{\mathrm{Z}}$ categories: 0–75 GeV, 75–150 GeV, 150–200 GeV, 200–300 GeV, and greater than 300 GeV. W+jets events are also expected to have a similar, though not identical, kinematics if the W boson decays into a neutrino and a charged lepton that is not reconstructed. The dilepton control region is thus used to estimate the correlation between $\langle m_{\mathrm{bb}} \rangle$ and N_{b} for V+jets events since the properties of the Higgs candidates are independent of the Z boson decay mode. However, when two or more b jets are required, the contamination from $\mathrm{t\bar{t}}$+jets events with leptonically decaying W bosons becomes large. For this reason, the correlation between $\langle m_{\mathrm{bb}} \rangle$ and $N_{\mathrm{b,M}}$, the number of jets passing the DeepCSV medium working point, is measured only for $N_{\mathrm{b,M}}$ =0 and $N_{\mathrm{b,M}}$ =1.

Figure 4.12 shows the distribution in $\langle m_{\mathrm{bb}} \rangle$ for $N_{\mathrm{b,M}} = 0$ and $N_{\mathrm{b,M}} = 1$ events as well as the relative background contribution, which is dominated by Z+jets events. Using the $N_{\mathrm{b,M}} = 1$ category to define the SR and SB and the $N_{\mathrm{b,M}} = 0$ category to define the CSR and CSB, κ factors are calculated for each $p_{\mathrm{T}}^{\mathrm{Z}}$ and ΔR_{max} category. The κ factors are shown in Figure 4.13. Again, agreement is relatively good and independent of $p_{\mathrm{T}}^{\mathrm{Z}}$. Subsequently, the analysis regions are integrated across $p_{\mathrm{T}}^{\mathrm{Z}}$ categories, and the larger of the data-simulation disagreement and the systematic uncertainty in the simulation is

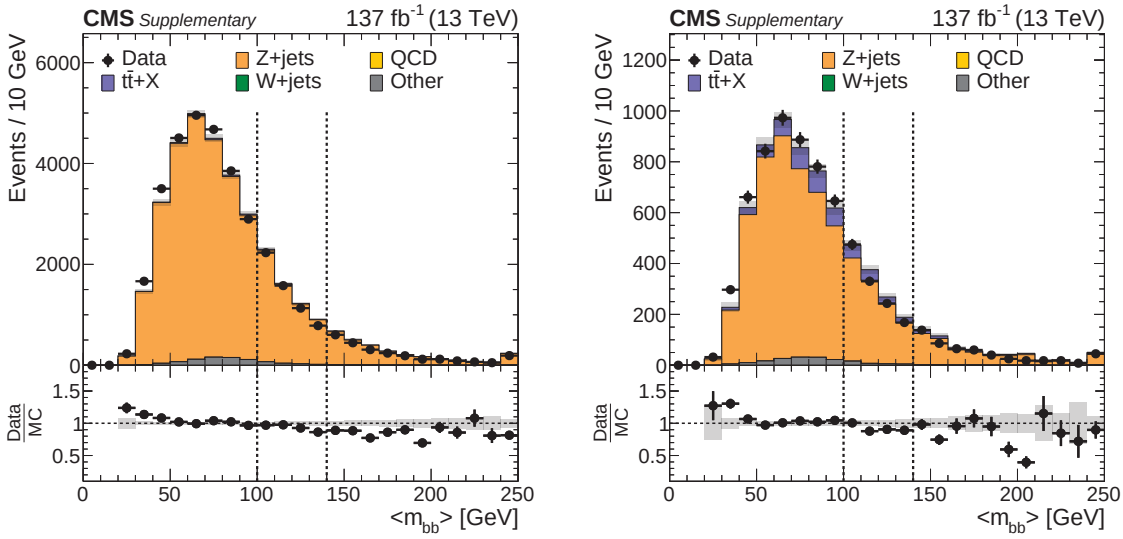

Figure 4.12: Distribution in $\langle m_{\mathrm{bb}} \rangle$ of events in the dilepton control sample showing the data in black and the simulated events as a stacked histogram with colors corresponding to the background type in the $N_{\mathrm{b,M}} = 1$ category (left) and in the $N_{\mathrm{b,M}} = 2$ category (right). Any correlation between $\langle m_{\mathrm{bb}} \rangle$ and N_{b} should manifest as a difference in these $\langle m_{\mathrm{bb}} \rangle$ shapes.

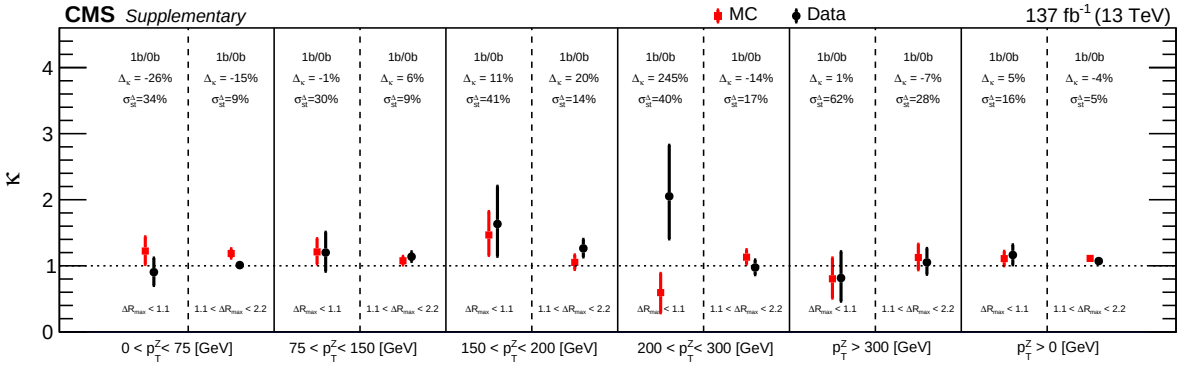

Figure 4.13: κ factors measured in data (black) and simulation (red) across $p_{\mathrm{T}}^{\mathrm{Z}}$, and ΔR_{max} categories in the dilepton control sample.

taken as the scale of systematic uncertainty in κ for V+jets events. The final relative uncertainties are 16% and 5% for the $\Delta R_{\mathrm{max}} < 1.1$ and $1.1 < \Delta R_{\mathrm{max}} < 2.2$ categories respectively.

κ systematic uncertainty for QCD multijet events

Although QCD multijet multijet events are expected to only make up a small part of the background, such events primarily enter the analysis selection due to mismeasurement, which means the simulated predictions are sensitive to how well the CMS detector is modeled in simulation. For this reason, extra care is taken with QCD multijet events and a separate low-$\Delta\phi$ control sample is used to measure the uncertainty in the background estimation for these events. The selections for the low-$\Delta\phi$ control sample are similar to the baseline selection, except with the following modifications:

- $p_{\mathbf{T}}^{\mathbf{miss}}$ **selections** As with the search region, events are required to have $p_{\mathrm{T}}^{\mathrm{miss}} > 150$ GeV, pass the $p_{\mathrm{T}}^{\mathrm{miss}}$ filters, have $p_{\mathrm{T}}^{\mathrm{miss}}/p_{\mathrm{T,calo}}^{\mathrm{miss}} < 2$, and have $p_{\mathrm{T}}^{\mathrm{miss}}/H_{\mathrm{T}}^{\mathrm{miss}} < 2$. Events are required, however, to fail one of the $\Delta\phi_i$ selections. That is, the $\vec{p}_{\mathrm{T}}^{\mathrm{miss}}$ must be either within ΔR of 0.5 of one of the leading two jets or within ΔR of 0.3 of the third or fourth jet. This defines a samples that is enhanced in events where the $p_{\mathrm{T}}^{\mathrm{miss}}$ originates from undermeasured jets.

- **Jet selections** The requirements of four or five AK4 jets is identical to the baseline selection, however no requirement is placed on the number of b jets since such a requirement causes significant contamination from $\mathrm{t\bar{t}}$+jets events.

- **Lepton and isolated track selections** The veto requirements on leptons and isolated tracks are identical to the resolved topology baseline selection.

- **Higgs boson candidate selections** The selections on Higgs candidates are iden-

tical to the resolved topology baseline selection.

The selections for the low-$\Delta\phi$ control sample are similar to the baseline selections except that the $\Delta\phi$ selection is inverted to create a sample enriched in QCD multijet events. The sample is split into $p_{\mathrm{T}}^{\mathrm{miss}}$ and ΔR_{max} categories with the same boundaries as the search region. However, as with the dilepton control sample, requiring two b jets causes a large contamination from $\mathrm{t\bar{t}}$+jets events. For this reason, the correlation between $\langle m_{\mathrm{bb}} \rangle$ and the number of b-tagged jets is evaluated by comparing the $N_{\mathrm{b,M}} = 0$ and $N_{\mathrm{b,M}} = 1$ regions. Figure 4.14 shows the distribution in $\langle m_{\mathrm{bb}} \rangle$ for the $N_{\mathrm{b,M}} = 0$ and $N_{\mathrm{b,M}} = 1$ categories in the low-$\Delta\phi$ control sample. These categories can be seen to be dominated by QCD multijet events.

Using the $N_{\mathrm{b,M}} = 1$ category to define the SR and SB and the $N_{\mathrm{b,M}} = 0$ category to define the CSR and CSB as in the dilepton control sample, κ factors are calculated for each $p_{\mathrm{T}}^{\mathrm{miss}}$ and ΔR_{max} category. Figure 4.15. Agreement is good across $p_{\mathrm{T}}^{\mathrm{miss}}$ categories, so the data are again integrated across $p_{\mathrm{T}}^{\mathrm{miss}}$ categories. The larger of the data-simulation disagreement and the systematic uncertainty in the simulation for this control sample is then taken as the scale of systematic uncertainty in κ for QCD multijet events. The final relative uncertainties are 9% and 7% for the $\Delta R_{\mathrm{max}} < 1.1$ and $1.1 < \Delta R_{\mathrm{max}} < 2.2$ categories respectively.

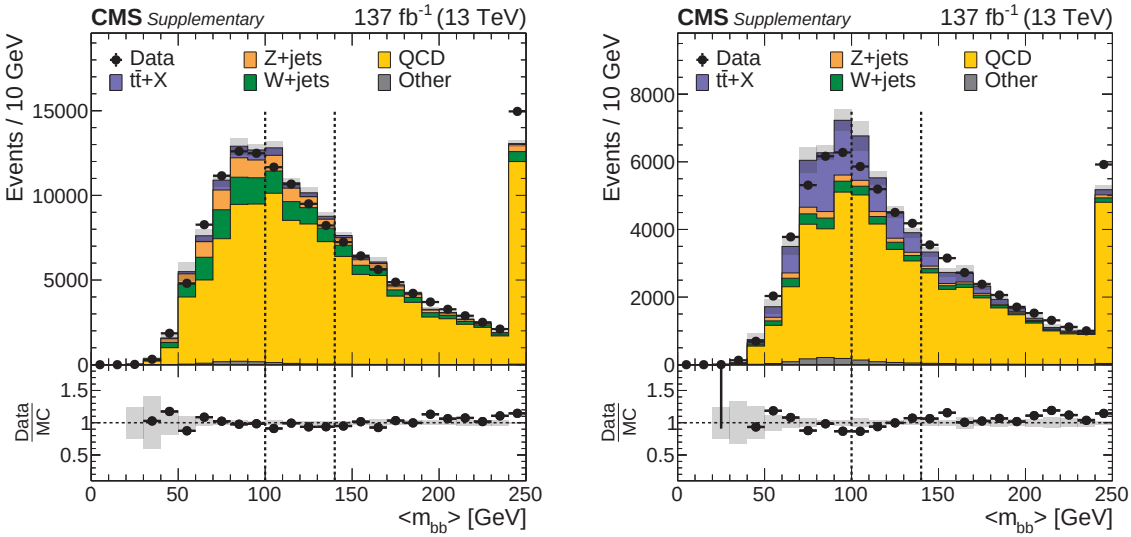

Figure 4.14: Distribution in $\langle m_{\mathrm{bb}} \rangle$ of events in the low-$\Delta\phi$ control sample showing the data in black and the simulated events as a stacked histogram with colors corresponding to the background type in the $N_{\mathrm{b,M}} = 1$ category (left) and in the $N_{\mathrm{b,M}} = 2$ category (right). Any correlation between $\langle m_{\mathrm{bb}} \rangle$ and N_{b} should manifest as a difference in these $\langle m_{\mathrm{bb}} \rangle$ shapes.

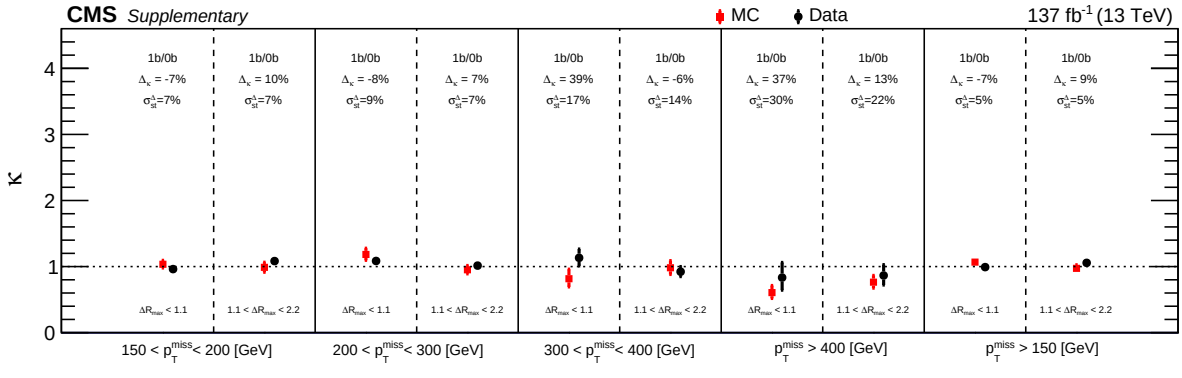

Figure 4.15: κ factors measured in data (black) and simulation (red) across $p_{\mathrm{T}}^{\mathrm{miss}}$, and ΔR_{max} categories in the low-$\Delta\phi$ control sample.

Overall systematic uncertainty in κ

As previously stated, the systematic uncertainty in the resolved topology background estimation method is captured entirely by κ since the ABCD prediction gives an exact background prediction up to statistical fluctuations in the absence of correlation between $\langle m_{\mathrm{bb}} \rangle$ and N_{b}. The overall uncertainty in κ is taken to be the combination of the statistical uncertainty from the measurement of κ in simulation and the uncertainty due to possible mismodeling in simulation. The mismodeling uncertainty for $\mathrm{t\bar{t}}$+jets, V+jets, and QCD multijet events are taken from the uncertainties measured in the single-lepton, dilepton, and low-$\Delta\phi$ control samples respectively. The uncertainty from mismodeling for each component in each $p_{\mathrm{T}}^{\mathrm{miss}}$, N_{b}, and ΔR_{max} category is then the mismodeling uncertainty from the control region, weighted to the fraction of $\mathrm{t\bar{t}}$+jets, V+jets, or QCD multijet events in that particular category in simulation. An additional uncertainty in the fraction of $\mathrm{t\bar{t}}$+jets, V+jets, and QCD multijet events in each category was investigated, but found to be negligible. Table 4.3 shows the final uncertainties in κ for each category of the resolved topology.

4.3.2 Boosted topology background uncertainties

The uncertainty in the background estimation method for the boosted topology stems from both the κ factor parametrizing correlation between the Higgs boson candidate masses and the number of double-b tagged jets as well as from the predicted fraction f_i of background in each $p_{\mathrm{T}}^{\mathrm{miss}}$ category. Uncertainties on these two pieces are evaluated

Table 4.3: Overall uncertainties in κ and thus in the resolved topology background estimation method for each $p_{\mathrm{T}}^{\mathrm{miss}}$, N_{b}, and ΔR_{max} category. The four sources of uncertainty in κ are the statistical uncertainty from the measurement in the simulation, and the uncertainties related to mismodeling in simulation for $\mathrm{t\bar{t}}$+jets, V+jets, and QCD multijet events measured in the single-lepton, dilepton, and low-$\Delta\phi$ control samples respectively.

Source		Uncertainty [%]							
	$p_{\mathrm{T}}^{\mathrm{miss}}$ [GeV]	150–200		200–300		300–400		>400	
	N_{b}	3	4	3	4	3	4	3	4
		$1.1 < \Delta R_{\mathrm{max}} < 2.2$							
κ stat. unc.		4	6	4	8	10	17	20	31
	$\mathrm{t\bar{t}}$	2	9	2	9	1	8	1	8
$\Delta\kappa$(data, MC)/κ	V+jets	<1	<1	1	<1	1	1	2	2
	QCD	<1	<1	<1	1	<1	<1	<1	1
κ total syst. unc.		2	9	2	9	1	8	2	9
		$\Delta R_{\mathrm{max}} < 1.1$							
κ stat. unc.		11	16	13	19	43	38	52	57
	$\mathrm{t\bar{t}}$	12	17	10	16	6	12	6	8
$\Delta\kappa$(data, MC)/κ	V+jets	1	1	4	5	10	6	6	10
	QCD	<1	<1	<1	2	<1	<1	<1	<1
κ total syst. unc.		12	17	11	17	12	13	8	13

separately.

The κ factors are measured in simulation, and the statistical uncertainty from this measurement is taken as one source of systematic uncertainty in κ. Several steps are used to evaluate the uncertainty in κ due to mismodeling in simulation. A boosted topology single-lepton control sample is defined with the boosted topology baseline selection modified to require exactly one control region quality lepton with $m_{\mathrm{T}} < 100$ GeV and remove the isolated track veto requirement and the $\Delta\phi$ requirements. Figure 4.16 shows the background estimate and observed background yields in this control sample following a procedure analogous to the search region. The SR, SB, CSR, and CSB equivalents in this region are used to measure κ in simulation and data, and the larger of the data-simulation disagreement and the simulation statistical uncertainty is taken as the uncertainty in κ due to simulation mismodeling of lost lepton events. This procedure yields relative uncertainties of 9% and 13% in κ for the $N_{\mathrm{H}} = 1$ and $N_{\mathrm{H}} = 2$ regions respectively. A single-photon validation sample is also defined by requiring one photon, a proxy for Z bosons decaying to neutrinos, with $p_{\mathrm{T}}^{\mathrm{miss}} \geq 200$ GeV after the photon's vector momentum is added to the $\vec{p}_{\mathrm{T}}^{\mathrm{miss}}$. Figure 4.17 shows the background estimate and background yields in this control sample, again analogously to the search region. The κ factors measured in this region are found to be compatible between data and simulation within statistical uncertainties, but the statistical uncertainty in data is found to be too large to make a meaningful evaluation of mismodeling uncertainty. Subsequently, the single-photon region is used only for validation, and additional uncertainties are as-

signed to cover remaining effects of mismodeling in simulation. The following variations are made to simulation and the relative changes in κ for each variation are added in quadrature to derive a final simulation mismodeling uncertainty:

- The double-b tagging and mistagging efficiencies are varied up and down by the uncertainty measured in Section 3.2.3 by varying the scale factors applied simulated events.

- The reconstructed jet energy is varied up and down by the uncertainties in jet energy scale derived in Section 2.3.5.

- The reconstructed jet energy resolution is varied by the uncertainties in jet energy resolution derived in Section 2.3.5.

- The amount of initial-state radiation in $\mathrm{t\bar{t}}$+jets events is varied by varying the associated correction scale factors described in Section 3.3.3 by 50% of their nominal values.

- The renormalization and factorization scales of the matrix-element calculation are simultaneously varied by a factor of between 0.5 and 2 by introducing appropriate scale factors, with the constraint that the two scales should not differ by more than a factor of 2.

This procedure yields a total mismodeling uncertainty in κ of 4% for the $N_{\mathrm{H}} = 1$ category and 6% for the $N_{\mathrm{H}} = 2$ category.

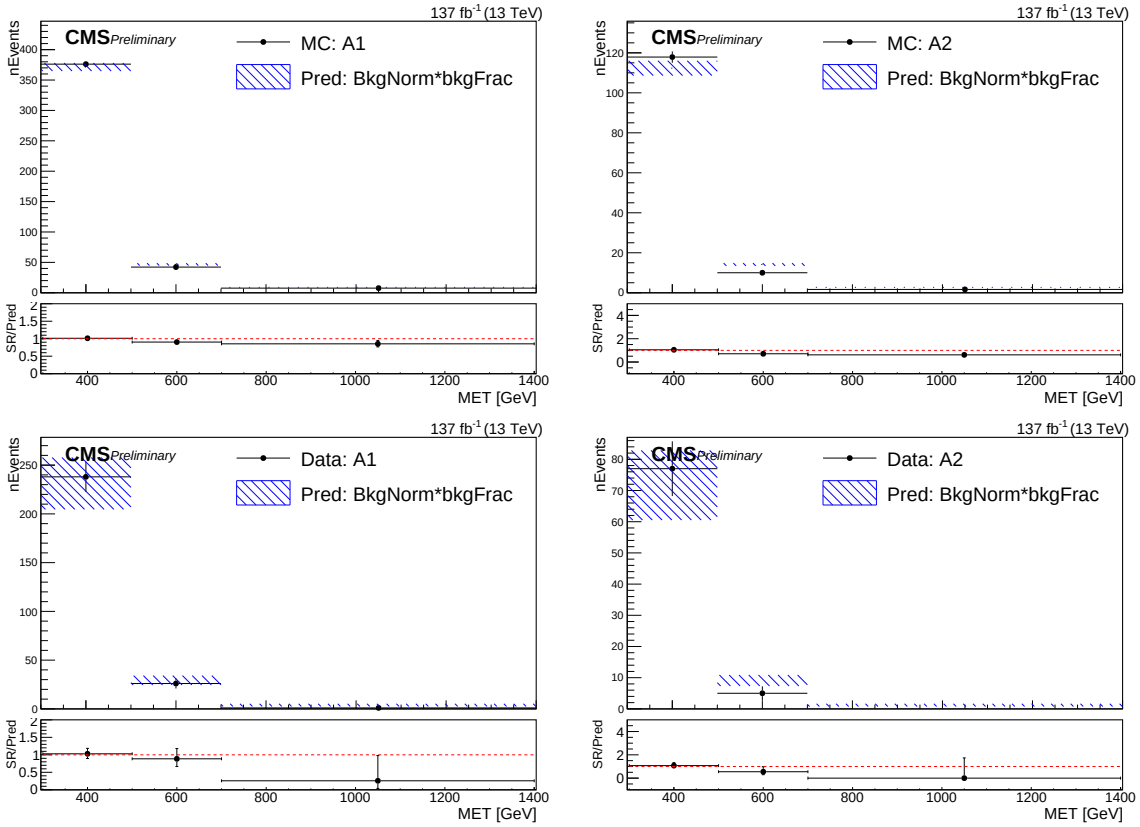

Figure 4.16: The boosted topology background estimate, shown as a blue hatched box, compared to the actual background yield in that region, shown as black data points, in the $N_{\mathrm{H}} = 1$ region (left) and the $N_{\mathrm{H}} = 2$ region (right) for simulation (top) and data (bottom) in the boosted topology single-lepton control sample. Overall good agreement is observed, and the $p_{\mathrm{T}}^{\mathrm{miss}}$-integrated κ factors in simulation and data are used to assign a systematic uncertainty in κ.

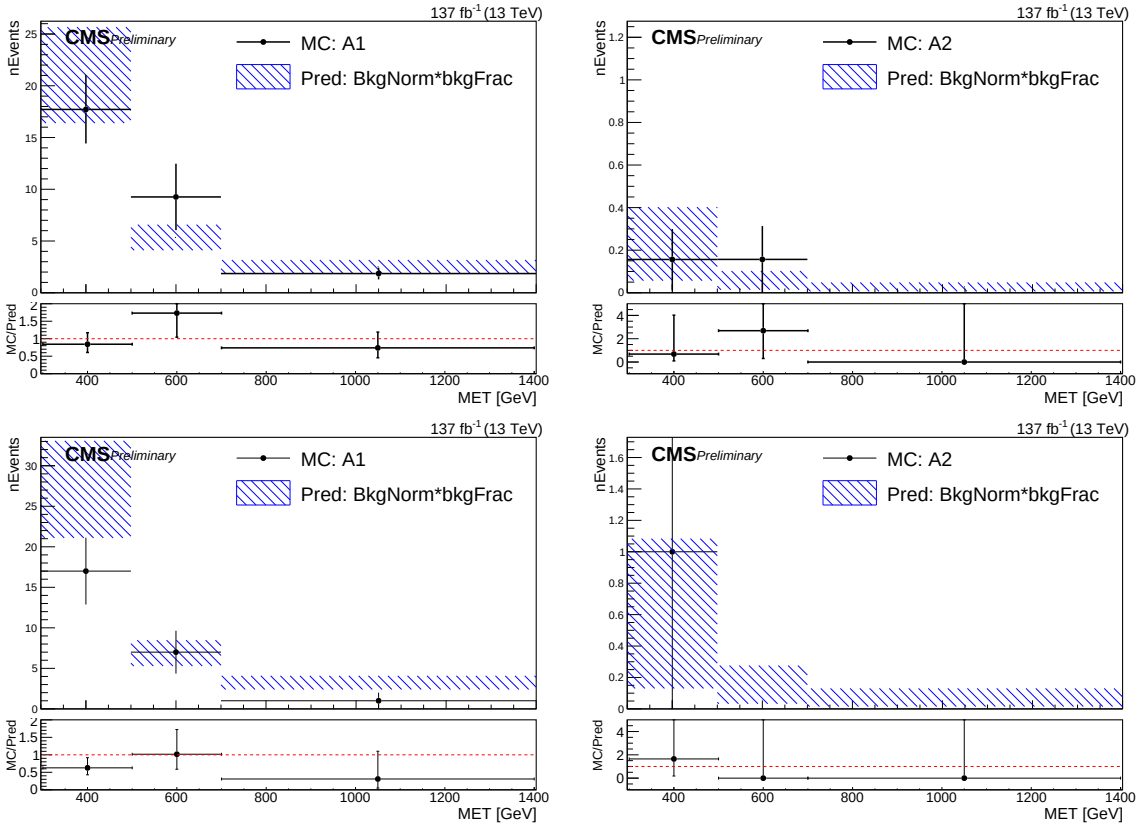

Figure 4.17: The boosted topology background estimate, shown as a blue hatched box, compared to the actual background yield in that region, shown as black data points, in the $N_{\mathrm{H}} = 1$ region (left) and the $N_{\mathrm{H}} = 2$ region (right) for simulation (top) and data (bottom despite the label reading "MC") in the boosted topology single-photon control sample. Overall agreement is observed, but the large statistical uncertainty in data makes this region a poor measure of data-simulation differences.

Since the $p_{\mathrm{T}}^{\mathrm{miss}}$ fraction factors f_i are taken from the 0H+b control region in data, the systematic uncertainty in these factors arises from differences in the $p_{\mathrm{T}}^{\mathrm{miss}}$ distribution between the 0H+b control region and the signal regions. This is evaluated with simulation by examining the ratio between the percentage of events falling into each $p_{\mathrm{T}}^{\mathrm{miss}}$ category in the signal regions and in the 0H+b control region. This ratio is shown in the bottom panel of the right plot of Figure 4.9. A linear fit is performed to this ratio as a function of $p_{\mathrm{T}}^{\mathrm{miss}}$ and the difference between the central value of the fit in each bin and the $p_{\mathrm{T}}^{\mathrm{miss}}$-averaged value is taken as systematic uncertainty in f_i. This uncertainty is referred to as the $p_{\mathrm{T}}^{\mathrm{miss}}$ shape closure uncertainty. Since simulation was used to evaluate the uncertainty stemming from the difference between the signal regions and the 0H+b control region, additional uncertainties are assigned to address any mismodeling in simulation. First, an uncertainty in the simulated background composition is assigned by varying the fraction of Z+jets background by a factor of 2 and 0.5 and taking the larger of the relative differences in each $p_{\mathrm{T}}^{\mathrm{miss}}$ category. Second, the same five variations in simulation described for the κ mismodeling uncertainty are performed along with a variation on the b-tagging efficiency within the uncertainties measured in Section 3.2.3 are performed and the resulting relative differences are added in quadrature to produce an estimate of potential uncertainty from mismodeling in simulation.

Table 4.4 summarizes the sources of systematic uncertainty in the boosted topology background estimate. The uncertainties in κ, which are shown above the middle horizontal line, stem from the statistical uncertainty in the measurement of κ and simulation

Table 4.4: Summary of systematic uncertainties in the background prediction for the boosted signature. The uncertainties in κ and thus the integrated background prediction are given above the middle horizontal lines while those in f_i and thus the distribution across $p_{\mathrm{T}}^{\mathrm{miss}}$ categories are given below the horizontal line.

Source	$p_{\mathrm{T}}^{\mathrm{miss}}$ [GeV]	Uncertainty [%]	
		1H	2H
κ simulation statistical uncertainty	>300	4	17
Lost lepton Δ(data, simulation)	>300	9	13
κ simulation modeling	>300	4	6
$p_{\mathrm{T}}^{\mathrm{miss}}$ shape closure	[300, 500]	2	13
	[500, 700]	3	19
	>700	9	63
Simulation background composition	[300, 500]	3	
	[500, 700]	7	
	>700	32	
$p_{\mathrm{T}}^{\mathrm{miss}}$ shape simulation modeling	[300, 500]	1	
	[500, 700]	2	
	>700	5	

mismodeling, which is evaluated using a combination of a data control sample and variations of the simulation. The uncertainties in f_i, which are shown below the middle horizontal line, stem from differences in the $p_{\mathrm{T}}^{\mathrm{miss}}$ distribution between the 0H+b region and the signal regions. This is evaluated in simulation as the closure uncertainty, then additional uncertainties due to simulation mismodeling are assigned by varying the background composition as well as various simulation parameters that may be mismodeled.

4.3.3 Signal uncertainties

If a signal is found to be present, the total yield of events can be used to extract the rate of HH(4b)+$p_{\mathrm{T}}^{\mathrm{miss}}$ events. To accurately extract a rate of signal events, the systematic uncertainty in signal acceptance in each signal region due to each aspect of

the analysis must be quantified. Each source of systematic uncertainty corresponds to a nuisance parameter as described in the next section, but these nuisance parameters are constrained to a general scale. This section describes how the scale of each source of systematic uncertainty is evaluated. The scale of each systematic uncertainty will in general be different for each signal model considered. Table 4.5 provides the median 68% percentile range of values for the scale of each systematic uncertainty across the signal models considered by this analysis. The following list describes how the scale of each source of systematic uncertainty in the signal event yields is determined.

- **Simulated sample size** The statistical uncertainty of the signal event yield predictions in simulation is taken as one source of systematic uncertainty.

- **Initial-state radiation** The momentum distribution of initial-state radiation is varied by varying the scale factors described in Section 3.3.3 by 100% of their nominal value for the TChiHH and TChiHH-G models or by 50% of their nominal value for the T5HH models, and the change in signal event yields is taken as the associated uncertainty scale.

- **Theoretical prediction** The uncertainty in simulation from the matrix element calculation is evaluated by varying the renormalization and factorization scales simultaneously by factors of 0.5 and 2 with the constraint that the two be within a factor of 2 of each other. This is implemented using scale factors and the largest resulting change in signal event yields is taken as the uncertainty scale.

- **Pileup modeling** As described in Section 3.3.3, the scale factors used to correct the pileup distribution in simulation to match that in data are derived using luminosity measurements and the inelastic p-p cross section measured in Ref. [384]. The systematic uncertainty due to pileup is evaluated by varying these scale factors by 5%, roughly the uncertainty in the inelastic cross section measurement, and measuring the change in signal event yields.

- **Integrated luminosity** A flat systematic uncertainty of 1.6% is taken to correspond to the uncertainty in the measured integrated luminosity of the data set used in this analysis as determined by the CMS luminosity group.

- **Jet energy scale** The jet energy corrections described in Section 2.3.5 are varied within the uncertainties described in the same section and the measured change in the signal event yields is taken as the scale of systematic uncertainty associated with jet energy scale.

- **Jet energy resolution** The jet energy resolution corrections, also described in Section 2.3.5, are varied within their measured uncertainties and the change in signal event yields is taken as the scale of systematic uncertainties associated with jet energy resolution.

- **Isolated track modeling** To account for any mismodeling of isolated tracks in simulation, 50% of the difference between the nominal signal event yields and the signal event yields in the absence of an isolated track veto is taken as the scale

of uncertainty associated with isolated track modeling. This uncertainty is mainly relevant for events with small mass splitting. A similar uncertainty is not evaluated for the isolated lepton veto requirements since nearly 100% of signal events pass the isolated lepton veto requirement, making such an uncertainty negligible.

- **ECAL prefiring corrections** The correction factors used to emulate the effect of early ECAL trigger primitives described in Section 3.3.3 are varied within their measured uncertainties and the change in signal event yields is taken as the scale of associated systematic uncertainties. The overall effect is less than 1%.

- **Trigger efficiency** The trigger efficiencies measured in Section 3.3.4 are varied within the uncertainties evaluated in the same section and the change in signal event yields is taken as the scale of associated systematic uncertainty. The scale of the trigger-associated systematic uncertainty can be very large for signal models with small mass splitting that typically have low $p_{\mathrm{T}}^{\mathrm{miss}}$, but is under 4% for all categories with $p_{\mathrm{T}}^{\mathrm{miss}} > 300$ GeV.

- **Soft-drop mass** As discussed in Section 3.2.2, a correction is applied soft-drop mass based on the 2.6 GeV discrepancy observed in the W boson mass peak in data and simulation. Subsequently, a relative uncertainty of 2.6 GeV/m_{W} is assigned to the soft-drop mass, and the change in signal event yields when the soft-drop mass of AK8 jets is varied within this uncertainty range is taken as the scale of associated systematic uncertainties.

- **b-tagging efficiency** The efficiencies for tagging b jets and mistagging c jets with the DeepCSV algorithm are varied together within the uncertainties whose measurement is described in Section 3.2.3. The change in signal event yields in each signal region is taken as the scale of systematic uncertainties associated with b-tagging efficiency.

- **b-mistagging efficiency** The probability for misidentifying usdg jets as b jets with the DeepCSV algorithm at various working points is varied within the uncertainties described in Section 3.2.3, and the resulting change to signal event yields is taken as the scale of systematic uncertainties associated with mistagging light flavor jets.

- **Double-b-tagging efficiency** The efficiencies for identifying double-b jets and misidentifying other jets with the DeepDoubleBvL algorithm are varied simultaneously, and the subsequent change to signal event yields in each signal region is taken as the scale of associated systematic uncertainties.

- **FastSim jet quality requirements** Possible uncertainty due to the jet identification requirements that are applied to the full simulation and data but not FastSim samples as well as the uncertainty due to the removal of jets due to the FastSim jet filter described in Section 3.3.2 is encoded in a flat 1% uncertainty as the effect of the jet quality requirements and the FastSim jet filter is never larger than 1%.

- **FastSim missing transverse momentum** As discussed in Section 3.3.3 the av-

erage of reconstructed $p_{\mathrm{T}}^{\mathrm{miss}}$ and generator-level $p_{\mathrm{T}}^{\mathrm{miss}}$ is taken as the nominal value of $p_{\mathrm{T}}^{\mathrm{miss}}$ for FastSim samples due to the fact that FastSim displays a worse $p_{\mathrm{T}}^{\mathrm{miss}}$ resolution than samples generated with the full Geant4 simulation. The $p_{\mathrm{T}}^{\mathrm{miss}}$ is then varied by half the difference between the reconstructed and generator-level $p_{\mathrm{T}}^{\mathrm{miss}}$ values and the resulting changes to signal event yields are taken as the scale of the associated systematic uncertainty.

- **FastSim soft-drop mass** The correction factors for soft-drop mass in FastSim samples described in Section 3.3.3 are varied by 100% of their nominal value and the changes to signal event yields are taken as the scale of the associated systematic uncertainty.

- **FastSim b-tagging efficiency** The FastSim scale factors for tagging b and c jets with the DeepCSV algorithm described in Section 3.3.3 are varied by 100% and the resulting changes in the signal events yields are taken as the scale of associated systematic uncertainties.

- **FastSim b-mistagging efficiency** The FastSim scale factors for mistagging usdg jets with the DeepCSV algorithm described in Section 3.3.3 are similarly varied by 100% and the resulting changes in signal event yields are taken as the associated scale of systematic uncertainty.

- **FastSim double-b-tagging efficiency** The FastSim scale factors for tagging and mistagging jets with the DeepDoubleBvL algorithm are varied simultaneously

Table 4.5: Sources of systematic uncertainties and the associated impact on the signal yields obtained from simulation, reported as the median 68% percentile range among all signal regions for every mass point across the signal model scans. Entries reported as 0 correspond to values smaller than 0.5%.

Source	Relative uncertainty [%]	
	Resolved	Boosted
Simulated sample size	0–18	1–15
Initial-state radiation	0–2	0–18
Renormalization and factorization scales	0–2	0–7
Pileup corrections	0–2	0–9
Integrated luminosity	1.6	
Jet energy scale	0–7	0–12
Jet energy resolution	0–7	0–7
Isolated track veto	1–20	1–8
ECAL prefiring corrections	0	0
Trigger efficiency	1–13	0–4
Soft-drop mass resolution	0	0–9
b-tagging efficiency	2–7	0
b-mistagging efficiency	1–3	0
double-b-tagging efficiency	0	6–15
Uncertainties attributable to FastSim		
Jet quality requirements	1	
$p_{\mathrm{T}}^{\mathrm{miss}}$ modeling	0–13	0–12
m_{J} resolution	0	2–4
b-tagging efficiency	0–1	0
b-mistagging efficiency	0–1	0
double-b-tagging efficiency	0	0–1

by 100% of their nominal value, and the changes to events yields in the signal region are taken as the scale of associated systematic uncertainty.

4.4 Statistical model

4.4.1 Description of the statistical model

This section describes the statistical model used for the final evaluation of the analysis. The observable random variables are the event yields in each region of the analysis. For simplicity, the model for a single set of SR, SB, CSR, and CSB regions in the resolved topology is considered first. The yields in these regions will be denoted $N_{\mathrm{SR}}^{\mathrm{data}}$, $N_{\mathrm{SB}}^{\mathrm{data}}$, $N_{\mathrm{CSR}}^{\mathrm{data}}$, and $N_{\mathrm{CSB}}^{\mathrm{data}}$. The distribution of event yields in a given region is described by a Poisson distribution, which is defined by the probability distribution function

$$f_{\mathrm{pois}}(N;\mu) = \frac{\mu^N e^{-\mu}}{N!}. \tag{4.4}$$

The Poisson distribution is described by a single parameter, the mean μ. The mean of the Poisson distribution will be taken to be

$$\mu = r\mu^{\mathrm{sig}} + \mu^{\mathrm{bkg}} \tag{4.5}$$

where μ^{bkg} is the expected number of background events in the specified category, μ^{sig} is the expected number of signal events in the category, and r is a multiplicative factor called the signal strength. The background-only model is thus specified by fixing $r = 0$, while the nominal combined signal-plus-background model is specified by fixing $r = 1$.

The value of μ^{bkg} for each category is determined by the background estimation

method. The background estimation method exploits the fact that the μ^{bkg} values for each ABCD region are not independent. The μ^{bkg} values for the four regions are related by the ABCD condition

$$\frac{\mu^{\text{bkg}}_{\text{SR}}}{\mu^{\text{bkg}}_{\text{SB}}} = \left(\prod_{i \in \text{bkg.syst.s}} \theta_i^{\sigma_{\theta i}} \right) \kappa \times \frac{\mu^{\text{bkg}}_{\text{CSR}}}{\mu^{\text{bkg}}_{\text{CSB}}} \tag{4.6}$$

where the κ and θ_i parameters are nuisance parameters described below and the $\sigma_{\theta i}$ are constants also described below. Note that this is a relation between the means of the Poisson distributions, not between the observed event yields as the observed event yields may differ from the Poisson mean due to statistical fluctuations.

Sources of systematic uncertainty are encoded in the statistical model as floating nuisance parameters. These include κ itself as well as additional multiplicative θ_i parameters used to encode the various systematic effects considered in the analysis. For the example of a single set of ABCD regions in the resolved topology, the three background systematic uncertainty θ_i parameters are $\theta_{\text{t}\bar{\text{t}}+jets}$, $\theta_{\text{V}+jets}$, and θ_{QCD}, which collectively describe the systematic uncertainty in simulation modeling. Each systematic uncertainty is constrained by one auxiliary measurement described in Section 4.3. In this way, the statistical model allows for these parameters to change while constraining them from being pulled too far from their nominal values. The quantity κ is constrained by assuming that the value κ^{simu} taken from simulation is a measurement from a Gaussian distribution with a mean equal to the true value of κ and a standard deviation σ_κ equal to the statistical uncertainty of the measurement in simulation. The probability density for this auxiliary

measurement is given by

$$f_{\text{gaus}}(\kappa^{\text{simu}};\kappa,\sigma_\kappa) = \frac{1}{\sigma_\kappa\sqrt{2\pi}} e^{-\frac{1}{2}\left(\frac{\kappa^{\text{simu}}-\kappa}{\sigma_\kappa}\right)^2}. \tag{4.7}$$

Each θ_i parameter is constrained by taking a value of 1 to be a measurement from a log-normal distribution with log mean $\log\theta_i$ and log standard deviation 1. This auxiliary measurement is encoded by the probability density given by

$$f_{\text{log-norm}}(x=1;\log\theta,\sigma=1) = \frac{1}{x\sigma\sqrt{2\pi}} e^{-\frac{(\log x-\log\theta)^2}{2\sigma^2}}. \tag{4.8}$$

When multiplying a signal yield as in Equation 4.6, the θ parameters are exponentiated to the $\sigma_{\theta i}$ power where $\sigma_{\theta i}$ is a constant set so $e^{\pm\sigma_{\theta i}}$ is a factor that varies the yield within the relative uncertainties measured in the previous section. The quantity $\sigma_{\theta i}$ is allowed to change depending on the sign of θ in order to capture the effect of sources of asymmetric uncertainty. Note that κ and θ_i are parameters of the probability distribution functions, not the auxiliary random variables being measured.

The equation

$$\mu^{\text{sig}} = \left(\prod_{i\in\text{sig.syst.s}} \theta_i^{\sigma_{\theta i}}\right) \mu^{\text{sig}}_{\text{nominal}}. \tag{4.9}$$

shows the value of μ^{sig} for each region, which is simply equal to the number of events predicted using simulation, $\mu^{\text{sig}}_{\text{nominal}}$, multiplied by various nuisance parameters θ_i that encode the sources of systematic uncertainty in the signal yield described in Section 4.3.3. Each signal systematic uncertainty θ_i parameter is again constrained by an auxiliary

measurement from a log-normal distribution as shown in Equation 4.8.

The extension of this model to multiple ABCD regions requires a discussion of correlations between regions. Other than $\theta_{\mathrm{MC}j}$, the systematic uncertainty arising from the statistical uncertainty in simulated signal yields in region j, each of the signal and background θ_i systematic uncertainty parameters is treated as fully correlated across all analysis regions including both reconstruction topologies. This is implemented by using the same θ_i for each region, possibly with a different exponent $\sigma_{\theta ij}$ for each region j. The correlation across regions is sensible as mismodeling in the simulation or corrections is not specific to any analysis region. Note that pairs of $N_{\mathrm{b}} = 3$ and $N_{\mathrm{b}} = 4$ SRs also share CSRs and CSBs, which also introduces correlation between different regions.

The statistical model for the boosted topology is almost perfectly analogous to that for the resolved topology. The event yields in the 0H+b sideband regions, $N^{\mathrm{data}}_{\text{0H+b } p_{\mathrm{T}}^{\mathrm{miss}} \text{ bin } i}$, are treated as three additional observations from poisson distributions whose means $\mu_{\text{0H+b } p_{\mathrm{T}}^{\mathrm{miss}} \text{ bin } i}$ are used in the formula constraining the background estimate:

$$\frac{\mu^{\mathrm{bkg}}_{\text{SR } p_{\mathrm{T}}^{\mathrm{miss}} \text{ bin } j}}{\mu^{\mathrm{bkg}}_{\mathrm{SB}}} = \left(\prod_{i \in \text{bkg.syst.s}} \theta_i^{\sigma_{\theta ij}} \right) \frac{\mu_{\text{0H+b } p_{\mathrm{T}}^{\mathrm{miss}} \text{ bin } j}}{\sum_{i \in p_{\mathrm{T}}^{\mathrm{miss}} \text{ bins}} \mu_{\text{0H+b } p_{\mathrm{T}}^{\mathrm{miss}} \text{ bin } i}} \frac{\mu^{\mathrm{bkg}}_{\mathrm{CSR}}}{\mu^{\mathrm{bkg}}_{\mathrm{CSB}}}. \tag{4.10}$$

Note that unlike the resolved topology, κ is taken to be unity and the systematic uncertainty due to the statistical uncertainty in the determination of κ in simulation is treated as a log-normal parameter $\theta_{\text{ABCD stats}}$ just like all other nuisance parameters. The signal yields μ^{sig} are treated in exactly the same way as the resolved topology.

To summarize, the statistical model used in this analysis can be described by the

probability distribution function given by

$$
\begin{aligned}
f = & \prod_{j \in \text{resolved SRs}} f_{\text{pois}}\left(N_j^{\text{data}}; r\theta_{\text{MC}j}^{\sigma_{\theta \text{MC}j}} \left(\prod_{i \in \text{other sig.syst.s}} \theta_i^{\sigma_{\theta ij}}\right) \mu_j^{\text{sig}} \right. \\
& \left. + \left(\prod_{i \in \text{bkg.syst.s}} \theta_i^{\sigma_{\theta ij}}\right) \kappa_j \times \frac{\mu_{\text{CSR}j}^{\text{bkg}}}{\mu_{\text{CSB}j}^{\text{bkg}}} \mu_{\text{SB}j}^{\text{bkg}}\right) \\
& \times \prod_{j \in \text{boosted SRs}} f_{\text{pois}}\left(N_j^{\text{data}}; r\theta_{\text{MC}j}^{\sigma_{\theta \text{MC}j}} \left(\prod_{i \in \text{other sig.syst.s}} \theta_i^{\sigma_{\theta ij}}\right) \mu_j^{\text{sig}} \right. \\
& \left. + \left(\prod_{i \in \text{bkg.syst.s}} \theta_i^{\sigma_{\theta ij}}\right) \frac{\mu_{\text{0H+b}j}^{\text{bkg}}}{\sum_{i \in p_{\text{T}}^{\text{miss}} \text{ bins}} \mu_{\text{0H+b}i}^{\text{bkg}}} \frac{\mu_{\text{boosted CSR}}^{\text{bkg}}}{\mu_{\text{boosted CSB}}^{\text{bkg}}} \mu_{\text{SB}j}^{\text{bkg}}\right) \\
& \times \prod_{j \in \text{SBs,CSRs,CSBs,0H+b bins}} f_{\text{pois}}\left(N_j^{\text{data}}; r\theta_{\text{MC}j}^{\sigma_{\theta \text{MC}j}} \left(\prod_{i \in \text{other sig.syst.s}} \theta_i^{\sigma_{\theta ij}}\right) \mu_j^{\text{sig}} \right. \\
& \left. + \mu_j^{\text{bkg}}\right) \\
& \times \prod_{i \in \text{resolved SRs}} f_{\text{gaus}}(\kappa_i^{\text{simu}}; \kappa_i, \sigma_{\kappa_i}) \\
& \times \prod_{i \in \theta \text{ nuisance parameters}} f_{\text{log-norm}}(1; \log\theta_i, 1)
\end{aligned}
\tag{4.11}
$$

There are 61 primary measurements of random variables, the event yields in each SR, SB, CSR, CSB, and 0H+b region. These are joined by 102 auxiliary random variable measurements, the values κ^{simu} for the 16 resolved topology κ parameters and 86 observations of 1 for the θ_i nuisance parameters. The probability distribution function of Equation 4.11 describes the joint distribution in these random variables using 142 free parameters: 39 independent background Poisson means μ^{bkg} for the non-SR regions, 16 resolved topology κ parameters, 86 θ_i parameters, and the signal strength modifier r.

The Poisson means for the SRs are expressed in terms of the other parameters using Equations 4.6 and 4.10. The μ^{sig} parameters, the gaussian standard deviation σ_κ parameters, and the nuisance exponents $\sigma_{\theta ij}$ parameters are all treated as fixed constants. In Equation 4.11, parameters such as $\mu^{\text{bkg}}_{\text{CSR}i}$ refer to the appropriate CSR region for a signal region i so that the same $\mu^{\text{bkg}}_{\text{CSR}i}$ will appear twice for the different N_{b} signal regions.

4.4.2 Fitting and signal extraction procedure

The results of this analysis are quantified as measurements of the signal strength r for each simplified model of supersymmetry considered. The signal strength r can also be thought of as the cross section for supersymmetric particle production in units of the nominal cross section considered for each model. In the case supersymmetric particles do not exist, the true value of r is zero. For this reason, measurements of r are presented as "limits" on possible nonzero values.

The limits are constructed following the standard procedure outlined in Ref. [385]. These procedures are based around the likelihood function $\mathcal{L}$, which is numerically equivalent to the probability distribution function f given in Equation 4.11 but interpreted as a function of the distribution parameters with the observed random variables fixed. The

limit-setting procedure utilizes the LHC limit-setting test statistic

$$\tilde{q}_r = \begin{cases} -2\log\frac{\mathcal{L}(r,\hat{\theta}(r);\,\text{data})}{\mathcal{L}(\hat{r},\hat{\theta}(\hat{r});\,\text{data})} & 0 < \hat{r} < r \\ -2\log\frac{\mathcal{L}(r,\hat{\theta}(r);\,\text{data})}{\mathcal{L}(0,\hat{\theta}(0);\,\text{data})} & \hat{r} < 0 < r \\ 0 & \hat{r} > r \end{cases} \tag{4.12}$$

where $\mathcal{L}$ is the likelihood function, θ denotes all of the nuisance parameters including the μ^{bkg} and κ parameters, $\hat{\theta}(r)$ is the maximum likelihood estimator for the nuisance parameters as a function of r, $\hat{r}$ is the maximum likelihood estimator for r, and "data" represents the measured values of the random variables. The Neyman-Pearson lemma [386] states that the ratio of likelihoods provides an optimal discriminator between two hypotheses. The LHC limit-setting test statistic can thus be interpreted as an optimal discriminator between the hypothesis of signal strength r and the most likely signal strength less than r after taking into account that signal strength must be nonnegative. The logarithm, being a monotonic function, and the overall multiplicative constant do not affect the optimality and are used simply for numerical convenience. In the following discussion, the LHC limit-setting test statistic $\tilde{q}_r$ is viewed as a family of random variables parametrized by r.

The limit setting procedure relies also on confidence intervals [387], sets constructed so that a fixed proportion of confidence intervals contain the true value of a given parameter. This analysis uses the Neyman construction with $\tilde{q}_r$: a value r is considered to be in the

$X\%$ confidence interval if the probability for measuring a value of $\tilde{q}_r$ greater than the observed value given the r hypothesis is greater than $X\%$, that is

$$P(\tilde{q}_r > \tilde{q}_{r\text{obs}}|r) = 1 - F(\tilde{q}_r; r) > X\% \tag{4.13}$$

where $F(\tilde{q}_r; r)$ is the cumulative distribution function of $\tilde{q}_r$ under the r hypothesis. While the probability distribution for the $\tilde{q}_r$ test statistics can be computed manually by generating a simulated data set with the probability distribution function in Equation 4.11, the advantage of profiled likelihood test statistics such as $\tilde{q}_r$ is that the probability distribution in the large sample limit is known analytically and is independent of the nuisance parameters θ. As shown in Ref. [388], the asymptotic form for the cumulative distribution function of $\tilde{q}_r$ assuming the true signal strength is r' is

$$F(\tilde{q}_r; r') = \begin{cases} \Phi\left(\sqrt{\tilde{q}_r} - \frac{r-r'}{\sigma}\right) & \tilde{q}_r \leq r^2/\sigma^2 \\ \Phi\left(\frac{\tilde{q}_r - (r^2 - 2rr')/\sigma^2}{2r/\sigma}\right) & \tilde{q}_r > r^2/\sigma^2 \end{cases} \tag{4.14}$$

where Φ is the Gaussian cumulative distribution function and σ is the standard deviation of the distribution of $\hat{r}$. The quantity σ is typically computed from the Asimov data set, the pseudo data set in which the observed event yields exactly match the probability distribution function mean prediction in each bin. For a true signal strength of r', σ is then

$$\sigma^2 = \frac{(r - r')^2}{\tilde{q}_{r,\text{A}}} \tag{4.15}$$

where $\tilde{q}_{r,\mathrm{A}}$ is the test statistic calculated with the Asimov data set. Equations 4.13 and 4.14 can then be used to build approximate confidence intervals for r.

Although confidence intervals are related to the possible values of r, they do not capture the sensitivity of an experiment to distinguish between the presence of signal ($r > 0$) and the background-only hypothesis ($r = 0$). For this reason, the limits presented for the HH(4b)+$p_{\mathrm{T}}^{\mathrm{miss}}$ analysis use the $\mathrm{CL_s}$ construction described in Ref. [389, 390]. The basic idea of the $\mathrm{CL_s}$ construction is to extend the confidence interval by including all values of r for which

$$\frac{P(\tilde{q}_r > \tilde{q}_{r\mathrm{obs}}|r)}{P(\tilde{q}_r > \tilde{q}_{r\mathrm{obs}}|0)} = \frac{1 - F(\tilde{q}_r; r)}{1 - F(\tilde{q}_r; 0)} > X\% \tag{4.16}$$

Since probabilities are necessarily less than or equal to 1, dividing by a probability ensures that the $\mathrm{CL_s}$ interval cannot be smaller than the corresponding confidence interval and thus that at least $X\%$ of $X\%$ $\mathrm{CL_s}$ intervals must contain the true value of r. Furthermore, by dividing by the probability of measuring a larger $\tilde{q}_r$ under the background hypothesis, values of $\tilde{q}_r$ that are better described by the background hypothesis are weighted up so that r is more likely to be contained in the $\mathrm{CL_s}$ interval. This means that the confidence interval is more extended when there is little discrimination between the signal and background-only hypotheses. The edge of the $X\%$ $\mathrm{CL_s}$ interval is said to be the limit on r and values of r outside of the $X\%$ $\mathrm{CL_s}$ interval are said to be excluded at a confidence level of $X\%$.

It can also be of interest to quantify the compatibility of the data with the background-

only hypothesis. In this case, the LHC significance test statistic

$$q_0 = \begin{cases} -2\log\frac{\mathcal{L}(0,\hat{\theta}(0);\text{data})}{\mathcal{L}(\hat{r},\hat{\theta}(\hat{r});\text{data})} & \hat{r} > 0 \\ -2\log\frac{\mathcal{L}(0,\hat{\theta}(0);\text{data})}{\mathcal{L}(0,\hat{\theta}(0);\text{data})} & \hat{r} < 0 \end{cases} \tag{4.17}$$

is employed. As noted previously, a monotonic function of the likelihood ratio provides an optimal discriminant between two hypotheses, which are signal strengths of 0 and $\hat{r}$ in this case. By construction, smaller values of q_0 are more background-like while larger values are more signal-like. The overall compatibility with the background-only hypothesis is given by the p-value

$$p_0 = P(q_0 > q_{0\text{obs}}|0) = 1 - F(q_0; 0) \tag{4.18}$$

the probability to observe a value of q_0 more incompatible with the background hypothesis than that observed. The cumulative distribution function of q_0 again has an asymptotic form

$$F(q_0; r') = \Phi\left(\sqrt{q_0} - \frac{r'}{\sigma}\right) \tag{4.19}$$

in the large sample limit [388], which can be used to calculate an approximate p-value. It is common in particle physics to report the significance

$$Z = \Phi^{-1}(1 - p_0) \tag{4.20}$$

where a significance of 3 ($p = 1.35 \times 10^{-3}$) is typically taken as the threshold for evidence for a signal and a significance of 5 ($p = 2.86 \times 10^{-7}$) is typically taken as the threshold for a discovery of the signal.

The statistical methods described here are implemented using the CMS combine tool, which is based on the RooStats/RooFit packages [391–393]. These procedures are applied in the next chapter to extract the limits on the signal strength r, presented in terms of the cross section $\sigma = r\sigma_{\text{nominal}}$.

Chapter 5

Results, interpretation, and combination

This chapter presents the results of the HH(4b)+$p_{\mathrm{T}}^{\mathrm{miss}}$ analysis and the resulting interpretations in the three simplified models of supersymmetry discussed previously. In addition, the HH(4b)+$p_{\mathrm{T}}^{\mathrm{miss}}$ analysis is incorporated into an "electroweak SUSY combination" along with five other analyses that use CMS Run 2 data. This chapter discusses electroweak SUSY combination, the simplified models of higgsino production considered by the combination, and the results interpreted in these models.

Section 5.1 shows the observed event yields in the various categories considered by the HH(4b)+$p_{\mathrm{T}}^{\mathrm{miss}}$ analysis and compares them with the background predictions. These results are then interpreted as exclusion limits in parameter space for the simplified models of supersymmetry considered by the analysis. Models with sufficiently high production cross section are excluded.

Section 5.2 describes the electroweak SUSY combination with a focus on the two higgsino models, which feature gravitino and bino-like LSPs, respectively. The combination

methodology, as well as an overview of each of the other analyses entering the combination, are provided. The exclusion limits for the higgsino models based on the observed data are then presented.

5.1 Results and interpretations

5.1.1 Results

Figures 5.1 and 5.2 show distributions in $\langle m_{\mathrm{bb}} \rangle$ of the unblinded data for the resolved topology (black data points) together with a rough representation of the background estimate (cyan histograms). Although each plot integrates several of the categories used in the full statistical model, realistic signal models would generally appear as an excess of events with $\langle m_{\mathrm{bb}} \rangle$ near the Higgs boson mass across categories, as shown by the red, green, and violet histograms showing representative signal yields for the simulatd SUSY models. Overall, the $\langle m_{\mathrm{bb}} \rangle$ shapes observed in the $N_{\mathrm{b}} = 3$ and $N_{\mathrm{b}} = 4$ categories match well with those from the $N_{\mathrm{b}} = 2$ categories and thus do not show any large excesses in the Higgs boson mass region.

Figure 5.3 shows the m_J distributions of the unblinded data for the boosted topology, together with the expected event yields from simulation for background and selected signal models. Note that the actual background estimate is not shown in these figures. As for the resolved topology, the presence of signal would be characterized by an excess in the Higgs boson mass window. Overall, the m_J shapes follow a generally smooth

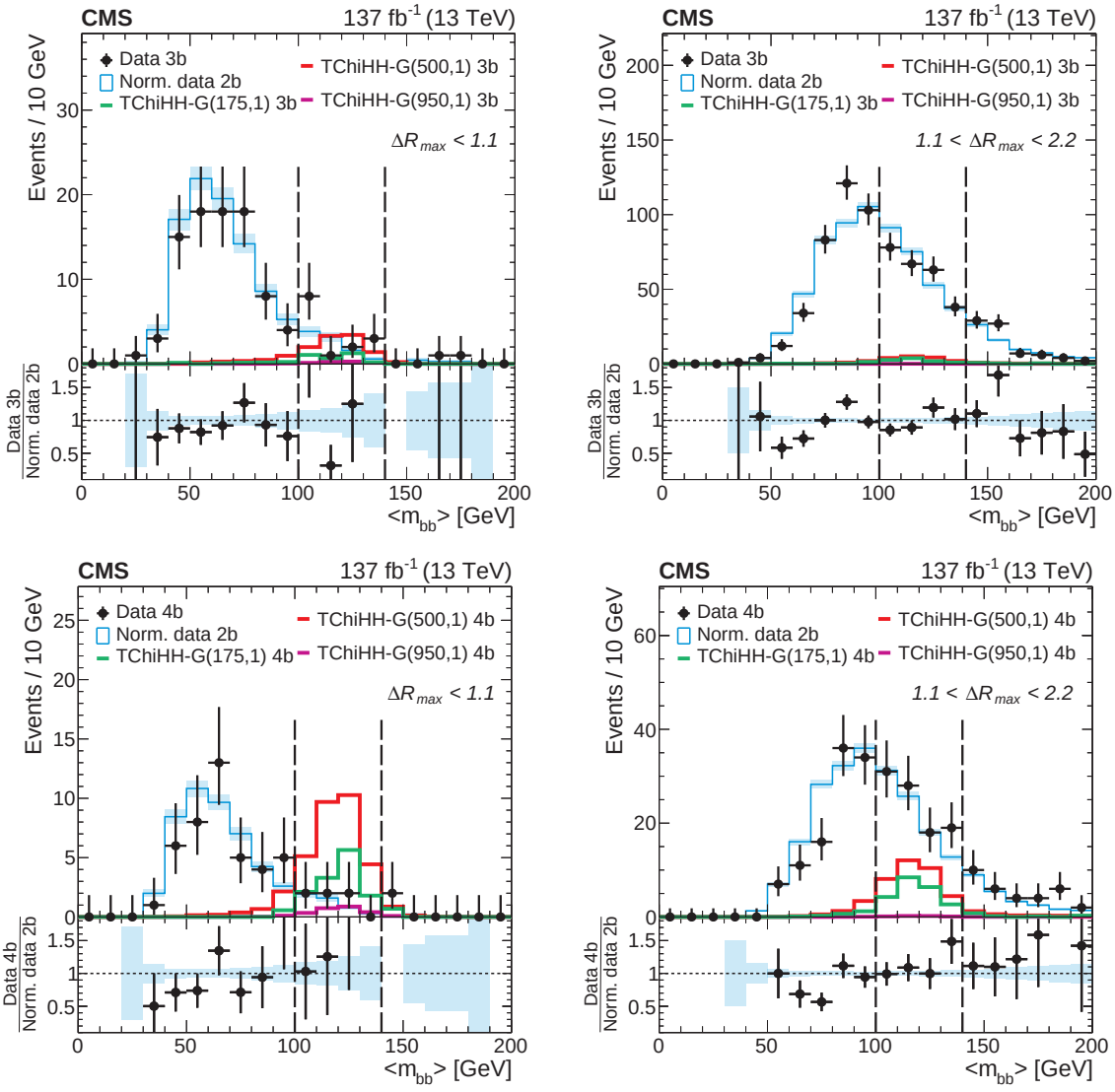

Figure 5.1: Distribution in $\langle m_{\mathrm{bb}} \rangle$ for $N_{\mathrm{b}} = 3$ (upper row) and $N_{\mathrm{b}} = 4$ (lower row) data in the $\Delta R_{\mathrm{max}} < 1.1$ (left) and $1.1 < \Delta R_{\mathrm{max}} < 2.2$ (right) categories of the resolved topology integrated in $p_{\mathrm{T}}^{\mathrm{miss}}$ categories. The overlaid cyan histograms are the data from the $N_{\mathrm{b}} = 2$ category scaled to match the $N_{\mathrm{b}} = 3$ of r yield and weighted by the appropriate κ factors, thus providing a visual representation of the background estimation method. The green, red, and violet histograms represent the TChiHH-G signal model yields for three different signal mass points showing the enhancement that would be produced by the presence of a signal. The bottom panels show the ratio between the data in the $N_{\mathrm{b}} = 3$ or 4 categories and the weighted data from the $N_{\mathrm{b}} = 2$ category.

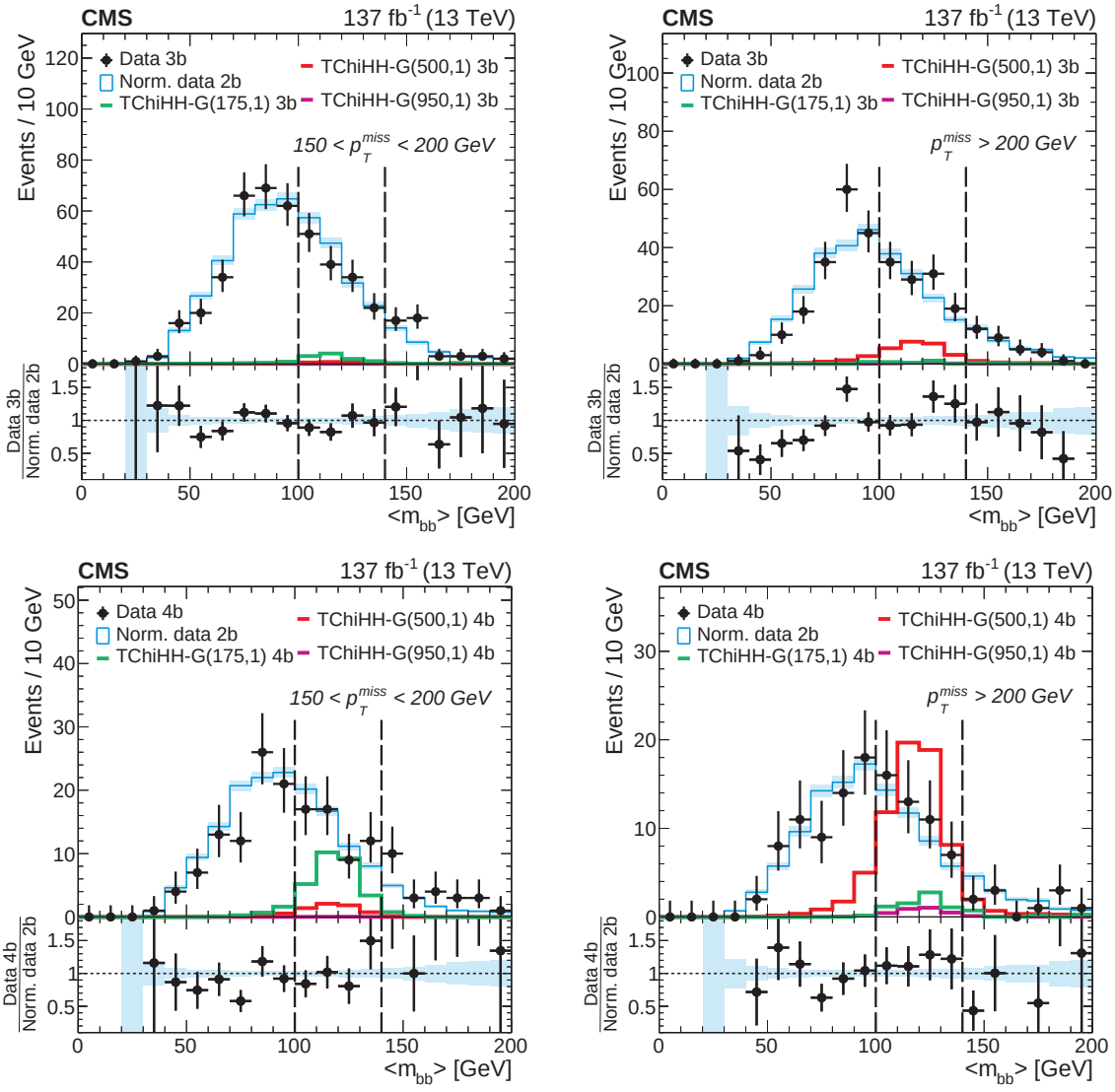

Figure 5.2: Distribution in $\langle m_{\mathrm{bb}} \rangle$ for $N_{\mathrm{b}} = 3$ (upper row) and $N_{\mathrm{b}} = 4$ (lower row) data in the $150 < p_{\mathrm{T}}^{\mathrm{miss}} < 200$ GeV (left) and $p_{\mathrm{T}}^{\mathrm{miss}} > 200$ GeV (right) categories of the resolved topology integrated in ΔR_{max} categories. The overlaid cyan histograms are the data from the $N_{\mathrm{b}} = 2$ category scaled to match the $N_{\mathrm{b}} = 3$ of r yield and weighted by the appropriate κ factors, thus providing a visual representation of the background estimation method. The green, red, and violet histograms represent the TChiHH-G signal model yields for three different signal mass points showing the enhancement that would be produced by the presence of a signal. The bottom panels show the ratio between the data in the $N_{\mathrm{b}} = 3$ or 4 categories and the weighted data from the $N_{\mathrm{b}} = 2$ category.

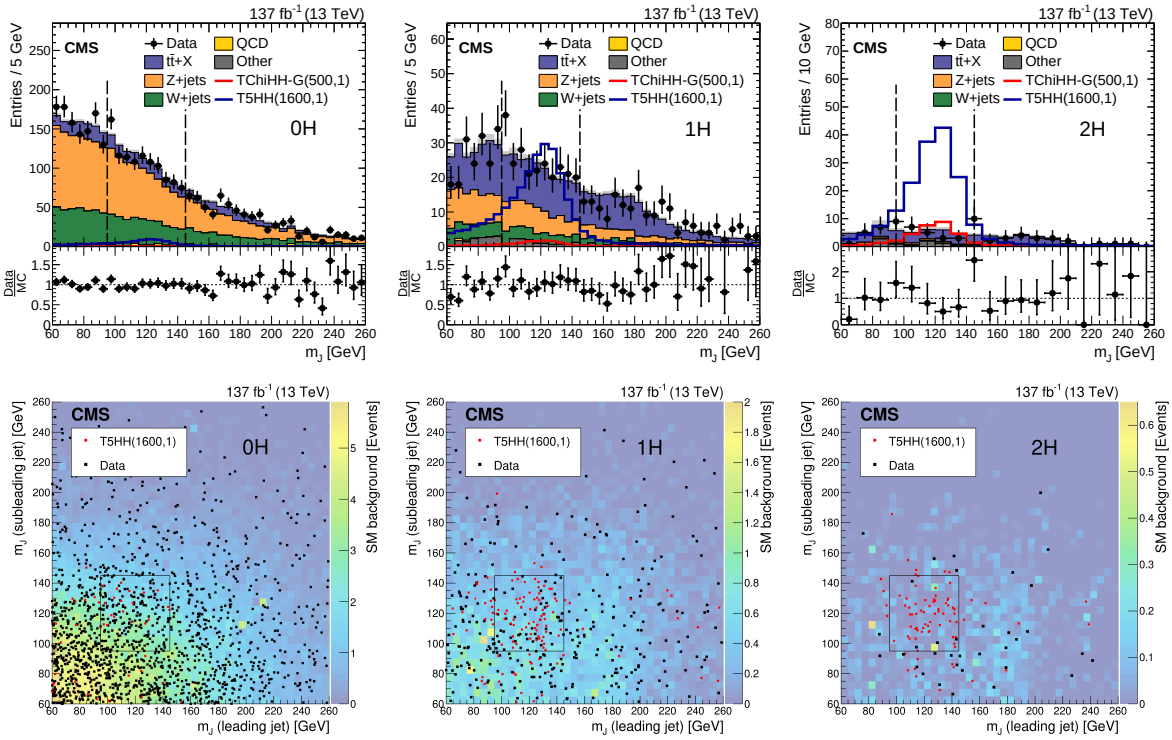

Figure 5.3: Distribution in Higgs boson candidate mass m_J of data events in the $N_H = 0$ (left), $N_H = 1$ (middle), and $N_H = 2$ (right) categories of the boosted topology integrated across p_T^{miss} bins. The bottom plots show events as a scatter plot in the two-dimensional m_J plane while the top plots show a one-dimensional histogram with two entries per event as m_J is defined per-Higgs boson candidate. Expected yields from simulation are overlaid as stacked solid colored histograms on the top plots and a color map on the bottom plots, though it should be noted the background estimation method used in the statistical analysis is the data-driven approach described in Section 4.2.2. Expected yields from signal models are shown as outlined histograms in the top plots and as the red scatter plot in the bottom plots.

distribution without any strong signs of a signal-like excess.

Tables 5.1 and 5.2 show the event yields in each category of the resolved and boosted topologies, respectively, together with both the background prediction using the simple method described in Section 4.2 and the maximum likelihood fit background yield using the full statistical model described in Section 4.4. The yields observed in data and the predicted background yields are also displayed in Figure 5.4.

The predicted background yields generally agree well with the observed data yields across the 22 signal regions including both the resolved and boosted topology. However, in the $N_{\mathrm{b}} = 3$, $300 < p_{\mathrm{T}} < 400$ GeV, $\Delta R_{\mathrm{max}} < 1.1$ category of the resolved topology, referred to hereafter as "bin 11", the data yield is somewhat larger than both of the background predictions. The simple background prediction for this category is only $0.06^{+0.11}_{-0.04}$ whereas the observed number of events is 4. The small prediction for the background event yields is due to the SB, CSR, and CSB yields of 2, 45, and 2 respectively. Several pieces of evidence suggest that downward fluctuations in the CSR and SB cause the background estimate to be low. First, the fit with the full statistical model, which allows fluctuations in the data yields, gives a background event yield estimate of $0.72^{+0.53}_{-0.33}$, which is considerably larger than the simple estimate. Second, the event yields in simulation for the SB, CSR, and CSB in this category are 6.5 ± 1.8, 47.2 ± 2.3, and 6.3 ± 0.5. Although this analysis uses a data-driven background estimate to avoid reliance on simulation, the simulation does an overall good job of describing event yields across the different categories, which supports the idea that these yields are closer in this case to the true means than the observed yields in data. Finally, signal models tend to be spread out across categories due to the stochastic nature of the kinematic variables $p_{\mathrm{T}}^{\mathrm{miss}}$ and ΔR_{max}, making a large signal contribution to this single bin unlikely.

Figure 5.5 shows event displays for two data events that enter the HH(4b)+$p_{\mathrm{T}}^{\mathrm{miss}}$ signal regions from 2018. The event shown on the left has five jets, the four jets corresponding to the two Higgs boson candidate and one lower p_{T} jet at high $|\eta|$, and a $p_{\mathrm{T}}^{\mathrm{miss}}$ value of

Table 5.1: The κ factor, the predicted yield $N_{\mathrm{SR}}^{\mathrm{pred}}$ using the simple background estimation method described in Section 4.2.1, the maximum likelihood fit background yield $\hat{\mu}_{\mathrm{SR}}^{\mathrm{bkg}}$ from the full statistical method described in Section 4.4, and the observed yield $N_{\mathrm{SR}}^{\mathrm{data}}$ for each signal region of the resolved topology. The first and second uncertainties in the κ factors are statistical and systematic, respectively while the uncertainties in $N_{\mathrm{SR}}^{\mathrm{pred}}$ and $\hat{\mu}_{\mathrm{SR}}^{\mathrm{bkg}}$ include both statistical and systematic contributions.

Bin	ΔR_{max}	N_{b}	$p_{\mathrm{T}}^{\mathrm{miss}}$ [GeV]	κ	$N_{\mathrm{SR}}^{\mathrm{pred}}$	$\hat{\mu}_{\mathrm{SR}}^{\mathrm{bkg}}$	$N_{\mathrm{SR}}^{\mathrm{data}}$
1	1.1–2.2	3	150–200	$1.09 \pm 0.04 \pm 0.02$	161^{+14}_{-13}	$149.7^{+8.9}_{-8.5}$	138
2			200–300	$0.92 \pm 0.04 \pm 0.02$	$90.4^{+9.7}_{-9.0}$	$91.5^{+6.9}_{-6.5}$	91
3			300–400	$0.94 \pm 0.09 \pm 0.01$	$11.5^{+3.4}_{-2.7}$	$12.8^{+2.6}_{-2.2}$	14
4			>400	$0.98^{+0.19}_{-0.16} \pm 0.02$	$2.8^{+2.3}_{-1.4}$	$2.8^{+1.4}_{-1.0}$	3
5		4	150–200	$1.13 \pm 0.09 \pm 0.08$	$53.5^{+8.8}_{-7.8}$	$54.1^{+5.6}_{-5.2}$	54
6			200–300	$0.96 \pm 0.07 \pm 0.07$	$28.3^{+5.6}_{-4.8}$	$33.2^{+4.2}_{-3.9}$	38
7			300–400	$0.89^{+0.16}_{-0.15} \pm 0.05$	$2.6^{+1.5}_{-1.1}$	$3.2^{+1.3}_{-1.0}$	4
8			>400	$0.92^{+0.27}_{-0.22} \pm 0.07$	$2.6^{+2.4}_{-1.4}$	$1.27^{+0.98}_{-0.63}$	0
9	<1.1	3	150–200	$1.05^{+0.18}_{-0.15} \pm 0.12$	$5.1^{+1.6}_{-1.3}$	$5.9^{+1.4}_{-1.2}$	8
10			200–300	$1.04^{+0.14}_{-0.13} \pm 0.11$	$2.17^{+0.79}_{-0.60}$	$2.31^{+0.73}_{-0.57}$	2
11			300–400	$0.72^{+0.33}_{-0.22} \pm 0.08$	$0.06^{+0.11}_{-0.04}$	$0.72^{+0.53}_{-0.33}$	4
12			>400	$1.24^{+0.67}_{-0.45} \pm 0.10$	$0.89^{+1.42}_{-0.60}$	$0.52^{+0.65}_{-0.35}$	0
13		4	150–200	$1.26^{+0.21}_{-0.20} \pm 0.23$	$2.68^{+1.06}_{-0.79}$	$2.58^{+0.85}_{-0.67}$	1
14			200–300	$1.21^{+0.22}_{-0.21} \pm 0.22$	$1.26^{+0.62}_{-0.44}$	$1.62^{+0.65}_{-0.48}$	3
15			300–400	$2.35^{+0.88}_{-0.72} \pm 0.34$	$0.42^{+0.61}_{-0.27}$	$1.16^{+0.87}_{-0.55}$	1
16			>400	$0.94^{+0.53}_{-0.36} \pm 0.13$	$0.67^{+1.10}_{-0.46}$	$0.78^{+0.76}_{-0.43}$	1

Table 5.2: The $p_{\mathrm{T}}^{\mathrm{miss}}$-integrated predicted background event yield $N_{\mathrm{bkg}}^{\mathrm{SR,tot}}$, the predicted fraction per $p_{\mathrm{T}}^{\mathrm{miss}}$ bin f_i, and the $p_{\mathrm{T}}^{\mathrm{miss}}$ bin specific predicted background event yield $N_{\mathrm{SR}}^{\mathrm{pred}}$ derived with the simple background estimation method described in Section 4.2.2 together with the maximum likelihood fit background yield $\hat{\mu}_{\mathrm{SR}}^{\mathrm{bkg}}$ from the full statistical method described in Section 4.4, and the observed yield $N_{\mathrm{SR}}^{\mathrm{data}}$ for each signal region of the boosted topology. All uncertainties include both statistical and systematic contributions.

Bin	N_{H}	$p_{\mathrm{T}}^{\mathrm{miss}}$ [GeV]	$N_{\mathrm{bkg}}^{\mathrm{SR,tot}}$	f_i	$N_{\mathrm{SR}}^{\mathrm{pred}}$	$\hat{\mu}_{\mathrm{SR}}^{\mathrm{bkg}}$	$N_{\mathrm{SR}}^{\mathrm{data}}$
17		300–500		0.789 ± 0.030	$33.6^{+6.1}_{-5.2}$	$37.0^{+4.2}_{-4.0}$	42
18	1	500–700	42.6 ± 4.2	0.172 ± 0.028	$7.3^{+2.0}_{-1.6}$	$7.2^{+1.5}_{-1.3}$	6
19		>700		0.039 ± 0.014	$1.65^{+1.04}_{-0.66}$	$1.50^{+0.75}_{-0.53}$	1
20		300–500		0.789 ± 0.030	$4.0^{+1.5}_{-1.1}$	$4.0^{+1.2}_{-1.0}$	4
21	2	500–700	5.1 ± 1.0	0.172 ± 0.028	$0.88^{+0.40}_{-0.28}$	$0.74^{+0.29}_{-0.21}$	0
22		>700		0.039 ± 0.014	$0.20^{+0.21}_{-0.10}$	$0.14^{+0.13}_{-0.07}$	0

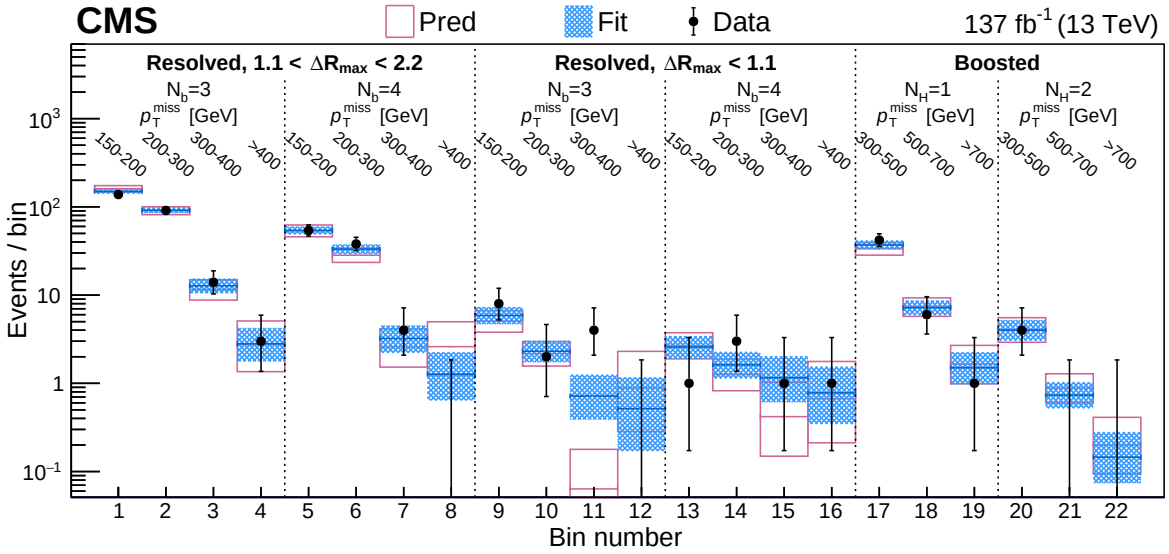

Figure 5.4: Observed data yields $N_{\mathrm{SR}}^{\mathrm{data}}$ shown as black points together with the simple background predictions $N_{\mathrm{SR}}^{\mathrm{pred}}$ described in Section 4.2 shown as pink boxes and the maximum likelihood fit background yields $\hat{\mu}_{\mathrm{SR}}^{\mathrm{bkg}}$ shown as blue shaded boxes for each signal region category across both resolved and boosted topologies.

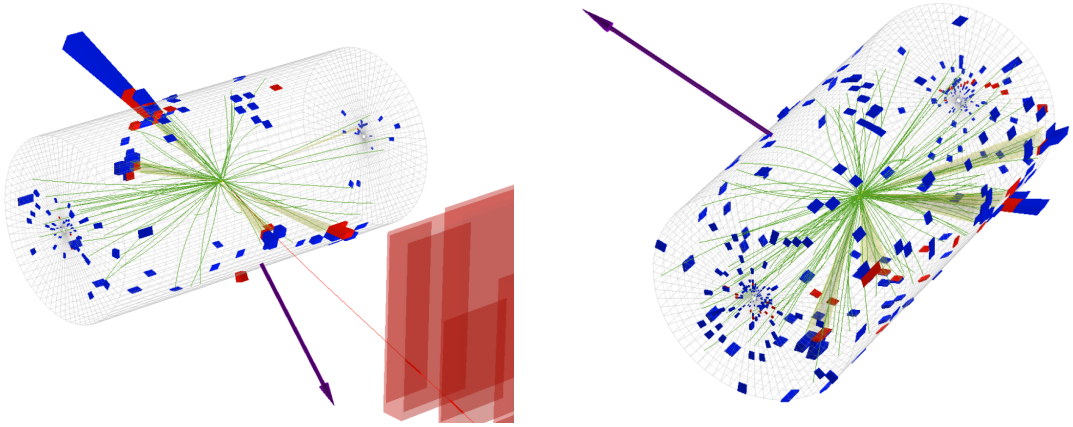

Figure 5.5: Event displays for two events entering the signal regions of the HH(4b)+$p_{\mathrm{T}}^{\mathrm{miss}}$ analysis created using the CMS fireworks program [394]. Reconstructed particle tracks are shown in green, calorimeter clusters are shown as red (ECAL) and blue (HCAL) blocks whose height corresponds to their energy, reconstructed muons are shown in red, the missing transverse momentum vector is shown in violet, and clustered jets are shown as yellow cones.

271 GeV. The event shown on the right has four jets corresponding to the two Higgs boson candidates and a very high $p_{\mathrm{T}}^{\mathrm{miss}}$ value of 378 GeV.

5.1.2 Interpretation

The observed data are interpreted as 95% $\mathrm{CL_s}$ limits on the considered signal models using the asymptotic approximations described in Section 4.4.2. Figure 5.6 shows the expected and observed limits for the TChiHH-G model as a function of higgsino mass. The nominal TChiHH-G cross section is excluded for higgsino masses between 175 and 1025 GeV, which represents the best exclusion for such a model at the time of publication. The excess in bin 11 results in limits that are slightly less stringent than the expected limits around the mass range 300–600 GeV, but all observed limits agree with the expectation within the 95% uncertainty band shown in yellow. The left plot of Figure 5.9

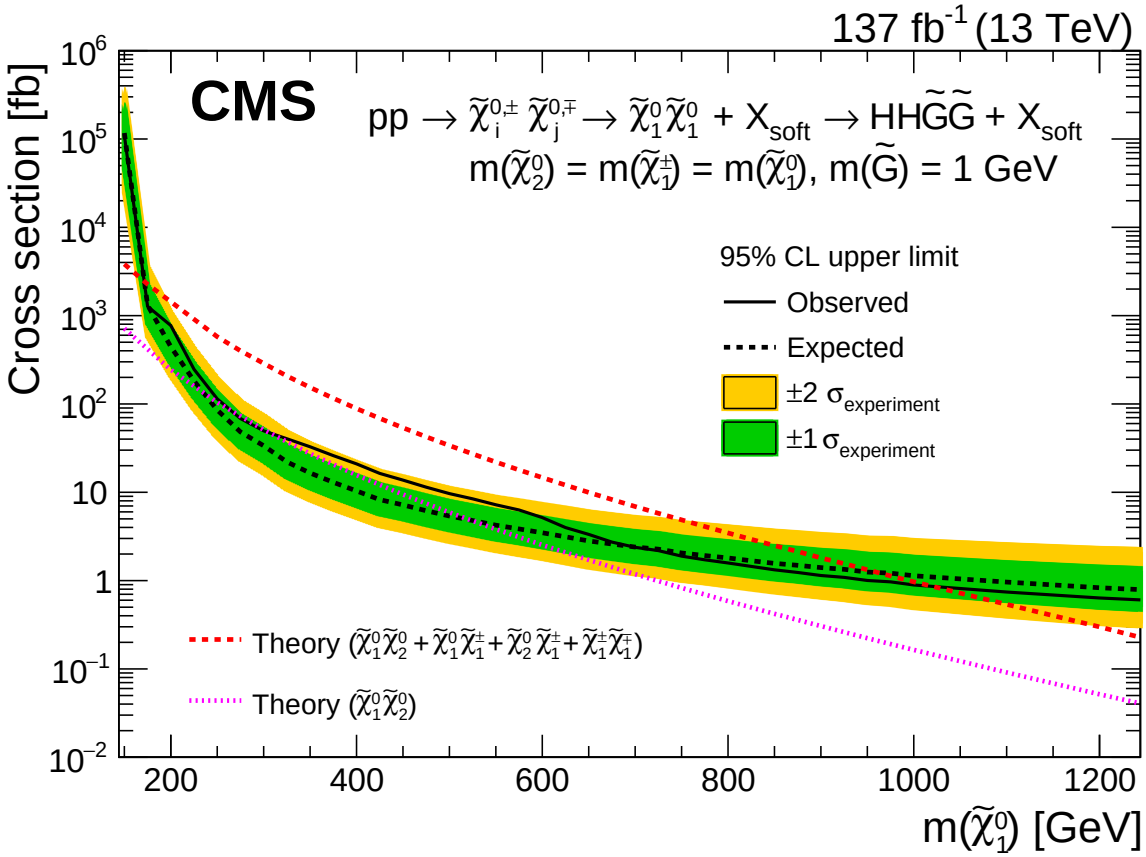

Figure 5.6: Observed (solid line) and expected (dashed line) 95% CL_s upper limits on higgsino production cross section as a function of higgsino mass $m(\tilde{\chi}_1^0)$ for the TChiHH-G model. The green and yellow bands represent the 68% and 95% uncertainty bands around the expected limit. The red dashed line shows the nominal cross section for the model ($r = 1$) while the violet dashed line shows the cross section for only neutral higgsino $\tilde{\chi}_1^0\tilde{\chi}_2^0$ production in which case the TChiHH-G model is effectively equivalent to the TChiHH model with the LSP mass set to 0.

shows the limits derived by the resolved and boosted topologies independently. The two reconstruction methods can be seen to be complementary with the resolved topology being more sensitive for higgsino masses below 800 GeV and the boosted topology being more sensitive for higgsino masses above 800 GeV.

Figure 5.7 shows the observed 95% CL_s limits for the TChiHH model as a function of higgsino and bino mass. It also shows the expected and observed regions for which the

nominal cross section of the model is excluded. Note that the bottom band of Figure 5.7 where the LSP mass is 0 GeV is effectively equivalent to Figure 5.6 using the violet cross section as the nominal model cross section. A sizeable portion of the plane shown in Figure 5.7 is expected to be excluded, however the expected limits are only slightly lower than the nominal cross section, which is why the dashed and dotted uncertainty bands are large. The excess in bin 11 again results in observed limits that are somewhat worse than expected, although the observed limits still lie within the 95% uncertainty band of the expected limits.

Figure 5.8 shows the expected and observed 95% CL_s limits as a function of gluino mass for the T5HH model. As shown in the right plot of Figure 5.9, the boosted topology is considerably more sensitive than the resolved topology for all gluino mass points considered. For this reason, the bin 11 excess does not strongly affect the limits and the observed and expected limits are very similar. Gluino masses up to 2330 GeV are excluded, again representing the best exclusion for this model at the time of publication.

Figure 5.10 shows the observed significance as a function of signal mass points for the TChiHH model and the T5HH model following the procedure detailed in Section 4.4.2. Since the significance quantifies the disagreement with the background-only hypothesis, the significances at the bottom band of the left plot of Figure 5.10 is equivalent to the significance for the TChiHH-G model. The significance values for the T5HH model are all less than 0, indicating the best fit signal strength is negative. The maximum significance in the TChiHH and TChiHH-G models is 2.0 at the point mass point $m(\widetilde{\chi}_2^0) =$

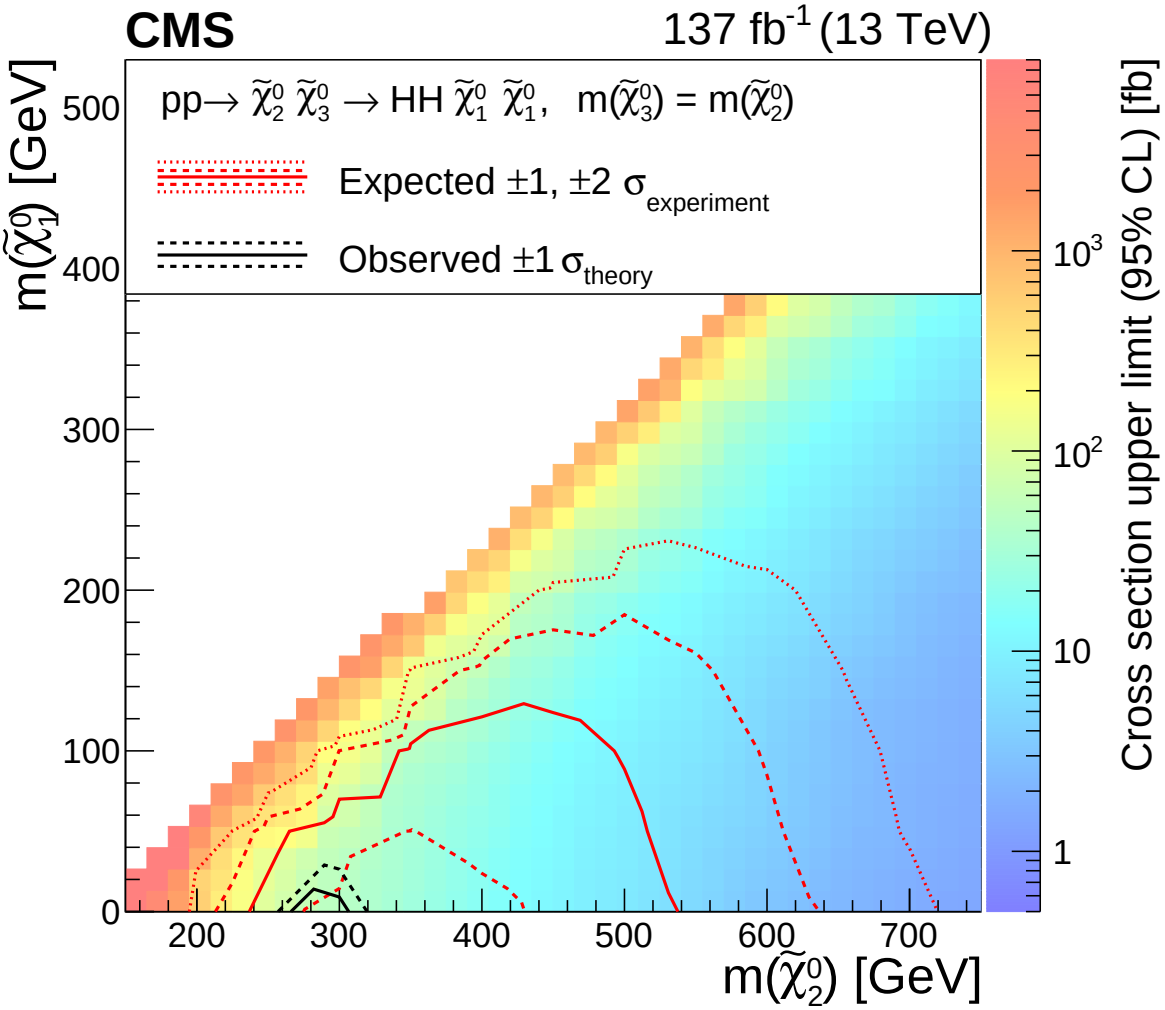

Figure 5.7: Observed 95% CL_s upper limits on higgsino production cross section as a function of higgsino mass $m(\tilde{\chi}_2^0)$ and bino mass $m(\tilde{\chi}_1^0)$ for the TChiHH model shown as a color plot. The region for which the expected upper limit is lower than the nominal cross section is outlined by the solid red line while the region where the observed upper limit is lower than the normal cross section is outlined by the solid black line. The 68% uncertainty bands of the expected and observed limits are shown as dashed lines while the 95% uncertainty band of the expected limits is shown as red dotted lines.

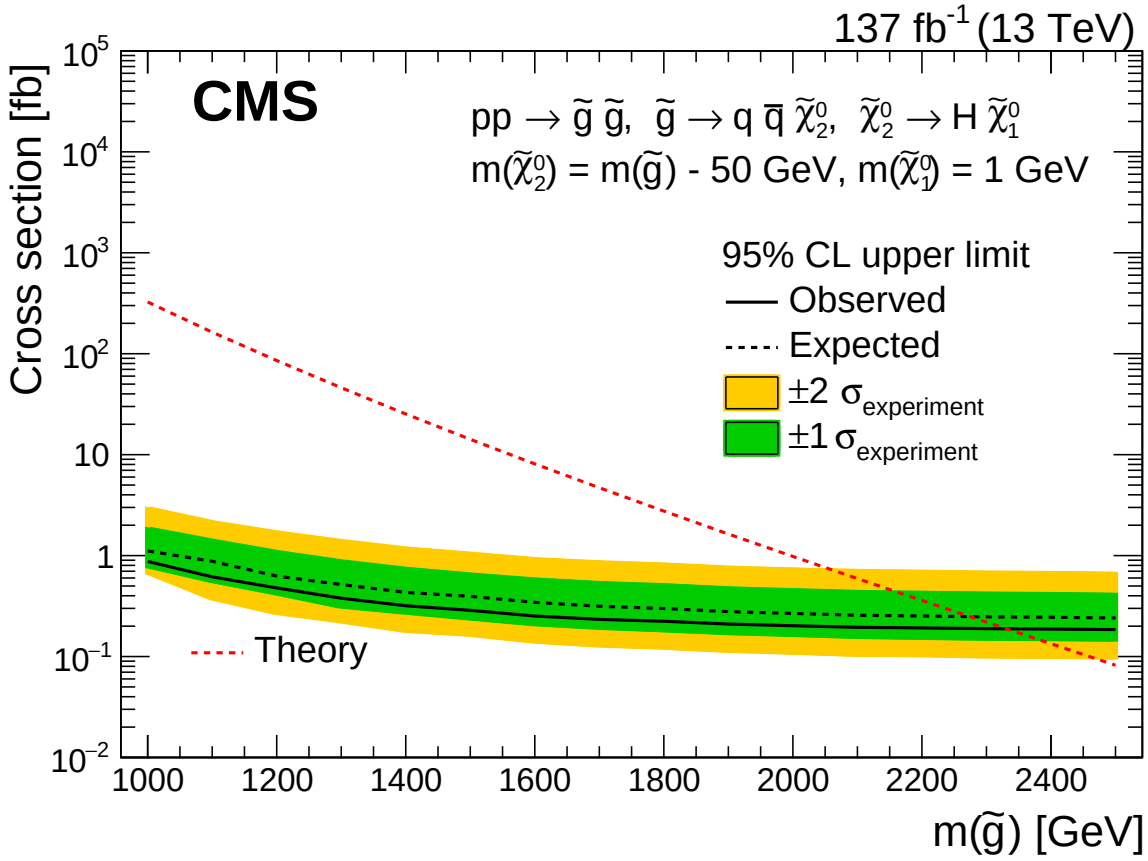

Figure 5.8: Observed (solid line) and expected (dashed line) 95% CL_s upper limits on gluino production cross section as a function of gluino mass $m(\tilde{g})$ for the T5HH model. The green and yellow bands represent the 68% and 95% uncertainty bands around the expected limit. The red dashed line shows the nominal cross section for the model.

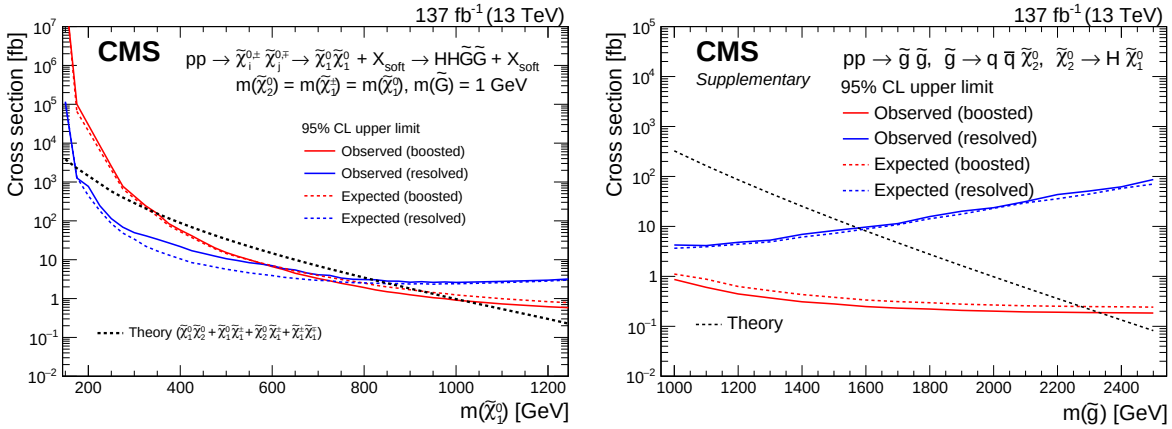

Figure 5.9: Observed (solid line) and expected (dashed line) 95% CL_s upper limits on higgsino production in the TChiHH-G model (left) and on gluino production in the T5HH model (right) for the resolved topology (blue) and the boosted topology only (red) without overlap removal applied. The black dashed lines show the nominal model cross sections.

450 GeV, $m(\tilde{\chi}_1^0) = 50$ GeV. Because the analysis has only weak sensitivity to different mass hypotheses, the global significance of the excess is slightly less than 2.0. This overall significance suggests the data are reasonably described by the SM hypothesis with 5% level fluctuations and no strong evidence for supersymmetric particle production is observed.

5.2 Electroweak SUSY combination

5.2.1 Signal models

The HH(4b)+$p_{\mathrm{T}}^{\mathrm{miss}}$ analysis is also combined with several other CMS analyses in other final states in order to present combined constraints on more general models of higgsino, wino, and slepton production as described in Ref. [4]. This electroweak SUSY combi-

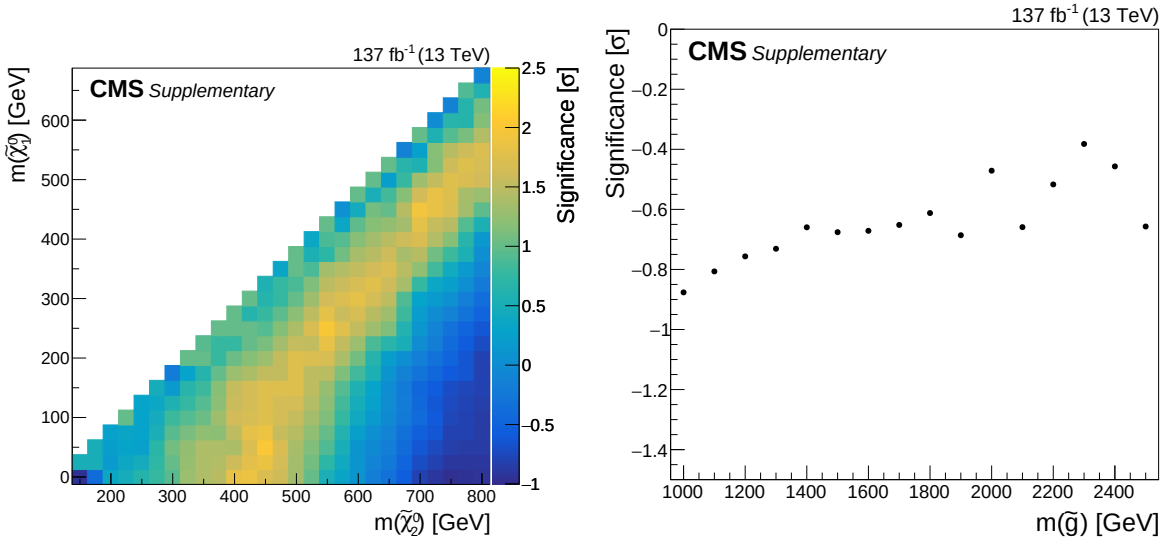

Figure 5.10: Significance as a function of higgsino mass $m(\widetilde{\chi}_2^0)$ and bino mass $m(\widetilde{\chi}_1^0)$ for the TChiHH model (left) and as a function of gluino mass $m(\widetilde{g})$ for the T5HH model (right). A negative significance represents a negative best-fit signal strength. Since significance measures only the incompatibility with background-only hypothesis, the bottom band of the left plot is equivalent to the significance for the TChiHH-G model.

nation targets four different simplified models of supersymmetry. This section describes the two models involving higgsino production for which the HH(4b)+$p_{\mathrm{T}}^{\mathrm{miss}}$ analysis is relevant. The descriptions of and results for the wino and slepton models can be found in the electroweak SUSY combination paper.

Higgsino-gravitino model

The higgsino-gravitino model considered in this combination is nearly identical to the TChiHH-G model considered by the HH(4b)+$p_{\mathrm{T}}^{\mathrm{miss}}$ analysis but with the modification that the lightest higgsino may decay into either a Higgs boson and a gravitino or a Z boson and a gravitino. The cross section is identical to the TChiHH-G cross section

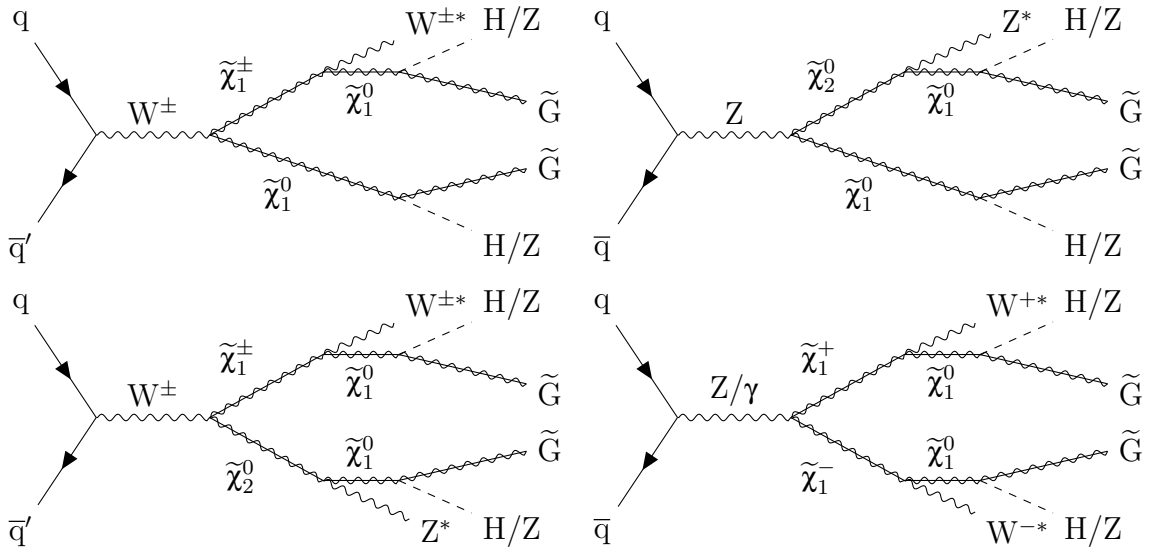

Figure 5.11: Feynman diagrams representing the higgsino-gravitino simplified model with production of higgsinos $\widetilde{\chi}_1^0$, $\widetilde{\chi}_1^\pm$, and $\widetilde{\chi}_2^0$, the heavier of which decay to soft particles represented as W* or Z* and the lightest higgsino, which then decays into a Higgs boson or a Z boson and a gravitino $\widetilde{\mathrm{G}}$, which is the LSP.

shown in Figure 3.4, while the relevant Feynman diagrams are shown in Figure 5.11. The free parameters of the model are the common higgsino mass $m_{\widetilde{\chi}_1^0}$ and the branching ratios of the lightest higgsino.

Higgsino-bino model

The higgsino-bino model features a bino-like LSP $\widetilde{\chi}_1^0$, with a mass $m_{\widetilde{\chi}_1^0}$, and four heavier nearly degenerate higgsino-like electroweakinos, $\widetilde{\chi}_2^0$, $\widetilde{\chi}_3^0$, and $\widetilde{\chi}_1^\pm$, with a common mass $m_{\widetilde{\chi}_1^\pm}$. The charged higgsinos are assumed to decay to a W boson and the LSP with a probability of 1 while the neutral higgsinos are assumed to decay to a Higgs boson and the LSP with probability 1. This makes the model identical to the HH(4b)+$p_{\mathrm{T}}^{\mathrm{miss}}$ TChiHH model for neutral higgsino production but yields additional $\mathrm{WH} + p_{\mathrm{T}}^{\mathrm{miss}}$ and $\mathrm{WW} + p_{\mathrm{T}}^{\mathrm{miss}}$

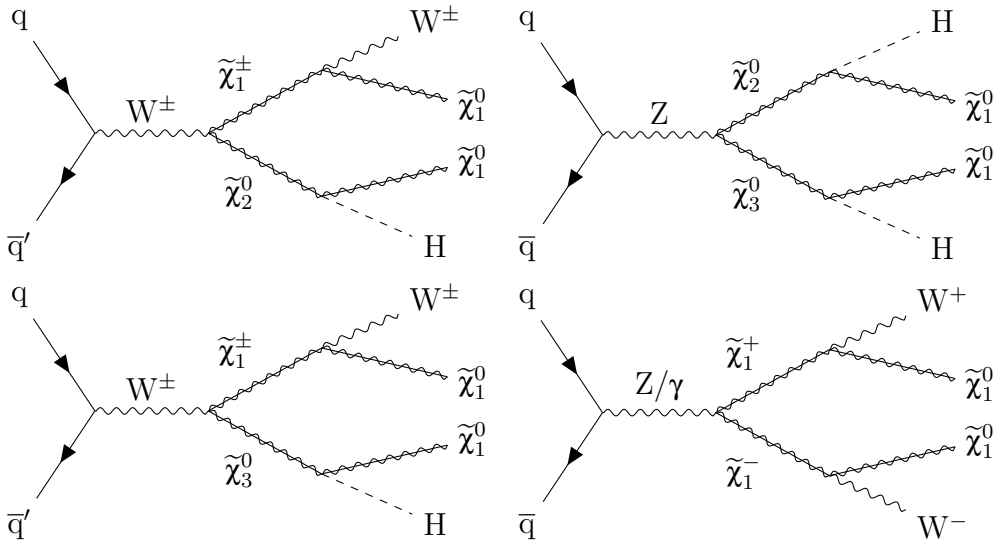

Figure 5.12: Feynman diagrams representing pair production of higgsinos in the higgsino-bino simplified model. The charged higgsinos $\widetilde{\chi}_1^{\pm}$ decay into a W boson and the bino-like LSP $\widetilde{\chi}_1^0$ while the neutral higgsinos $\widetilde{\chi}_2^0$ and $\widetilde{\chi}_3^0$ decay into a Higgs boson and the LSP.

signals when one or two charged higgsinos are produced. Since only the HH(4b)+$p_{\mathrm{T}}^{\mathrm{miss}}$ contributes to the $\mathrm{HH}+p_{\mathrm{T}}^{\mathrm{miss}}$ signature and no analyses in the combination specifically target the $\mathrm{WW}+p_{\mathrm{T}}^{\mathrm{miss}}$ signature, only the results for the $\mathrm{WH}+p_{\mathrm{T}}^{\mathrm{miss}}$ signature are shown in Section 5.2.3. The total cross section for any combination of charged and neutral higgsinos is shown in red in Figure 3.4 while the Feynman diagrams relevant to this model are shown in Figure 5.12. Simulated samples for the higgsino-bino model are generated by scanning across different masses for the LSP and the nearly degenerate higgsinos. Note that one could also consider cases where the neutral higgsinos have some probability to decay to a Z boson and the LSP, but such a case is not directly considered for the combination.

5.2.2 Input analyses and combination procedure

The electroweak SUSY combination combines six different analyses targeting different final states. This section provides a brief description of each of the analyses used in the combination. Note that only the portion of each analysis used in the combination is described here. More information can be found in the analyses' respective papers [3, 276, 332–335]. For the combination, some of the analyses are slightly modified to remove overlap between analyses. The statistical fit for all analyses is then performed simultaneously, correlating nuisance parameters that are common between the analyses.

Kinematic variables

There are a number of kinematic variables used throughout the analyses of the electroweak SUSY combination. The transverse mass m_{T} described in Section 3.2.1 can be calculated from the momentum of a visible system and $p_{\mathrm{T}}^{\mathrm{miss}}$, and gives a lower bound on the mass of a heavy particle decaying into the visible system and one or more undetected particles. The stransverse mass M_{T2} [395, 396] is a generalization of m_{T} to the case of pair production of particles, each of which decays into a visible system and undetected particles. M_{T2} is given by

$$M_{\mathrm{T2}} = \min_{\vec{p}_{\mathrm{T}}^{\,\mathrm{miss}(1)}+\vec{p}_{\mathrm{T}}^{\,\mathrm{miss}(2)}=\vec{p}_{\mathrm{T}}^{\,\mathrm{miss}}} \Big(\max(m_{\mathrm{T}}(\mathrm{sys}(1), \vec{p}_{\mathrm{T}}^{\,\mathrm{miss}(1)}), m_{\mathrm{T}}(\mathrm{sys}(2), \vec{p}_{\mathrm{T}}^{\,\mathrm{miss}(2)}))\Big) \tag{5.1}$$

where $\vec{p}_{\mathrm{T}}^{\,\mathrm{miss}(1)}$ and $\vec{p}_{\mathrm{T}}^{\,\mathrm{miss}(2)}$ are any purely transverse three-vectors whose sum is the total $\vec{p}_{\mathrm{T}}^{\,\mathrm{miss}}$ and $m_{\mathrm{T}}(\mathrm{sys(n)}, \vec{p}_{\mathrm{T}}^{\,\mathrm{miss}(n)})$ is the transverse mass calculated for a visible system n and

$\vec{p}_{\mathrm{T}}^{\,\mathrm{miss}(n)}$. Since a minimization is performed over all possible ways to split $\vec{p}_{\mathrm{T}}^{\,\mathrm{miss}}$ into two components corresponding to the undetected particles, M_{T2} is bounded above by the true m_{T} values, which are in turn bounded above by the mass of the new particle. Another generalization of m_{T} to the case of multiple particles that depends only on the visible systems is the cotransverse mass m_{CT} [397], which is defined

$$m_{\mathrm{CT}} = \sqrt{2p_{\mathrm{T}}^{(1)}p_{\mathrm{T}}^{(2)}(1+\cos(\Delta\phi_{(1)(2)}))}. \tag{5.2}$$

The cotransverse mass has a kinematic endpoint determined by the mass of the parent particle, the visible system, and the invisible system that reduces to the mass of the parent particle in the limit the visible and invisible system are massless. These variables are useful, not only for determining the mass of any new particles, but also for discriminating between signal and background. For example, the m_{T} of a lepton is bounded above by m_{W} for events with the decay $\mathrm{W} \to \ell\nu$. Similarly for dilepton $\mathrm{t\bar{t}}$+jets events, M_{T2} calculated with the b jets from the top quark decays is bounded above by m_{t} while m_{CT} calculated with b jets is bounded above by about 150 GeV. Some signal models may show values of m_{T}, M_{T2}, or m_{CT} that are much higher than the kinematic endpoints of common SM backgrounds.

The invariant mass of a pair of leptons will be denoted by $m_{\ell\ell}$, while that for three leptons will similarly be denoted by $m_{\ell\ell\ell}$. The variable $M_{\tau\tau}$ used in the $2/3\ell$ soft analysis is defined for dilepton events by rescaling the lepton p_{T} until the $p_{\mathrm{T}}^{\mathrm{miss}}$ vanishes and computing the invariant mass of the leptons. This is a rough approximation to the

invariant mass of a pair of tau leptons that decay into the visible leptons and neutrinos, which generate $p_{\mathrm{T}}^{\mathrm{miss}}$.

Two or three soft leptons, initial-state-radiation jets, and $p_{\mathrm{T}}^{\mathrm{miss}}$

The "2/3ℓ soft" analysis [276] targets final states with $p_{\mathrm{T}}^{\mathrm{miss}} > 125$ GeV, initial-state-radiation jets with $H_{\mathrm{T}} > 100$ GeV, and two or three electrons or muons with 3.3 or $5 < p_{\mathrm{T}} < 30$, including an opposite-sign same-flavor pair where the lower bound on the lepton p_{T} depends on the signal region and lepton flavor. In the combination, these final states are used to target models of supersymmetry where the mass splitting between the particles produced at the LHC and the LSP is small. The initial-state radiation is needed to provide a boost to the LSPs, creating substantial $p_{\mathrm{T}}^{\mathrm{miss}}$. The data are collected with $p_{\mathrm{T}}^{\mathrm{miss}}$ triggers, dimuon triggers, and dimuon-$p_{\mathrm{T}}^{\mathrm{miss}}$ cross triggers.

The main backgrounds are Drell-Yan events, $\mathrm{t\bar{t}}$+jets events, diboson events, and events with nonprompt or spurious leptons. Various kinematic and quality selections are applied to the different analysis categories to reduce these backgrounds. Dilepton events with $0 < M_{\tau\tau} < 160$ GeV are vetoed to reduce the contribution from Drell-Yan background. Events with b jets are vetoed to reduce the contribution from $\mathrm{t\bar{t}}$+jets background. The quantity $p_{\mathrm{T}}^{\mathrm{miss}}/H_{\mathrm{T}}$ is required to be between 2/3 and 1.4 to reduce QCD multijet events with $p_{\mathrm{T}}^{\mathrm{miss}}$ arising from mismeasurement as well as events without ISR. Various quality criteria are imposed on the leading jet to reject spurious jets and jets that are likely to be generated by leptons. The m_{T} for each lepton of dilepton

events is required to be less than 70 GeV to reduce backgrounds with $p_{\mathrm{T}}^{\mathrm{miss}}$ from W decays. Trilepton events with any opposite-sign same-flavor lepton pairs with invariant mass over 60 GeV are removed to suppress events with leptonically decaying Z bosons. Finally, events with $m_{\ell\ell}$ between 3 and 3.2 GeV or between 9 and 10.5 GeV are rejected to remove contributions from Υ and ψ mesons.

When targeting electroweakino models, events are first split based on the number of leptons, then into various $p_{\mathrm{T}}^{\mathrm{miss}}$ and $m_{\ell\ell}$ categories. A fit is performed to signal and background yields across the $p_{\mathrm{T}}^{\mathrm{miss}}$ and $m_{\ell\ell}$ categories. For the electroweak SUSY combination, the $m_{\ell\ell}$ binning is varied to optimize sensitivity to each signal model considered. When targeting the slepton model, events with two leptons are taken and split into categories of $p_{\mathrm{T}}^{\mathrm{miss}}$ and M_{T2}, which are again fit in order to extract signal and background contributions. In addition to the search regions, the fits include several control regions in order to constrain systematic uncertainties in the background yield. A control region with the $M_{\tau\tau}$ veto inverted is used to constrain Drell-Yan background, a control region with the b-jet veto inverted is used to constrain $\mathrm{t\bar{t}}$+jets background, a control region with the $m_{\mathrm{T}} < 70$ GeV selection changed to $m_{\mathrm{T}} > 90$ GeV is used to constrain the WW background, and a control region with two same-sign leptons is used to constrain the background from events with spurious and nonprompt leptons. In the electroweak SUSY combination, the WZ background is constrained by correlating nuisance parameters with the multilepton analysis described below since the original control region used to constrain this background has extensive overlap with the multilepton analysis. The

observed event yields in data are in relative agreement with the background prediction.

Two opposite-sign leptons and $p_{\mathrm{T}}^{\mathrm{miss}}$

The "2ℓ OS' analysis [332] searches for supersymmetry in final states with $p_{\mathrm{T}}^{\mathrm{miss}} > 100$ GeV and two opposite-sign same-flavor electrons or muons. The dilepton system is required to have an invariant mass of at least 20 GeV and p_{T} of at least 50 GeV. Dilepton triggers are used to collect the data.

Five categories of the 2ℓ OS analysis are used in the electroweak SUSY combination. The electroweakino boosted VZ, resolved VZ, and HZ regions all require the dilepton invariant mass $m_{\ell\ell}$ to be consistent with m_{Z}, while the slepton and slepton+jets regions require $m_{\ell\ell}$ to be away from the Z mass. The boosted VZ region additionally requires an AK8 jet with a two-pronged structure and a soft-drop mass between 65 and 105 GeV. The resolved VZ region additionally requires two AK4 jets whose invariant mass is less than 110 GeV and M_{T2} calculated with the two leptons to be at least 80 GeV to reduce the contribution from $\mathrm{t\bar{t}}$+jets background. The HZ region additionally requires two b-tagged AK4 jets with an invariant mass below 150 GeV. Furthermore, events in the HZ region must satisfy $M_{\mathrm{T2}} > 200$ GeV, where M_{T2} is calculated with two lepton and b jet pairs to reject the strongly dominant $\mathrm{t\bar{t}}$+jets background. The two slepton categories both require $M_{\mathrm{T2}} > 100$ GeV, where M_{T2} is calculated with the two leptons, and the slepton+jets category requiress the subleading lepton $p_{\mathrm{T}} > 1.2 p_{\mathrm{T,lead\ jet}}$ since only the only jets expected in signal are due to initial-state radiation. Each of these categories is

then split into subcategories based on the $p_{\mathrm{T}}^{\mathrm{miss}}$.

The primary backgrounds in the 2ℓ OS analysis include $\mathrm{t\bar{t}}$+jets events, events with a Z and prompt neutrinos, and Drell-Yan events with spurious $p_{\mathrm{T}}^{\mathrm{miss}}$. The backgrounds in which the lepton flavors are uncorrelated such as $\mathrm{t\bar{t}}$+jets events are estimated from a control region in which the same-flavor requirement is inverted. The background from events with Z bosons and real $p_{\mathrm{T}}^{\mathrm{miss}}$ is estimated using simulation constrained to control regions with additional leptons. Finally, background from Drell-Yan with spurious $p_{\mathrm{T}}^{\mathrm{miss}}$ in electroweakino categories is estimated using reweighted γ+jets events while the contribution of Drell-Yan events in slepton categories is constrained using a control sample requiring events to have $m_{\ell\ell}$ near the Z boson mass. The event yields measured in data are consistent with the background predictions, with some categories showing slightly fewer events than predicted.

Two same-sign leptons, or at least three leptons, and $p_{\mathrm{T}}^{\mathrm{miss}}$

The "multilepton" analysis [333] targets the production of electroweakinos in final states with $p_{\mathrm{T}}^{\mathrm{miss}}$ and leptonically decaying pairs of heavy bosons, resulting in at least two same-sign leptons. Hadronic tau lepton decays are also considered, in order to improve sensitivity to events with Higgs bosons that decay into tau lepton pairs. The data are collected with single- and multilepton triggers. A BDT is used to reduce the contribution from spurious and nonprompt leptons. For events with more than four leptons passing the BDT selection, only the four highest p_{T} leptons are considered. For the electroweak SUSY

combination, the leading lepton is required to have a $p_{\mathrm{T}} > 30$ GeV in each category in order to avoid overlap with the $2/3\ell$ soft analysis. The minimum lepton p_{T} varies between 10 and 25 GeV to ensure high trigger efficiency.

Events are sorted into twelve exclusive categories based on the number, flavor, and sign of the leptons present. Additional kinematic variables are then used to discriminate between signal and background in each category. In the following discussion, τ_{h} stands for a hadronic tau candidate, OSSF stands for opposite-sign same-flavor, OSOF stands for opposite-sign opposite-flavor, and light lepton refers to electrons or muons. Each category is defined, then any additional categorization or selection is described.

- **2ℓSS** This category requires exactly two light leptons that have the same charge and no τ_{h}'s. If there a third lepton is present that fails the BDT selection but forms an OSSF pair with one of the selected leptons with an invariant mass near m_{Z}, the event is vetoed. Events with more than one jet are removed to reduce the background from mismeasured $\mathrm{t\bar{t}}$+jets. Events are then categorized based on M_{T2} calculated with the two leptons, $p_{\mathrm{T}}^{\mathrm{miss}}$, and $p_T(\ell\ell)$.

- **3ℓA** This category requires exactly three light leptons with at least one OSSF pair and no τ_{h}'s. To discriminate against the irreducible SM W Z background, a parametric neural network is trained with $m_{\ell\ell}$ of the lepton pair with mass closest to m_{Z}, m_{T} of the third lepton, $p_{\mathrm{T}}^{\mathrm{miss}}$, m_{T} of all three leptons, $m_{\ell\ell\ell}$, H_{T}, and the scalar sum of the lepton p_{T} and $p_{\mathrm{T}}^{\mathrm{miss}}$. Events are categorized based on the neural network discriminator value. To validate this approach, a parallel categorization

based on $m_{\ell\ell}$ of the Z boson candidate, m_{T} of the non-Z lepton, m_{T} of all three leptons, $p_{\mathrm{T}}^{\mathrm{miss}}$, and H_{T} is performed.

- **3ℓB** This category requires exactly three light leptons without any OSSF pairs or τ_{h}'s. To enhance sensitivity to events including the decay $\mathrm{H} \to \mathrm{WW} \to \ell\nu\ell'\nu'$ where the leptons are expected to have small angular separation, events are categorized based on the minimum ΔR between two leptons.

- **3ℓC** This category requires exactly two light leptons forming an OSSF pair and exactly one τ_{h}. The invariant mass of the light leptons is required to be inconsistent with m_{Z} and events are categorized based on $p_{\mathrm{T}}^{\mathrm{miss}}$, m_{T} of the two light leptons, and M_{T2} to discriminate between signal and $\mathrm{t\bar{t}}$+jets background.

- **3ℓD** This category requires exactly two light leptons forming an OSOF pair and exactly one τ_{h}. To discriminate against the dominant $\mathrm{t\bar{t}}$+jets and Drell-Yan backgrounds, events are categorized based on M_{T2} of the two light leptons, $p_{\mathrm{T}}^{\mathrm{miss}}$, and the opposite-sign dilepton mass closest to m_{Z}.

- **3ℓE** This category requires exactly two light leptons that are the same sign and exactly one τ_{h}. Again, discrimination between signal and the dominant $\mathrm{t\bar{t}}$+jets and Drell-Yan background is achieved by categorizing events based on M_{T2} of of the leading-p_{T} light lepton and the τ_{h}, $p_{\mathrm{T}}^{\mathrm{miss}}$, and the invariant mass of opposite sign leptons closest to m_{Z} if such a pair exists.

- **3ℓF** This category requires a light lepton and two τ_{h}'s. Events in this category

are further categorized based $p_{\mathrm{T}}^{\mathrm{miss}}$ as well as M_{T2} and the invariant mass of the leading-p_{T} τ_{h} and the light lepton.

- **4ℓG** This category requires four light leptons with two OSSF pairs. The pair with $m_{\ell\ell}$ closest to m_{Z} is taken as the first Z boson candidate while the other leptons are taken as the second Z boson candidate. Events are then categorized based on $m_{\ell\ell}$ of the second Z boson candidate to discriminate against backgrounds without two Z bosons as well as M_{T2} of the two Z candidates.

- **4ℓH** This category requires four light leptons with less than two OSSF pairs. The pair of opposite-sign leptons with $m_{\ell\ell}$ closest to m_{Z} is taken as a Z boson candidate if such a pair exists, otherwise any pair of leptons with $m_{\ell\ell}$ closest to m_{Z} is taken as a Z boson candidate. The remaining two highest p_{T} leptons are taken as a Higgs boson candidate. Events are categorized based on the $m_{\ell\ell}$ of the Z boson candidate and the ΔR of the Higgs boson candidate.

- **4ℓI** This category requires exactly three light leptons and one τ_{h}. Events in this category are split into further categories the same way as category 4ℓH.

- **4ℓJ** This category requires two light leptons and two τ_{h}'s with two OSSF pairs. Events in this category are split into further categories the same way as for category 4ℓH.

- **4ℓK** This category requires two light leptons and two τ_{h}'s with less than two OSSF pairs. Events in this category are split into further categories the same way as for

category 4ℓH.

The primary source of background in the 2ℓSS category is events with spurious leptons or charge mismeasurement. For categories 3ℓA and 4ℓG/H, the primary backgrounds are diboson events while in category 3ℓB and categories with τ_h's, the primary backgrounds are Drell-Yan and $t\bar{t}$+jets events with spurious or nonprompt leptons. Sources of background with prompt leptons as well as those where the leptons result from the conversion of a photon are estimated from simulation, but constrained by control regions in data with low p_T^{miss}. The background from spurious leptons is estimated using events with leptons that pass looser criteria but do not pass the full criteria together with a "tight-to-loose" factor to extrapolate the number of spurious leptons passing the full lepton selections. The background arising from electrons with mismeasured charge is estimated using opposite-sign lepton events in data together with charge mismeasurement probabilities derived from simulation. The observed yields in data agree with the predicted background yields.

One lepton, two b jets, and p_T^{miss}

The "1ℓ2b" analysis [334] searches for electroweakino production in the channel with a leptonically decaying W boson, a Higgs boson decaying into a pair of bottom quarks, and p_T^{miss}. The data are selected with p_T^{miss} and single-lepton triggers. The analysis requires exactly one electron or muon with $p_T > 30$ GeV, two b-tagged AK4 jets with an invariant mass between 90 and 150 GeV, and $p_T^{miss} > 125$ GeV.

Additional sensitivity is obtained by requiring m_{T} of the lepton to be at least 150 GeV and m_{CT} of the two b jets to be at least 200 GeV. This aids in rejecting W+jets and $\mathrm{t\bar{t}}$+jets background. After the basic selections on physics objects, m_{T}, and m_{CT}, the remaining events are categorized into twelve search categories based on the $p_{\mathrm{T}}^{\mathrm{miss}}$, number of jets, and the presence of a Higgs-tagged AK8 jet.

The primary backgrounds in the 1ℓ2b analysis are $\mathrm{t\bar{t}}$+jets events and W+jets events. The contribution to the search region from backgrounds involving top quarks is estimated from a data control region with the m_{CT} requirement inverted together with a transfer factor measured in simulation and validated in other data samples. The contribution from W+jets, WW, and WZ events is estimated from a data control region with one or fewer b-tagged jets together with a transfer factor measured in simulation. The small contribution from other background sources is estimated using simulation. The observed event yields in the data search regions are consistent with the background prediction.

Four b jets and $p_{\mathrm{T}}^{\mathrm{miss}}$

The "HH(4b)+$p_{\mathrm{T}}^{\mathrm{miss}}$" analysis [3] is the main topic of this thesis. The analysis strategy is outlined in Chapter 4. For the combination, the boosted topology $N_{\mathrm{H}} = 1$ region with a single double-b-tagged AK8 jet is removed to avoid overlap with the hadronic WX analysis.

Four jets and $p_{\mathrm{T}}^{\mathrm{miss}}$

The "hadronic WX" analysis [335] targets production of electroweakinos with large mass splitting by searching for final states with large $p_{\mathrm{T}}^{\mathrm{miss}}$ and and two hadronically decaying heavy bosons, either W W, W Z, or W H, reconstructed as two AK8 jets. The high branching ratio for hadronic decays provides sensitivity to signal models with heavy electroweakinos, which have smaller production cross sections. A larger mass splitting also makes it more likely the "child" boson will have high enough momentum to be reconstructed as a single AK8 jet. The data are collected with $p_{\mathrm{T}}^{\mathrm{miss}}$ triggers. The analysis requires two AK8 jets, no more than six AK4 jets, $p_{\mathrm{T}}^{\mathrm{miss}} > 200$ GeV, $H_{\mathrm{T}} > 300$ GeV, and no charged leptons.

The hadronic WX defines four signal regions, each of which is divided into several $p_{\mathrm{T}}^{\mathrm{miss}}$ categories. The b-veto signal region requires no b-tagged AK4 jets and two W/Z candidates that have soft-drop mass m_{J} between 65 and 105 GeV and are tagged as boosted W/Z boson candidates with two different tagging algorithms. The b tag+W category requires a b-tagged AK4 jet and a W-tagged AK8 jet with $65 < m_{\mathrm{J}} < 105$ GeV. The b tag+WH category requires one W-tagged AK8 jet with $65 < m_{\mathrm{J}} < 105$ GeV along with one double-b-tagged AK8 jet with $75 < m_{\mathrm{J}} < 140$ GeV. An additional b tag+H category is omitted from the combination to avoid overlap with the HH(4b)+$p_{\mathrm{T}}^{\mathrm{miss}}$ analysis.

The primary backgrounds in the hadronic WX analysis are W+jets, Z+jets, and $\mathrm{t\bar{t}}$+jets events. These backgrounds are estimated using control regions in data together

with transfer factors from simulation. For the b-veto signal region, the control regions are defined by inverting the tagging requirements on the two W/Z candidates. For the b tag signal regions, the control regions are defined by both inverting the requirements on the tagged AK8 jets as well as by requiring the presence of a lepton. The observed yields in data match the predictions from the background estimation method.

5.2.3 Results and interpretations

As with the HH(4b)+$p_{\mathrm{T}}^{\mathrm{miss}}$ analysis, the results of the electroweak SUSY combination are interpreted as 95% $\mathrm{CL_s}$ signal model limits calculated using the asymptotic approximations described in Section 4.4.2. Figure 5.13 shows the expected and observed limits on production cross section for the higgsino-gravitino model as a function of higgsino mass for branching fraction $B(\widetilde{\chi}_1^0 \to \widetilde{\mathrm{G}}\mathrm{H})$ values of 1, 0.5, and 0. Figure 5.14 shows the exclusion region for the higgsino-gravitino model assuming the nominal cross section as a function of higgsino mass and branching fraction for each input analysis sensitive to this model as well as for the combination. It is also shown which analysis is most sensitive for each parameter choice. Depending on the branching fractions, a lower limit of between 740 and 1025 GeV is set on the higgsino mass in these simplified models. Because the observed yields in the 2ℓ OS and HH(4b)+$p_{\mathrm{T}}^{\mathrm{miss}}$ analyses are respectively slightly below and above the predicted yields, the limits are slightly stronger than expected when the branching fraction to Z bosons is higher and slightly weaker than expected when the branching fraction to Higgs bosons is higher. The expected and observed limits are in

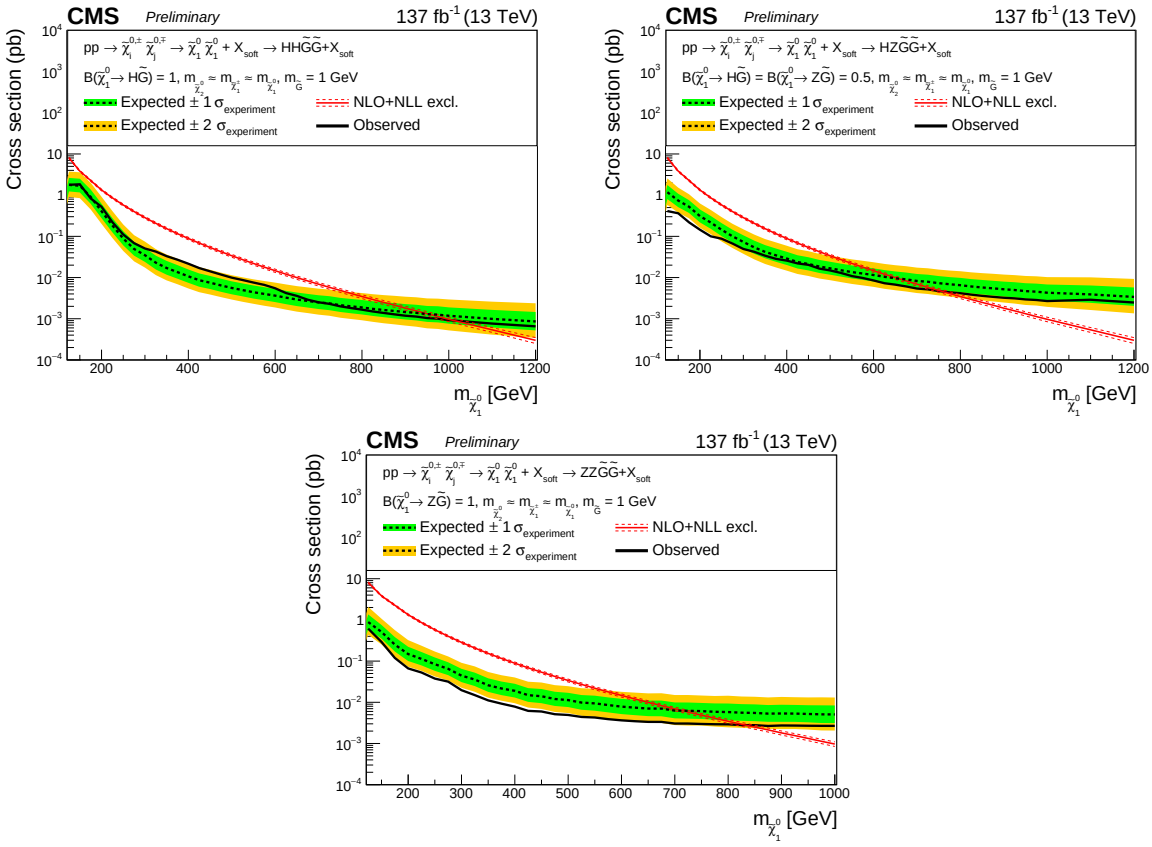

Figure 5.13: Observed (solid line) and expected (dashed line) 95% CL_s upper limits on the higgsino production cross section as a function of higgsino mass $m_{\widetilde{\chi}_1^0}$ for the higgsino-gravitino model with a 100% branching fraction for $\widetilde{\chi}_1^0 \to H\widetilde{G}$ (top left), a 50% branching fraction for $\widetilde{\chi}_1^0 \to H\widetilde{G}$ and a 50% branching fraction for $\widetilde{\chi}_1^0 \to Z\widetilde{G}$ (top right), and a 100% branching fraction for $\widetilde{\chi}_1^0 \to Z\widetilde{G}$ (bottom). The green and yellow bands represent the 68% and 95% uncertainty bands around the expected limit. The red line shows the nominal cross section for the model.

overall reasonable agreement.

Figure 5.15 shows the cross section limits for the higgsino-bino model in the plane of higgsino mass and bino-like LSP mass along with the region excluded assuming the nominal cross section in the case where one charged and one neutral higgsino are produced. The expected and observed exclusion regions agree within the 68% uncertainty band. For small LSP masses, higgsino masses between 225 GeV and 800 GeV are excluded.

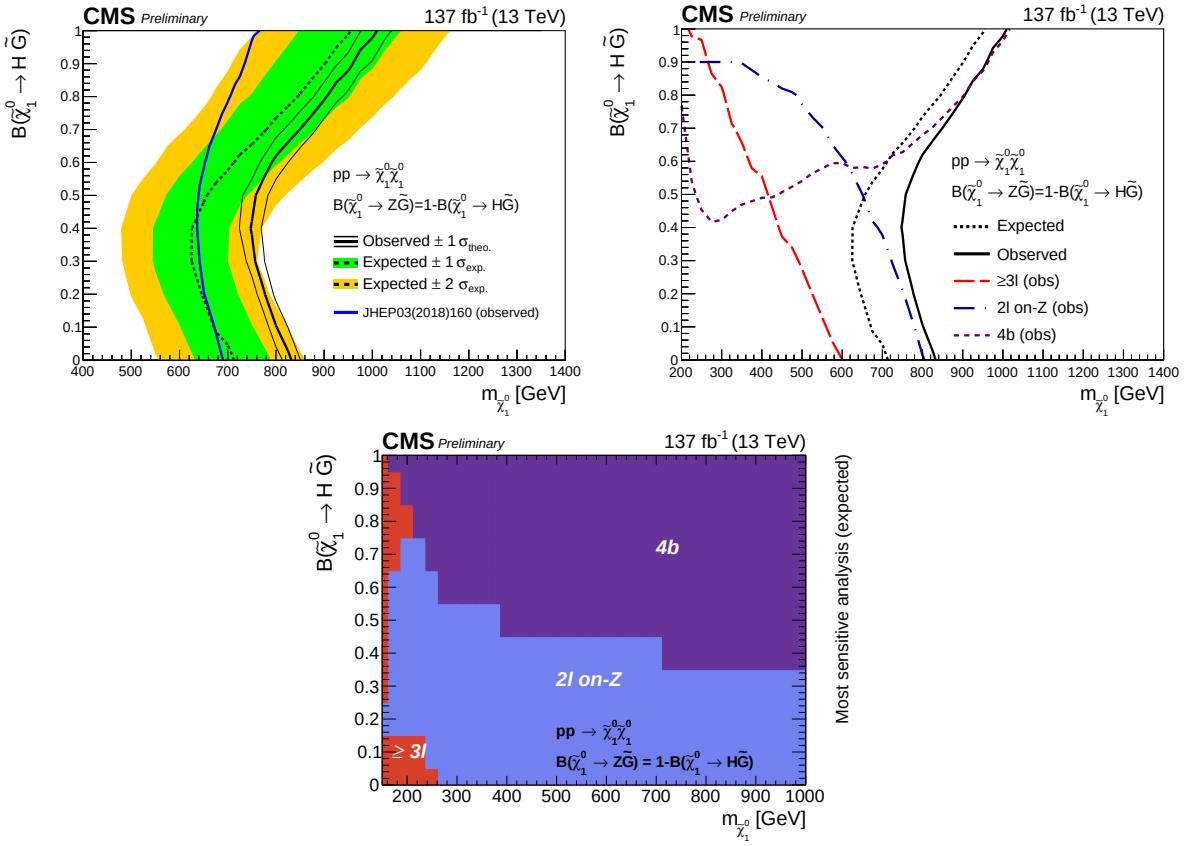

Figure 5.14: (top left) Observed (solid line) and expected (dashed line) exclusion region for the nominal cross section of the higgsino-gravitino model as a function of higgsino mass $m_{\tilde{\chi}_1^0}$ and branching fraction $B(\tilde{\chi}_1^0 \to \mathrm{H}\tilde{\mathrm{G}})$ where it is assumed all higgsinos that do not decay into a Higgs boson and a gravitino decay into a Z boson and a gravitino. The green and yellow bands represent the 68% and 95% uncertainty bands around the expected limit, and the blue line shows the observed limit for the previous CMS electroweak SUSY combination [327]. (top right) Observed exclusion in the same plane for the multilepton analysis (red dashed line), the 2ℓ OS analysis (blue dot dashed line), the HH(4b)+$p_{\mathrm{T}}^{\mathrm{miss}}$ analysis (violet short dashed line), and the combination (solid black line) as well as the expected exclusion for the combination (black dotted line). (bottom) Most sensitive analysis for each point in the higgsino mass-branching fraction plane where the multilepton analysis denoted "≥3l" is shown in red, the 2ℓ OS analysis denoted "2l on-Z" is shown in blue, and the HH(4b)+$p_{\mathrm{T}}^{\mathrm{miss}}$ analysis denoted "4b" is shown in violet.

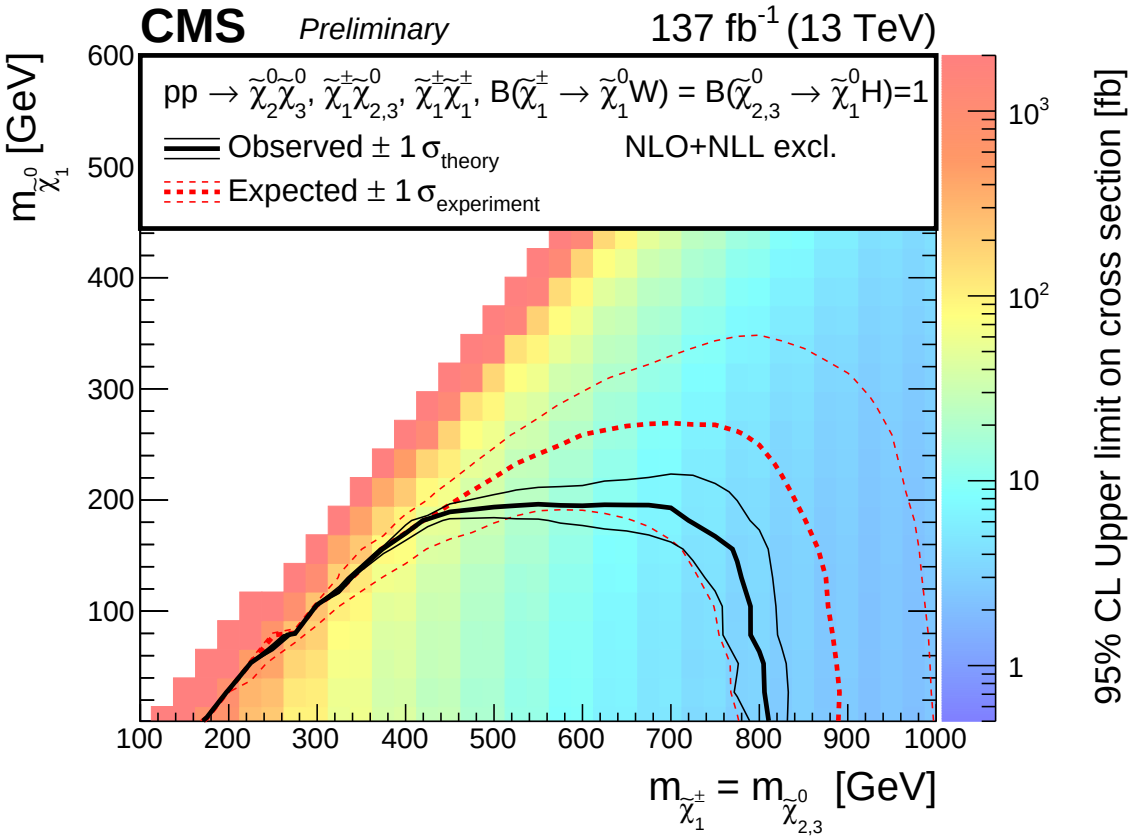

Figure 5.15: Observed 95% CL_s upper limits on the higgsino production cross section as a function of higgsino mass $m_{\tilde{\chi}_2^0} = m_{\tilde{\chi}_3^0} = m_{\tilde{\chi}_1^\pm}$ and bino mass $m_{\tilde{\chi}_1^0}$ for the higgsino-bino model shown as a color plot. The region for which the expected upper limit is lower than the nominal cross section is outlined by the dashed red line while the region where the observed upper limit is lower than the normal cross section is outlined by the thick solid black line. The 68% uncertainty bands of the expected and observed limits are shown as thin lines with the same style.

Chapter 6

Further work and conclusions

In the absence of any sign of supersymmetry so far, it is important to look for other leads that may answer the hierarchy problem. One particularly appealing program involves measurements of the Higgs boson, which are often sensitive to the sorts of BSM physics that might solve the hierarchy problem. Section 6.1 gives an overview of the $H \to Z\gamma$ analysis and describes some ongoing work on increasing the analysis acceptance by increasing the trigger efficiency as well as rather general work on overtraining of machine learning-based multivariate analysis discriminants that are likely to be important to the $H \to Z\gamma$ categorization scheme. Section 6.2 gives an overall summary of this thesis and is followed by Section 6.3, which provides an outlook on the current status of supersymmetry and the hierarchy problem.

6.1 Higgs decay to a Z boson and a photon

6.1.1 Overview

As described in Section 1.1.9, the higher the energy cutoff scale Λ_{UV} for the standard model, the more fine-tuning is required to keep the Higgs quadratic coefficient at the electroweak scale. It is for this reason that one generally expects new laws of physics at scales not much higher than the electroweak scale. However, despite searches for new particles such as higgsinos, the LHC experiments have not discovered any new particles so far. It is thus of great interest to consider measurements of the known particles that might provide indirect evidence for new laws of physics. If new degrees of freedom are responsible for the naturalness of the Higgs potential, it is likely that they will also modify the couplings of the Higgs boson, which makes measurements of the Higgs boson and its couplings an attractive probe of theories addressing the hierarchy problem.

One relatively rare decay of the Higgs boson that has not yet been observed is the decay $\mathrm{H} \to \mathrm{Z}\gamma$, which has a branching fraction of about 0.15% [151]. The best limits on the Higgs production cross section times the branching ratio for this decay are currently 3.6 and 4.1 times the SM prediction by the ATLAS and CMS collaborations respectively [398,399]. This section describes work on the ongoing CMS $\mathrm{H} \to \mathrm{Z}\gamma$ analysis, which will be performed after more data has been collected during LHC Run 3. Since the data are still being collected and the analysis strategy is still being refined, only the overall strategy of the analysis and details on selected studies are presented here.

The H $\rightarrow$ Zγ analysis targets the decay H $\rightarrow$ Zγ where the Z boson subsequently decays to a pair of electrons or muons. The primary Feynman diagrams for this process in the standard model are shown in Figure 6.1. The final signature is two electrons or muons together with a photon whose combined three-body invariant mass, $m_{\ell\ell\gamma}$, is near the Higgs boson mass, 125 GeV. The primary backgrounds arise from nonresonant $q\overline{q} \rightarrow Z\gamma$ production as well as Drell-Yan events with a spurious photon, which are shown schematically in Figure 6.2.

Figure 6.3 shows the distribution in $m_{\ell\ell\gamma}$ for dilepton plus photon events with some loose quality criteria and kinematic selections applied for CMS Run 2 simulation scaled to 340 fb^{-1}, the approximate projected integrated luminosity of data for LHC Run 2 and Run 3. The signal is expected to appear as a small enhancement near 125 GeV while the background distribution is relatively smooth on mass scales much larger than the expected spread of the signal peak. The background will be estimated by performing a fit to the invariant mass distribution of data events. For the most basic approach, the significance for the signal hypothesis is expected to be around $Z = 1.6$. However, the sensitivity can be improved by splitting events into categories with a relatively higher or lower proportion of signal events as is done in Refs. [398,399]. There are also other methods for improving the analysis sensitivity including increasing the efficiency for selecting or reconstructing signal events and improving the invariant mass resolution. The next sections describe two ongoing studies that could be used to improve the H $\rightarrow$ Zγ analysis: one related to trigger strategy and another related to training of machine learning-based multivariate

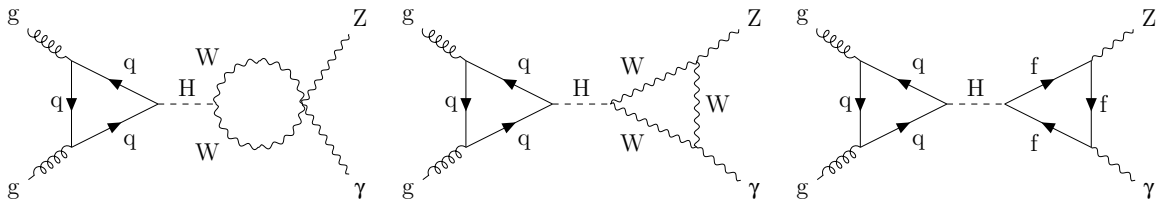

Figure 6.1: Primary Feynman diagrams for the process gg → H → Zγ. A Higgs is produced through a quark loop (dominated by the top quark, as the top quark Yukawa coupling is the largest) and can decay to a Z boson and a photon through a loop involving either a W boson or a fermion f.

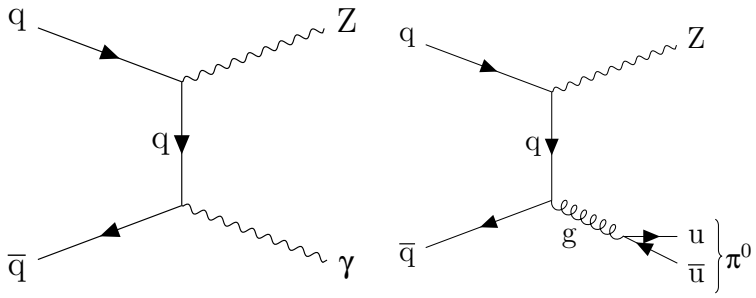

Figure 6.2: Representative Feynman diagrams for the two largest backgrounds in the H → Zγ analysis, qq̄ → Zγ and qq̄ → Z with a spurious photon. The spurious photon is shown here as a neutral pion, which is one common source, but by no means the only source of spurious photons.

analysis discriminants.

6.1.2 Trigger strategy

In [399], events are selected using dielectron and dimuon triggers. However, as described in Section 2.3.8, reconstruction of electron and muon physics objects at the HLT level is seeded by Level-1 electron/photon and muon objects. For this reason, some electrons and muons that can be reconstructed with the offline reconstruction algorithms are not reconstructed by the HLT. It is thus possible to recover additional acceptance for signal events by including also events captured with single-electron and single-muon

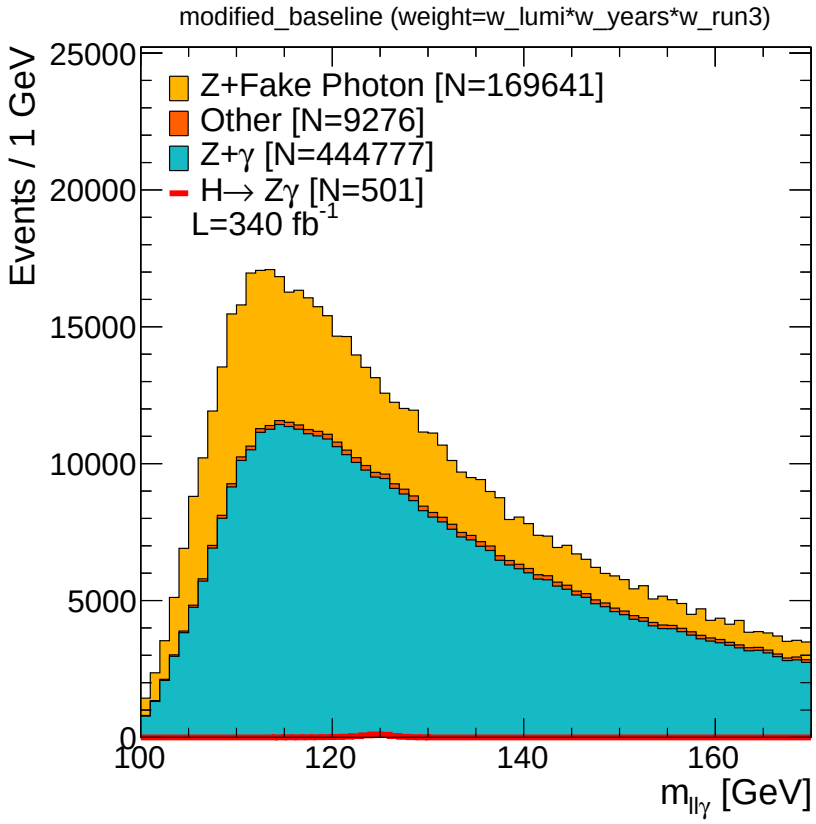

Figure 6.3: CMS Run 2 simulation of three-body invariant mass distribution for events with two opposite-sign electrons or muons together with a photon after basic quality and kinematics requirements scaled to 340 fb^{-1}, the approximate projected integrated luminosity that will be obtained with LHC Run 2 and Run 2 data. The distribution for simulated background processes are shown as a solid stacked histogram with $q\bar{q} \to Z\gamma$ events shown in teal, Drell-Yan events with a spurious photon shown in light orange, and other background processes in dark orange. The distribution for the signal $H \to Z\gamma$ process is shown as an outlined red histogram.

triggers. The dilepton triggers and single-lepton triggers used in this study are listed in Table 6.1.

Figure 6.4 shows the efficiency in simulation for electron and muon channel events as a function of lead lepton p_{T} for only dilepton triggers as well as for the logical OR of both dilepton and single lepton triggers. With the addition of the single-lepton triggers, the total signal acceptance in the electron channel increases from 78% to 89%, and the signal acceptance in the muon channel increases from 87% to 96%. Data-simulation scale factors were derived from measurements of trigger efficiency in simulation and data, and applied as weights to the simulated events. The dilepton trigger efficiencies are taken to be the product of the efficiencies for each lepton to pass its respective criteria times an overall constant efficiency. Note that the scale factors must include the nonnegligible correlation between the triggers, which is taken into account by splitting events into exclusive categories based on whether the leptons in the events were reconstructed and passed different trigger quality working points, as is done for the b-tagging scale factors mentioned in Section 3.3.3.

The increase in trigger efficiency for signal and background events was measured in simulation with data-simulation scale factors applied and found to be compatible between the two. The addition of the single lepton triggers can thus be simply taken as an overall efficiency improvement for both signal and background. Figure 6.5 shows distributions in lepton p_{T}, lepton η, and $m_{\ell\ell\gamma}$ of the simulated signal sample for events passing dilepton triggers, as well as for events passing single lepton triggers but failing dilepton triggers.

Table 6.1: Triggers used in the H → Zγ analysis trigger studies and the associated years of data taking. The triggers listed above the horizontal line are the dilepton triggers while those listed below the horizontal line are the single lepton triggers.

Trigger name	Years used
HLT_Ele23_Ele12_CaloIdL_TrackIdL_IsoVL	2016,2017,2018
HLT_Mu17_TrkIsoVVL_Mu8_TrkIsoVVL_DZ	2016
HLT_Mu17_TrkIsoVVL_TkMu8_TrkIsoVVL_DZ	2016
HLT_Mu17_TrkIsoVVL_Mu8_TrkIsoVVL_DZ_Mass8	2017,2018
HLT_Mu17_TrkIsoVVL_Mu8_TrkIsoVVL_DZ_Mass3p8	2017,2018
HLT_Ele27_WPTight_Gsf	2016
HLT_Ele35_WPTight_Gsf	2017
HLT_Ele32_WPTight_Gsf_L1DoubleEG	2017
HLT_Ele32_WPTight_Gsf	2018
HLT_IsoMu24	2016,2017,2018
HLT_IsoMu27	2017

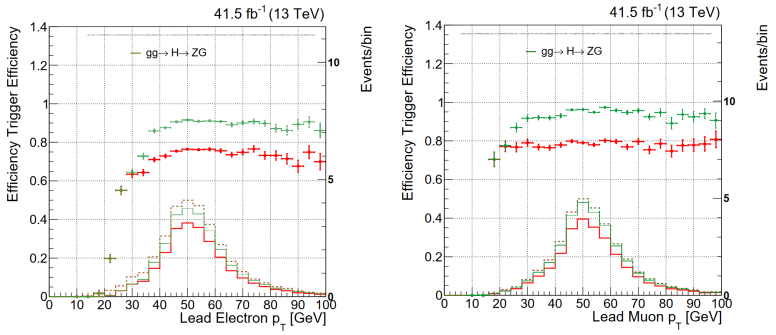

Figure 6.4: Trigger efficiency of signal events in the electron channel (left) and muon channel (right) for dilepton triggers (red) and the logical OR of dilepton and single lepton triggers (green) as a function of leading lepton p_{T}. Note that data-simulation scale factors have been applied to the simulated events to correct trigger efficiencies.

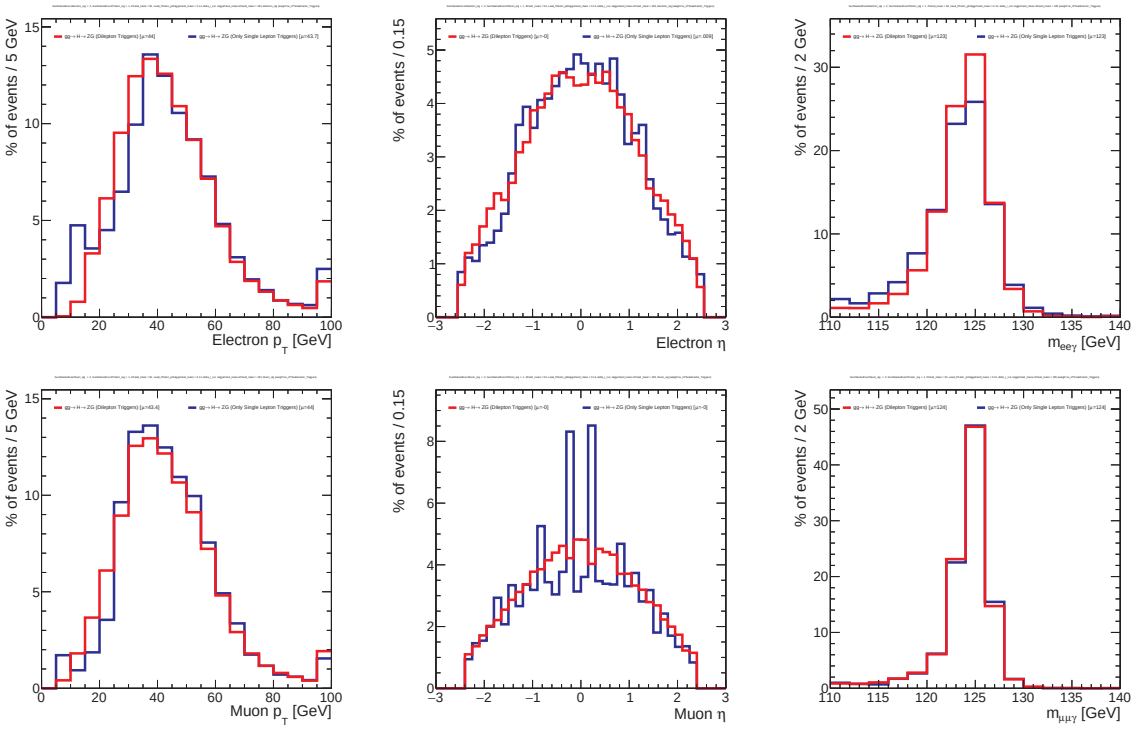

Figure 6.5: Relative distribution in lepton p_{T} (left), lepton η (center), and $m_{\ell\ell\gamma}$ (right) of signal in the electron channel (top) and muon channel (bottom) for events passing dilepton triggers (red) or events passing single lepton trigger but failing dilepton triggers (blue).

It is found that electron events that fail the dilepton triggers are slightly more likely to have FSR or bremsstrahlung photons that are not captured in the superclusters of the electrons and that muon events that fail the dilepton triggers are more likely to have a muon in η regions of the detector with reduced efficiency. The overall differences between the events passing the dilepton triggers and those added by single lepton triggers are not large, and the added events are suitable for analysis.

There remains further work related to the trigger strategy. The data-simulation trigger scale factors are currently measured using the NanoAOD format, which does not retain sufficient information to reconstruct HLT-level quantities for every event. The

trigger efficiency measurements can thus only be performed for a subset of events, limiting the statistical precision on the efficiencies and scale factors. Additional measurements using a different data format (MiniAOD) are required to derive more precise scale factors as well as their associated systematic uncertainties. Furthermore, all the studies detailed in this section have only been performed for Run 2 samples and must be checked also for Run 3 samples as they become available. Finally, there is some indication that an approximately 1-3% efficiency in signal acceptance can be gained by incorporating diphoton triggers and muon-photon cross triggers. The exact efficiency improvement is not known since data-simulation scale factors would need to be derived to determine the true efficiency improvement. Diphoton triggers have potential to recover efficiency since the diphoton triggers that do not have requirements on tracks effectively treat electrons as photons, and those that do have requirements on tracks can be used to recover electrons whose tracks were not reconstructed by the HLT algorithm. This also means that highly nontrivial correlations exist between the photon and lepton-only triggers. Triggers with photons may or may not be used in the final analysis depending on the total improvement and the difficulty of integrating them with the lepton-only triggers.

6.1.3 Categorization and multivariate analysis studies

A large part of the $H \to Z\gamma$ analysis sensitivity is dependent on how events are classified into different signal-enhanced categories. This categorization is connected with the different Higgs production mechanisms shown in Figure 6.6, since different production

mechanisms may produce different physics objects in addition to the Z boson and the photon from the Higgs decay. Work on this classification is ongoing, but it is currently planned that events will be split into a number of categories targeting ZH, $W^{\pm}H$, and $t\bar{t}H$ associated Higgs production; a number of categories targeting vector boson fusion Higgs production; and a number of categories targeting gluon-gluon fusion Higgs production. Associated production events are characterized by the presence of additional physics objects produced in the decays of the W boson, the Z boson, or the top quarks. The presence of these physics objects such as b jets, additional leptons, or large $p_{\mathrm{T}}^{\mathrm{miss}}$ may be used to select events for the associated production categories. Vector boson fusion events are characterized by the presence of two widely separated jets, the presence of which can be used to select events for the vector boson fusion categories. Events not selected for the associated production or vector boson fusion categories are considered for the gluon-gluon fusion categories. It is planned that the division of the associated production categories will depend on the additional physics objects present. In contrast, signal-background discrimination in the vector boson fusion and gluon-gluon fusion categories depends primarily on event kinematics and physics object quality variables.

The increase in analysis sensitivity from the divisions between the various vector boson fusion and gluon-gluon fusion categories depends on how well one can discriminate between signal and background. Various methods to discriminate signal and background exist, but one commonly employed method is to train a machine learning-based multivariate discriminant to separate signal and background events in simulation. Selections

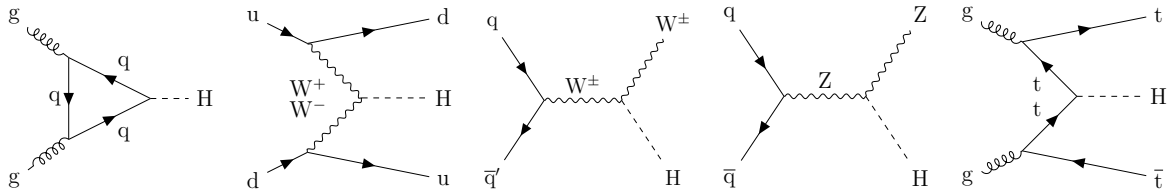

Figure 6.6: Representative Feynman diagrams showing the five primary Higgs production mechanisms at the LHC in order from left to right: gluon-gluon fusion, vector boson fusion, associated production of a W boson and a Higgs boson, associated production of a Z boson and a Higgs boson, and associated production of a top quark pair and a Higgs boson.

on the discriminant can then be used to divide the data into different categories with different levels of relative signal enhancement. Note that if the machine learning discriminant training is too sensitive to fluctuations in the training sample, these fluctuations could negatively affect the discriminant performance in other samples and bias the performance evaluation in the training sample, a phenomenon known as "overtraining". To study this, various BDT discriminants were trained using the kinematic and quality variables described in Table 6.2 to separate gluon-gluon fusion $H \to Z\gamma$ signal from the primary $q\overline{q} \to Z\gamma$ and Drell-Yan plus spurious photon backgrounds. The parameters of the training were varied to study their effects on overtraining. While a BDT discriminant may or may not be the signal-background discriminant used in the final analysis, it is nonetheless useful as a benchmark and for comparison. The general conclusions regarding overtraining are also not specific to a BDT discriminant.

The BDT is implemented using the TMVA package [400]. The BDT algorithm involves constructing many decision trees, each of which identifies events as signal-like (1) or background-like (-1). A single tree is constructed using a weighted set of events by

Table 6.2: Variables used in the training of a BDT discriminant to separate $H \to Z\gamma$ signal from the primary $q\bar{q} \to Z\gamma$ and Drell-Yan plus spurious photon backgrounds together with a description of each.

Variables	Description
Photon MVA discriminant	MVA discriminant for separating true and spurious photons described in Section 2.3.8
Min$\Delta R(\ell, \gamma)$	Minimum ΔR between the photon and one of the leptons
$p_{T\ell\ell\gamma}/m_{\ell\ell\gamma}$	p_T of the Higgs boson candidate divided by its invariant mass
Photon p_T uncertainty	Estimated uncertainty in photon p_T determination
Max$\Delta R(\ell, \gamma)$	Maximum ΔR between the photon and one of the leptons
cos(Θ)	Cosine of the angle between one of the colliding partons and the Z boson in the Higgs rest frame
Photon η	Pseudorapidity of the photon
cos(θ)	Cosine of the angle between the photon and one of the leptons in the Higgs rest frame
Leading lepton p_T	p_T of the leading p_T lepton
Subleading lepton p_T	p_T of the subleading p_T lepton
ϕ	Angle between the plane containing the two leptons and the photon and the plane containing the photon and the initial partons in the Higgs rest frame

iteratively splitting the set by picking a division in one of the provided variables that maximizes $p(1-p)$ where p is the purity of signal events in the more pure subset. After a tree is trained, the adaptive boost algorithm [401] updates events weights by multiplying the weight of previously misclassified events by $\alpha^\beta = [(1-r)/r]^\beta$ where r is the total misclassification rate and β is a constant learning rate parameter. Subsequent trees are thus expected to compensate for misclassification in previous ones. An average of the trees' outputs weighted by $\log(\alpha_i)$ is then taken as the final discriminator. A few of the notable BDT parameters include the number of trees used, the maximum depth allowed for the trees, and the minimum fraction of events allowed in a single division or "node" constructed by a tree.

The performance of a signal-background discriminant can be quantified in a number of ways. One common method is by plotting the efficiency ϵ_s for selecting signal events with a given selection on the discriminant as a function of ϵ_b, the efficiency for selecting background events with the selection. This is called a receiver operating characteristic

(ROC) curve. The area under this curve (AUC),

$$\mathrm{AUC} = \int \epsilon_{\mathrm{s}} d\epsilon_{\mathrm{b}}, \tag{6.1}$$

is a commonly used metric of overall discriminant performance. In a physics analysis, the expected significance of an excess of events from a signal process over a Poisson-distributed background is approximately the number of expected signal events divided by the square root of the expected number of background events, $N_{\mathrm{s}}/\sqrt{N_{\mathrm{b}}}$. In a multicategory analysis, the total significance can be approximated by taking the sum in quadrature of the significance values from each category. Assuming that the categories of an analysis are determined by splitting events based on a discriminant, the continuum-limit significance improvement (CSI) where the signal yield in each category is $d\epsilon_{\mathrm{s}}$ and the background yield in each category is $d\epsilon_{\mathrm{b}}$ can be shown to be

$$\mathrm{CSI} = \sqrt{\int \left(\frac{d\epsilon_{\mathrm{s}}}{d\epsilon_{\mathrm{b}}}\right)^2 d\epsilon_{\mathrm{b}}}. \tag{6.2}$$

This is another metric of overall discriminant performance. To quantify overtraining, the simulated sample is typically divided into two exclusive subsets called a training sample and a test sample. The training sample is used to train the discriminant while the test sample is used to evaluate the presence of overtraining. In the limit of no overtraining, the discriminant should perform identically for the training and test samples. The difference in AUC or CSI for the training and test samples is thus one metric of overtraining.

Another commonly used metric is the Kolmogorov-Smirnov (K-S) test p-value [402, 403], which quantifies how likely it is that two observed distributions arose from the same probability distribution function. The distribution in discriminant is constructed for the training and test samples, and the largest difference in their empirical distribution functions is taken as a test statistic, which follows a known probability distribution function from which a p-value is extracted.

Figure 6.7 shows the AUC and ROC for the training and test samples as well as K-S test p-values as parameters of the BDT and training are varied. As the number of training events is increased, the overtraining decreases as can be seen from the more similar AUC and CSI values between the testing and training data sets as well as the increasing K-S test p-value. Increasing the training sample size also generically increases the true (test sample) performance. The number of trees in the BDT, the maximum tree depth, and minimum node size all show a similar pattern: increasing the complexity of the BDT classifier by increasing the number of trees, increasing the maximum allowed depth, or decreasing the minimum node size results in better performance but also more overtraining. Overtraining can thus be curtailed at the cost of performance by tuning these parameters. The performance and overtraining are also shown as a function of the number of variables provided to the BDT, which is varied by adding variables one at a time in order of maximal individual discrimination, which is the top-to-bottom order of Table 6.2. Adding additional variables again increases performance at the cost of overtraining, but since the later variables do not increase performance drastically, they

can be omitted to reduce overtraining. Studies involving MVA discriminants such as the BDT discriminant considered here must generally be careful of results that could be affected by overtraining, though comparisons between the training and test samples do provide an estimate of the size of the systematic uncertainty due to overtraining. Additional systematic uncertainties due to mismodeling in simulation may need to be considered separately.

Much work remains to determine a sensitive and robust categorization for the $\mathrm{H} \to \mathrm{Z}\gamma$ analysis. The fundamental categorization scheme for the associated production categories is still under investigation, as are the methods that will be used to divide the vector boson fusion and gluon-gluon fusion categories. However, it is likely the a machine learning-based tivariate technique will be used, at least for comparison. The studies in this section outline one potential challenge for such machine learning-based techniques as well as potential mitigation methods. As more data are gathered and the analysis strategy is refined, one hopes that the $\mathrm{H} \to \mathrm{Z}\gamma$ process will be discovered and measured.

6.2 Summary

This thesis has presented a search for the production of higgsinos in final states with four b jets and missing transverse momentum $p_{\mathrm{T}}^{\mathrm{miss}}$ using approximately 137 fb^{-1} of 13 TeV proton-proton collision data collected by the Compact Muon Solenoid (CMS) experiment at the Large Hadron Collider (LHC). Such a signature might be expected in some natural models of supersymmetry in which higgsinos are light enough to be

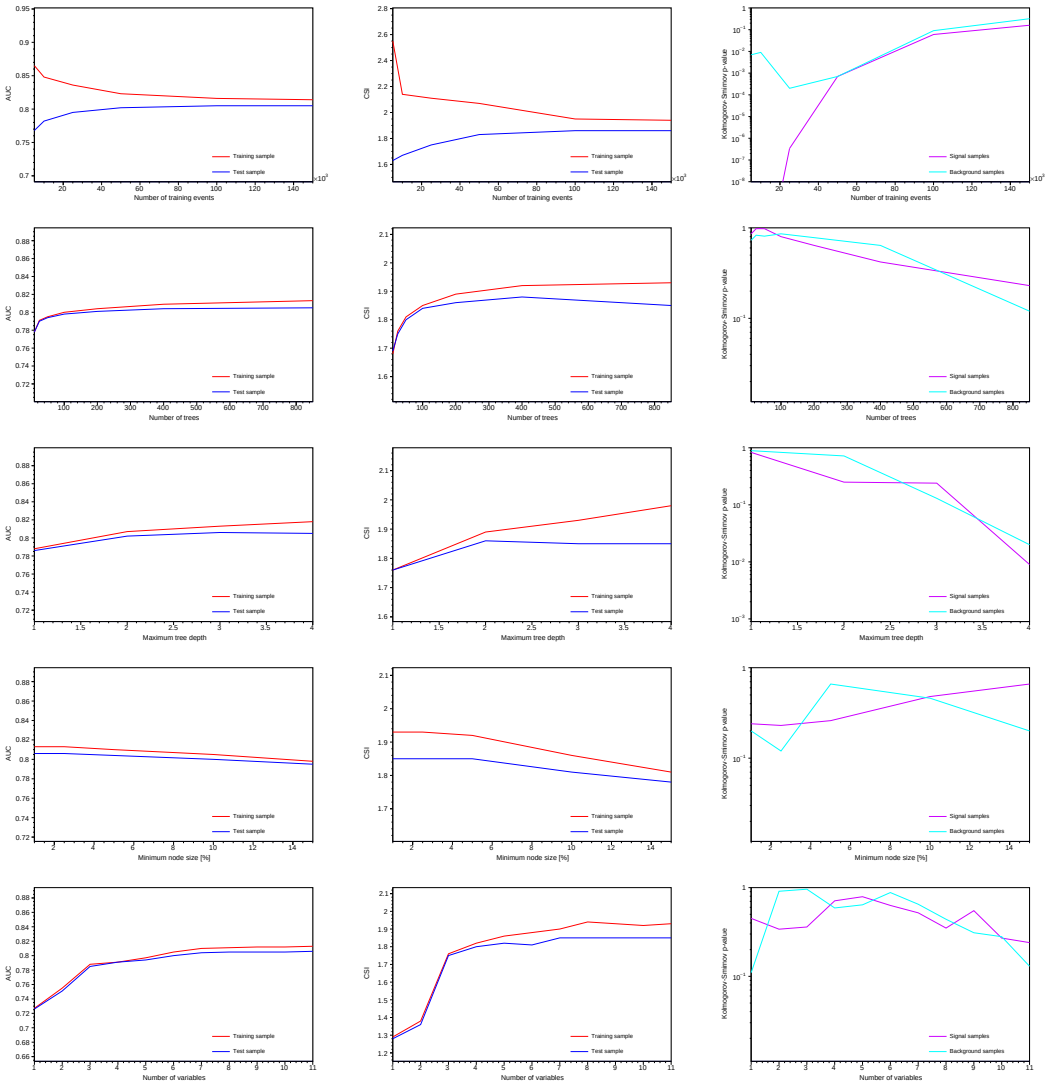

Figure 6.7: Metrics of performance and overtraining as various parameters of the BDT and training are varied. The left column shows the area under the curve for the discriminant in the training (red) and test (blue) sample, the middle column shows the continuous significance improvement approximation for the discriminant in the training (red) and test (blue) samples, and the right column shows the Kolmogorov-Smirnov test p-values for the signal (violet) and background (cyan) shapes. From top to bottom, the rows vary the number of training events, the number of trees in the BDT discriminant, the maximum tree depth, the minimum node size, and the number of variables. Note that even on the linear plots, the y-axis does not extend to zero.

produced at the LHC but are not the lightest supersymmetric particle (LSP).

The search selects events with substantial $p_{\mathrm{T}}^{\mathrm{miss}}$ and two Higgs boson candidates formed from either two pairs of jets (the resolved topology) or two fat jets (the boosted topology). These two reconstruction methods are complementary with the resolved and boosted topologies providing more sensitivity to models with a smaller and larger mass difference between the higgsinos and LSPs respectively. The large $p_{\mathrm{T}}^{\mathrm{miss}}$ is used during online reconstruction to select events that will be saved for offline analysis by the trigger system. The dominant standard model backgrounds are $\mathrm{t\bar{t}}$+jets, W+jets, and Z+jets events, which are the most common processes with neutrinos, the primary standard model source of large $p_{\mathrm{T}}^{\mathrm{miss}}$.

The background from standard model processes is estimated using a data-driven method. Events passing the baseline selection for the resolved topology are divided into "ABCD" regions based on the number of b-tagged jets, N_{b}, and the average Higgs boson candidate mass $\langle m_{\mathrm{bb}} \rangle$. The Higgs boson candidates are required to be similar in mass so that $\langle m_{\mathrm{bb}} \rangle$ reflects the mass of both Higgs boson candidates. Signal events are expected to mostly populate the signal regions, which require $\langle m_{\mathrm{bb}} \rangle$ to be in a window around the Higgs boson mass and N_{b} to be at least three. The event yields in the other ABCD regions are used to estimate the background event yields in the signal region using the observation that N_{b} is approximately uncorrelated with $\langle m_{\mathrm{bb}} \rangle$. Specifically, the shape of the distribution of events in $\langle m_{\mathrm{bb}} \rangle$ in the $N_{\mathrm{b}} = 2$ category is combined with the yields of events with $\langle m_{\mathrm{bb}} \rangle$ outside the Higgs mass window in the $N_{\mathrm{b}} \geq 3$ categories to predict

the signal region yields. A small correction factor is used to capture uncertainties due to any small correlation between $\langle m_{\mathrm{bb}} \rangle$ and N_{b} and checked in various control samples. Events are also categorized based on their $p_{\mathrm{T}}^{\mathrm{miss}}$ and their ΔR_{max}, the larger of the angular separation of the jets in a single Higgs boson candidate, and the background estimation is performed independently in each of these larger categories.

The analysis strategy for events reconstructed with the boosted topology is largely parallel to that of the resolved topology. Events are separated into ABCD regions based on the masses m_J of the two Higgs candidates and the number of double-b-tagged fat jets, N_{H}. The background event yields in the signal regions, which require N_{H} to be nonzero and the m_J of both jets to be in a two-dimensional window around the Higgs boson mass, is estimated by taking the $N_{\mathrm{H}} = 0$ category distribution shape in m_J and scaling it based on the yields in $N_{\mathrm{H}} \geq 1$ categories outside the Higgs window in m_J. Events are also split based on $p_{\mathrm{T}}^{\mathrm{miss}}$, but unlike the resolved topology, the background estimation is first performed inclusively in the $p_{\mathrm{T}}^{\mathrm{miss}}$ categories, then the fraction of events in each $p_{\mathrm{T}}^{\mathrm{miss}}$ category is predicted using the distribution in $p_{\mathrm{T}}^{\mathrm{miss}}$ of events in a single-b-tagged subregion of the $N_{\mathrm{H}} = 0$ category. The uncertainty in the background estimation method is evaluated using a control sample in data together with simulation, accounting for known discrepancies between data and simulation.

The observed event yields in the signal region are relatively consistent with the background-only hypothesis with the exception of one category out of twenty-two, which is likely the result of a statistical fluctuation. Various sources of uncertainty on the back-

ground estimation and the signal acceptance are considered and a statistical model is used to extract limits on the higgsino production cross section. Higgsinos with mass between 175 and 1025 GeV are excluded in a simplified model of pair production of nearly degenerate higgsinos decaying to a Higgs boson, a gravitino, and possibly additional low-p_{T} particles that are not reconstructed. For a simplified model of pair production of neutral higgsinos decaying to a Higgs boson and a bino-like LSP, higgsino masses around 265 to 305 GeV are excluded when the bino mass is nearly 0. Finally, gluino masses up to 2330 GeV are excluded in a simplified model of gluino production in which the gluinos decay into higgsinos, which in turn decay to a Higgs boson and the LSP.

The HH(4b)+$p_{\mathrm{T}}^{\mathrm{miss}}$ analysis is also combined with several another analyses as part of the CMS electroweak SUSY combination. A generalized model of higgsino production in which the lightest higgsino decays into a Higgs boson or a Z boson together with a gravitino is considered. In this model, higgsinos with a mass between 127 and 750–1025 GeV, where the upper bound depends on the branching fractions, are excluded. Another model including charged and neutral higgsino production with the charged higgsino decaying to a W boson and a bino-like LSP and the neutral higgsino decaying into a Higgs boson and a bino-like LSP is considered. In this model, higgsino mass ranges as large as 225–800 GeV are excluded depending on the LSP mass. The limits from the HH(4b)+$p_{\mathrm{T}}^{\mathrm{miss}}$ analysis as well as the combination represent the current most stringent limits on the considered models.

Finally, ongoing work on an analysis searching for the rare decay of a Higgs boson

and a Z boson was briefly outlined. The key idea of the analysis is to search for resonant production of a lepton pair and a photon, which appears as a localized excess in the three-body invariant mass above a relatively smooth background that can be estimated with a fit outside of the expected resonance location. Additional sensitivity is derived by classifying events into various exclusive categories with various levels of relative signal enhancement. It is found that using a combination of dilepton and single-lepton triggers can provide significantly increased efficiency for signal events. Additionally, the performance and overtraining of machine learning-based multivariate analysis discriminants is studied and found to depend on the training sample size and discriminant parameters. The parameters can be adjusted to limit the extent of overtraining. Additional work remains to improve the sensitivity and robustness of the analysis before the target data is fully collected.

6.3 Outlook

6.3.1 Outlook on supersymmetry

Natural theories of supersymmetry generally predict higgsinos with a mass $m(\widetilde{\chi}) \lesssim 350$ GeV, two top squarks and one bottom squark with a mass $m(\widetilde{\mathrm{t}}), m(\widetilde{\mathrm{b}}) \lesssim 700$ GeV, and gluinos with a mass $m(\widetilde{\mathrm{g}}) \lesssim 1.5$ TeV [132–134]. Figure 6.8 shows a set of limits on models of gluino production as well as a particular model of top squark production from the ATLAS and CMS experiments respectively. These results exclude the nominal cross

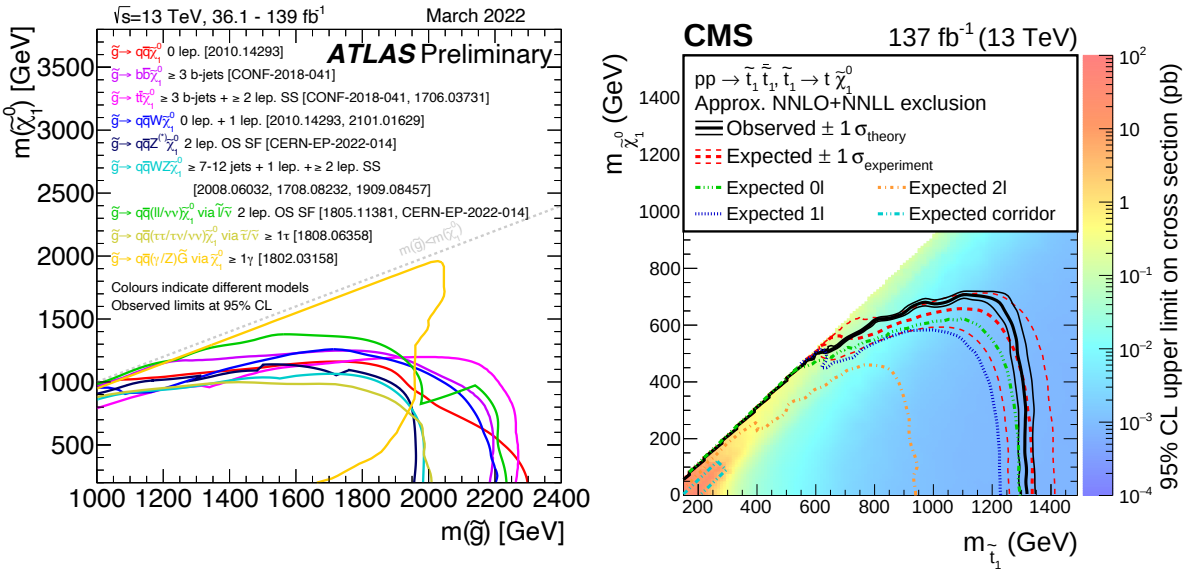

Figure 6.8: (left) Excluded region for various simplified models of gluino production in the gluino mass $m(\tilde{g})$ and LSP mass $m(\tilde{\chi}_1^0)$ plane from various analyses performed by the ATLAS collaboration targeting pair production of gluinos in various decay modes. Figure from Ref. [404]. (right) Excluded region for a simplified model of top squark pair production in the top squark mass $m_{\tilde{t}}$ and LSP mass $m_{\tilde{\chi}_1^0}$ plane assuming a 100% branching fraction for the decay $\tilde{t} \to t\tilde{\chi}_1^0$ using the combination of several analyses by the CMS collaboration. Figure from Ref. [405].

sections for gluino masses up to 2.2 TeV and top squark masses up to 1.3 TeV for small LSP masses. Furthermore, the measured Higgs boson mass of approximately 125 GeV may suggest a large top squark mass [129], which is also in conflict with naturalness.

Since the criterion of naturalness most strongly constrains the mass of higgsinos, it is of considerable interest to examine current limits on higgsino production. Limits on higgsinos are strongly dependent on the mass splitting between the different superpartners. In the case of a higgsino-like LSP and a mass splitting between higgsinos on the order of 0.3 GeV or less, a disappearing track signature can be used to exclude higgsinos with mass up to approximately 200 GeV as shown in Figure 6.9. When the mass

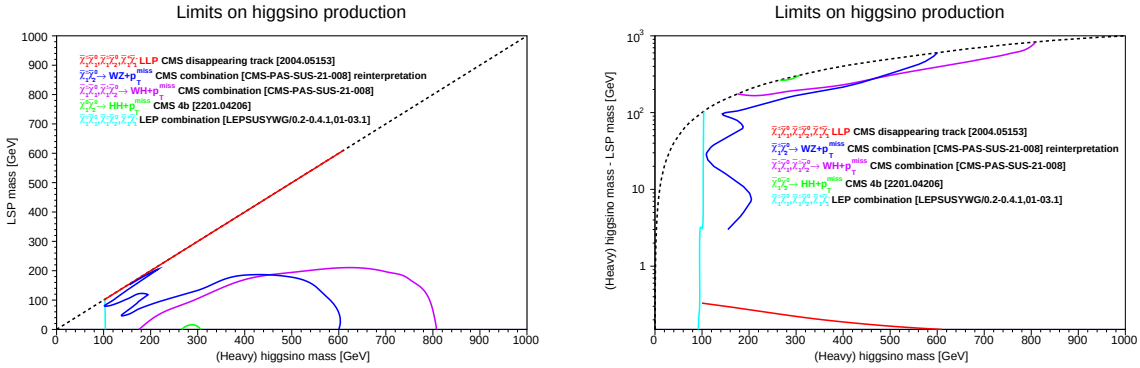

Figure 6.9: Excluded region for simplified models of higgsino production in the plane of higgsino mass and LSP mass (left) and in the plane of higgsino mass and higgsino-LSP mass difference (right) from a disappearing track analysis by the CMS collaboration [245] (red), a reinterpretation of the wino WZ + $p_{\mathrm{T}}^{\mathrm{miss}}$ model of the CMS electroweak SUSY combination [4] (blue), the WH + $p_{\mathrm{T}}^{\mathrm{miss}}$ model of the CMS electroweak SUSY combination (violet), the CMS HH(4b)+$p_{\mathrm{T}}^{\mathrm{miss}}$ analysis (green), and a combination of analyses targeting prompt decays and long-lived higgsinos by the LEP collaborations [407, 408] (cyan). The border of the physical region is outlined with a dotted line.

splitting is above around 1 GeV, analyses targeting a soft lepton signature such as the $2/3\ell$ soft analysis described in Section 5.2.2 can be used to exclude higgsino masses up to 100–200 GeV. There does exist a region with mass splitting around 0.3–3 GeV where the strongest exclusion is around 100 GeV from LEP experiments, though it has been suggested in Ref. [406] that a search for a soft displaced track signature with existing LHC data could be used to extend limits in this region. In the case the mass splitting between the produced higgsinos and the LSP is large, then searches such as the HH(4b)+$p_{\mathrm{T}}^{\mathrm{miss}}$ search and electroweak SUSY combination described in this analysis are sensitive to higgsino masses as large as 1025 GeV. To summarize, there exist mass values well within the natural range for which higgsinos are not excluded by current limits; however, no strong evidence for higgsino production has been observed so far.

There are also various constraints on supersymmetry from outside of collider experiments. The assumption that the LSP is the primary component of dark matter implies that the parameters of supersymmetry must be chosen to agree with the observed dark matter density and furthermore that the lack of evidence for dark matter in direct and indirect detection experiments can be used to put constraints on theories of supersymmetry. Dark matter direct detection experiments are sensitive to many neutralino LSP models, but the neutralino-nucleon cross section and thus constraints from these experiments are highly sensitive to the mixing between higgsinos and gauginos [277]. Indirect detection using astronomical measurements also provides complementary constraints that are dependent instead on dark matter annihilation cross sections and the spatial distribution of dark matter [409]. Electron electric dipole moment (EDM) experiments provide complementary bounds on supersymmetry that do not rely on the LSP being the primary component of dark matter. These experiments place limits on the size of the EDM of the electron, which is affected by one loop diagrams involving selectrons and multiloop diagrams with other supersymmetric particles. This translates into $O(10\ \text{TeV})$ limits on selectrons and $O(0.1\text{–}1\ \text{TeV})$ limits on other superpartners that are similar to those set by collider experiments, though the limits on charginos again have additional dependence on the mixing between the higgsinos and gauginos [410].

While TeV-scale supersymmetry capable of providing a dark matter candidate and gauge coupling unification may exist, the lack of evidence for supersymmetry in collider searches and other experiments currently seems to suggest that minimal theories of su-

persymmetry may not be able to provide a fully natural explanation of the observed Higgs potential. Making a more conclusive statement will, however, require more data and additional analysis.

6.3.2 Outlook on the hierarchy problem

The quadratic sensitivity of the SM Higgs potential quadratic coefficient μ^2 to parameters at high energy scales makes the discovery of a SM-like Higgs boson and nothing else at the LHC rather surprising. The higher the scale to which the standard model is a good effective theory, the more the theory must be fine-tuned. One would thus generally expect some physics beyond the standard model to appear near the TeV scale. One might also hope that these new laws of physics do not suffer from the same naturalness problem.

In this thesis, supersymmetry has been presented as one potential solution to this naturalness problem. However, evidence from experiments, such as the HH(4b)+$p_{\mathrm{T}}^{\mathrm{miss}}$ analysis described in this thesis, has not borne out the prediction of supersymmetric particles. It should be noted that supersymmetry is not the only solution to the naturalness problem. Symmetries other than supersymmetry can be used to protect μ^2 from large contributions. Such theories that don't feature strongly interacting new states like the top squarks of supersymmetry are referred to as "neutral naturalness," and are less strongly constrained by current data, with the strongest general constraints often coming from measurements of Higgs couplings [411]. An entirely different class of theories are

pseudo-nambu-goldstone composite Higgs theories [412–414], in which the Higgs potential is ultimately set by the new interaction responsible for creating the composite Higgs state. These theories generally predict modifications to the Higgs couplings as well as new particles at the TeV scale, and are also somewhat less constrained than supersymmetry. There also exist more exotic theories that can address the naturalness problem such as those involving extra dimensions near the TeV scale [415, 416], dynamic mechanisms that drive μ^2 to a small value [417], or reheating mechanisms that preferentially populate lower energy sectors in the case many sectors exist [418].

It is entirely possible that new physics capable of explaining the naturalness of μ^2 is around the corner or even buried in data that has already been collected. Only by exhaustively searching for such new physics can one be confident that there is no new physics near the TeV scale, a finding that would itself teach us much about nature. It is thus as important as ever that experimental collaborations continue to search for new laws of physics, whether through direct searches for new physics or through measurements of the known particles.

Bibliography

[1] **ATLAS** Collaboration, G. Aad *et. al.*, *Observation of a new particle in the search for the Standard Model Higgs boson with the ATLAS detector at the LHC*, *Phys. Lett. B* **716** (2012) 1–29, [arXiv:1207.7214].

[2] **CMS** Collaboration, S. Chatrchyan *et. al.*, *Observation of a New Boson at a Mass of 125 GeV with the CMS Experiment at the LHC*, *Phys. Lett. B* **716** (2012) 30–61, [arXiv:1207.7235].

[3] **CMS** Collaboration, A. Tumasyan *et. al.*, *Search for higgsinos decaying to two Higgs bosons and missing transverse momentum in proton-proton collisions at* $\sqrt{s}$ *= 13 TeV*, *JHEP* **05** (2022) 014, [arXiv:2201.04206].

[4] **CMS** Collaboration, *Combined search for electroweak production of winos, binos, higgsinos, and sleptons in proton-proton collisions at* $\sqrt{s}$ *= 13 TeV*, CMS Physics Analysis Summary CMS-PAS-SUS-21-008, 2023. `http://cds.cern.ch/record/2853345`.

[5] M. Srednicki, *Quantum field theory*. Cambridge University Press, 1, 2007.

[6] M. E. Peskin and D. V. Schroeder, *An Introduction to quantum field theory*. Addison-Wesley, Reading, USA, 1995.

[7] V. A. Kostelecky and N. Russell, *Data Tables for Lorentz and CPT Violation*, *Rev. Mod. Phys.* **83** (2011) 11–31, [arXiv:0801.0287].

[8] O. W. Greenberg, *Why is CPT fundamental?*, *Found. Phys.* **36** (2006) 1535–1553, [hep-ph/0309309].

[9] G. Lüders, *On the equivalence of invariance under time reversal and under particle-antiparticle conjugation for relativistic field theories*, *Dan. Mat. Fys. Medd.* **28** (1954) 1–17.

[10] W. Pauli, L. Rosenfelf, and V. Weisskopf, *Niels Bohr and the Development of Physics*. McGraw-Hill, New York, USA, 1955.

[11] R. Jost, *A remark on the C.T.P. theorem*, *Helv. Phys. Acta* **30** (1957) 409–416.

[12] H. Lehmann, K. Symanzik, and W. Zimmermann, *On the formulation of quantized field theories*, *Nuovo Cim.* **1** (1955) 205–225.

[13] K. G. Wilson and J. Kogut, *The renormalization group and the epsilon expansion*, *Physics Reports* **12** (1974), no. 2 75–199.

[14] F. Bloch and A. Nordsieck, *Note on the Radiation Field of the electron*, *Phys. Rev.* **52** (1937) 54–59.

[15] T. Kinoshita, *Mass singularities of Feynman amplitudes*, *J. Math. Phys.* **3** (1962) 650–677.

[16] T. D. Lee and M. Nauenberg, *Degenerate Systems and Mass Singularities*, *Phys. Rev.* **133** (1964) B1549–B1562.

[17] J. C. Collins, D. E. Soper, and G. F. Sterman, *Factorization of Hard Processes in QCD*, *Adv. Ser. Direct. High Energy Phys.* **5** (1989) 1–91, [hep-ph/0409313].

[18] J. D. Bjorken and E. A. Paschos, *Inelastic Electron Proton and gamma Proton Scattering, and the Structure of the Nucleon*, *Phys. Rev.* **185** (1969) 1975–1982.

[19] J. D. Bjorken, *Asymptotic Sum Rules at Infinite Momentum*, *Phys. Rev.* **179** (1969) 1547–1553.

[20] V. N. Gribov and L. N. Lipatov, *Deep inelastic e p scattering in perturbation theory*, *Sov. J. Nucl. Phys.* **15** (1972) 438–450.

[21] L. N. Lipatov, *The parton model and perturbation theory*, *Yad. Fiz.* **20** (1974) 181–198.

[22] G. Altarelli and G. Parisi, *Asymptotic Freedom in Parton Language*, *Nucl. Phys. B* **126** (1977) 298–318.

[23] Y. L. Dokshitzer, *Calculation of the Structure Functions for Deep Inelastic Scattering and e+ e- Annihilation by Perturbation Theory in Quantum Chromodynamics.*, *Sov. Phys. JETP* **46** (1977) 641–653.

[24] G. Luisoni and S. Marzani, *QCD resummation for hadronic final states*, *J. Phys. G* **42** (2015), no. 10 103101, [arXiv:1505.04084].

[25] E. Noether, *Invariant Variation Problems*, *Gott. Nachr.* **1918** (1918) 235–257, [physics/0503066].

[26] J. C. Ward, *An Identity in Quantum Electrodynamics*, *Phys. Rev.* **78** (1950) 182.

[27] Y. Takahashi, *On the generalized Ward identity*, *Nuovo Cim.* **6** (1957) 371.

[28] K. Raman and G. Sudarshan, *Current algebras and generalized Ward Takahashi identities*, *Phys. Lett.* **21** (1966) 450.

[29] S. R. Coleman and J. Mandula, *All Possible Symmetries of the S Matrix*, *Phys. Rev.* **159** (1967) 1251–1256.

[30] W. Pauli, *Relativistic Field Theories of Elementary Particles*, *Rev. Mod. Phys.* **13** (1941) 203–232.

[31] C.-N. Yang and R. L. Mills, *Conservation of Isotopic Spin and Isotopic Gauge Invariance*, *Phys. Rev.* **96** (1954) 191–195.

[32] L. Faddeev and V. Popov, *Feynman diagrams for the Yang-Mills field*, *Phys. Lett. B* **25** (1967) 29–30.

[33] Y. Nambu and G. Jona-Lasinio, *Dynamical Model of Elementary Particles Based on an Analogy with Superconductivity. 1.*, *Phys. Rev.* **122** (1961) 345–358.

[34] J. Goldstone, A. Salam, and S. Weinberg, *Broken Symmetries*, *Phys. Rev.* **127** (1962) 965–970.

[35] S. A. Bludman and A. Klein, *Broken Symmetries and Massless Particles*, *Phys. Rev.* **131** (1963) 2364–2372.

[36] F. Englert and R. Brout, *Broken Symmetry and the Mass of Gauge Vector Mesons*, *Phys. Rev. Lett.* **13** (1964) 321–323.

[37] P. W. Higgs, *Broken Symmetries and the Masses of Gauge Bosons*, *Phys. Rev. Lett.* **13** (1964) 508–509.

[38] G. S. Guralnik, C. R. Hagen, and T. W. B. Kibble, *Global Conservation Laws and Massless Particles*, *Phys. Rev. Lett.* **13** (1964) 585–587.

[39] S. Weinberg, *A Model of Leptons*, *Phys. Rev. Lett.* **19** (1967) 1264–1266.

[40] A. Salam, *Weak and Electromagnetic Interactions*, *Conf. Proc. C* **680519** (1968) 367–377.

[41] S. L. Glashow, *Partial Symmetries of Weak Interactions*, *Nucl. Phys.* **22** (1961) 579–588.

[42] M. Gell-Mann, *A Schematic Model of Baryons and Mesons*, *Phys. Lett.* **8** (1964) 214–215.

[43] G. Zweig, *An SU(3) model for strong interaction symmetry and its breaking. Version 1*, Tech. Rep. CERN-TH-401, 1, 1964.

[44] H. Fritzsch, M. Gell-Mann, and H. Leutwyler, *Advantages of the Color Octet Gluon Picture*, *Phys. Lett. B* **47** (1973) 365–368.

[45] N. Cabibbo, *Unitary Symmetry and Leptonic Decays*, *Phys. Rev. Lett.* **10** (1963) 531–533.

[46] M. Kobayashi and T. Maskawa, *CP Violation in the Renormalizable Theory of Weak Interaction*, *Prog. Theor. Phys.* **49** (1973) 652–657.

[47] **DES** Collaboration, T. M. C. Abbott *et. al.*, *Dark Energy Survey Year 3 results: Cosmological constraints from galaxy clustering and weak lensing*, *Phys. Rev. D* **105** (2022), no. 2 023520, [arXiv:2105.13549].

[48] **Particle Data Group** Collaboration, R. L. Workman, *Review of Particle Physics*, *PTEP* **2022** (2022) 083C01.

[49] J. F. Donoghue, *Introduction to the effective field theory description of gravity*, in *Advanced School on Effective Theories*, 6, 1995. gr-qc/9512024.

[50] S. M. Carroll, *Spacetime and Geometry*. Cambridge University Press, 7, 2019.

[51] R. Davis, Jr., D. S. Harmer, and K. C. Hoffman, *Search for neutrinos from the sun*, *Phys. Rev. Lett.* **20** (1968) 1205–1209.

[52] **Super-Kamiokande** Collaboration, Y. Fukuda *et. al.*, *Evidence for oscillation of atmospheric neutrinos*, *Phys. Rev. Lett.* **81** (1998) 1562–1567, [hep-ex/9807003].

[53] **SNO** Collaboration, Q. R. Ahmad *et. al.*, *Measurement of the rate of* $\nu_e + d \to p + p + e^-$ *interactions produced by* ^8B *solar neutrinos at the Sudbury Neutrino Observatory*, *Phys. Rev. Lett.* **87** (2001) 071301, [nucl-ex/0106015].

[54] P. Minkowski, $\mu \to e\gamma$ *at a Rate of One Out of* 10^9 *Muon Decays?*, *Phys. Lett. B* **67** (1977) 421–428.

[55] P. Ramond, *The Family Group in Grand Unified Theories*, in *International Symposium on Fundamentals of Quantum Theory and Quantum Field Theory*, 2, 1979. hep-ph/9809459.

[56] M. Gell-Mann, P. Ramond, and R. Slansky, *Complex Spinors and Unified Theories*, *Conf. Proc. C* **790927** (1979) 315–321, [arXiv:1306.4669].

[57] T. Yanagida, *Horizontal gauge symmetry and masses of neutrinos*, *Conf. Proc. C* **7902131** (1979) 95–99.

[58] R. N. Mohapatra and G. Senjanovic, *Neutrino Mass and Spontaneous Parity Nonconservation*, *Phys. Rev. Lett.* **44** (1980) 912.

[59] B. Pontecorvo, *Inverse beta processes and nonconservation of lepton charge*, *Zh. Eksp. Teor. Fiz.* **34** (1957) 247.

[60] Z. Maki, M. Nakagawa, and S. Sakata, *Remarks on the unified model of elementary particles*, *Prog. Theor. Phys.* **28** (1962) 870–880.

[61] G. Degrassi, S. Di Vita, J. Elias-Miro, J. R. Espinosa, G. F. Giudice, G. Isidori, and A. Strumia, *Higgs mass and vacuum stability in the Standard Model at NNLO*, *JHEP* **08** (2012) 098, [arXiv:1205.6497].

[62] J. C. Pati and A. Salam, *Unified Lepton-Hadron Symmetry and a Gauge Theory of the Basic Interactions*, *Phys. Rev. D* **8** (1973) 1240–1251.

[63] H. Georgi and S. L. Glashow, *Unity of All Elementary Particle Forces*, *Phys. Rev. Lett.* **32** (1974) 438–441.

[64] H. Georgi, *Particles and Fields*, in *Proceedings of the APS Div. of Particles and Fields* (C. Carlson, ed.), p. 575, 1975.

[65] H. Fritzsch and P. Minkowski, *Unified Interactions of Leptons and Hadrons*, *Annals Phys.* **93** (1975) 193–266.

[66] F. Gursey, P. Ramond, and P. Sikivie, *A Universal Gauge Theory Model Based on E6*, *Phys. Lett. B* **60** (1976) 177–180.

[67] U. Amaldi, W. de Boer, and H. Furstenau, *Comparison of grand unified theories with electroweak and strong coupling constants measured at LEP*, *Phys. Lett. B* **260** (1991) 447–455.

[68] **SNO+** Collaboration, M. Anderson *et. al.*, *Search for invisible modes of nucleon decay in water with the SNO+ detector*, *Phys. Rev. D* **99** (2019), no. 3 032008, [arXiv:1812.05552].

[69] **Super-Kamiokande** Collaboration, A. Takenaka *et. al.*, *Search for proton decay via $p \to e^+\pi^0$ and $p \to \mu^+\pi^0$ with an enlarged fiducial volume in Super-Kamiokande I-IV*, *Phys. Rev. D* **102** (2020), no. 11 112011, [arXiv:2010.16098].

[70] C. Abel *et. al.*, *Measurement of the Permanent Electric Dipole Moment of the Neutron*, *Phys. Rev. Lett.* **124** (2020), no. 8 081803, [arXiv:2001.11966].

[71] J. R. Ellis and M. K. Gaillard, *Strong and Weak CP Violation*, *Nucl. Phys. B* **150** (1979) 141–162.

[72] S. Weinberg, *The Cosmological Constant Problem*, *Rev. Mod. Phys.* **61** (1989) 1–23.

[73] S. Weinberg, *Implications of Dynamical Symmetry Breaking*, *Phys. Rev. D* **13** (1976) 974–996. [Addendum: Phys.Rev.D 19, 1277–1280 (1979)].

[74] E. Gildener, *Gauge Symmetry Hierarchies*, *Phys. Rev. D* **14** (1976) 1667.

[75] L. Susskind, *Dynamics of Spontaneous Symmetry Breaking in the Weinberg-Salam Theory*, *Phys. Rev. D* **20** (1979) 2619–2625.

[76] G. 't Hooft, C. Itzykson, A. Jaffe, H. Lehmann, P. K. Mitter, I. M. Singer, and R. Stora, eds., *Recent Developments in Gauge Theories. Proceedings, Nato Advanced Study Institute, Cargese, France, August 26 - September 8, 1979*, vol. 59, 1980.

[77] A. D. Sakharov, *Violation of CP Invariance, C asymmetry, and baryon asymmetry of the universe*, *Pisma Zh. Eksp. Teor. Fiz.* **5** (1967) 32–35.

[78] F. Zwicky, *Die Rotverschiebung von extragalaktischen Nebeln*, *Helv. Phys. Acta* **6** (1933) 110–127.

[79] V. C. Rubin and W. K. Ford, Jr., *Rotation of the Andromeda Nebula from a Spectroscopic Survey of Emission Regions*, *Astrophys. J.* **159** (1970) 379–403.

[80] D. Clowe, A. Gonzalez, and M. Markevitch, *Weak lensing mass reconstruction of the interacting cluster 1E0657-558: Direct evidence for the existence of dark matter*, *Astrophys. J.* **604** (2004) 596–603, [astro-ph/0312273].

[81] **WMAP** Collaboration, D. N. Spergel *et. al.*, *First year Wilkinson Microwave Anisotropy Probe (WMAP) observations: Determination of cosmological parameters*, *Astrophys. J. Suppl.* **148** (2003) 175–194, [astro-ph/0302209].

[82] **Planck** Collaboration, N. Aghanim *et. al.*, *Planck 2018 results. VI. Cosmological parameters*, *Astron. Astrophys.* **641** (2020) A6, [arXiv:1807.06209]. [Erratum: Astron.Astrophys. 652, C4 (2021)].

[83] F. Iocco, G. Mangano, G. Miele, O. Pisanti, and P. D. Serpico, *Primordial Nucleosynthesis: from precision cosmology to fundamental physics*, *Phys. Rept.* **472** (2009) 1–76, [arXiv:0809.0631].

[84] P. Villanueva-Domingo, O. Mena, and S. Palomares-Ruiz, *A brief review on primordial black holes as dark matter*, *Front. Astron. Space Sci.* **8** (2021) 87, [arXiv:2103.12087].

[85] R. Coy, T. Hambye, M. H. G. Tytgat, and L. Vanderheyden, *Domain of thermal dark matter candidates*, *Phys. Rev. D* **104** (2021), no. 5 055021, [arXiv:2105.01263].

[86] S. P. Martin, *A Supersymmetry primer*, *Adv. Ser. Direct. High Energy Phys.* **18** (1998) 1–98, [hep-ph/9709356].

[87] R. Haag, J. T. Lopuszanski, and M. Sohnius, *All Possible Generators of Supersymmetries of the s Matrix*, *Nucl. Phys. B* **88** (1975) 257.

[88] P. Fayet and J. Iliopoulos, *Spontaneously Broken Supergauge Symmetries and Goldstone Spinors*, *Phys. Lett. B* **51** (1974) 461–464.

[89] G. R. Farrar and P. Fayet, *Phenomenology of the Production, Decay, and Detection of New Hadronic States Associated with Supersymmetry*, *Phys. Lett. B* **76** (1978) 575–579.

[90] S. Weinberg, *Supersymmetry at Ordinary Energies. 1. Masses and Conservation Laws*, *Phys. Rev. D* **26** (1982) 287.

[91] N. Sakai and T. Yanagida, *Proton Decay in a Class of Supersymmetric Grand Unified Models*, *Nucl. Phys. B* **197** (1982) 533.

[92] R. Barbier *et. al.*, *R-parity violating supersymmetry*, *Phys. Rept.* **420** (2005) 1–202, [hep-ph/0406039].

[93] S. Dimopoulos and D. W. Sutter, *The Supersymmetric flavor problem*, *Nucl. Phys. B* **452** (1995) 496–512, [hep-ph/9504415].

[94] P. Nath and R. L. Arnowitt, *Generalized Supergauge Symmetry as a New Framework for Unified Gauge Theories*, *Phys. Lett. B* **56** (1975) 177–180.

[95] R. L. Arnowitt, P. Nath, and B. Zumino, *Superfield Densities and Action Principle in Curved Superspace*, *Phys. Lett. B* **56** (1975) 81–84.

[96] D. Z. Freedman, P. van Nieuwenhuizen, and S. Ferrara, *Progress Toward a Theory of Supergravity*, *Phys. Rev. D* **13** (1976) 3214–3218.

[97] S. Deser and B. Zumino, *Consistent Supergravity*, *Phys. Lett. B* **62** (1976) 335.

[98] D. Z. Freedman and P. van Nieuwenhuizen, *Properties of Supergravity Theory*, *Phys. Rev. D* **14** (1976) 912.

[99] E. Cremmer, B. Julia, J. Scherk, S. Ferrara, L. Girardello, and P. van Nieuwenhuizen, *Spontaneous Symmetry Breaking and Higgs Effect in Supergravity Without Cosmological Constant*, *Nucl. Phys. B* **147** (1979) 105.

[100] P. Fayet, *Supergauge Invariant Extension of the Higgs Mechanism and a Model for the electron and Its Neutrino*, *Nucl. Phys. B* **90** (1975) 104–124.

[101] L. O'Raifeartaigh, *Spontaneous Symmetry Breaking for Chiral Scalar Superfields*, *Nucl. Phys. B* **96** (1975) 331–352.

[102] K. A. Intriligator, N. Seiberg, and D. Shih, *Supersymmetry breaking, R-symmetry breaking and metastable vacua*, *JHEP* **07** (2007) 017, [hep-th/0703281].

[103] A. H. Chamseddine, R. L. Arnowitt, and P. Nath, *Locally Supersymmetric Grand Unification*, *Phys. Rev. Lett.* **49** (1982) 970.

[104] R. Barbieri, S. Ferrara, and C. A. Savoy, *Gauge Models with Spontaneously Broken Local Supersymmetry*, *Phys. Lett. B* **119** (1982) 343.

[105] L. E. Ibanez, *Locally Supersymmetric SU(5) Grand Unification*, *Phys. Lett. B* **118** (1982) 73–78.

[106] L. J. Hall, J. D. Lykken, and S. Weinberg, *Supergravity as the Messenger of Supersymmetry Breaking*, *Phys. Rev. D* **27** (1983) 2359–2378.

[107] N. Ohta, *GRAND UNIFIED THEORIES BASED ON LOCAL SUPERSYMMETRY*, *Prog. Theor. Phys.* **70** (1983) 542.

[108] J. R. Ellis, D. V. Nanopoulos, and K. Tamvakis, *Grand Unification in Simple Supergravity*, *Phys. Lett. B* **121** (1983) 123–129.

[109] L. Alvarez-Gaume, J. Polchinski, and M. B. Wise, *Minimal Low-Energy Supergravity*, *Nucl. Phys. B* **221** (1983) 495.

[110] M. Dine and W. Fischler, *A Phenomenological Model of Particle Physics Based on Supersymmetry*, *Phys. Lett. B* **110** (1982) 227–231.

[111] C. R. Nappi and B. A. Ovrut, *Supersymmetric Extension of the SU(3) x SU(2) x U(1) Model*, *Phys. Lett. B* **113** (1982) 175–179.

[112] L. Alvarez-Gaume, M. Claudson, and M. B. Wise, *Low-Energy Supersymmetry*, *Nucl. Phys. B* **207** (1982) 96.

[113] M. Dine and A. E. Nelson, *Dynamical supersymmetry breaking at low-energies*, *Phys. Rev. D* **48** (1993) 1277–1287, [hep-ph/9303230].

[114] M. Dine, A. E. Nelson, and Y. Shirman, *Low-energy dynamical supersymmetry breaking simplified*, *Phys. Rev. D* **51** (1995) 1362–1370, [hep-ph/9408384].

[115] M. Dine, A. E. Nelson, Y. Nir, and Y. Shirman, *New tools for low-energy dynamical supersymmetry breaking*, *Phys. Rev. D* **53** (1996) 2658–2669, [hep-ph/9507378].

[116] A. Brignole, L. E. Ibanez, and C. Munoz, *Towards a theory of soft terms for the supersymmetric Standard Model*, *Nucl. Phys. B* **422** (1994) 125–171, [hep-ph/9308271]. [Erratum: Nucl.Phys.B 436, 747–748 (1995)].

[117] S. Dimopoulos and S. Raby, *Supercolor*, *Nucl. Phys. B* **192** (1981) 353–368.

[118] E. Witten, *Dynamical Breaking of Supersymmetry*, *Nucl. Phys. B* **188** (1981) 513.

[119] M. Dine, W. Fischler, and M. Srednicki, *Supersymmetric Technicolor*, *Nucl. Phys. B* **189** (1981) 575–593.

[120] S. Dimopoulos and H. Georgi, *Softly Broken Supersymmetry and SU(5)*, *Nucl. Phys. B* **193** (1981) 150–162.

[121] N. Sakai, *Naturalness in Supersymmetric Guts*, *Z. Phys. C* **11** (1981) 153.

[122] R. K. Kaul and P. Majumdar, *Cancellation of Quadratically Divergent Mass Corrections in Globally Supersymmetric Spontaneously Broken Gauge Theories*, *Nucl. Phys. B* **199** (1982) 36.

[123] J. E. Kim and H. P. Nilles, *The mu Problem and the Strong CP Problem*, *Phys. Lett. B* **138** (1984) 150–154.

[124] G. F. Giudice and A. Masiero, *A Natural Solution to the mu Problem in Supergravity Theories*, *Phys. Lett. B* **206** (1988) 480–484.

[125] H. Goldberg, *Constraint on the Photino Mass from Cosmology*, *Phys. Rev. Lett.* **50** (1983) 1419. [Erratum: Phys.Rev.Lett. 103, 099905 (2009)].

[126] J. R. Ellis, J. S. Hagelin, D. V. Nanopoulos, K. A. Olive, and M. Srednicki, *Supersymmetric Relics from the Big Bang*, *Nucl. Phys. B* **238** (1984) 453–476.

[127] J. M. Cline, *Is electroweak baryogenesis dead?*, *Phil.Trans.Roy.Soc.Lond.A* **376** (2018) 2114, [arXiv:1704.08911].

[128] A. Strumia, *Naturalness of supersymmetric models*, in *34th Rencontres de Moriond: Electroweak Interactions and Unified Theories*, pp. 441–446, 1999. hep-ph/9904247.

[129] E. Bagnaschi, G. F. Giudice, P. Slavich, and A. Strumia, *Higgs Mass and Unnatural Supersymmetry*, *JHEP* **09** (2014) 092, [arXiv:1407.4081].

[130] D. O. Caldwell, R. M. Eisberg, D. M. Grumm, M. S. Witherell, B. Sadoulet, F. S. Goulding, and A. R. Smith, *Laboratory Limits on Galactic Cold Dark Matter*, *Phys. Rev. Lett.* **61** (1988) 510.

[131] M. Abdughani, L. Wu, and J. M. Yang, *Status and prospects of light bino-higgsino dark matter in natural SUSY*, *Eur. Phys. J. C* **78** (2018), no. 1 4, [arXiv:1705.09164].

[132] S. Dimopoulos and G. F. Giudice, *Naturalness constraints in supersymmetric theories with nonuniversal soft terms*, *Phys. Lett. B* **357** (1995) 573–578, [hep-ph/9507282].

[133] R. Barbieri and D. Pappadopulo, *S-particles at their naturalness limits*, *JHEP* **10** (2009) 061, [arXiv:0906.4546].

[134] M. Papucci, J. T. Ruderman, and A. Weiler, *Natural SUSY Endures*, *JHEP* **09** (2012) 035, [arXiv:1110.6926].

[135] **CMS** Collaboration, *Search for supersymmetry in proton-proton collisions at 13 TeV in final states with jets and missing transverse momentum*, *JHEP* **10** (2019) 244, [arXiv:1908.04722].

[136] **ATLAS** Collaboration, G. Aad *et. al.*, *Search for squarks and gluinos in final states with jets and missing transverse momentum using 139 fb^{-1} of $\sqrt{s}$ =13 TeV pp collision data with the ATLAS detector*, *JHEP* **02** (2021) 143, [arXiv:2010.14293].

[137] **LHC Higgs Cross Section Working Group** Collaboration, "SUSY Cross Sections." `https://twiki.cern.ch/twiki/bin/view/LHCPhysics/SUSYCrossSections`.

[138] **CMS** Collaboration, A. M. Sirunyan *et. al.*, *Measurements of production cross sections of the Higgs boson in the four-lepton final state in proton–proton collisions at $\sqrt{s} = 13$ TeV*, *Eur. Phys. J. C* **81** (2021), no. 6 488, [arXiv:2103.04956].

[139] **NNPDF** Collaboration, R. D. Ball *et. al.*, *Parton distributions from high-precision collider data*, *Eur. Phys. J. C* **77** (2017), no. 10 663, [arXiv:1706.00428].

[140] T. Lenzi, *Development and Study of Different Muon Track Reconstruction Algorithms for the Level-1 Trigger for the CMS Muon Upgrade with GEM Detectors*, Master's thesis, U. Brussels (main), 2013.

[141] C. W. Fabjan and F. Gianotti, *Calorimetry for particle physics*, *Rev. Mod. Phys.* **75** (2003) 1243–1286.

[142] L. D. Landau, *On the Energy Loss of Fast Particles by Ionisation*, *J. Phys. (USSR)* **8** (1944).

[143] P. V. Vavilov, *Ionization losses of high-energy heavy particles*, *Sov. Phys. JETP* **5** (1957) 749–751.

[144] T. S. Virdee, *Experimental techniques*, in *1998 European School of High-Energy Physics*, pp. 347–419, 1998.

[145] S. Menke. `https://www.mpp.mpg.de/~menke/elss/home.shtml`.

[146] T. Sjostrand, S. Mrenna, and P. Z. Skands, *PYTHIA 6.4 Physics and Manual*, *JHEP* **05** (2006) 026, [hep-ph/0603175].

[147] **CMS** Collaboration, S. Chatrchyan *et. al.*, *Shape, Transverse Size, and Charged Hadron Multiplicity of Jets in pp Collisions at 7 TeV*, *JHEP* **06** (2012) 160, [arXiv:1204.3170].

[148] **CMS** Collaboration, V. Khachatryan *et. al.*, *Jet energy scale and resolution in the CMS experiment in pp collisions at 8 TeV*, *JINST* **12** (2017), no. 02 P02014, [arXiv:1607.03663].

[149] **CMS** Collaboration, *Jet algorithms performance in 13 TeV data*, CMS Physics Analysis Summary CMS-PAS-JME-16-003, 2017.

[150] **CMS** Collaboration, A. M. Sirunyan *et. al.*, *Identification of heavy-flavour jets with the CMS detector in pp collisions at 13 TeV*, *JINST* **13** (2018), no. 05 P05011, [arXiv:1712.07158].

[151] LHC Higgs Cross Section Working Group, S. Dittmaier, C. Mariotti, G. Passarino, and R. Tanaka (Eds.), *Handbook of LHC Higgs Cross Sections: 1. Inclusive Observables*, *CERN-2011-002* (CERN, Geneva, 2011) [arXiv:1101.0593].

[152] **TOTEM** Collaboration, G. Antchev *et. al.*, *First measurement of elastic, inelastic and total cross-section at* $\sqrt{s} = 13$ *TeV by TOTEM and overview of cross-section data at LHC energies*, *Eur. Phys. J. C* **79** (2019), no. 2 103, [arXiv:1712.06153].

[153] J. Alwall *et. al.*, *Comparative study of various algorithms for the merging of parton showers and matrix elements in hadronic collisions*, *Eur. Phys. J. C* **53** (2008) 473–500, [arXiv:0706.2569].

[154] J. Alwall, R. Frederix, S. Frixione, V. Hirschi, F. Maltoni, O. Mattelaer, H. S. Shao, T. Stelzer, P. Torrielli, and M. Zaro, *The automated computation of tree-level and next-to-leading order differential cross sections, and their matching to parton shower simulations*, *JHEP* **07** (2014) 079, [arXiv:1405.0301].

[155] **NNPDF** Collaboration, R. D. Ball, V. Bertone, S. Carrazza, L. Del Debbio, S. Forte, A. Guffanti, N. P. Hartland, and J. Rojo, *Parton distributions with QED corrections*, *Nucl. Phys. B* **877** (2013) 290–320, [arXiv:1308.0598].

[156] **CMS** Collaboration. `https://twiki.cern.ch/twiki/bin/view/CMSPublic/PhysicsResultsCombined`.

[157] C. Bierlich *et. al.*, *A comprehensive guide to the physics and usage of PYTHIA 8.3*, *SciPost Phys. Codebases* **8** (2022) [arXiv:2203.11601].

[158] H. Wiedemann, *Particle Accelerator Physics*. Graduate Texts in Physics. Springer, Berlin, Germany, 2015.

[159] *LHC Machine*, *JINST* **3** (2008) S08001.

[160] S. van der Meer, *Calibration of the Effective Beam Height in the ISR*, Tech. Rep. CERN-ISR-PO-68-31, 6, 1968.

[161] **International Muon Collider** Collaboration, D. Schulte, *The Muon Collider*, *JACoW* **IPAC2022** (2022) TUIZSP2.

[162] R. Steerenberg *et. al.*, *Operation and performance of the CERN Large Hadron Collider during proton Run 2*, in *10th International Particle Accelerator Conference*, p. MOPMP031, 2019.

[163] **CMS** Collaboration, A. M. Sirunyan *et. al.*, *Performance of the CMS Level-1 trigger in proton-proton collisions at* $\sqrt{s} = 13$ *TeV*, *JINST* **15** (2020), no. 10 P10017, [arXiv:2006.10165].

[164] `https://lhc-commissioning.web.cern.ch/schedule/LHC-long-term.htm`.

[165] **CMS** Collaboration, "Public CMS Luminosity Information." `https://twiki.cern.ch/twiki/bin/view/CMSPublic/LumiPublicResults`.

[166] **CMS** Collaboration, S. Chatrchyan *et. al.*, *The CMS Experiment at the CERN LHC*, *JINST* **3** (2008) S08004.

[167] J. E. Augustin *et. al.*, *Measurement of e+ e- —> e+ e- and e+ e- —> mu+ mu- at SPEAR*, *Phys. Rev. Lett.* **34** (1975) 233.

[168] **CMS Tracker Group** Collaboration, W. Adam *et. al.*, *The CMS Phase-1 Pixel Detector Upgrade*, *JINST* **16** (2021), no. 02 P02027, [arXiv:2012.14304].

[169] **CMS** Collaboration, A. M. Sirunyan *et. al.*, *Particle-flow reconstruction and global event description with the CMS detector*, *JINST* **12** (2017), no. 10 P10003, [arXiv:1706.04965].

[170] **CMS** Collaboration, A. Tumasyan *et. al.*, *The Phase-2 Upgrade of the CMS Tracker*, CMS Technical Design Report CERN-LHCC-2017-009, CMS-TDR-014, CERN-LHCC-2017-009, CMS-TDR-014, 6, 2017.

[171] **CMS** Collaboration, J. N. Butler and T. Tabarelli de Fatis, *A MIP Timing Detector for the CMS Phase-2 Upgrade*, CMS Technical Design Report CERN-LHCC-2019-003, CMS-TDR-020, 2019.

[172] **CMS** Collaboration, A. M. Sirunyan *et. al.*, *Electron and photon reconstruction and identification with the CMS experiment at the CERN LHC*, *JINST* **16** (2021), no. 05 P05014, [arXiv:2012.06888].

[173] **CMS** Collaboration, *The CMS hadron calorimeter project: Technical Design Report*, CMS Technical Design Report CERN-LHCC-97-031, CMS-TDR-2, CERN-LHCC-97-031, CMS-TDR-2, 1997.

[174] **CMS** Collaboration, *CMS Technical Design Report for the Phase 1 Upgrade of the Hadron Calorimeter*, CMS Technical Design Report CERN-LHCC-2012-015, CMS-TDR-010, 9, 2012.

[175] V. D. Elvira, *Measurement of the Pion Energy Response and Resolution in the CMS HCAL Test Beam 2002 Experiment*, Tech. Rep. CMS-NOTE-2004-020, CERN-CMS-NOTE-2004-020, 9, 2004.

[176] **CMS** Collaboration, *CASTOR very forward calorimeter performance in 2013 data in pPb and pp collisions*, CMS Physics Analysis Summary CMS-DP-2013-035 ; CERN-CMS-DP-2013-035, Nov, 2013.

[177] **CMS** Collaboration, V. Khachatryan *et. al.*, *The very forward CASTOR calorimeter of the CMS experiment*, *JINST* **16** (2021), no. 02 P02010, [arXiv:2011.01185].

[178] **CMS, TOTEM** Collaboration, M. Albrow *et. al.*, *CMS-TOTEM Precision Proton Spectrometer*, Technical Design Report CERN-LHCC-2014-021, TOTEM-TDR-003, CMS-TDR-13, 9, 2014.

[179] **CMS** Collaboration, *The CMS Precision Proton Spectrometer at the HL-LHC – Expression of Interest*, arXiv:2103.02752.

[180] **CMS** Collaboration, *The Phase-2 Upgrade of the CMS Barrel Calorimeters*, CMS Technical Design Report CERN-LHCC-2017-011, CMS-TDR-015, 9, 2017.

[181] **CMS** Collaboration, *The Phase-2 Upgrade of the CMS Endcap Calorimeter*, CMS Technical Design Report CERN-LHCC-2017-023, CMS-TDR-019, 2017.

[182] **CMS** Collaboration, A. M. Sirunyan *et. al.*, *Performance of the CMS muon detector and muon reconstruction with proton-proton collisions at* $\sqrt{s} = 13$ *TeV*, *JINST* **13** (2018), no. 06 P06015, [arXiv:1804.04528].

[183] **CMS** Collaboration, *Technical proposal for the upgrade of the CMS detector through 2020*, CMS Physics Analysis Summary CERN-LHCC-2011-006, CMS-UG-TP-1, LHCC-P-004, Jun, 2011.

[184] **CMS** Collaboration, A. Triossi *et. al.*, *The CMS Barrel Muon trigger upgrade*, *JINST* **12** (2017), no. 01 C01095.

[185] **CMS** Collaboration, A. Navarro Tobar, A. Triossi, I. Redondo-Fernández, D. Francia-Ferrero, C. F. Bedoya, J. J. Sastre-Álvaro, J. M. Cela Ruiz, D. D. Redondo-Ferrero, J. Fernandez Menendez, and J. F. de Troconiz, *CMS Drift Tubes Readout Phase 1 Upgrade*, *PoS* **TWEPP2018** (2019) 039.

[186] **CMS** Collaboration, S. Chatrchyan *et. al.*, *The Performance of the CMS Muon Detector in Proton-Proton Collisions at $\sqrt{s}$ = 7 TeV at the LHC*, *JINST* **8** (2013) P11002, [arXiv:1306.6905].

[187] **CMS** Collaboration, *The Phase-2 Upgrade of the CMS Muon Detectors*, CMS Technical Design Report CERN-LHCC-2017-012, CMS-TDR-016, 9, 2017.

[188] **CMS** Collaboration, *CMS Technical Design Report for the Level-1 Trigger Upgrade*, CMS Technical Design Report CERN-LHCC-2013-011, CMS-TDR-12, CMS-TDR-012, 6, 2013.

[189] T. Bawej *et. al.*, *The New CMS DAQ System for Run-2 of the LHC*, *IEEE Trans.Nucl.Sci.* **62** (2014), no. 3 1099–1103.

[190] **CMS** Collaboration, A. M. Sirunyan *et. al.*, *Performance of the CMS muon trigger system in proton-proton collisions at $\sqrt{s}$ = 13 TeV*, *JINST* **16** (2021) P07001, [arXiv:2102.04790].

[191] **CMS** Collaboration, A. M. Sirunyan *et. al.*, *Performance of missing transverse momentum reconstruction in proton-proton collisions at $\sqrt{s}$ = 13 TeV using the CMS detector*, *JINST* **14** (2019), no. 07 P07004, [arXiv:1903.06078].

[192] **CMS** Collaboration, *Data Parking and Data Scouting at the CMS Experiment*, CMS Detector Performance Summary CMS-DP-2012-022, CERN-CMS-DP-2012-022, 9, 2012.

[193] **CMS** Collaboration, R. Bainbridge, *Recording and reconstructing 10 billion unbiased b hadron decays in CMS*, *EPJ Web Conf.* **245** (2020) 01025.

[194] **CMS** Collaboration, *The Phase-2 Upgrade of the CMS Data Acquisition and High Level Trigger*, CMS Technical Design Report CERN-LHCC-2021-007 ; CMS-TDR-022, 3, 2021.

[195] J. Hegeman *et. al.*, *The CMS Timing and Control Distribution System*, in *2015 IEEE Nuclear Science Symposium and Medical Imaging Conference*, p. 7581984, 2016.

[196] **CMS** Collaboration, A. A. Zagozdzinska *et. al.*, *New Fast Beam Conditions Monitoring (BCM1F) system for CMS*, *JINST* **11** (2016), no. 01 C01088.

[197] **CMS** Collaboration, *CMS luminosity measurement for the 2018 data-taking period at* $\sqrt{s} = 13$ TeV, CMS Physics Analysis Summary CMS-PAS-LUM-18-002, 2019.

[198] **CMS** Collaboration, P. Lujan, *Performance of the Pixel Luminosity Telescope for Luminosity Measurement at CMS during Run2*, *PoS* **EPS-HEP2017** (2017) 504.

[199] **CMS** Collaboration, *The Phase-2 Upgrade of the CMS Beam Radiation Instrumentation and Luminosity Detectors*, CMS Technical Design Report CERN-LHCC-2021-008 ; CMS-TDR-023, 3, 2021.

[200] R. Brun and F. Rademakers, *ROOT: An object oriented data analysis framework*, *Nucl. Instrum. Meth. A* **389** (1997) 81–86.

[201] S. Gasperini, S. Rossi Tisbeni, D. Bonacorsi, and D. Lange, *Exploiting Big Data solutions for CMS computing operations analytics*, *PoS* **ISGC2022** (2022) 006.

[202] **CMS** Collaboration, G. Petrucciani, A. Rizzi, and C. Vuosalo, *Mini-AOD: A New Analysis Data Format for CMS*, *J. Phys. Conf. Ser.* **664** (2015), no. 7 7, [arXiv:1702.04685].

[203] **CMS** Collaboration, A. Rizzi, G. Petrucciani, and M. Peruzzi, *A further reduction in CMS event data for analysis: the NANOAOD format*, *EPJ Web Conf.* **214** (2019) 06021.

[204] **CMS** Collaboration, K. Ehatäht, *NANOAOD: a new compact event data format in CMS*, *EPJ Web Conf.* **245** (2020) 06002.

[205] **GEANT4** Collaboration, S. Agostinelli *et. al.*, *GEANT4–a simulation toolkit*, *Nucl. Instrum. Meth. A* **506** (2003) 250–303.

[206] **CMS** Collaboration, D. J. Lange, M. Hildreth, V. N. Ivantchenko, and I. Osborne, *Upgrades for the CMS simulation*, *J. Phys. Conf. Ser.* **608** (2015), no. 1 012056.

[207] **CMS** Collaboration, S. Abdullin, P. Azzi, F. Beaudette, P. Janot, and A. Perrotta, *The fast simulation of the CMS detector at LHC*, *J. Phys. Conf. Ser.* **331** (2011) 032049.

[208] A. Giammanco, *The Fast Simulation of the CMS Experiment*, *J. Phys. Conf. Ser.* **513** (2014) 022012.

[209] **CMS** Collaboration, A. M. Sirunyan *et. al.*, *Reconstruction of signal amplitudes in the CMS electromagnetic calorimeter in the presence of overlapping proton-proton interactions*, *JINST* **15** (2020), no. 10 P10002, [arXiv:2006.14359].

[210] **CMS** Collaboration, *Electromagnetic calorimeter calibration with 7 TeV data*, .

[211] **CMS** Collaboration, S. Chatrchyan *et. al.*, *Time Reconstruction and Performance of the CMS Electromagnetic Calorimeter*, *JINST* **5** (2010) T03011, [arXiv:0911.4044].

[212] **CMS** Collaboration, D. A. Petyt, *Anomalous APD signals in the CMS Electromagnetic Calorimeter*, *Nucl. Instrum. Meth. A* **695** (2012) 293–295.

[213] **CMS** Collaboration, S. Chatrchyan *et. al.*, *Energy Calibration and Resolution of the CMS Electromagnetic Calorimeter in pp Collisions at* $\sqrt{s} = 7$ *TeV*, *JINST* **8** (2013) P09009, [arXiv:1306.2016].

[214] **CMS** Collaboration, A. M. Sirunyan *et. al.*, *Calibration of the CMS hadron calorimeters using proton-proton collision data at* $\sqrt{s} = 13$ *TeV*, *JINST* **15** (2020), no. 05 P05002, [arXiv:1910.00079].

[215] **CMS HCAL** Collaboration, J. Lawhorn, *New method of out-of-time energy subtraction for the CMS hadronic calorimeter*, *J. Phys. Conf. Ser.* **1162** (2019), no. 1 012036.

[216] **CMS** Collaboration, S. Chatrchyan *et. al.*, *Description and performance of track and primary-vertex reconstruction with the CMS tracker*, *JINST* **9** (2014), no. 10 P10009, [arXiv:1405.6569].

[217] **CMS** Collaboration, G. L. Bayatian *et. al.*, *CMS Physics: Technical Design Report Volume 1: Detector Performance and Software*, CMS Technical Design Report CERN-LHCC-2006-001, CMS-TDR-8-1, CERN-LHCC-2006-001, CMS-TDR-8-1, 2006.

[218] T. Speer, W. Adam, R. Fruhwirth, A. Strandlie, T. Todorov, and M. Winkler, *Track reconstruction in the CMS tracker*, *Nucl. Instrum. Meth. A* **559** (2006) 143–147.

[219] **CMS** Collaboration, *2017 tracking performance plots*, CMS Detector Performance Summary CMS-DP-2017-015, CERN-CMS-DP-2017-015, Apr, 2017.

[220] W. Adam, R. Fruhwirth, A. Strandlie, and T. Todorov, *Reconstruction of electrons with the Gaussian sum filter in the CMS tracker at LHC*, *eConf* **C0303241** (2003) TULT009, [physics/0306087].

[221] **CMS** Collaboration, A. M. Sirunyan *et. al.*, *Performance of the reconstruction and identification of high-momentum muons in proton-proton collisions at* $\sqrt{s} =$ *13 TeV*, *JINST* **15** (2020), no. 02 P02027, [arXiv:1912.03516].

[222] M. Cacciari, G. P. Salam, and G. Soyez, *The anti-*k_{t} *jet clustering algorithm*, *JHEP* **04** (2008) 063, [arXiv:0802.1189].

[223] M. Cacciari, G. P. Salam, and G. Soyez, *FastJet User Manual*, *Eur. Phys. J.* **C72** (2012) 1896, [arXiv:1111.6097].

[224] M. Cacciari and G. P. Salam, *Pileup subtraction using jet areas*, *Phys. Lett. B* **659** (2008) 119, [arXiv:0707.1378].

[225] D. Bertolini, P. Harris, M. Low, and N. Tran, *Pileup Per Particle Identification*, *JHEP* **10** (2014) 059, [arXiv:1407.6013].

[226] **CMS** Collaboration, A. M. Sirunyan *et. al.*, *Pileup mitigation at CMS in 13 TeV data*, *JINST* **15** (2020), no. 09 P09018, [arXiv:2003.00503].

[227] **CMS** Collaboration, *Jet energy scale and resolution performance with 13 TeV data collected by CMS in 2016-2018*, CMS Detector Performance Summary CMS-DP-2020-019, CERN-CMS-DP-2020-019, Apr, 2020.

[228] M. A. Thomson, *Progress with particle flow calorimetry*, *eConf* **C0705302** (2007) SIM16, [arXiv:0709.1360].

[229] **CMS** Collaboration, *Jet energy scale and resolution measurement with Run 2 Legacy Data Collected by CMS at 13 TeV*, CMS Detector Performance Summary CMS-DP-2021-033 ; CERN-CMS-DP-2021-033, Sep, 2021.

[230] M. Dasgupta, A. Fregoso, S. Marzani, and G. P. Salam, *Towards an understanding of jet substructure*, *JHEP* **09** (2013) 029, [arXiv:1307.0007].

[231] S. Marzani, L. Schunk, and G. Soyez, *A study of jet mass distributions with grooming*, *JHEP* **07** (2017) 132, [arXiv:1704.02210].

[232] A. J. Larkoski, S. Marzani, G. Soyez, and J. Thaler, *Soft Drop*, *JHEP* **05** (2014) 146, [arXiv:1402.2657].

[233] **CMS** Collaboration, *Performance of b tagging algorithms in proton-proton collisions at 13 TeV with Phase 1 CMS detector*, CMS Detector Performance Summary CMS-DP-2018-033, CERN-CMS-DP-2018-033, Jun, 2018.

[234] J. Thaler and K. Van Tilburg, *Identifying Boosted Objects with N-subjettiness*, *JHEP* **03** (2011) 015, [arXiv:1011.2268].

[235] **CMS** Collaboration, *Performance of deep tagging algorithms for boosted double quark jet topology in proton-proton collisions at 13 TeV with the phase-0 cms detector*, CMS Detector Performance Summary CMS-DP-2018-046, CERN-CMS-DP-2018-046, Jul, 2018.

[236] **CMS** Collaboration, A. M. Sirunyan *et. al.*, *Performance of reconstruction and identification of τ leptons decaying to hadrons and ν_τ in pp collisions at $\sqrt{s} = 13$ TeV*, *JINST* **13** (2018), no. 10 P10005, [arXiv:1809.02816].

[237] **ATLAS** Collaboration, G. Aad *et. al.*, *Search for anomaly-mediated supersymmetry breaking with the ATLAS detector based on a disappearing-track signature in pp collisions at* $\sqrt{s} = 7$ *TeV*, *Eur. Phys. J. C* **72** (2012) 1993, [arXiv:1202.4847].

[238] **ATLAS** Collaboration, G. Aad *et. al.*, *Search for direct chargino production in anomaly-mediated supersymmetry breaking models based on a disappearing-track signature in pp collisions at* $\sqrt{s} = 7$ *TeV with the ATLAS detector*, *JHEP* **01** (2013) 131, [arXiv:1210.2852].

[239] **ATLAS** Collaboration, G. Aad *et. al.*, *Search for charginos nearly mass degenerate with the lightest neutralino based on a disappearing-track signature in pp collisions at* $\sqrt{s}$*=8 TeV with the ATLAS detector*, *Phys. Rev. D* **88** (2013), no. 11 112006, [arXiv:1310.3675].

[240] **ATLAS** Collaboration, M. Aaboud *et. al.*, *Search for long-lived charginos based on a disappearing-track signature in pp collisions at* $\sqrt{s} = 13$ *TeV with the ATLAS detector*, *JHEP* **06** (2018) 022, [arXiv:1712.02118].

[241] **ATLAS** Collaboration, G. Aad *et. al.*, *Search for long-lived charginos based on a disappearing-track signature using 136* fb^{-1} *of pp collisions at* $\sqrt{s}$ *= 13 TeV with the ATLAS detector*, *Eur. Phys. J. C* **82** (2022), no. 7 606, [arXiv:2201.02472].

[242] **CMS** Collaboration, V. Khachatryan *et. al.*, *Search for disappearing tracks in proton-proton collisions at* $\sqrt{s} = 8$ *TeV*, *JHEP* **01** (2015) 096, [arXiv:1411.6006].

[243] **CMS** Collaboration, A. M. Sirunyan *et. al.*, *Search for disappearing tracks as a signature of new long-lived particles in proton-proton collisions at* $\sqrt{s}$ *= 13 TeV*, *JHEP* **08** (2018) 016, [arXiv:1804.07321].

[244] **CMS** Collaboration, A. M. Sirunyan *et. al.*, *Searches for physics beyond the standard model with the* M_{T2} *variable in hadronic final states with and without disappearing tracks in proton-proton collisions at* $\sqrt{s}$ *= 13 TeV*, *Eur. Phys. J. C* **80** (2020), no. 1 3, [arXiv:1909.03460].

[245] **CMS** Collaboration, A. M. Sirunyan *et. al.*, *Search for disappearing tracks in proton-proton collisions at* $\sqrt{s}$ *= 13 TeV*, *Phys. Lett. B* **806** (2020) 135502, [arXiv:2004.05153].

[246] **CMS** Collaboration, *Search for supersymmetry in final states with disappearing tracks in proton-proton collisions at* 13 TeV, CMS Physics Analysis Summary CMS-PAS-SUS-21-006, 2023.

[247] **ATLAS** Collaboration, G. Aad *et. al.*, *Search for heavy long-lived charged particles with the ATLAS detector in pp collisions at* $\sqrt{s}$ *= 7 TeV*, *Phys. Lett. B* **703** (2011) 428–446, [arXiv:1106.4495].

[248] **ATLAS** Collaboration, G. Aad *et. al.*, *Searches for heavy long-lived charged particles with the ATLAS detector in proton-proton collisions at $\sqrt{s} = 8$ TeV*, *JHEP* **01** (2015) 068, [arXiv:1411.6795].

[249] **ATLAS** Collaboration, G. Aad *et. al.*, *Search for metastable heavy charged particles with large ionisation energy loss in pp collisions at $\sqrt{s} = 8$ TeV using the ATLAS experiment*, *Eur. Phys. J. C* **75** (2015), no. 9 407, [arXiv:1506.05332].

[250] **ATLAS** Collaboration, M. Aaboud *et. al.*, *Search for metastable heavy charged particles with large ionization energy loss in pp collisions at $\sqrt{s} = 13$ TeV using the ATLAS experiment*, *Phys. Rev. D* **93** (2016), no. 11 112015, [arXiv:1604.04520].

[251] **ATLAS** Collaboration, M. Aaboud *et. al.*, *Search for heavy charged long-lived particles in proton-proton collisions at $\sqrt{s} = 13$ TeV using an ionisation measurement with the ATLAS detector*, *Phys. Lett. B* **788** (2019) 96–116, [arXiv:1808.04095].

[252] **ATLAS** Collaboration, *Search for heavy, long-lived, charged particles with large ionisation energy loss in pp collisions at $\sqrt{s} = 13$ TeV using the ATLAS experiment and the full Run 2 dataset*, arXiv:2205.06013.

[253] **CMS** Collaboration, S. Chatrchyan *et. al.*, *Searches for Long-Lived Charged Particles in pp Collisions at $\sqrt{s}$=7 and 8 TeV*, *JHEP* **07** (2013) 122, [arXiv:1305.0491]. [Erratum: JHEP 11, 149 (2022)].

[254] **CMS** Collaboration, V. Khachatryan *et. al.*, *Search for Heavy Stable Charged Particles in pp collisions at $\sqrt{s} = 7$ TeV*, *JHEP* **03** (2011) 024, [arXiv:1101.1645].

[255] **CMS** Collaboration, V. Khachatryan *et. al.*, *Search for long-lived charged particles in proton-proton collisions at $\sqrt{s} = 13$ TeV*, *Phys. Rev. D* **94** (2016), no. 11 112004, [arXiv:1609.08382].

[256] **ATLAS** Collaboration, G. Aad *et. al.*, *Search for new phenomena with the monojet and missing transverse momentum signature using the ATLAS detector in $\sqrt{s} = 7$ TeV proton-proton collisions*, *Phys. Lett. B* **705** (2011) 294–312, [arXiv:1106.5327].

[257] **ATLAS** Collaboration, G. Aad *et. al.*, *Search for dark matter candidates and large extra dimensions in events with a jet and missing transverse momentum with the ATLAS detector*, *JHEP* **04** (2013) 075, [arXiv:1210.4491].

[258] **ATLAS** Collaboration, G. Aad *et. al.*, *Search for dark matter in events with a hadronically decaying W or Z boson and missing transverse momentum in pp collisions at $\sqrt{s} = 8$ TeV with the ATLAS detector*, *Phys. Rev. Lett.* **112** (2014), no. 4 041802, [arXiv:1309.4017].

[259] **ATLAS** Collaboration, G. Aad *et. al.*, *Search for new phenomena in final states with an energetic jet and large missing transverse momentum in pp collisions at $\sqrt{s}$ =8 TeV with the ATLAS detector*, *Eur. Phys. J. C* **75** (2015), no. 7 299, [arXiv:1502.01518]. [Erratum: Eur.Phys.J.C 75, 408 (2015)].

[260] **ATLAS** Collaboration, M. Aaboud *et. al.*, *Search for new phenomena in final states with an energetic jet and large missing transverse momentum in pp collisions at $\sqrt{s} = 13$ TeV using the ATLAS detector*, *Phys. Rev. D* **94** (2016), no. 3 032005, [arXiv:1604.07773].

[261] **ATLAS** Collaboration, M. Aaboud *et. al.*, *Search for dark matter produced in association with a hadronically decaying vector boson in pp collisions at $\sqrt{s}$ = 13 TeV with the ATLAS detector*, *Phys. Lett. B* **763** (2016) 251–268, [arXiv:1608.02372].

[262] **ATLAS** Collaboration, M. Aaboud *et. al.*, *Search for dark matter and other new phenomena in events with an energetic jet and large missing transverse momentum using the ATLAS detector*, *JHEP* **01** (2018) 126, [arXiv:1711.03301].

[263] **ATLAS** Collaboration, M. Aaboud *et. al.*, *Search for dark matter in events with a hadronically decaying vector boson and missing transverse momentum in pp collisions at $\sqrt{s} = 13$ TeV with the ATLAS detector*, *JHEP* **10** (2018) 180, [arXiv:1807.11471].

[264] **ATLAS** Collaboration, G. Aad *et. al.*, *Search for new phenomena in events with an energetic jet and missing transverse momentum in pp collisions at $\sqrt{s}$ =13 TeV with the ATLAS detector*, *Phys. Rev. D* **103** (2021), no. 11 112006, [arXiv:2102.10874].

[265] **CMS** Collaboration, S. Chatrchyan *et. al.*, *Search for Dark Matter and Large Extra Dimensions in Monojet Events in pp Collisions at $\sqrt{s} = 7$ TeV*, *JHEP* **09** (2012) 094, [arXiv:1206.5663].

[266] **CMS** Collaboration, V. Khachatryan *et. al.*, *Search for dark matter, extra dimensions, and unparticles in monojet events in proton-proton collisions at $\sqrt{s} = 8$ TeV*, *Eur. Phys. J. C* **75** (2015), no. 5 235, [arXiv:1408.3583].

[267] **CMS** Collaboration, V. Khachatryan *et. al.*, *Search for dark matter in proton-proton collisions at 8 TeV with missing transverse momentum and vector boson tagged jets*, *JHEP* **12** (2016) 083, [arXiv:1607.05764]. [Erratum: JHEP 08, 035 (2017)].

[268] **CMS** Collaboration, A. M. Sirunyan *et. al.*, *Search for dark matter produced with an energetic jet or a hadronically decaying W or Z boson at $\sqrt{s} = 13$ TeV*, *JHEP* **07** (2017) 014, [arXiv:1703.01651].

[269] **CMS** Collaboration, A. M. Sirunyan *et. al.*, *Search for new physics in final states with an energetic jet or a hadronically decaying W or Z boson and transverse momentum imbalance at $\sqrt{s} = 13$ TeV*, *Phys. Rev. D* **97** (2018), no. 9 092005, [arXiv:1712.02345].

[270] **CMS** Collaboration, A. Tumasyan *et. al.*, *Search for new particles in events with energetic jets and large missing transverse momentum in proton-proton collisions at $\sqrt{s}$ = 13 TeV*, *JHEP* **11** (2021) 153, [arXiv:2107.13021].

[271] **ATLAS** Collaboration, G. Aad *et. al.*, *Search for the electroweak production of supersymmetric particles in $\sqrt{s}$=8 TeV pp collisions with the ATLAS detector*, *Phys. Rev. D* **93** (2016), no. 5 052002, [arXiv:1509.07152].

[272] **ATLAS** Collaboration, M. Aaboud *et. al.*, *Search for electroweak production of supersymmetric states in scenarios with compressed mass spectra at $\sqrt{s} = 13$ TeV with the ATLAS detector*, *Phys. Rev. D* **97** (2018), no. 5 052010, [arXiv:1712.08119].

[273] **ATLAS** Collaboration, G. Aad *et. al.*, *Searches for electroweak production of supersymmetric particles with compressed mass spectra in $\sqrt{s}$ = 13 TeV pp collisions with the ATLAS detector*, *Phys. Rev. D* **101** (2020), no. 5 052005, [arXiv:1911.12606].

[274] **CMS** Collaboration, V. Khachatryan *et. al.*, *Search for supersymmetry in events with soft leptons, low jet multiplicity, and missing transverse energy in proton–proton collisions at $\sqrt{s}$=8 TeV*, *Phys. Lett. B* **759** (2016) 9–35, [arXiv:1512.08002].

[275] **CMS** Collaboration, A. M. Sirunyan *et. al.*, *Search for new physics in events with two soft oppositely charged leptons and missing transverse momentum in proton-proton collisions at $\sqrt{s}$ = 13 TeV*, *Phys. Lett. B* **782** (2018) 440–467, [arXiv:1801.01846].

[276] **CMS** Collaboration, A. Tumasyan *et. al.*, *Search for supersymmetry in final states with two or three soft leptons and missing transverse momentum in proton-proton collisions at $\sqrt{s}$ = 13 TeV*, *JHEP* **04** (2022) 091, [arXiv:2111.06296].

[277] J. Hisano, K. Ishiwata, N. Nagata, and T. Takesako, *Direct Detection of Electroweak-Interacting Dark Matter*, *JHEP* **07** (2011) 005, [arXiv:1104.0228].

[278] **ATLAS** Collaboration, G. Aad *et. al.*, *Searches for supersymmetry with the ATLAS detector using final states with two leptons and missing transverse momentum in $\sqrt{s} = 7$ TeV proton-proton collisions*, *Phys. Lett. B* **709** (2012) 137–157, [arXiv:1110.6189].

[279] **ATLAS** Collaboration, G. Aad *et. al.*, *Search for direct production of charginos and neutralinos in events with three leptons and missing transverse momentum in $\sqrt{s} = 7$ TeV pp collisions with the ATLAS detector*, *Phys. Lett. B* **718** (2013) 841–859, [arXiv:1208.3144].

[280] **ATLAS** Collaboration, G. Aad *et. al.*, *Search for supersymmetry in events with three leptons and missing transverse momentum in $\sqrt{s} = 7$ TeV pp collisions with the ATLAS detector*, *Phys. Rev. Lett.* **108** (2012) 261804, [arXiv:1204.5638].

[281] **ATLAS** Collaboration, G. Aad *et. al.*, *Search for supersymmetry in events with photons, bottom quarks, and missing transverse momentum in proton–proton collisions at a centre-of-mass energy of 7 TeV with the ATLAS detector*, *Phys. Lett. B* **719** (2013) 261–279, [arXiv:1211.1167].

[282] **ATLAS** Collaboration, G. Aad *et. al.*, *Search for direct slepton and gaugino production in final states with two leptons and missing transverse momentum with the ATLAS detector in pp collisions at $\sqrt{s} = 7$ TeV*, *Phys. Lett. B* **718** (2013) 879–901, [arXiv:1208.2884].

[283] **ATLAS** Collaboration, G. Aad *et. al.*, *Search for the direct production of charginos, neutralinos and staus in final states with at least two hadronically decaying taus and missing transverse momentum in pp collisions at $\sqrt{s} = 8$ TeV with the ATLAS detector*, *JHEP* **10** (2014) 096, [arXiv:1407.0350].

[284] **ATLAS** Collaboration, G. Aad *et. al.*, *Search for direct production of charginos and neutralinos in events with three leptons and missing transverse momentum in $\sqrt{s} = 8$TeV pp collisions with the ATLAS detector*, *JHEP* **04** (2014) 169, [arXiv:1402.7029].

[285] **ATLAS** Collaboration, G. Aad *et. al.*, *Search for supersymmetry in events with four or more leptons in $\sqrt{s} = 8$ TeV pp collisions with the ATLAS detector*, *Phys. Rev. D* **90** (2014), no. 5 052001, [arXiv:1405.5086].

[286] **ATLAS** Collaboration, G. Aad *et. al.*, *Search for direct production of charginos, neutralinos and sleptons in final states with two leptons and missing transverse momentum in pp collisions at $\sqrt{s} = 8$ TeV with the ATLAS detector*, *JHEP* **05** (2014) 071, [arXiv:1403.5294].

[287] **ATLAS** Collaboration, G. Aad *et. al.*, *Search for photonic signatures of gauge-mediated supersymmetry in 8 TeV pp collisions with the ATLAS detector*, *Phys. Rev. D* **92** (2015), no. 7 072001, [arXiv:1507.05493].

[288] **ATLAS** Collaboration, G. Aad *et. al.*, *Search for direct pair production of a chargino and a neutralino decaying to the 125 GeV Higgs boson in $\sqrt{s} = 8$ TeV pp collisions with the ATLAS detector*, *Eur. Phys. J. C* **75** (2015), no. 5 208, [arXiv:1501.07110].

[289] **ATLAS** Collaboration, M. Aaboud *et. al.*, *Search for the direct production of charginos and neutralinos in final states with tau leptons in $\sqrt{s} = 13$ TeV pp collisions with the ATLAS detector*, *Eur. Phys. J. C* **78** (2018), no. 2 154, [arXiv:1708.07875].

[290] **ATLAS** Collaboration, M. Aaboud *et. al.*, *Search for chargino-neutralino production using recursive jigsaw reconstruction in final states with two or three charged leptons in proton-proton collisions at $\sqrt{s} = 13$ TeV with the ATLAS detector*, *Phys. Rev. D* **98** (2018), no. 9 092012, [arXiv:1806.02293].

[291] **ATLAS** Collaboration, M. Aaboud *et. al.*, *Search for photonic signatures of gauge-mediated supersymmetry in 13 TeV pp collisions with the ATLAS detector*, *Phys. Rev. D* **97** (2018), no. 9 092006, [arXiv:1802.03158].

[292] **ATLAS** Collaboration, M. Aaboud *et. al.*, *Search for electroweak production of supersymmetric particles in final states with two or three leptons at $\sqrt{s} = 13$ TeV with the ATLAS detector*, *Eur. Phys. J. C* **78** (2018), no. 12 995, [arXiv:1803.02762].

[293] **ATLAS** Collaboration, M. Aaboud *et. al.*, *Search for chargino and neutralino production in final states with a Higgs boson and missing transverse momentum at $\sqrt{s} = 13$ TeV with the ATLAS detector*, *Phys. Rev. D* **100** (2019), no. 1 012006, [arXiv:1812.09432].

[294] **ATLAS** Collaboration, M. Aaboud *et. al.*, *Search for supersymmetry in events with four or more leptons in $\sqrt{s} = 13$ TeV pp collisions with ATLAS*, *Phys. Rev. D* **98** (2018), no. 3 032009, [arXiv:1804.03602].

[295] **ATLAS** Collaboration, M. Aaboud *et. al.*, *Search for pair production of higgsinos in final states with at least three b-tagged jets in $\sqrt{s} = 13$ TeV pp collisions using the ATLAS detector*, *Phys. Rev. D* **98** (2018), no. 9 092002, [arXiv:1806.04030].

[296] **ATLAS** Collaboration, G. Aad *et. al.*, *Search for electroweak production of charginos and sleptons decaying into final states with two leptons and missing transverse momentum in $\sqrt{s} = 13$ TeV pp collisions using the ATLAS detector*, *Eur. Phys. J. C* **80** (2020), no. 2 123, [arXiv:1908.08215].

[297] **ATLAS** Collaboration, G. Aad *et. al.*, *Search for chargino-neutralino production with mass splittings near the electroweak scale in three-lepton final states in $\sqrt{s}$=13 TeV pp collisions with the ATLAS detector*, *Phys. Rev. D* **101** (2020), no. 7 072001, [arXiv:1912.08479].

[298] **ATLAS** Collaboration, G. Aad *et. al.*, *Search for direct production of electroweakinos in final states with one lepton, missing transverse momentum and a Higgs boson decaying into two b-jets in pp collisions at $\sqrt{s} = 13$ TeV with the ATLAS detector*, *Eur. Phys. J. C* **80** (2020), no. 8 691, [arXiv:1909.09226].

[299] **ATLAS** Collaboration, G. Aad *et. al.*, *Search for direct production of electroweakinos in final states with missing transverse momentum and a Higgs boson decaying into photons in pp collisions at $\sqrt{s}$ = 13 TeV with the ATLAS detector*, *JHEP* **10** (2020) 005, [arXiv:2004.10894].

[300] **ATLAS** Collaboration, G. Aad *et. al.*, *Search for chargino-neutralino pair production in final states with three leptons and missing transverse momentum in $\sqrt{s} = 13$ TeV pp collisions with the ATLAS detector*, *Eur. Phys. J. C* **81** (2021), no. 12 1118, [arXiv:2106.01676].

[301] **ATLAS** Collaboration, G. Aad *et. al.*, *Search for charginos and neutralinos in final states with two boosted hadronically decaying bosons and missing transverse momentum in pp collisions at $\sqrt{s}$ = 13 TeV with the ATLAS detector*, *Phys. Rev. D* **104** (2021), no. 11 112010, [arXiv:2108.07586].

[302] **ATLAS** Collaboration, G. Aad *et. al.*, *Search for supersymmetry in events with four or more charged leptons in 139 fb^{-1} of $\sqrt{s}$ = 13 TeV pp collisions with the ATLAS detector*, *JHEP* **07** (2021) 167, [arXiv:2103.11684].

[303] **ATLAS** Collaboration, *Search for direct pair production of sleptons and charginos decaying to two leptons and neutralinos with mass splittings near the W-boson mass in $\sqrt{s} = 13$ TeV pp collisions with the ATLAS detector*, arXiv:2209.13935.

[304] **ATLAS** Collaboration, *Search for direct production of electroweakinos in final states with one lepton, jets and missing transverse momentum and in p p collisions at $\sqrt{s}$ = 13 TeV with the ATLAS detector*, ATLAS Conference Note ATLAS-CONF-2022-059, 2022.

[305] **ATLAS** Collaboration, *Searches for new phenomena in events with two leptons, jets, and missing transverse momentum in* 139 fb^{-1} *of $\sqrt{s} = 13$ TeV pp collisions with the ATLAS detector*, Tech. Rep. CERN-EP-2022-014, 4, 2022.

[306] **ATLAS** Collaboration, *Search for electroweak SUSY production in final states with two τ-leptons in $\sqrt{s} = 13$ TeV pp collisions with the ATLAS detector*, ATLAS Conference Note ATLAS-CONF-2023-029, 2023.

[307] **ATLAS** Collaboration, *Search for pair-produced Higgsinos decaying via Higgs or Z bosons to final states containing a pair of photons and a pair of b-jets with the ATLAS detector*, ATLAS Conference Note ATLAS-CONF-2023-009, 2023.

[308] **ATLAS** Collaboration, G. Aad *et. al.*, *Search for direct production of winos and higgsinos in events with two same-charge leptons or three leptons in pp collision data at $\sqrt{s} = 13$ TeV with the ATLAS detector*, Tech. Rep. CERN-EP-2023-063, 5, 2023.

[309] **CMS** Collaboration, S. Chatrchyan *et. al.*, *Search for physics beyond the standard model using multilepton signatures in pp collisions at $\sqrt{s} = 7$ TeV*, *Phys. Lett. B* **704** (2011) 411–433, [arXiv:1106.0933].

[310] **CMS** Collaboration, S. Chatrchyan *et. al.*, *Search for electroweak production of charginos and neutralinos using leptonic final states in pp collisions at $\sqrt{s} = 7$ TeV*, *JHEP* **11** (2012) 147, [arXiv:1209.6620].

[311] **CMS** Collaboration, S. Chatrchyan *et. al.*, *Search for anomalous production of multilepton events in pp collisions at $\sqrt{s} = 7$ TeV*, *JHEP* **06** (2012) 169, [arXiv:1204.5341].

[312] **CMS** Collaboration, S. Chatrchyan *et. al.*, *Search for Top Squark and Higgsino Production using Diphoton Higgs Boson Decays*, *Phys. Rev. Lett.* **112** (2014) 161802, [arXiv:1312.3310].

[313] **CMS** Collaboration, V. Khachatryan *et. al.*, *Searches for electroweak production of charginos, neutralinos, and sleptons decaying to leptons and W, Z, and Higgs bosons in pp collisions at 8 TeV*, *Eur. Phys. J. C* **74** (2014), no. 9 3036, [arXiv:1405.7570].

[314] **CMS** Collaboration, V. Khachatryan *et. al.*, *Searches for electroweak neutralino and chargino production in channels with Higgs, Z, and W bosons in pp collisions at 8 TeV*, *Phys. Rev. D* **90** (2014), no. 9 092007, [arXiv:1409.3168].

[315] **CMS** Collaboration, S. Chatrchyan *et. al.*, *Search for anomalous production of events with three or more leptons in pp collisions at $\sqrt{s} = 8$ TeV*, *Phys. Rev. D* **90** (2014) 032006, [arXiv:1404.5801].

[316] **CMS** Collaboration, V. Khachatryan *et. al.*, *Search for supersymmetry in the vector-boson fusion topology in proton-proton collisions at $\sqrt{s} = 8$ TeV*, *JHEP* **11** (2015) 189, [arXiv:1508.07628].

[317] **CMS** Collaboration, V. Khachatryan *et. al.*, *Search for supersymmetry in events with a photon, a lepton, and missing transverse momentum in pp collisions at $\sqrt{s} = 8$ TeV*, *Phys. Lett. B* **757** (2016) 6–31, [arXiv:1508.01218].

[318] **CMS** Collaboration, V. Khachatryan *et. al.*, *Search for electroweak production of charginos in final states with two τ leptons in pp collisions at $\sqrt{s} = 8$ TeV*, *JHEP* **04** (2017) 018, [arXiv:1610.04870].

[319] **CMS** Collaboration, V. Khachatryan *et. al.*, *Search for supersymmetry in electroweak production with photons and large missing transverse energy in pp collisions at $\sqrt{s} = 8$ TeV*, *Phys. Lett. B* **759** (2016) 479–500, [arXiv:1602.08772].

[320] **CMS** Collaboration, A. M. Sirunyan *et. al.*, *Search for supersymmetry with Higgs boson to diphoton decays using the razor variables at $\sqrt{s} = 13$ TeV*, *Phys. Lett. B* **779** (2018) 166–190, [arXiv:1709.00384].

[321] **CMS** Collaboration, A. M. Sirunyan *et. al.*, *Search for gauge-mediated supersymmetry in events with at least one photon and missing transverse momentum in pp collisions at $\sqrt{s} = 13$ TeV*, *Phys. Lett. B* **780** (2018) 118–143, [arXiv:1711.08008].

[322] **CMS** Collaboration, A. M. Sirunyan *et. al.*, *Search for new phenomena in final states with two opposite-charge, same-flavor leptons, jets, and missing transverse momentum in pp collisions at $\sqrt{s} = 13$ TeV*, *JHEP* **03** (2018) 076, [arXiv:1709.08908].

[323] **CMS** Collaboration, A. M. Sirunyan *et. al.*, *Search for electroweak production of charginos and neutralinos in WH events in proton-proton collisions at $\sqrt{s} = 13$ TeV*, *JHEP* **11** (2017) 029, [arXiv:1706.09933].

[324] **CMS** Collaboration, A. M. Sirunyan *et. al.*, *Search for electroweak production of charginos and neutralinos in multilepton final states in proton-proton collisions at $\sqrt{s} = 13$ TeV*, *JHEP* **03** (2018) 166, [arXiv:1709.05406].

[325] **CMS** Collaboration, A. M. Sirunyan *et. al.*, *Search for Higgsino pair production in pp collisions at $\sqrt{s} = 13$ TeV in final states with large missing transverse momentum and two Higgs bosons decaying via $H \to b\bar{b}$*, *Phys. Rev. D* **97** (2018), no. 3 032007, [arXiv:1709.04896].

[326] **CMS** Collaboration, A. M. Sirunyan *et. al.*, *Search for supersymmetry in events with a photon, a lepton, and missing transverse momentum in proton-proton collisions at $\sqrt{s} = 13$ TeV*, *JHEP* **01** (2019) 154, [arXiv:1812.04066].

[327] **CMS** Collaboration, A. M. Sirunyan *et. al.*, *Combined search for electroweak production of charginos and neutralinos in proton-proton collisions at $\sqrt{s} = 13$ TeV*, *JHEP* **03** (2018) 160, [arXiv:1801.03957].

[328] **CMS** Collaboration, A. M. Sirunyan *et. al.*, *Searches for pair production of charginos and top squarks in final states with two oppositely charged leptons in proton-proton collisions at $\sqrt{s} = 13$ TeV*, *JHEP* **11** (2018) 079, [arXiv:1807.07799].

[329] **CMS** Collaboration, A. M. Sirunyan *et. al.*, *Search for supersymmetry in events with a τ lepton pair and missing transverse momentum in proton-proton collisions at $\sqrt{s} = 13$ TeV*, *JHEP* **11** (2018) 151, [arXiv:1807.02048].

[330] **CMS** Collaboration, A. M. Sirunyan *et. al.*, *Search for supersymmetry with a compressed mass spectrum in the vector boson fusion topology with 1-lepton and 0-lepton final states in proton-proton collisions at $\sqrt{s} = 13$ TeV*, *JHEP* **08** (2019) 150, [arXiv:1905.13059].

[331] **CMS** Collaboration, A. M. Sirunyan *et. al.*, *Search for supersymmetry using Higgs boson to diphoton decays at $\sqrt{s} = 13$ TeV*, *JHEP* **11** (2019) 109, [arXiv:1908.08500].

[332] **CMS** Collaboration, A. M. Sirunyan *et. al.*, *Search for supersymmetry in final states with two oppositely charged same-flavor leptons and missing transverse momentum in proton-proton collisions at $\sqrt{s} = 13$ TeV*, *JHEP* **04** (2021) 123, [arXiv:2012.08600].

[333] **CMS** Collaboration, A. Tumasyan *et. al.*, *Search for electroweak production of charginos and neutralinos in proton-proton collisions at $\sqrt{s} = 13$ TeV*, *JHEP* **04** (2022) 147, [arXiv:2106.14246].

[334] **CMS** Collaboration, A. Tumasyan *et. al.*, *Search for chargino-neutralino production in events with Higgs and W bosons using 137 fb^{-1} of proton-proton collisions at $\sqrt{s} = 13$ TeV*, *JHEP* **10** (2021) 045, [arXiv:2107.12553].

[335] **CMS** Collaboration, A. Tumasyan *et. al.*, *Search for electroweak production of charginos and neutralinos at s=13TeV in final states containing hadronic decays of WW, WZ, or WH and missing transverse momentum*, *Phys. Lett. B* **842** (2023) 137460, [arXiv:2205.09597].

[336] **CMS** Collaboration, *Search for new physics in multijet events with at least one photon and large missing transverse momentum in proton-proton collisions at 13 TeV*, CMS Physics Analysis Summary CMS-PAS-SUS-21-009, 2023.

[337] **LHC Higgs Cross Section Working Group** Collaboration, J. R. Andersen *et. al.*, *Handbook of LHC Higgs Cross Sections: 3. Higgs Properties*, arXiv:1307.1347.

[338] **LHC Higgs Cross Section Working Group** Collaboration, D. de Florian *et. al.*, *Handbook of LHC Higgs Cross Sections: 4. Deciphering the Nature of the Higgs Sector*, arXiv:1610.07922.

[339] N. Arkani-Hamed, P. Schuster, N. Toro, J. Thaler, L.-T. Wang, B. Knuteson, and S. Mrenna, *MARMOSET: The Path from LHC Data to the New Standard Model via On-Shell Effective Theories*, hep-ph/0703088.

[340] J. Alwall, P. Schuster, and N. Toro, *Simplified Models for a First Characterization of New Physics at the LHC*, *Phys. Rev. D* **79** (2009) 075020, [arXiv:0810.3921].

[341] J. Alwall, M.-P. Le, M. Lisanti, and J. G. Wacker, *Model-Independent Jets plus Missing Energy Searches*, *Phys. Rev. D* **79** (2009) 015005, [arXiv:0809.3264].

[342] **LHC New Physics Working Group** Collaboration, D. Alves, *Simplified Models for LHC New Physics Searches*, *J. Phys. G* **39** (2012) 105005, [arXiv:1105.2838].

[343] S. Dimopoulos, M. Dine, S. Raby, and S. D. Thomas, *Experimental signatures of low-energy gauge mediated supersymmetry breaking*, *Phys. Rev. Lett.* **76** (1996) 3494–3497, [hep-ph/9601367].

[344] K. T. Matchev and S. D. Thomas, *Higgs and Z boson signatures of supersymmetry*, *Phys. Rev. D* **62** (2000) 077702, [hep-ph/9908482].

[345] J. T. Ruderman and D. Shih, *General Neutralino NLSPs at the Early LHC*, *JHEP* **08** (2012) 159, [arXiv:1103.6083].

[346] G. Bozzi, B. Fuks, and M. Klasen, *Threshold Resummation for Slepton-Pair Production at Hadron Colliders*, *Nucl. Phys. B* **777** (2007) 157–181, [hep-ph/0701202].

[347] J. Debove, B. Fuks, and M. Klasen, *Threshold resummation for gaugino pair production at hadron colliders*, *Nucl. Phys. B* **842** (2011) 51–85, [arXiv:1005.2909].

[348] B. Fuks, M. Klasen, D. R. Lamprea, and M. Rothering, *Gaugino production in proton-proton collisions at a center-of-mass energy of 8 TeV*, *JHEP* **10** (2012) 081, [arXiv:1207.2159].

[349] B. Fuks, M. Klasen, D. R. Lamprea, and M. Rothering, *Precision predictions for electroweak superpartner production at hadron colliders with Resummino*, *Eur. Phys. J. C* **73** (2013) 2480, [arXiv:1304.0790].

[350] B. Fuks, M. Klasen, D. R. Lamprea, and M. Rothering, *Revisiting slepton pair production at the Large Hadron Collider*, *JHEP* **01** (2014) 168, [arXiv:1310.2621].

[351] J. Fiaschi and M. Klasen, *Slepton pair production at the LHC in NLO+NLL with resummation-improved parton densities*, *JHEP* **03** (2018) 094, [arXiv:1801.10357].

[352] J. Fiaschi and M. Klasen, *Neutralino-chargino pair production at NLO+NLL with resummation-improved parton density functions for LHC Run II*, *Phys. Rev. D* **98** (2018), no. 5 055014, [arXiv:1805.11322].

[353] W. Beenakker, M. Klasen, M. Kramer, T. Plehn, M. Spira, and P. M. Zerwas, *The Production of charginos / neutralinos and sleptons at hadron colliders*, *Phys. Rev. Lett.* **83** (1999) 3780–3783, [hep-ph/9906298]. [Erratum: Phys.Rev.Lett. 100, 029901 (2008)].

[354] W. Beenakker, C. Borschensky, M. Krämer, A. Kulesza, and E. Laenen, *NNLL-fast: predictions for coloured supersymmetric particle production at the LHC with threshold and Coulomb resummation*, *JHEP* **12** (2016) 133, [arXiv:1607.07741].

[355] W. Beenakker, R. Hopker, M. Spira, and P. M. Zerwas, *Squark and gluino production at hadron colliders*, *Nucl. Phys. B* **492** (1997) 51–103, [hep-ph/9610490].

[356] A. Kulesza and L. Motyka, *Threshold resummation for squark-antisquark and gluino-pair production at the LHC*, *Phys. Rev. Lett.* **102** (2009) 111802, [arXiv:0807.2405].

[357] A. Kulesza and L. Motyka, *Soft gluon resummation for the production of gluino-gluino and squark-antisquark pairs at the LHC*, *Phys. Rev. D* **80** (2009) 095004, [arXiv:0905.4749].

[358] W. Beenakker, S. Brensing, M. Kramer, A. Kulesza, E. Laenen, and I. Niessen, *Soft-gluon resummation for squark and gluino hadroproduction*, *JHEP* **12** (2009) 041, [arXiv:0909.4418].

[359] W. Beenakker, S. Brensing, M. Kramer, A. Kulesza, E. Laenen, and I. Niessen, *NNLL resummation for squark-antisquark pair production at the LHC*, *JHEP* **01** (2012) 076, [arXiv:1110.2446].

[360] W. Beenakker, T. Janssen, S. Lepoeter, M. Krämer, A. Kulesza, E. Laenen, I. Niessen, S. Thewes, and T. Van Daal, *Towards NNLL resummation: hard matching coefficients for squark and gluino hadroproduction*, *JHEP* **10** (2013) 120, [arXiv:1304.6354].

[361] W. Beenakker, C. Borschensky, M. Krämer, A. Kulesza, E. Laenen, V. Theeuwes, and S. Thewes, *NNLL resummation for squark and gluino production at the LHC*, *JHEP* **12** (2014) 023, [arXiv:1404.3134].

[362] **CMS** Collaboration, V. Khachatryan *et. al.*, *Measurements of Inclusive W and Z Cross Sections in pp Collisions at $\sqrt{s} = 7$ TeV*, *JHEP* **01** (2011) 080, [arXiv:1012.2466].

[363] P. Nason, *A New method for combining NLO QCD with shower Monte Carlo algorithms*, *JHEP* **11** (2004) 040, [hep-ph/0409146].

[364] S. Frixione, P. Nason, and C. Oleari, *Matching NLO QCD computations with Parton Shower simulations: the POWHEG method*, *JHEP* **11** (2007) 070, [arXiv:0709.2092].

[365] S. Alioli, P. Nason, C. Oleari, and E. Re, *NLO single-top production matched with shower in POWHEG: s- and t-channel contributions*, *JHEP* **09** (2009) 111, [arXiv:0907.4076]. [Erratum: JHEP 02, 011 (2010)].

[366] S. Alioli, P. Nason, C. Oleari, and E. Re, *A general framework for implementing NLO calculations in shower Monte Carlo programs: the POWHEG BOX*, *JHEP* **06** (2010) 043, [arXiv:1002.2581].

[367] E. Re, *Single-top Wt-channel production matched with parton showers using the POWHEG method*, *Eur. Phys. J. C* **71** (2011) 1547, [arXiv:1009.2450].

[368] S. Bolognesi, Y. Gao, A. V. Gritsan, K. Melnikov, M. Schulze, N. V. Tran, and A. Whitbeck, *On the spin and parity of a single-produced resonance at the LHC*, *Phys. Rev. D* **86** 095031, [arXiv:1208.4018].

[369] A. V. Gritsan, R. Röntsch, M. Schulze, and M. Xiao, *Constraining anomalous Higgs boson couplings to the heavy flavor fermions using matrix element techniques*, *Phys. Rev. D* **94** (2016), no. 5 055023, [arXiv:1606.03107].

[370] T. Sjöstrand, S. Ask, J. R. Christiansen, R. Corke, N. Desai, P. Ilten, S. Mrenna, S. Prestel, C. O. Rasmussen, and P. Z. Skands, *An introduction to PYTHIA 8.2*, *Comput. Phys. Commun.* **191** (2015) 159–177, [arXiv:1410.3012].

[371] M. L. Mangano, M. Moretti, F. Piccinini, and M. Treccani, *Matching matrix elements and shower evolution for top-quark production in hadronic collisions*, *JHEP* **01** (2007) 013, [hep-ph/0611129].

[372] R. Frederix and S. Frixione, *Merging meets matching in MC@NLO*, *JHEP* **12** (2012) 061, [arXiv:1209.6215].

[373] **CMS** Collaboration, *Event generator tunes obtained from underlying event and multiparton scattering measurements*, *Eur. Phys. J. C* **76** (2016), no. 3 155, [arXiv:1512.00815].

[374] **CMS** Collaboration, A. M. Sirunyan *et. al.*, *Extraction and validation of a new set of CMS PYTHIA8 tunes from underlying-event measurements*, *Eur. Phys. J. C* **80** (2020), no. 1 4, [arXiv:1903.12179].

[375] M. Czakon, P. Fiedler, and A. Mitov, *Total Top-Quark Pair-Production Cross Section at Hadron Colliders Through $O(\alpha_S^4)$*, *Phys. Rev. Lett.* **110** (2013) 252004, [arXiv:1303.6254].

[376] M. Czakon and A. Mitov, *Top++: A Program for the Calculation of the Top-Pair Cross-Section at Hadron Colliders*, *Comput. Phys. Commun.* **185** (2014) 2930, [arXiv:1112.5675].

[377] **Particle Data Group** Collaboration, M. Tanabashi *et. al.*, *Review of Particle Physics*, *Phys. Rev. D* **98** (2018), no. 3 030001.

[378] R. Gavin, Y. Li, F. Petriello, and S. Quackenbush, *FEWZ 2.0: A code for hadronic Z production at next-to-next-to-leading order*, *Comput. Phys. Commun.* **182** (2011) 2388–2403, [arXiv:1011.3540].

[379] R. Gavin, Y. Li, F. Petriello, and S. Quackenbush, *W Physics at the LHC with FEWZ 2.1*, *Comput. Phys. Commun.* **184** (2013) 208–214, [arXiv:1201.5896].

[380] Y. Li and F. Petriello, *Combining QCD and electroweak corrections to dilepton production in FEWZ*, *Phys. Rev. D* **86** (2012) 094034, [arXiv:1208.5967].

[381] T. Gehrmann, M. Grazzini, S. Kallweit, P. Maierhöfer, A. von Manteuffel, S. Pozzorini, D. Rathlev, and L. Tancredi, W^+W^- *Production at Hadron Colliders in Next to Next to Leading Order QCD*, *Phys. Rev. Lett.* **113** (2014), no. 21 212001, [arXiv:1408.5243].

[382] F. Cascioli, T. Gehrmann, M. Grazzini, S. Kallweit, P. Maierhöfer, A. von Manteuffel, S. Pozzorini, D. Rathlev, L. Tancredi, and E. Weihs, *ZZ production at hadron colliders in NNLO QCD*, *Phys. Lett. B* **735** (2014) 311–313, [arXiv:1405.2219].

[383] **CMS** Collaboration, S. Chatrchyan *et. al.*, *Search for Top-Squark Pair Production in the Single-Lepton Final State in pp Collisions at* $\sqrt{s}$ *= 8 TeV*, *Eur. Phys. J. C* **73** (2013), no. 12 2677, [arXiv:1308.1586].

[384] **CMS** Collaboration, A. M. Sirunyan *et. al.*, *Measurement of the inelastic proton-proton cross section at* $\sqrt{s} = 13$ *TeV*, *JHEP* **07** (2018) 161, [arXiv:1802.02613].

[385] **ATLAS, CMS, LHC Higgs Combination Group** Collaboration, *Procedure for the LHC Higgs boson search combination in Summer 2011*, Tech. Rep. CMS-NOTE-2011-005, ATL-PHYS-PUB-2011-011, ATL-PHYS-PUB-2011-11, 8, 2011.

[386] J. Neyman and E. S. Pearson, *On the Problem of the Most Efficient Tests of Statistical Hypotheses*, *Phil. Trans. Roy. Soc. Lond. A* **231** (1933), no. 694-706 289–337.

[387] J. Neyman, *Outline of a Theory of Statistical Estimation Based on the Classical Theory of Probability*, *Phil. Trans. Roy. Soc. Lond. A* **236** (1937), no. 767 333–380.

[388] G. Cowan, K. Cranmer, E. Gross, and O. Vitells, *Asymptotic formulae for likelihood-based tests of new physics*, *Eur. Phys. J. C* **71** (2011) 1554, [arXiv:1007.1727]. [Erratum: Eur.Phys.J.C 73, 2501 (2013)].

[389] T. Junk, *Confidence level computation for combining searches with small statistics*, *Nucl. Instrum. Meth. A* **434** (1999) 435–443, [hep-ex/9902006].

[390] A. L. Read, *Presentation of search results: The CL(s) technique*, *J. Phys. G* **28** (2002) 2693–2704.

[391] I. Antcheva *et. al.*, *ROOT: A C++ framework for petabyte data storage, statistical analysis and visualization*, *Comput. Phys. Commun.* **180** (2009) 2499–2512, [arXiv:1508.07749].

[392] L. Moneta, K. Belasco, K. S. Cranmer, S. Kreiss, A. Lazzaro, D. Piparo, G. Schott, W. Verkerke, and M. Wolf, *The RooStats Project*, *PoS* **ACAT2010** (2010) 057, [arXiv:1009.1003].

[393] W. Verkerke and D. P. Kirkby, *The RooFit toolkit for data modeling*, *eConf* **C0303241** (2003) MOLT007, [physics/0306116].

[394] D. Kovalskyi, M. Tadel, A. Mrak-Tadel, B. Bellenot, V. Kuznetsov, C. D. Jones, L. Bauerdick, M. Case, J. Mulmenstadt, and A. Yagil, *Fireworks: A Physics Event Display for CMS*, *J. Phys. Conf. Ser.* **219** (2010) 032014.

[395] C. G. Lester and D. J. Summers, *Measuring masses of semiinvisibly decaying particles pair produced at hadron colliders*, *Phys. Lett. B* **463** (1999) 99–103, [hep-ph/9906349].

[396] A. Barr, C. Lester, and P. Stephens, *m(T2): The Truth behind the glamour*, *J. Phys. G* **29** (2003) 2343–2363, [hep-ph/0304226].

[397] D. R. Tovey, *On measuring the masses of pair-produced semi-invisibly decaying particles at hadron colliders*, *JHEP* **04** (2008) 034, [arXiv:0802.2879].

[398] **ATLAS** Collaboration, G. Aad *et. al.*, *A search for the $Z\gamma$ decay mode of the Higgs boson in pp collisions at $\sqrt{s}$ = 13 TeV with the ATLAS detector*, *Phys. Lett. B* **809** (2020) 135754, [arXiv:2005.05382].

[399] **CMS** Collaboration, A. Tumasyan *et. al.*, *Search for Higgs boson decays to a Z boson and a photon in proton-proton collisions at $\sqrt{s}$ = 13 TeV*, *JHEP* **05** (2023) 233, [arXiv:2204.12945].

[400] A. Hocker *et. al.*, *TMVA - Toolkit for Multivariate Data Analysis*, tech. rep., 3, 2007.

[401] Y. Freund and R. E. Schapire, *A Decision-Theoretic Generalization of On-Line Learning and an Application to Boosting*, *J. Comput. Syst. Sci.* **55** (1997), no. 1 119–139.

[402] A. Kolmogorov, *Sulla determinazione empirica di una legge di distribuzione*, *G. Ist. Ital. Attuari* **4** (1933) 83–91.

[403] N. Smirnov, *Table for estimating the goodness of fit of empirical distributions*, *Annals of Mathematical Statistics* **19** (1948), no. 2 279–281.

[404] **ATLAS** Collaboration, *SUSY Summary Plots March 2022*, 2022. `http://cds.cern.ch/record/2805985`.

[405] **CMS** Collaboration, A. Tumasyan *et. al.*, *Combined searches for the production of supersymmetric top quark partners in proton–proton collisions at* $\sqrt{s} = 13$ *TeV*, *Eur. Phys. J. C* **81** (2021), no. 11 970, [arXiv:2107.10892].

[406] H. Fukuda, N. Nagata, H. Oide, H. Otono, and S. Shirai, *Cornering Higgsinos Using Soft Displaced Tracks*, *Phys. Rev. Lett.* **124** (2020), no. 10 101801, [arXiv:1910.08065].

[407] **LEP2 SUSY Working Group, ALEPH, DELPHI, L3, OPAL** Collaboration, *Combined LEP Chargino Results, up to 208 GeV for large m0* , Tech. Rep. LEPSUSYWG/01-03.1, 2001. `https://lepsusy.web.cern.ch/lepsusy/www/inos_moriond01/charginos_pub.html`.

[408] **LEP2 SUSY Working Group, ALEPH, DELPHI, L3, OPAL** Collaboration, *Combined LEP Chargino Results, up to 208 GeV for low DM*, Tech. Rep. LEPSUSYWG/02-04.1, 2002. `https://lepsusy.web.cern.ch/lepsusy/www/inoslowdmsummer02/charginolowdm_pub.html`.

[409] T. R. Slatyer, *Indirect Detection of Dark Matter*, in *Theoretical Advanced Study Institute in Elementary Particle Physics: Anticipating the Next Discoveries in Particle Physics*, pp. 297–353, 2018. arXiv:1710.05137.

[410] C. Cesarotti, Q. Lu, Y. Nakai, A. Parikh, and M. Reece, *Interpreting the Electron EDM Constraint*, *JHEP* **05** (2019) 059, [arXiv:1810.07736].

[411] B. Batell, M. Low, E. T. Neil, and C. B. Verhaaren, *Review of Neutral Naturalness*, in *Snowmass 2021*, 3, 2022. arXiv:2203.05531.

[412] D. B. Kaplan and H. Georgi, *SU(2) x U(1) Breaking by Vacuum Misalignment*, *Phys. Lett. B* **136** (1984) 183–186.

[413] D. B. Kaplan, H. Georgi, and S. Dimopoulos, *Composite Higgs Scalars*, *Phys. Lett. B* **136** (1984) 187–190.

[414] M. J. Dugan, H. Georgi, and D. B. Kaplan, *Anatomy of a Composite Higgs Model*, *Nucl. Phys. B* **254** (1985) 299–326.

[415] N. Arkani-Hamed, S. Dimopoulos, and G. R. Dvali, *The Hierarchy problem and new dimensions at a millimeter*, *Phys. Lett. B* **429** (1998) 263–272, [hep-ph/9803315].

[416] I. Antoniadis, N. Arkani-Hamed, S. Dimopoulos, and G. R. Dvali, *New dimensions at a millimeter to a Fermi and superstrings at a TeV*, *Phys. Lett. B* **436** (1998) 257–263, [hep-ph/9804398].

[417] P. W. Graham, D. E. Kaplan, and S. Rajendran, *Cosmological Relaxation of the Electroweak Scale*, *Phys. Rev. Lett.* **115** (2015), no. 22 221801, [arXiv:1504.07551].

[418] N. Arkani-Hamed, T. Cohen, R. T. D'Agnolo, A. Hook, H. D. Kim, and D. Pinner, *Solving the Hierarchy Problem at Reheating with a Large Number of Degrees of Freedom*, *Phys. Rev. Lett.* **117** (2016), no. 25 251801, [arXiv:1607.06821].